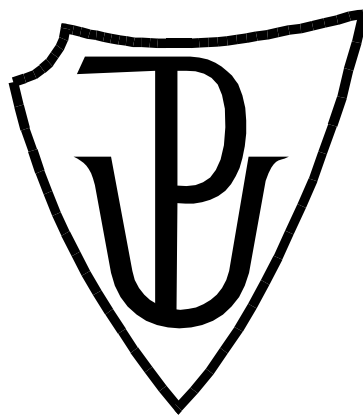


**PALACKÝ UNIVERSITY OLOMOUČ**

**Faculty of Science**

**Department of Biochemistry**



**Dynamic properties of membranes, cytoskeleton and  
reactive oxygen species during polar growth of  
plant cells**

**Ph.D. Thesis**

**Author: Mgr. Lenka Kuběnová (Vaškebová)**

**Study program: P1416 Biochemistry**

**Supervisor: prof. Mgr. Miroslav Ovečka, Ph.D.**

**Form of study: Full-time study**

**Submitted: September 2022**

I hereby declare that this Ph.D. thesis has been written solely by me. All the sources cited in this thesis are listed in the reference list. All published results included in this work are approved by co-authors.

In Olomouc .....

.....

Lenka Kuběnová

## Poděkování

Největší poděkování patří mému školiteli prof. Mirovi Ovečkovi, za zodpovědné a odborné vedení po celou dobu mého vysokoškolského studia; za všechny cenné rady a za čas, který mi vždy ochotně věnoval.

Dále bych chtěla poděkovat vedoucímu katedry Biotechnologií prof. Jozefovi Šamajovi, díky němuž celá práce mohla vzniknout a také za přínosné diskuze, rady a nápady.

Samozřejmě bych chtěla poděkovat celému kolektivu katedry Biotechnologií, kteří byli vždy přátelští; a za cenné diskuze, rady a ochotu vždy pomoci, kdykoliv bylo potřeba.

Během studia jsem měla možnost strávit tři měsíce na zahraniční stáži v Max-Planck Institutu v Dráďanech. Proto bych chtěla poděkovat Dr. Pavlovi Tomančákovi za umožnění této stáže v jeho laboratoři, celému jeho kolektivu, a především Dr. Sabastianovi Bundschuhovi, že měl trpělivost mě naučit nové mikroskopické techniky.

Speciální poděkování patří mému manželovi Martinovi, za neuvěřitelnou trpělivost a podporu, bez které bych to nezvládla a mému úžasnému synovi Matouškovi, který mi vždy dokáže vytvořit úsměv na tváři. Bez pochyby však i zbytku rodiny za podporu a ochotu mě vždy vyslechnout a za to, že ve mně vždy věří.

Tato práce byla z největší části financována Grantovou agenturou České Republiky (GAČR), 19-18675S, na téma „Objasnění rolí aktinu, NADP oxidázy a strukturních sterolů ve vrcholovém růstu kořenových vlásků pomocí pokročilé mikroskopie a proteomiky” a Evropským fondem pro regionální rozvoj (ERDF), projekt č. CZ.02.1.01/0.0/0.0/16\_019/0000827, „Rostliny jako prostředek udržitelného globálního rozvoje”. Dále pak byla podpořena studentským IGA projektem (IGA\_PrF\_2016\_012; IGA\_PrF\_2022\_014) Přírodovědecké fakulty, Univerzity Palackého v Olomouci.

## **Acknowledgements**

The greatest thanks belong to my supervisor prof. Miroslav Ovečka, for responsible and professional leadership throughout my university studies; for all the valuable advices and for his precious time, which he always willingly gave to me.

My thanks further belong to prof. Jozef Šamaj, the leader of Department of Biotechnology, not only for his willingness to provide the infrastructure for the experiments, but also for helpful discussions, suggestions and ideas.

I also would like to thank my colleagues from the Department of Biotechnology, which were always very friendly and for their useful advices, discussions and willingness to help whenever I needed it.

During my Ph.D. studies, I completed a three-month internship at the Max-Planck Institute in Dresden. Therefore, many thanks to Dr. Pavel Tomančák, who is the leader of the income laboratory, to his entire team, and especially thanks mainly to Dr. Sebastian Bundschuh for teaching me new microscopic techniques.

Finally, I would specially like to thank my husband Martin for his incredible patience and support, without which I could not have done it; to my wonderful son Matoušek, who always manages to put a smile on my face and also, to the rest of my family for their willingness to always listen to me and for their amazing faith in me.

This work was supported by the Czech Science Foundation (GAČR), grants no. 19-18675S, with topic “Clarification of actin, NADPH oxidase and structural sterol roles in root hair tip growth using advanced microscopy and proteomics.“, by European Regional Development Fund (ERDF), project “Plants as a tool for sustainable global development” No. CZ.02.1.01/0.0/0.0/16\_019/0000827, and also by student grants provided by Palacký University, IGA PřF UP (IGA\_PrF\_2016\_012; IGA\_PrF\_2022\_014).

## Bibliografická identifikace

Jméno a příjmení autora:	Mgr. Lenka Kuběnová (Vaškebová)
Název práce:	Dynamika membrán, cytoskeletu a reaktivních forem kyslíku při polárním růstu rostlinných buněk
Typ práce:	Disertační
Pracoviště:	Katedra biotechnologií, Přírodovědecká fakulta, Univerzita Palackého v Olomouci
Vedoucí práce:	prof. Mgr. Miroslav Ovečka, Ph.D.
Rok obhajoby práce:	2022
Klíčová slova:	<i>A. thaliana</i> , abiotický stres, ACTIN2, cytoskelet, konfokální mikroskopie s Airyscan detektorem, kořenové vlásky, “ligh-sheet” mikroskopie, mikroskopie s rotujícím diskem, NADPH oxidasa (RHD2), polární růst, pozorování živých buněk, steroly, vesikulární transport, vývoj kořene
Počet stran:	175
Počet příloh:	0
Jazyk:	Anglický

### Abstrakt

Kořenové vlásky a jejich apikální růst slouží jako excelentní model pro studium polárního prodlužování buněk. Díky nim je rostlina stabilněji ukotvena v půdě, zvětšují povrch kořenového systému, což vede k efektivnějšímu příjmu vody a živin, a v neposlední řadě se podílejí na interakci s mikroby. Iniciace a následný polární růst kořenových vlásků je velice složitý proces, který zahrnuje mnoho navzájem propojených mechanismů. Mezi nezbytné děje nutné k založení a udržení polárního růstu kořenových vlásků patří polarizace cytoskeletu, vezikulární transport a lokalizované ukládání buněčné stěny v místě trichoblastu, ze kterého budoucí kořenových vlásek vyrůstá. Současný stav poznání, zabývající se právě procesy vývoje kořenových vlásků a jejich polárního růstu,

je shrnutý v teoretické části této disertační práce. Hlavním cílem praktické části byla důkladná charakteristika dvou rozdílných mutantů (*der1-3* a *rhd2-1*) rostlin *Arabidopsis thaliana*, kteří mají poruchu růstu kořenových vlásků.

Mutant *der1-3* („*defective root hairs 1*“) má bodovou mutaci v *ACTIN2* genu. *ACTIN2* je nejvíce se vyskytující isovarianta aktinu ze skupiny isovariant vegetativního aktinu. *ACTIN2* je zároveň nezbytnou součástí mechanismu růstu kořenových vlásků. Identifikace *der1-3* mutantu byla proto založená na vyhledávání fenotypu krátkých kořenových vlásků. Pomocí důkladného fenotypování rostlin, studia pletiv kořenového systému a analýz na subcelulární úrovni jsme zjistili, že mutace v *ACT2* genu má výraznější efekt na celkový vývoj a růst rostlin, což v předchozích studiích tohoto mutantu popsáno nebylo. Dále pak, díky lepším růstovým parametrům, zvýšené dynamiky aktinového cytoskeletu a účinnější biochemické ochrany *der1-3* mutantu po působení oxidativního stresu bylo zjištěno, že je více odolný na tento typ stresu oproti kontrolním rostlinám. Získané výsledky podpořili fakt, že aktinový cytoskelet nehraje roli jen při růstu a vývoji rostlin a kořenových vlásků, ale že ovlivňuje i reakci rostlin na oxidativní stres. To vše dohromady by mohlo mít slibný potenciál v budoucím zemědělském a biotechnologickém využití.

V apikální části plazmatické membrány (PM) rostoucích kořenových vlásků *A. thaliana* se nachází NADPH oxidasa typu C, pojmenována jako „respiratory burst oxidase homolog protein C/ROOT HAIR-DEFECTIVE 2“ (*AtRBOHC/RHD2*). Tato oxidasa tvoří reaktivní formy kyslíku (ROS), které mimo jiné udržují polární růst kořenových vlásků. Bodová mutace v *RHD2* genu způsobuje fenotyp krátkých kořenových vlásků, čímž je *rhd2-1* („*root hair defective 2*“) mutant charakteristický. V této části jsme detailně popsali časoprostorovou distribuci a dynamické vlastnosti transportu *AtRBOHC/RHD2* proteinu do plazmatické membrány rostoucích kořenových vlásků. S využitím různých pokročilých mikroskopických metod a pomocí následných kvantitativních mikroskopických analýz, trasování jednotlivých kompartmentů a pomocí subcelulárních kolokalizací jsme popsali komplexní mechanismus transportu a recyklace *AtRBOHC/RHD2* v rámci apikální PM během tvorby a následného apikálního růstu kořenového vlásku u *Arabidopsis*.

Nová data, prezentovaná v této disertační práci, byla získána s využitím pokročilých mikroskopických metod pro rychlé snímání dynamických procesů (konfokální mikroskopie s rotujícím diskem), dlouhodobé vývojové snímání za podmínek, blízcích se těm environmentálním („*light-sheet*“ fluorescenční mikroskopie)

a pro snímání s vysokým rozlišením (konfokální laserová skenovací mikroskopie s Airyscan detektorem). Kombinace nižší míry fototoxicity, většího rozlišení a vyšší rychlosti snímání v průběhu delšího časového úseku umožnila studium živých rostlin v téměř přirozených podmínkách, přinášející fyziologicky relevantní výsledky.

## Bibliographic identification

Name and surname:	Mgr. Lenka Kuběnová (Vaškebová)
Title of thesis:	Dynamic properties of membranes, cytoskeleton and reactive oxygen species during polar growth of plant cells.
Type of thesis:	Ph.D.
Department:	Department of Biotechnology, Faculty of Science, Palacký University in Olomouc
Supervisor:	prof. Mgr. Miroslav Ovečka, Ph.D.
Year of defence:	2022
Keywords:	<i>A. thaliana</i> , abiotic stress, ACTIN2, Airyscan confocal microscopy, cytoskeleton, light-sheet microscopy, live-cell imaging, NADPH oxidase (RHD2), polar growth, root development, root hairs, spinning-disk microscopy, sterols, vesicular transport
Numer of pages:	175
Number of appendixes:	0
Language:	English

## Abstract

Root hair (RH) tip growth represents an excellent model of polar apical cell expansion in plants. RHs play important functions in anchoring plants in soil, increasing root absorption surface for water a nutrient uptake, and interactions with microbes. The process of RH initiation and RH tip growth maintenance is a complex process. It requires polarization of the cytoskeleton, membrane trafficking, and localized cell wall deposition at the RH initiation side of the trichoblasts. The current knowledge linked to the process of RH formation and tip growth is summarized in the theoretical part of the thesis. The



main topic of the thesis was thorough characterization of two different *Arabidopsis thaliana* mutants (*der1-3* and *rhd2-1*), that are defective in RH tip growth.

The mutant *der1-3* (*deformed root hairs 1*) possess a single-point mutation in the *ACTIN2* gene. Product of this gene, ACTIN2, is the most abundant vegetative actin isoform, and is required for RH tip growth. Based on this fact, *der1-3* mutant was identified according to its RH phenotype. Our thorough plant phenotyping, tissue patterning, and subcellular localization analyses revealed that this mutation in the *ACT2* gene has deeper effects on plant growth and development, which has not known before. Moreover, we found that *der1-3* mutant is more resistant to mild and severe oxidative stress. This was demonstrated by better growth parameters, enhanced preservation of actin dynamics, and more effective biochemical protection of the mutant in stress conditions. These data supported better understanding of the actin cytoskeleton roles not only in plant growth and development, but also in plant reactions to oxidative stress, which is promising for potential future agricultural and biotechnological applications.

NADPH oxidase type C in *A.thaliana*, annotated as respiratory burst oxidase homolog protein C/ROOT HAIR-DEFECTIVE 2 (AtRBOHC/RHD2), is localized at the apical plasma membrane (PM) of growing RHs where generates reactive oxygen species (ROS), indispensable for the maintenance of the RH tip growth. Single point mutation in *RBOHC/RHD2* gene generates mutant *rhd2* (*root hair defective 2*) with RH phenotype. We characterised in detail the spatiotemporal pattern and mechanism of the AtRBOHC/RHD2 subcellular delivery to the PM during RH formation. Quantitative microscopy, single particle tracking, and subcellular colocalization analyses using different advanced microscopic methods demonstrated the complex nature of AtRBOHC/RHD2 delivery, maintenance, and recycling at the apical PM during RH formation in *Arabidopsis*.

Novel data presented in the thesis were received by utilization of advanced microscopy methods for fast image acquisition (spinning disk confocal microscopy), near environmental developmental imaging (light-sheet fluorescence microscopy), and super-resolution (Airyscan confocal laser scanning microscopy). Combining lower value of phototoxicity, enhanced resolution, and faster imaging speed with longer observation allowed study of living plants in almost natural conditions, bringing physiologically relevant results.

## Content

<b>1. Aims of the thesis.....</b>	<b>12</b>
<b>2. Current state-of-the-art .....</b>	<b>13</b>
2.1 <i>Arabidopsis thaliana</i> as a model organism .....	13
2.2 Anatomical structure of <i>Arabidopsis</i> primary root .....	13
2.3 Root hairs and polar growth.....	15
2.3.1 Trichoblast/atrichoblast determination.....	15
2.3.2 Polar growth of root hairs .....	15
2.3.3 Sub-cellular organization and polarity of root hairs .....	17
2.4 Essential factors influencing the polar tip growth of root hairs .....	19
2.4.1 Organization and dynamics of the endomembrane system.....	19
2.4.2 Structural sterols and lipid rafts .....	23
2.4.3 Reactive oxygen species .....	26
2.4.4 Microtubules and actin cytoskeleton.....	31
2.5 Conventional and advanced microscopy techniques.....	36
2.5.1 Confocal laser scanning microscopy (CLSM) .....	37
2.5.2 Spinning-disk microscopy (SD).....	38
2.5.3 Airyscan confocal laser scanning microscopy (ACLSM).....	39
2.5.4 Light-sheet fluorescence microscopy (LSFM).....	40
<b>3. Materials and methods .....</b>	<b>43</b>
3.1 Plant material and growth conditions.....	43
3.2 Transformation and crossing.....	44
3.3 Application of stress factors.....	45
3.4 Phenotypic analysis .....	46
3.4.1 Phenotype, growth and biomass production of <i>der1-3</i> mutant plants.....	46
3.4.2 Oxidative stress .....	46
3.5 Immunolabelling of microtubules by the whole-mount method.....	47

3.6 Histochemical detection of O <sup>2+</sup> and H <sub>2</sub> O <sub>2</sub> production .....	47
3.7 Modelling of ACTIN2 protein structure .....	48
3.8 Preparation of samples for microscopy .....	48
3.9 Application of stress factors directly at the microscope stage .....	49
3.10 FM4-64 and phalloidin staining .....	49
3.11 Filipin III and auxinole application.....	50
3.12 Microscopic imaging.....	51
3.12.1 Epifluorescence microscopy .....	51
3.12.2 Spinning disk microscopy (SD) .....	51
3.12.3 Confocal laser scanning microscopy (CLSM) .....	53
3.12.4. Airyscan confocal laser scanning microscopy (Airyscan CLSM) .....	54
3.12.5 Light-sheet fluorescence microscopy (LSFM).....	55
3.12.6 Data acquisition and analysis .....	56
<b>4. Results .....</b>	<b>57</b>
4.1 Single-point <i>ACT2</i> gene mutation in the <i>Arabidopsis</i> root hair mutant <i>der1-3</i> affects overall actin organization, root growth and plant development.....	57
4.2 Single amino acid exchange in ACTIN2 confers increased tolerance to oxidative stress in <i>Arabidopsis der1-3</i> mutant.....	72
4.2.1 Supplements .....	98
4.3 ROOT HAIR DEFECTIVE 2 vesicular delivery to the apical plasma membrane domain during <i>Arabidopsis</i> root hair development.....	102
4.3.1 Supplements .....	127
<b>5. General conclusions .....</b>	<b>136</b>
<b>6. References .....</b>	<b>146</b>
<b>7. Abbreviations .....</b>	<b>168</b>
<b>8. Curriculum vitae .....</b>	<b>173</b>

## **1. Aims of the thesis**

- Summary of the recent knowledge on polar growth of plant cells (especially on root hair growth) and its regulation at molecular and cellular levels, in particular the proportion of vesicular transport, cytoskeleton and signalling of reactive oxygen species (ROS).
- Optimization of cultivation conditions; test of different types, quality, composition and mechanic properties of cultivation media and conditions for long-term experiments of continuous primary root growth and root hairs development under the physiological conditions.
- Preparation of transgenic plants with control or mutant genotype (carrying genetically encoded markers for actin cytoskeleton, vesicular transport, and NADPH oxidase) by crossing or transformation and their subsequent selection and genotyping.
- Microscopic study of structural and dynamic parameters of the cytoskeleton and endosomal compartments during root hair development in living transgenic plants.
- Qualitative and quantitative evaluations of mutant root hair growth with fluorescence markers expression and observation of interactions between plasma membrane, endosomal compartments, and cytoskeleton during individual stages of root hair tip growth.

## **2. Current state-of-the-art**

### **2.1 *Arabidopsis thaliana* as a model organism**

*Arabidopsis thaliana* (L.) Heynh, is a small annual dicotyledonous plant belonging to the *Brassicaceae* family. *Arabidopsis* was established as a model organism in 1985 (Meyerowitz and Pruitt, 1985) due to its short life cycle, enough seeds in the next generation, simple anatomical and morphological organization of organs and tissues, and small genome size (Meyerowitz, 2001). The *Arabidopsis* genome is organized into five chromosomes, contains approximately 25 500 genes and it was completely sequenced in 2000 (The *Arabidopsis* Genome Initiative, 2000). Plants of *A. thaliana* are widely used as model also in all fields of plant biology, mainly because their individual organs generally have a small number of cell layers, and therefore one can observe them microscopically as a whole without the need to prepare anatomical sections (Boerjan *et al.*, 1992; Koornneef and Meinke 2010).

### **2.2 Anatomical structure of *Arabidopsis* primary root**

The root is vegetative, leafless, underground plant organ, which firmly anchors the plant in the soil. Its main functions are especially water and nutrient uptake, gravitropic growth, and mediating the plant's relationship with soil microorganisms. The root system of dicots consists of one primary root with lateral roots of different orders (Foreman and Dolan, 2001). The longitudinal zonation of primary root tip consists of 4 consecutive zones (Figure 1A). First is a meristematic zone, which together with population of cells dividing mitotically contains also stem cells and root initials in stem cell niche. Then follows a transition zone in which cells terminating cell division are prepared for rapid cell elongation in the subsequent elongation zone. In the proximal part of the elongation zone, root hairs (RHs) also start to be formed. The last is differentiation zone, where elongated cells acquire their final function and RHs continue to develop and grow (Dolan *et al.*, 1993).

The radial zonation of *Arabidopsis thaliana* primary root is a well-defined, formed from cell layers arranged in concentric cylinders (Figure 1B). Simplicity of this arrangement serves as a model for the study of plant organogenesis. Peripherally is located the epidermis, which consists of trichoblast and atrichoblast epidermal cells. Trichoblasts are cells, from which RHs grow and atrichoblasts are cells without RHs. This is partially controlled by a topological signalling, as trichoblasts are normally

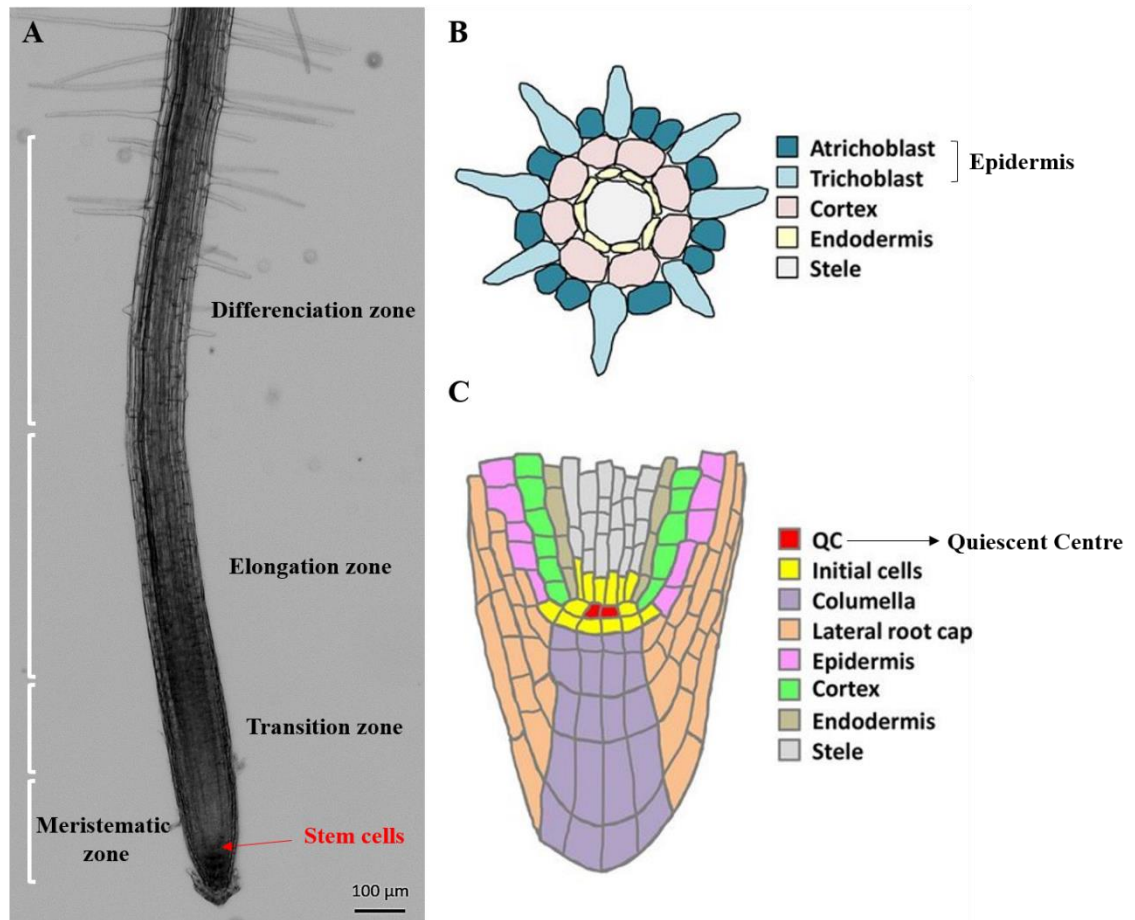


**Figure 1: Root anatomical structure.** (A) Individual zones of the *Arabidopsis* primary root. (B) Transverse section of a root at an early stage of root hairs. (C) Organization of cells in the root tip. Adapted from Takatsuka and Umeda (2015).

in contact with two cortical cells and atrichoblasts with only one (Figure 1B). On the radial section it is obvious that, trichoblasts are located above the anticlinal walls of cortical cells and atrichoblasts are located along the outer periclinal walls of cortical cells (Dolan *et al.*, 1994). The next layer is the cortex, then the endodermis and the root central cylinder, forming stele. The stele comprises of the vascular tissues (xylem, phloem and vascular parenchyme) surrounded by associated supporting tissue (pericycle). Xylem transports water upwards and transport of photosynthesis products from sources to sinks and various signal molecules is secured by phloem (Benfey and Scheres, 2000; Takatsuka and Umeda, 2015). All mentioned plants tissues have a basis in initials cells of root tip meristematic zone (Figure 1C). The root meristematic zone begins with four sets of initial cells that surround a quiescent centre. The quiescent centre is made up of mitotically inactive cells (Scheres *et al.*, 2002). The most apical part of the root is called the root cap, which consists of lateral root cap cells and columella cells (Figure 1C). The root cap

secretes slime, which protects root apex, especially root apical meristems during the growth in substrate. Columella cells (called statocysts) contain statoliths (plastids with giant and numerous starch grains), which sediment in the cell and thus help the plant recognition of the orientation in the direction of gravity. Therefore, the root grows downwards and it is positively gravitropic (Chen *et al.*, 1999; Evert *et al.*, 2006).

## 2.3 Root hairs and polar growth

### 2.3.1 Trichoblast/atrichoblast determination

The epidermal cells are arranged in files of non-hair cells (atrichoblasts) and hair cells (trichoblasts) according to their position relative to the underlying cortex cells of *Arabidopsis* root (Dolan *et al.*, 1994; Datta *et al.*, 2011). This position-dependent mechanism of epidermal cells differentiation is very important even before the formation of RHs, at the stage of cell specification.

Epidermal cell fate take place very early during root development. Immature hair cells are distinct from non-hair cells. Differences are mainly in their size, cytoplasmic density, rate of

the cell division, vacuolation and chromatin organization. For instance, trichoblasts have smaller size and more dense cytoplasm (Xu *et al.* 2005; Costa and Shaw 2006; Datta *et al.*, 2011). The pattern of the root epidermis in formation of RHs is a species-specific in plants. *Arabidopsis thaliana* has a striped pattern of hair and non-hair cell files (Figure 2), meaning that tricho/atrichoblasts are developed in separate longitudinal files. Morphologically it means that trichoblast files alternate with one or two atrichoblast files (Dolan *et al.*, 1994; Pemberton *et al.*, 2001). The striated pattern is established by intracellular and intercellular genetic regulatory network that involves feedback loops and protein movement between neighbouring cells (Datta *et al.*, 2011).

### 2.3.2 Polar growth of root hairs

RHs start growth as lateral tubular extension at the basal side of the root epidermal cells called trichoblasts in the proximal end of the root elongation zone. They are involved in anchoring the plant, considerably increase root surface area and help with water and

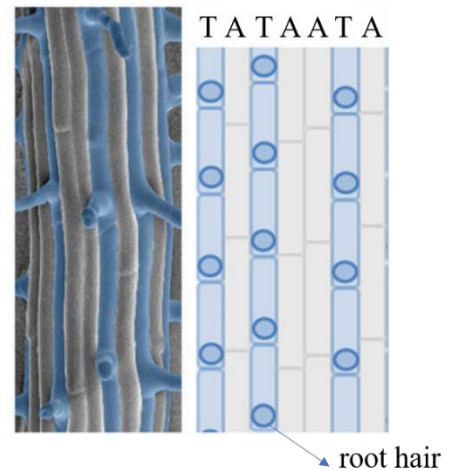


**Figure 2:** Trichoblast (T)/atrichoblast (A) pattern in *Arabidopsis* root epidermis. Adapted from Datta *et al.*, 2011.

mineral ions uptake from the soil, which in turn supports sustained plant growth. RH are also important for plant interaction with soil-borne microbes, which takes in the rhizosphere. Arabidopsis RHs are excellent model for study of plant cell and developmental biology and physiology. Their position at the root surface, simple structure, and fast growth enable easy visualization and manipulation during experiments. On the other hand, RHs are not essential for plant survival, allowing the isolation and analysis different types of mutant plants, that have RH-specific alternations in structure, function, and development (Carol and Dolan, 2002; Grierson and Schiefelbein, 2002). One of the most impressive characteristics of RHs is their polar extension at the apex, the tip growth, which includes polarization in cellular organization leading to a special tip-localized cell expansion.

Progression of RH development and growth is divided into the three discrete growth phases (Figure 3). First starts with the site selection at the outer tangential cell wall in the basal end of the trichoblast, which is followed by the migration of the nucleus from the middle part of the trichoblast to the base close to the developing hair. Local acidification of the cell wall causes its thinning and remodelling in the selected side and

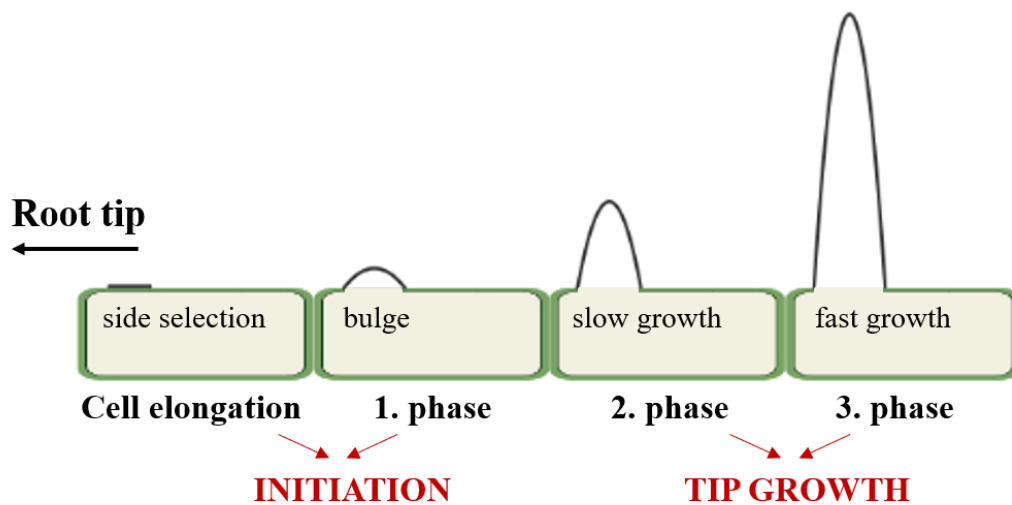


**Figure 3:** Graphic representation of individual phases of root hair tip growth. Adapted from Grierson and Schiefelbein, 2002.

then a bulge develops (Carol and Dolan, 2002). The second phase is typical for very slow RH tip growth from bulge. When the RH has 20 to 40  $\mu\text{m}$ , the transition to the third phase begins and RHs tip growth is then very fast. Tip growth of RHs is very fast, reaching 1-2  $\mu\text{m}\cdot\text{min}^{-1}$  (Dolan *et al.*, 1994). RH tip elongation is supported by proper organization of polarized cytoplasm, rapid exocytosis, endocytosis, and vesicle recycling, cell wall biosynthesis, and an incorporation of membrane material at the tip. The nucleus also migrates into the RH and keeps more-or-less standard distance from the growing tip. In



the differentiation zone of the root, RHs grow to reach their final size (length), end to be fully developed (mature), and their tips become vacuolated (Dolan *et al.*, 1994; Foreman and Dolan, 2001). The wild type RH in *A. thaliana* reach a length of around 0.8 mm with an 11  $\mu\text{m}$  in diameter, depending on the plant ecotype and local growing conditions (Galway *et al.*, 1997).

### **2.3.3 Sub-cellular organization and polarity of root hairs**

RHs contain the similar organelles like other plant cells, but with some specifics related to the fact, that the root system is located in the soil without access to light, while the stem and leaves develop in the above-ground space with full illumination. So, the main difference is the absence of chloroplasts, or chlorophyll in plastids. However, the root system contains different types of plastids. There are, for example, amyloplasts, which are filled with starch granules synthesized from imported photosynthates. It is also a place of very active oxidative pentose phosphate pathway, which generates energy to assimilate nitrogen (Scheres *et al.*, 1994; Neuhaus and Emes, 2000). Another difference is in import/export mechanisms of nutrients, ions, and water. Cells in root and shoot differ in types of channels and transporters in the plasma membrane (PM). Nevertheless, root and shoot are interconnected and active signalling between them coordinate these activities (Jiang *et al.*, 2012).

Cell polarity is generally defined as an asymmetry in a cell, or a state in which the organization of compartments within a cell is asymmetric about a particular axis. In plants, cell polarity is essential for development, growth and morphogenesis (Yang, 2008). Polar cell growth can be described as a morphological process in which the cell elongates in a certain direction. A typical model for observing polar growth in higher plants are the RHs and the pollen tubes. Growing RH has a characteristic polarized organization predominantly of the cytoskeleton, membrane trafficking, and cell wall deposition (Figure 4). The RH tip is covered by the cell wall and the PM. The cell wall is made up mainly of primary layers of cellulose. Cellulose is synthesized by cellulose-synthesizing enzymatic complexes at the PM, but other components important for cell wall structure and composition (such as pectins and xyloglycans), which are formed in the endomembrane system - endoplasmic reticulum (ER) and Golgi apparatus (GA), are transported to the tip by a vesicular transport (Foreman and Dolan, 2001). Vesicles are

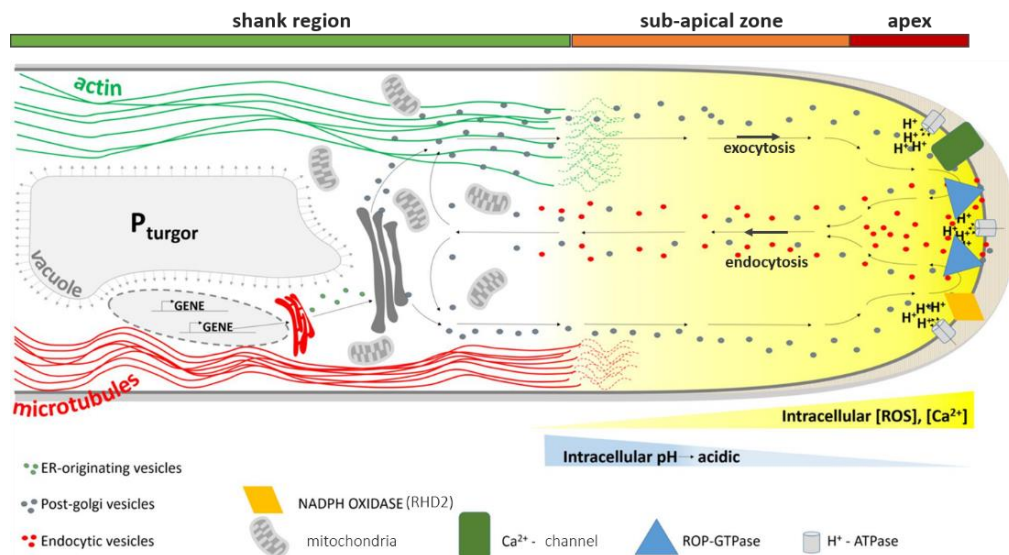


**Figure 4:** Schematic cytoarchitecture of growing root hair tip. Tip-focused vesicles are formed from exocytotic and endocytotic vesicles (in apex and sub-apical zone), which are transported by actin cables (green). Microtubules cables (red) control the growth direction of root hair. Also, NADPH oxidase (RHD2), ROP proteins and  $\text{Ca}^{2+}$ - permeable ion channels are localized at the root hair tip. All of this together creates a tip-focused calcium and ROS gradient (yellow gradient). The remaining organelles are located in shank region of root hair. Adapted from Balcerowicz *et al.*, 2015.

transported along actin filaments in a so called “reverse fountain” type of streaming (Ovečka *et al.*, 2005; Balcerowicz *et al.*, 2015). Actin filaments (AFs) are localized between secretory vesicles in the apical part of RH, where they form bundles. Bundles of AFs are oriented parallel to the longitudinal axis of the RH. Microtubules (MT) have also the same orientation as the AF, but MT are located at the cell cortex directly under the PM and they are important for controlling of RH growth direction (Galway *et al.*, 1997; Era *et al.*, 2009; Balcerowicz *et al.*, 2015). Most other RH organelles do not reach the apex, but they are in the shank region of RH. In addition to mitochondria, they are plastids, GA (Golgi stacks and trans-Golgi network - TGN), smooth and rough ER, and endosomes. ER is in a condensed form in the growing RH. Condensation already occurs in the trichoblast, at the place where the RH is initiated. ER is condensed until the RH reaches its maximum length and stops growing. Subsequently, the ER reverts to its original form and is present along the entire length of the RH (Ridge *et al.*, 1999). GA is often clustered along the ER (Zheng and Chen, 2011). The nucleus also moves from its central position in the trichoblast to the site of initiation and then to the growing RH. The nucleus has a stable distance from the tip of growing RH, but when the polar growth

stops, the nucleus can be located in any position at the RH (Galway *et al.*, 1997; Ketelaar *et al.*, 2002). When the RH completes its growth, the entire RH cell is mostly filled with a vacuole (Carol and Dolan, 2002).

The major signal mechanism indispensable for the polar RH growth is a tip-focused gradient of  $\text{Ca}^{2+}$  in the cytosol (yellow gradient in Figure 4), which regulates the activity of vesicular trafficking, generation of reactive oxygen species (ROS), and organization of the cytoskeleton in growing tip.  $\text{Ca}^{2+}$ - permeable ion channels (green rectangle in Figure 4) are localized at the apical PM (Miedema *et al.*, 2008). ROS (yellow gradient in Figure 4) are required for RH growth and they are generated by NADPH oxidase encoded by *AtrbohC/RHD2* gene. RHD2 is localized in apical part PM of RH (yellow rhombus in Figure 4). This ROS production is regulated by ROP GTPases (blue triangle in Figure 4; Foreman *et al.*, 2003). RHD2, ROS, and  $\text{Ca}^{2+}$  are interconnected by a positive feedback mechanism, which determines RH polarity and its tip growth (Carol *et al.*, 2005, Takeda *et al.*, 2008).

## **2.4 Essential factors influencing the polar tip growth of root hairs**

### **2.4.1 Organization and dynamics of the endomembrane system**

Membrane intracellular transport is the one of the most basic processes of the cellular dynamics and physiology, which is highly conserved within eukaryotic cells (individual species of yeasts, plants or animals). Endomembrane transport is ensured by vesicles than move between membrane-bound organelles (i.e. the endoplasmic reticulum - ER, Golgi apparatus - GA, the trans-Golgi network - TGN, multivesicular endosomes/bodies - MVB, lysosomes/vacuoles/pre-vacuolar compartments - PVC and the plasma membrane - PM) in eukaryotic cells (Baluška *et al.*, 2002; Ito and Uemura, 2022). Although plant cells have a rigid cell wall and high turgor pressure, their endocytotic activity is very dynamic (Hawes *et al.*, 1995; Baluška *et al.*, 2002; Šamaj *et al.*, 2004). In general, membrane trafficking between two compartments consists of four sequential steps. The first is called „buding” step, which includes the transfer of the cargo into a specific domain on the donor membrane and then starts its packing into the transport intermediate (vesicle). The next step („transport” step) means intermediate transport of vesicle between donor compartment to the target compartment by means of motor proteins and cytoskeleton (mainly F-actin) interactions. Next, the intermediate vesicles dock to target membrane, which is mediated by specific proteins (such as Rab GTPases and SNARE proteins) in the third „tethering” step. As the last comes the fusion („fusion”

step) of the transport intermediate vesicle with the targeted membrane and release of the cargo (Ito and Uemura, 2022). Generation, targeted transport, and fusion of vesicles are essential processes also for development and polar tip growth of RHs. The apical zone of growing RH is enriched with secretory (exocytotic), endocytic, and recycling vesicles, balancing fine equilibrium of macromolecule supply, retrieval, and recycling mainly materials for growing PM and cell wall (Šamaj *et al.*, 2006; Campanoni and Blatt, 2007). The exocytosis (secretion) by the vesicles fusing with the PM deliver the cargo outside of the cell (red arrows in Figure 5). The endocytosis support movement of cargo molecules from PM into the cell (blue arrows in Figure 5). It is thus involved in the internalization of molecules from the PM and from the external environment. Moreover, it supports also the recycling of the PM and the cell wall material, and the uptake of signalling molecules for further degradation (Šamaj *et al.*, 2005). These two pathways are very closely linked during polar tip growth of RHs.

Universally in plant cells, the exocytosis vesicles have 100-150 nm in diameter and are generated in the GA. The production rate is 2-4 vesicles per minute per one Golgi cisterna. However, in some hypersecretory cells (such as pollen tubes) it can be many thousands of vesicles per minute (Picton and Steer, 1983; Campanoni and Blatt, 2007). The process of exocytosis is controlled by many important proteins including Rop-GTPases that regulate actin cytoskeleton. For example, Rop2 is localized in the apical part of the growing RH and serves as their positive regulator. ARFs (ADP-ribosyl factors) mediate the formation of vesicles on the donor membrane and group of Rab GTPases responsible for the vesicle fusion with the target membrane (Campanoni and Blatt, 2007; Kang *et al.*, 2017). Recent study shows, that RabA2 and RabA3, but not other RabA members, regulate exocytosis (Pang *et al.* 2022). On the other hand, RabA1 and RabA4 members, which are expressed in *Arabidopsis thaliana*, are also accumulated in tips of growing RHs. But they take part in different molecular machinery that coordinate secretion of vesicles from the TGN (in comparison of RabA2 and RabA3). They also regulate distinct trafficking steps at the TGN compared to other Rabs (Preuss *et al.* 2004; Asaoka *et al.* 2013). Regulation of exocytosis includes SNARE proteins, which were previously mentioned as mediators of the final stage of vesicle fusion with the PM or with target membranes within the endomembrane system (Campanoni and Blatt, 2007; Ito and Uemura, 2022).

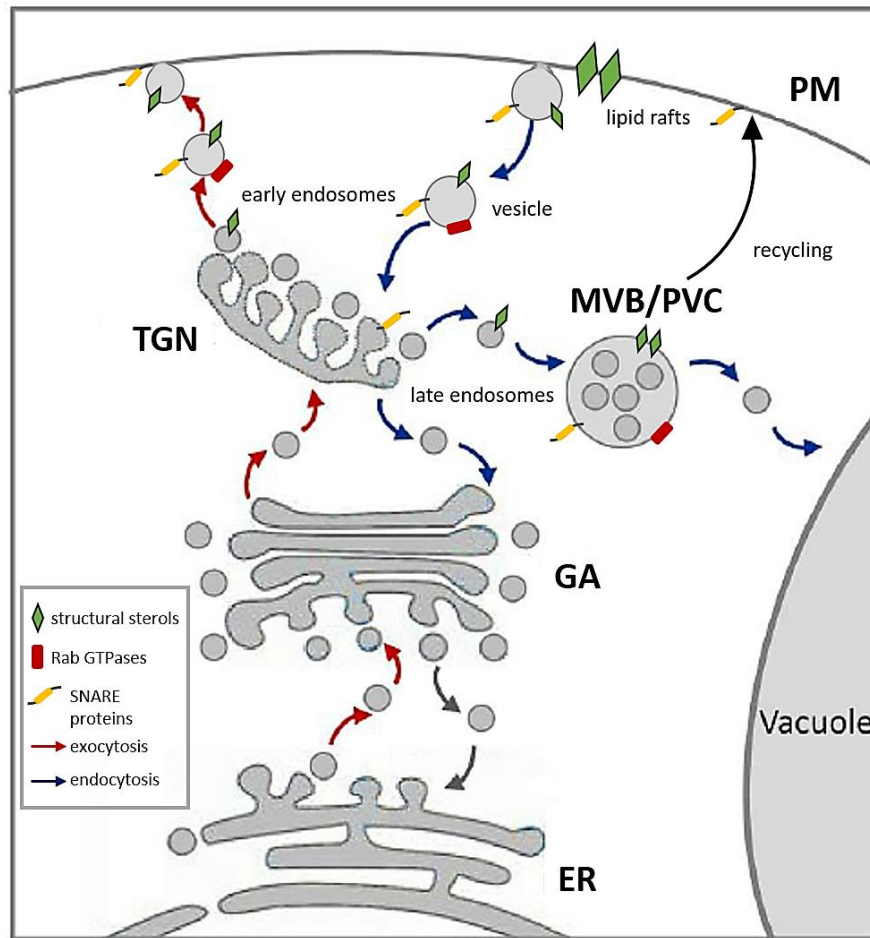


**Figure 5: The endomembrane system/trafficking in plants.** Schematic representation of the secretory and endocytotic pathway. ER: endoplasmic reticulum, TGN: trans-Golgi network, EE: early endosome, MVB: multivesicular body, PVC: prevacuolar compartment and PM: plasma membrane. The exocytosis is marked with red arrows. The way of an endocytic vesicle is indicated by blue arrows. Adapted from Bandmann, 2011.

In terms of complexity, the most robust is the endocytotic pathway. In general, endocytosis is involved in molecule internalization from the PM (including the outer space of the cell), in recycling of the PM and PM-resident proteins as part of the uptake and degradation of signalling molecules. The process of endocytosis is important not only for polar growth, but it plays further roles in auxin-related intracellular communication, gravitropic responses, stomata movement, cytokinesis, cell wall morphogenesis, and also in the elimination of pathogens and initiation of symbiosis with microorganisms (Šamaj *et al.*, 2005). There are four different types of endocytosis identified in plants: clathrin-dependent (the most common), clathrin-independent (addicted to lipid rafts), fluid-phase endocytosis, and phagocytosis. The plant endocytotic vesicles usually have around 70-90 nm. Endosomal compartments represent endomembrane trafficking hubs categorized into

four main types (depicted in Figure 5). First class is represented by early endosomes/TGNs that are involved in rapid recycling processes of membrane molecules in the cytoplasm. Furthermore, early endosomal/TGN compartments merge secretory and endocytic pathways (Barth and Holstein, 2004; Viotti *et al.*, 2010; Contento and Bassham, 2012; Qi and Zheng, 2013). The next class are freely moving recycling vesicles, originating from the TGN, mediating the secretion and recycling of the PM materials (Šamaj *et al.*, 2005). Next are late endosomes or multivesicular bodies/prevacuolar compartments (MVB/PVC) that are involved in transport pathways toward vacuoles. These compartments may serve as crossroad between endocytotic (recycling) and synthetic pathways. The newly synthesized material will either go into the vacuole or to the PM leaving the cell outside. The structure and molecular characteristics of MVB/PVC are well defined. A well-characterized binding domain of late endosomes is the FYVE domain, which is involved in signal transduction from phosphoinositol-3-phosphate-binding proteins to early endosomes. (Uemura *et al.*, 2004; Bottanelli *et al.*, 2011; Contento and Bassham, 2012). The fourth type are the lytic vacuoles, compartments that are specialized for lytic degradation (Šamaj *et al.*, 2005). The main regulators of endocytotic pathway are Rab GTPases, which belong to Ras GTPase superfamily. They exist in two stages: GTP-bound „active” and GDP-bound „inactive” form. Activation of Rab GTPase is caused by exchange of GDP for GTP, which is catalysed by GEFs (GUANINE NUCLEOTIDE EXCHANGE FACTORS; Zerial *et al.* 2001; Grosshans *et al.* 2006). In Arabidopsis genome has been identified 57 *RAB* genes. Their products are divided into 8 groups (Rab1/RabD, Rab5/RabF, Rab6/RabH, Rab7/RabG, Rab8/RabE, Rab11/RabA, Rab2/RabB and Rab18/RabC). Each of them has different subcellular localization and marks different membranes of the endomembrane system (Pereira-Leal *et al.*, 2001; Rutherford *et al.*, 2002; Ueda *et al.* 2002; Woollard *et al.*, 2008). The second most important regulators are SNARE (SOLUBLE *N*-ETHYLMALIMIDE-SENSITIVE FACTOR ATTACHMENT PROTEIN RECEPTORS) proteins. They play a key role in regulation of fusion between the transport intermediate vesicles and its target membrane („tethering” step). Intermediate vesicles contain R-SNARE (or vesicles v-SNAREs) proteins and Q-SNARE (target t-SNAREs) proteins are in the membrane of target compartment (Fasshauer *et al.* 1998; Ito and Uemura, 2022). Other most important regulators are other small GTPases, called Rho GTPases, which control structure, rearrangements and dynamic properties of F-actin cytoskeleton (Yang, 2002).

As already mentioned above, the apex of RHs is enriched with secretion vesicles. A balance must be maintained between the rate of exocytosis and endocytosis to ensure an adequate flow of PM and cell wall material for polar RH growth (Campanoni and Blatt, 2007). An invaluable tool for vital studying secretion pathways and endosomal compartments in plants are styryl dyes (FM dyes) that bind to the lipid structure of membranes. For example, FM4-64 and FM1-43 showed rapid binding to PM associated with their intense fluorescence, followed by internalization of FM-labelled membranes in the form of dense population of vesicles in growing RHs. Further fate of FM-positive vesicles was related to their passing through the entire endocytotic pathway via late endosomes until they fused with the vacuole (Ovečka *et al.*, 2005). The development of translationally fused fluorescent protein markers enabled detailed analysis and characterization of distinct endosomal compartments in living cells. The most commonly used fluorescent molecular markers are Rab GTPase Homolog A1d (RabA1d) and Vesicle transport v-SNARE 12 (VTI12) for detection of the early endosomal/TGN compartments (Sanderfoot *et al.*, 2001; Uemura *et al.*, 2004; Ovečka *et al.*, 2010; Berson *et al.*, 2014). Late endosomes were detected by using a fluorescent molecular marker based on the FYVE domain (Gillooly *et al.*, 2001; Voigt *et al.*, 2005a). Other members of the Rab GTPase family, including RabF2a, RabF1 (Ueda *et al.*, 2004; Voigt *et al.*, 2005a; Haas *et al.*, 2007), and RabF2b (Geldner *et al.*, 2009), have been verified as molecular markers for late endosomal compartments, eventually colocalizing with FYVE domain. The dynamic properties of early and late endosomes using fluorescent molecular markers have been thoroughly described in the growing RHs of Arabidopsis (von Wangenheim *et al.*, 2016b).

#### **2.4.2 Structural sterols and lipid rafts**

Structural sterols are an indispensable part of biological membranes. They are incorporated in membranes in their free form. Sterols in plants are molecules derived from isoprenoids, and the most common plant sterols are  $\beta$ -sitosterol, stigmasterol and campesterol. Structural sterols interact with membrane phospholipids and sphingolipids (Figure 6), which is indispensable for modulation of membrane fluidity and permeability (Clouse, 2002; Ovečka *et al.*, 2010; Valitova *et al.*, 2016). The other function is also their regulation role. Biosynthetic pathway of structural sterols is related to production of brassinosteroids. They have common precursors, but final steps of both biosynthetic pathways are independent (Lindsey *et al.*, 2003). The PM as a lipid - protein bilayer, is

structurally and functionally partitioned into membrane micro- and nanodomains, called „lipid rafts” (Figure 6). Clustering of phospholipids, proteins, and sterols in the extracellular leaflet of PM confers spatial organization of protein complexes, supporting their assembly into signalling complexes. Thus, structural sterols are involved in the maintenance not only physical, but also physiological properties of membranes and membrane proteins (Clouse, 2002; Stanislas *et al.*, 2015).

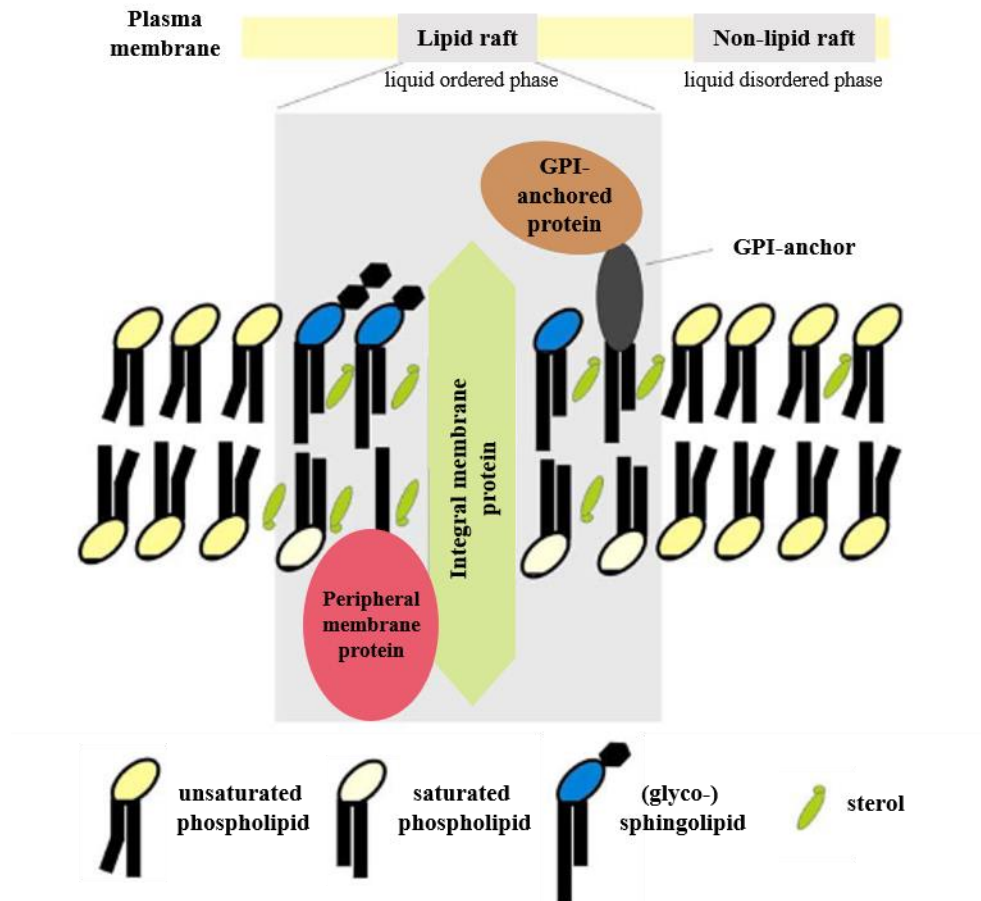


**Figure 6: Structure of plasma membrane nanodomains („lipid rafts”).** The schematic structure of „lipid raft” (grey box), which consists of phospholipids, sphingolipids, sterols and membrane-associated polypeptides, including glycosylphosphatidylinositol (GPI)-anchored polypeptides, peripheral, and integral PM proteins. Adapted from Bhat and Panstruga, 2005.

In *A. thaliana*, the importance of structural sterols in plant development and growth was proven through the mutations of genes encoding proteins involved in their biosynthesis pathway. These mutations result in altered plant development, defined as dwarf plant phenotype with defects in tissue patterning. Consequently, the mutant plants have changes in structural sterol composition (Clouse, 2002). The best described are mutants in genes encoding main proteins involved in the biosynthesis of structural sterols. Mutants *Fk* and *hydra2*, possessing the mutation in *FACKEL* gene encoding for sterol-



14-reductase, have very short hypocotyls and cotyledons connected directly to short roots. This phenotype is caused by defective cell division during embryogenesis (Schrick *et al.*, 2000). Mutant *hydra2* has misbalance in the structural sterol ratio composition and the severity of this mutation is shown by the fact that homozygous mutations are lethal (Souter *et al.*, 2002). In other mutants, such as *dwf7* (*dwarf7*) / *ste1* (*sterol1*; mutation affecting sterol-C5(6)-desaturase; Choe *et al.*, 1999), *dwf5* (mutation affecting sterol reductase; Choe *et al.*, 2000), or *dim* (*diminuto*) / *dwf1* (mutation affecting sterol isomerase/reductase; Klahre *et al.*, 1998) the same dwarf phenotype has been achieved (Choe *et al.*, 2000). The pleiotropic effects of these mutations have been also revealed. For example, *dwf7* mutant has slower cell division rates (Cheon *et al.*, 2010), *dwf5* mutant produce seeds with aberrant shape (Choe *et al.*, 2000; Jiang and Lin, 2013). Thus, mutants defective in sterol methyltransferase activity (*smt1* and *smt2;1* mutants) exhibit altered ratios of sitosterol, campesterol and cholesterol. These misbalances are accompanied by loss of fertility, altered gravitropism and disrupted root cell polarity. Serious defects in cell polarity were noticed also during the early RH development (Schaeffer *et al.*, 2001; Willemsen *et al.*, 2003).

Structural sterols are locally accumulated in the PM of future site of the RH formation in the trichoblast. The PM-specific sterol accumulation is an early indicator of the initiation site of RH. This accumulation was documented also in the „bulge” and in apical part of growing RHs. The relation of this specific structural sterols accumulation to the tip growth was approved by the observation that this gradient disappears, when the RHs terminate the tip growth. (Ovečka *et al.*, 2010). The other earliest markers of RH initiation on trichoblasts are small GTPases ROP2 and ROP4 (Molendijk *et al.*, 2001; Jones *et al.*, 2002). It has been shown that the activation-dependent acylation of ROPs and their consequent partitioning in „lipid rafts” could play a central role during the establishment of polarity in plants (Sorek *et al.*, 2007). Structural sterols regulate vesicular trafficking, signalling, protein localization in membranes and selecting exo- and endocytic cargo molecules (Menon, 2002; Lindsey *et al.*, 2003), particularly in tip-growing RHs (Ovečka *et al.*, 2010) and pollen tubes (Liu *et al.*, 2009). Vesicular transport provides a large amount of material needed for PM and cell wall enlargement in tip-growing cells (Hepler *et al.*, 2001). one of the main representative of membrane phospholipids is Phosphatidylinositol-4,5-bisphosphate (PtdIns(4,5)P<sub>2</sub>), which is required for cell polarity, endocytosis and vesicle recycling in plants. The Phosphatidylinositol Phosphate 5-Kinase 3 (PIP5K3), required for PtdIns(4,5)P<sub>2</sub>

biosynthesis in *Arabidopsis*, is also localized in emerging bulges and in tips of growing RHs (Braun *et al.*, 1999; Kusano *et al.*, 2008; Stenzel *et al.*, 2008).

### 2.4.3 Reactive oxygen species

Reactive oxygen species (ROS) are modified forms of atmospheric oxygen that are characterized by a partially reduced or excited form. They are produced by metabolic processes or are generated as a result of environmental stress (Mittler *et al.*, 2017). The most commonly occurring forms of ROS in living organisms are singlet oxygen ( $^1\text{O}_2$ ), superoxide ( $\text{O}_2^-$ ), hydroxyl radical ( $\text{OH}^\cdot$ ), and hydrogen peroxide ( $\text{H}_2\text{O}_2$ ). In plants, ROS are mainly produced within the electron transport chains in chloroplasts and mitochondria, and during photorespiration in peroxisomes (del Río *et al.*, 2006; Gleason *et al.*, 2011; Pospíšil, 2016; Foyer, 2018). In addition, they can be produced also in the cytosol, apoplast, nucleus and endomembrane system (Gechev *et al.*, 2006; Ashtamker *et al.*, 2007). The most stable ROS molecule is  $\text{H}_2\text{O}_2$ , which can be kept in its original form up to 1 ms (Dat *et al.*, 2000). ROS have dual role in plants biology. They are present mainly as toxic by-products originating from aerobic metabolism or they can be accumulated after exposure to environmental stresses. These ROS has strong ability to react with proteins, lipids or nucleic acids and cause serious damage to these biomacromolecules (Singh *et al.*, 2016). However, ROS also serve as signalling molecules. Since ROS are very small molecules, they can pass through the membranes (Overmyer *et al.*, 2003; Mittler, 2017). As signalling molecules, they regulate numerous plant developmental processes, including cell proliferation and differentiation, programmed cell death, seed germination, gravitropism, RH pollen tube growth (Singh *et al.*, 2016). ROS are necessary in response to biotic and abiotic stimuli (Dvořák *et al.*, 2021). The misbalance between different ROS forms is potentially dangerous for cells, and therefore it is important to maintain cellular ROS homeostasis. Both low and high ROS levels are undesirable for plant cells. The ROS homeostasis is controlled by the activity of antioxidant enzymes from the family of superoxide dismutases (SODs), catalases, peroxidases, glutathione peroxidases, iron uptake/storage regulating proteins, and a network of thio- and glutaredoxins (Vanderauwera *et al.*, 2011; Mittler, 2017; Dvořák *et al.*, 2021).

ROS are important signal molecules in the ontogenetic development of the entire root. Different types of ROS are produced and accumulated in different root zones. This precise distribution of ROS in root plays role in the regulation of root stem cell

proliferation and differentiation (Tsukagoshi, 2016; Zeng *et al.*, 2017; Yang *et al.*, 2018). In *A. thaliana*, the cells of the quiescent centre and the nearest surrounding stem cells of the root meristem have the strongest negative potential, which is caused by the high concentration of superoxide ( $O_2^{\cdot-}$ ). On the contrary, the cells of the transition and elongation zones of the root are in a significantly oxidized state due of the high concentration of hydrogen peroxide ( $H_2O_2$ ). The distribution of the redox gradient within the root apex is under control of UPBEAT1 (UPB1), a transcription factor regulating the expression of a wide range of genes encoding for peroxidases. (Tsukagoshi *et al.*, 2010; Perilli *et al.*, 2012; Del Pozo, 2016; Jiang *et al.*, 2016; Zhou *et al.*, 2020).

Likewise, ROS play a key role in the regulation of cell growth in general, including tip growth of RHs. ROS can be generated inside the cell (intracellularly) or in apoplast (extracellularly). Intracellular ROS in growing RHs originates mainly from mitochondria, peroxisomes and from cytosolic reaction mediated by ER (Figure 7). The main producer of apoplastic ROS are NADPH oxidases (NOX), which are located at the PM. The other producers of apoplastic ROS are cell wall peroxidases and amino-oxidases (Qi *et al.*, 2017). Generated superoxide in apoplast is degraded to  $H_2O_2$  and  $O_2$  by the catalytic activity of enzymes such as superoxide dismutase (SOD; Bowler *et al.*, 1992), apoplastic oxalate oxidase, diamine oxidase, and peroxidase (Federico and Angelini, 1986; Caliskan and Cuming, 1998). Subsequently,  $H_2O_2$  generated in the apoplast is degraded using peroxidases that are secreted into the apoplast (Trevisan *et al.*, 2019), but it can also be transported back to the cytoplasm through the PM via aquaporins (Mangano *et al.*, 2016). Plants NADPH oxidases are encoded by *RESPIRATORY BURST OXIDASE HOMOLOG (RBOH)*; Sagi and Fluhr, 2006) genes. In *A. thaliana*, there is 10 type of AtRBOHs (AtRBOHA-J) produced, and the functions of most of them are well described. Preferentially in the root RBOHB, RBOHC, RBOHG members are present, nevertheless RBOHD, RBOHE a RBOHF also play a role in growth of the main root and lateral roots. RBOHH and RBOHJ are important for growth of pollen tubes (Mhamdi and Van Breusegem, 2018). In particular, RBOHA is produced in the embryo, where takes part in abscisic acid (ABA) signalling, and subsequently positively regulate seed maturation (Müller *et al.*, 2009). ROS in apical part of growing RHs are generated by RBOHC (Foreman *et al.*, 2003). RBOHD is producer of ROS in answer to stress factors (Liu and He, 2016). Together with RBOHF it is also involved in defense reactions of the plant to pathogens (Torres *et al.*, 2002). RBOHE is involved in pollen development (Xie *et al.*, 2014) and RBOHI provides a response to drought stress (He *et al.*, 2017). The least

studied oxidases are RBOHA and RBOHG. It has been shown, that NADPH oxidases activity is connected to structural sterols in the membranes. Proteomic studies identified NADPH oxidases NtRBOHD, StRBOHB, and AtRBOHB with other PM proteins enriched in the detergent-resistant membrane fraction of suspension cells (Morel *et al.*, 2006; Srivastava *et al.*, 2013). In parallel, subcellular visualization revealed AtRBOHD localization to the PM and dynamic spots in the cells and its endocytosis via membrane microdomains can be induced by salt stress (Hao *et al.*, 2014).

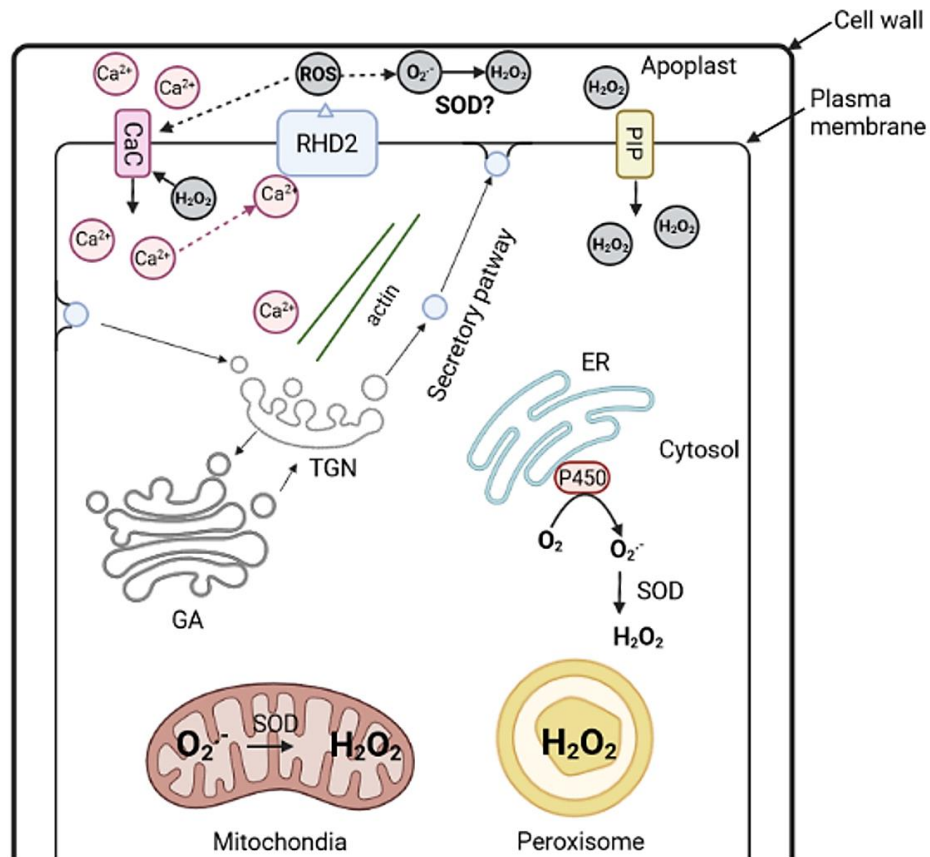


**Figure 7: ROS production in the growing root hairs.** ROS are generated intracellularly mainly by mitochondria, peroxisomes and by ER directly in the cytosol. The extracellular production is mostly secured by NADPH oxidase called RHD2 (RBOHC). ROS generated by RHD2, gradients of Ca<sup>2+</sup> and pH are key components to keep sustainable RH growth. Partially adapted from Mangano *et al.*, 2016 and created by <https://biorender.com/> application.

Only NADPH oxidase type C (AtRBOHC) is present in growing RHs. RBOHC, which is encoded by the *RHD2* (*ROOT HAIR DEFECTIVE2*) gene locus, is localized at the apical PM in RH. ROS, generated by RHD2 oxidase, Ca<sup>2+</sup> ions and a certain pH value are the key components in maintaining polar tip growth of RHs. Regulation of polar RH growth is provided by their oscillatory feedback loops (Mangano *et al.*, 2016). A typical gradient of Ca<sup>2+</sup> ions is present in the cytoplasm at the apical part of RHs, which is

responsible for the regulation of vesicular transport activity (positively stimulate exocytosis; Carroll *et al.*, 1998), the production of ROS, for the organization of the cytoskeleton (especially AFs) and the determination of the RH growth direction (Bibikova *et al.*, 1997).  $\text{Ca}^{2+}$  ions are transported inwardly to the cytoplasm through the PM by calcium channels (CaC). These channels are activated by ROS from both side of the PM. Apoplastic ROS (mainly  $\text{O}_2^-$ ) activates CaC from the outside and  $\text{H}_2\text{O}_2$  from the inside;  $\text{H}_2\text{O}_2$  is transported into the cytoplasm via aquaporins (PIPs). Transmembrane gradient of pH at the RH tip is maintained by  $\text{H}^+$ -ATPases (AHA). The most abundant electrogenic pumps exporting protons ( $\text{H}^+$ ) from the cell in the growing RH is AHA2 (Mangano *et al.*, 2016). Therefore, the apoplast has acidic pH and a negative membrane potential is created on the cytoplasmic leaflet of the PM (Falhof *et al.*, 2016). The whole mechanism works in the mode of a positive feedback loops (Figure 7).

Loss-of-function mutations in the *AtRBOHC/RHD2* locus in *rhd2* mutants resulted in short RHs (Figure 8). Therefore, absent RHD2 means that gradients of ROS and  $\text{Ca}^{2+}$  ions in the apical zone of RHs is not generated (Schiefelbein and Somerville, 1990; Foreman *et al.*, 2003). The application of external ROS or pH alkalization has ability partially rescue the polar tip growth of RHs in *rhd2* mutant, due to renewed activity of  $\text{Ca}^{2+}$  channels in the PM (Monshausen *et al.*, 2007). The same short RH phenotype was achieved by the NADPH oxidases inhibitor application (diphenyleneiodonium; DPI) in wild-type plants, which disrupted ROS production at the apex of growing RHs (Foreman *et al.*, 2003). These studies confirm, that the interplay between RBOHC/RHD2 activity, accumulation of ROS and  $\text{Ca}^{2+}$  ions are essential for the polar RH tip growth (Foreman *et al.*, 2003; Carol *et al.*, 2005). RBOHC activation involves ROP ("Rho of plants") GTPases, namely ROP2, ROP4 and ROP6, and they are transported already to the future RH initiation site in trichoblasts with the involvement of RopGEF3 factors (Carol *et al.*, 2005; Denninger *et al.*, 2019). Transcriptomic analysis positively detected RHD2 transcripts in cells of the root epidermis of diverse root zones from the proximal meristem to the elongation zone (Foreman *et al.*, 2003). The transformation of *rhd2* mutant with *GFP:RHD2* construct driven under the native promotor fully rescued its short RH phenotype. Tissue- and cell type-specific localization studies of GFP-RHD2 lines showed, that signal is particularly prominent in trichoblasts and accumulate at the bulges and apices of growing RHs (Takeda *et al.*, 2008).



**Figure 8:** Root hair phenotype (arrow) of *rhd2* mutant. Scale bar is 100  $\mu\text{m}$ .

### 2.4.4.1 Oxidative stress

ROS are formed as the first signalling molecules during most of abiotic and biotic stresses. They are kind of a connecting bridge between the initial stress stimulus and the subsequent responses of the cell at the molecular level (Mittler *et al.*, 2017). The increased level of ROS is mainly connected with oxidative stress, which is associated with heavy metal intoxication (Liu *et al.*, 2010), ozone poisoning (Miles *et al.*, 2005; 2009), and osmotic stress (Kim *et al.*, 2011) among others. The next step in response to stress to pass the signal is mitogen-activated protein

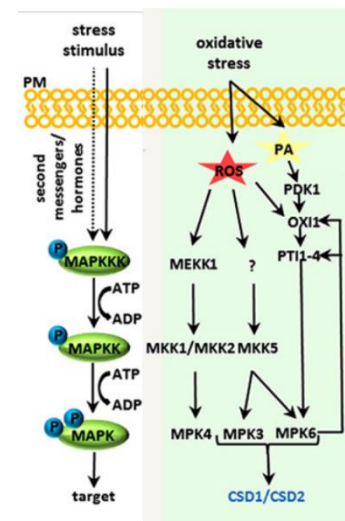


**Figure 9:** Schematic representation of the connections between second messengers (ROS, PA-phosphatidic acid), MAPK modules and target (transcription factors are blue; CSD1/2 - Cu/Zn superoxide dismutase) that regulate oxidative stress responses in *Arabidopsis thaliana*. Adapted from Smékalová *et al.*, 2013.

kinase (MAPK) signalling cascade (Figure 9). Signal transduction is a stepwise post-translational phosphorylation cascade, where activated MAP kinase kinase kinases (MAPKKK, MAP3K or MEKK) phosphorylate the serine or threonine residues in the appropriate MAP kinase kinases (MAPKK, MAP2K or MKK), then MAPKKs phosphorylate the threonine and tyrosine residues of their MAP kinases (MAPK, MPK) partner (Sihna *et al.*, 2011; Capone *et al.*, 2004). Phosphorylated MAPKs regulate the activities of diverse targets including transcription factors (Ishihama and Yoshioka, 2012), cytoskeletal proteins (Šamajová *et al.*, 2013), and other protein kinases (Popescu *et al.*, 2009). The MAPK module is a multienzyme complex, which plays a role both in stress reactions and adaptation processes, but also in the regulation of cell division, differentiation, programmed cell death, but also in symbiosis and pathogenesis (Smékalová *et al.*, 2013). The most prominent stress-induced MAPKs in *Arabidopsis* are MPK3, MPK4 and MPK6 (Colcombet and Hirt, 2008). All these three MAP kinases are also activated during oxidative stress (Lumbreras *et al.*, 2010; Pitzschke *et al.*, 2009), where MPK4 is activated via a well-defined MEKK1-MKK1/2 pathway (Pitzschke *et al.*, 2009). Detailed studies of MPK3/6 activation showed, that they affect the *OXI1* (*OXIDATIVE SIGNAL-INDUCIBLE*) gene expression. Thus, at a high concentration of ROS, transcription of the *OXI1* gene is induced (Rentel *et al.*, 2004). The OXI1 protein has many functions including the maintenance of normal RH growth under stressful conditions. Impaired H<sub>2</sub>O<sub>2</sub>-induced activation of both MPK3 and MPK6 has

been reported in the *oxil* mutant (Miles *et al.*, 2009, Xing *et al.*, 2013). Such a wide variety of defense mechanisms is essential for the plant survival, as they are immobile organisms and often face various changes in environmental conditions.

#### **2.4.4 Microtubules and actin cytoskeleton**

The plant cytoskeleton consists of MTs, AFs, and associated proteins that are involved in intracellular processes and facilitates their reorganization. MTs and AFs together form a flexible network, which mainly participate on cell growth, morphogenesis and polarity (Foreman and Dolan, 2001; Sampathkumar, 2011). Furthermore, it is also important for cell division, vesicular trafficking, migration of organelles and signalling (Fu *et al.*, 2005; Goode *et al.*, 2000). Both cytoskeletal networks consist of non-covalently-produced filamentous polymers, with broad range of size and dynamic properties (Komis *et al.*, 2015a).

##### **2.4.4.1 Microtubules**

MTs are hollow tubules from tubulin heterodimers of one  $\alpha$ - and one  $\beta$ -tubulin polypeptides. Both tubulin subunits have a molecular weight of 55 kDa. The one MT tubules has around 24 nm in diameter and is composed mostly of 13 protofilaments. (Goddard *et al.*, 1994; Lloyd and Chan, 2004). A protofilament is formed from heterodimers, where  $\alpha$ - and  $\beta$ -tubulin alternate. Two  $\alpha$ -tubulins or two  $\beta$ -tubulins are never adjacent to each other (Figure 10). MTs has two ends at which polymerization or depolymerization of individual tubulin heterodimers occurs (Figure 10). Minus (-) end is more stable and it can be connected with MT organization center (MTOC), specific places where MTs begin to grow (Goddard *et al.*, 1994). Depolymerization of MTs takes place mostly on the (-) end. Plus (+) end is more active and unstable with high range of dynamic instability (Ehrhardt and Shaw, 2006), characterized by MT growth on this side (polymerization), but also by subunits loss (depolymerization). Depolymerization is less abundant compared to polymerization (growth). MT growth is driven by GTP hydrolysis to GDP. GTP-tubulin connects with (+) end of MT and then it grows. Hydrolyzed GDP-tubulins are released from (-) end (depolymerization). Growing MT is composed mainly from GDP-tubulins (Desai and Mitchison, 1997; Caplow and Fee, 2003). Interestingly,

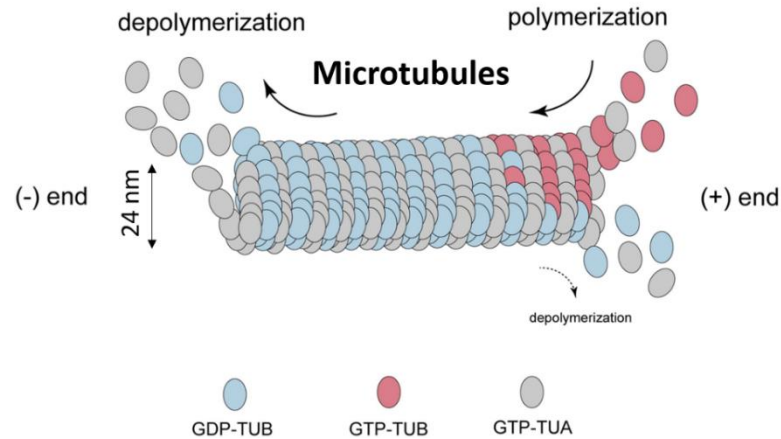


**Figure 10: Schematic diagram of microtubule structure and dynamics.** MTs are formed from  $\alpha$ -tubulin (TUA) and  $\beta$ -tubulin (TUB) heterodimers. Plus (+) end is very dynamic, where polymerization is dominant. Minus (-) end is mostly stable and MTs are shortened (shrinkage) from this end. Adapted from Li and Day, 2018.

TUA is constitutively bound to GTP and TUB alternates between GTP and GDP forms (Li and Day, 2018). Shortening of MT on (+) end or growing of MT on (-) end can happen, but this process is slower (Desai and Mitchison, 1997). Polymerization and depolymerization of MTs are highly dynamic processes addicted to cell needs. The speed of polymerization and depolymerization is very variable. It may take minutes or less (Goddard *et al.*, 1994). It was shown, that MTs growth rate is around  $4 \mu\text{m}\cdot\text{min}^{-1}$  and the shrinkage rate is around  $7 \mu\text{m}\cdot\text{min}^{-1}$  (Van Damme *et al.*, 2004). The genome of *A. thaliana* encodes 6 isoforms of  $\alpha$ -tubulin, designated AtTUA1-AtTUA6 (Kopczak *et al.*, 1992), 9 isoforms of  $\beta$ -tubulin, designed as AtTUB1-AtTUB9 (Snustad *et al.*, 1992), and 2 isoforms  $\gamma$ - tubulins, which are functionally redundant (Liu *et al.*, 1994). Genes for most of these isoforms are expressed during whole plant development, only genes for TUB1 and TUB9 are predominantly expressed only in reproductive organs (Carpenter *et al.*, 1992; Cheng *et al.*, 2001).

MTs play an indispensable role in plant cell division, through specific arrangements of mitotic MTs organized in district arrays. In the first stages, such as preprophase and early prophase, preprophase band (PPB) is formed, which predicts the future cell division site. Later in late prophase, mitotic spindle is formed, which is a major MT mitotic structure. MTs of the mitotic spindle are connected to kinetochores of sister chromatins of chromosomes and segregate them to the opposite poles of the cell during the successive stages of metaphase, anaphase and telophase. The final stage is cytokinesis, where MTs form phragmoplast, delivering vesicles to the nascent cell plate and expanding



centrifugally to meet the cortical domain predetermined by the PPB (Fowler and Quatrano, 1997; Rasmussen *et al.*, 2013; de Keijzer *et al.*, 2014). Spatial determination of the cell division site, cell division plate (CDP) and its orientation significantly determine plant morphogenesis, anatomy and development (Müller, 2012; Smolarkiewicz and Dhonukshe, 2013; Zhang *et al.*, 2016). Not surprisingly, AFs also play an important role in cell division, although AFs are arranged at different spatial and temporal distribution in comparison to MTs. AFs are necessary for early stage of PPB formation, but then they are less abundant during PPB completion (Takeuchi *et al.*, 2016). After PPB disassembly, the place behind is left as an actin depleted zone. This place is located at the cell cortex, persists and marks the division site throughout mitosis and cytokinesis. AFs form trans-vacuolar cytoplasmic strands around the mitotic spindle and later on also around the newly reconstructed nuclei after mitosis (Lloyd and Traas, 1998; Smith, 2001). AFs contribute with MTs to phragmoplast assembly, functionally cooperate in the deposition of the cell plate, and establish CDP orientation by narrowing the phragmoplast leading edges to cortical site predicted by PPB (Sampathkumar *et al.*, 2011; Kojo *et al.*, 2013). Importance of MTs and AFs for proper CDP orientation has been proved in many studies after either pharmacological treatments or using appropriate mutants (reviewed by Rasmussen *et al.*, 2013).

RHs have two independent networks of MTs (CMTs - cortical microtubules; EMTs - endoplasmic microtubules). CMTs are present along the entire length of the RHs and EMTs are inside the RHs and interconnect nuclei with RH tips. CMTs are present in all RH growth stages, only during transition from a bulge stage into fast RH growing stage cortical MTs are less detectable (Foreman and Dolan, 2001; Sieberer *et al.*, 2002, 2005). Endoplasmic MTs start to appear in late bulge stage, where cytoplasm is accumulating at the tip of the bulge and forms a cytoplasmic dense region. EMTs are present until stop of RH growth (Van Bruaene *et al.*, 2004). Depolymerization of MTs by oryzalin or MTs stabilization by taxol showed that RHs continue their growth without a significant drop in growth rate, but with a wavy pattern. This proves that MTs control RHs growth direction, but they are dispensable for tip growth of RHs (Bibikova *et al.*, 1997, 1999; Ketelaar *et al.*, 2002).

#### **2.4.4.2 Actin filaments**

AFs are the second prominent components of cytoskeleton in eukaryotic cells. AF has the shape of a double helix (13 nm in diameter), which is formed by globular actin

subunits (G-actins). One half turn of the double helix has 13-14 subunits of G-actins (Staiger, 2000). The one F-actin subunit has about 42 kDa (Sheterline *et al.*, 1998). The actin cytoskeleton is very dynamic, and the AFs also have (+) and (-) ends, similar to MTs (Figure 11). Typical feature of AFs is their ability to perform dynamic structural reorganizations (Wasteneys and Galway, 2003; Staiger and Blanchoin, 2006). The polymerization (growth) of AFs occurs as a result of ATP hydrolysis. The (+) pole represent fast growing end of AFs. However, growth also occurs at the (-) end, but more slowly. It is important, that a balance is always maintained between growth and shrinkage of AFs (Staiger, 2000).

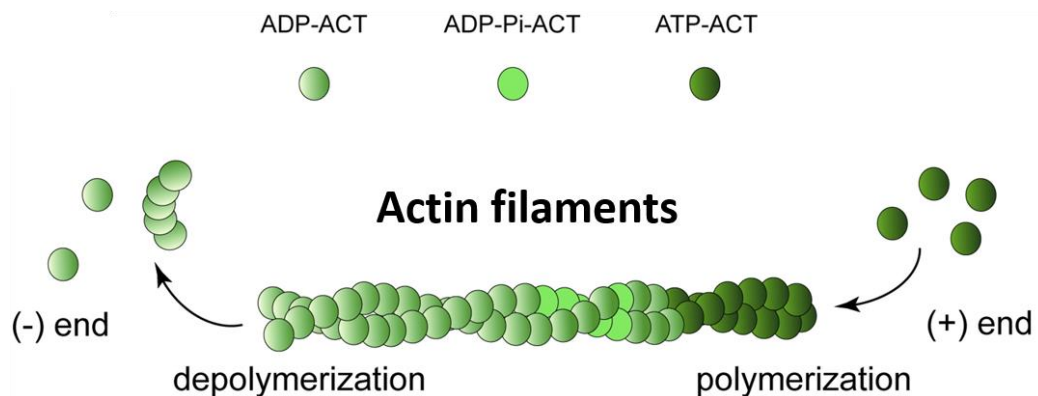


**Figure 11:** Schematic diagram of actin filament dynamics. Polymerization is mainly at the (+) end and depolymerization dominates at the (-) end. Dynamic changes occur by ATP hydrolysis of G-actin subunits. Adapted from Li and Day, 2018.

AFs are important in many cellular processes (such as cytoplasmic streaming, organelle movement, vesicular trafficking) and developmental processes (such as establishment and maintenance of cell polarity and shape, cell division plane determination, tip growth; Volkmann and Baluška, 1999; Wasteneys and Galway, 2003; Šamaj *et al.*, 2004; Staiger and Blanchoin, 2006). AFs also have important functions in signalling events triggered by diverse external stimuli and their remodelling is part of abiotic and biotic stress response mechanisms in plants (Zhou *et al.*, 2010). Actin dynamic is regulated by actin binding proteins (ABP), which have a different distribution in the cells (Ramachandran *et al.*, 2000). These proteins are divided into the four individual groups according to their function. The first are proteins, which bind and/or cover monomeric actin subunits (G-actin binding proteins); the second ones regulate F-actin polymerization/depolymerization. The next are proteins ensuring F-actin cross-linking and the last group consists of myosin motor proteins. The most studied ABPs are profilins, which belong to the first group. The profilins mask G-actin subunits and subsequently the

depolymerization of F-actin occurs (Staiger, 2000; McCurdy *et al.*, 2001; Xue and Robinson, 2013; Komis *et al.*, 2015a).

The *A. thaliana* genome encodes eight actin genes divided into two classes. The vegetative group, which is typically expressed in all vegetative tissues, possess 3 actin genes (*ACT2*, *ACT7* and *ACT8*). The second group of genes (reproductive class) are expressed mainly in pollen tubes and ovules and contains *ACT1*, *ACT3*, *ACT4*, *ACT11* and *ACT12* (Meagher *et al.*, 1999; Kandasamy *et al.*, 2007). Members of the vegetative and reproductive actin have different expression pattern and function, although they only have 4-7 % differences at the amino acid sequence level (Kandasamy *et al.*, 2007). The *ACT8* and *ACT2* genes have similar expression pattern, while the last vegetative actin gene (*ACT7*) is expressed mainly in young expanding vegetative tissues (Meagher *et al.*, 1999). The overexpression (or overproduction) of actins shows various defect in actin structure. For example, the *ACT1* gene overexpression caused the formation of sheet- or star-like aberrant actin structures in vegetative cells, leading to different thickness and orientation of AFs in comparison to control cells (Kandasamy *et al.*, 2002). However, *ACT2* gene overproduction has only little effect on plant morphology and the structure of AFs in vegetative tissues (Kandasamy *et al.*, 2002). The *ACT2* isoform is more attracted in plant biology studies than other isoforms, because the *ACT2* gene expression is the highest among the actin genes in *Arabidopsis*. This is proven by a study where some vegetative plant organs contain up to 50 % of *ACT2* mRNA out of the total actin mRNA amount (McDowell *et al.*, 1996).

That essential role of *ACT2* for proper RH tip growth has been proven by genetic approaches using either chemically-induced single-point mutations (Ringli *et al.*, 2002) or insertional knockout mutations (Gilliland *et al.*, 2002). Varying degrees of the short RH phenotype were shown by three *der1* (*deformed root hairs*) allelic mutants, isolated after EMS (ethyl methanesulphonate) mutagenesis in the C24 ecotype background. The strongest effect on RHs growth was described in *der1-2* and *der1-3* mutants (Figure 12; Ringli *et al.*, 2002). Surprisingly, the *ACTIN2* expression level is not affected by single point mutation in *DER1* locus (Ringli *et al.*, 2002). Other mutations in the *ACT2* gene also showed a defect in the growth of RHs, but they have accumulated also other types of phenotypic changes. For example, *act2-2D* mutant (EMS mutagenesis in *Ler* background) has trichoblasts without any bulges and has shorter AFs bundles as

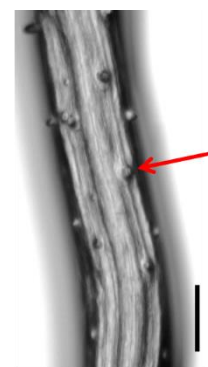


**Figure 12:** Root hair phenotype (arrow) of *der1-3* mutant. Scale bar is 100  $\mu$ m.

comparing to wild type (Nishimura *et al.*, 2003). T-DNA insertional loss-of-function mutants in *ACT2* gene, *act2-1* (Gilliland *et al.*, 2002) and *act2-3* (Nishimura *et al.*, 2003) do not show defects in RH initiation, but their RHs are shorter than those of wild-type plants (Gilliland *et al.*, 2002; Nishimura *et al.*, 2003). Studies based on mutagenesis of genes for vegetative actins revealed that *ACT7* is involved in root growth, epidermal cell specification, cell division and root architecture, while *ACT2* and *ACT8* are essential for RH tip growth (Gilliland *et al.*, 1998).

In RHs, actin cytoskeleton has more diverse structure in comparison to MTs (Higaki *et al.*, 2006). RH tips are enriched in vesicles and AFs, among others, regulate vesicular trafficking, which is essential for tip growth. Interestingly, actin (+) plus ends are highly enriched in the apical dome of RHs (Vazquez *et al.*, 2014). The involvement of AFs in RHs tip growth was demonstrated by analyses with the effects of actin disrupting drugs. Cytochalasin D binds to the growing end of AFs (Pollard and Mooseker 1981) and stops polymerization and elongation of net-axial fine bundles of AFs at the subapical RH zone and stops tip growth (Miller *et al.*, 1999). Latrunculin B treatment causes AFs depolymerization, resulting in RH growth arrest (Baluška *et al.*, 2000). In overall, these experiments proved that actin cytoskeleton is essential in both the process of RH initiation and proper RH tip growth (Braun *et al.*, 1999; Pei *et al.*, 2012).

## **2.5 Conventional and advanced microscopy techniques**

Microscopy is analytical instrumental technique for imaging of different organisms, including plants, at the supra-cellular, cellular, and sub-cellular levels. Advances of microscopy techniques combining wide-field light microscopy, multispectral fluorescent microscopy, up to sub-diffraction super-resolution microscopy have made it possible to observe the organization and dynamics of cells and most of the organelles and subcellular compartments in cells of living plants down to the nanoscale (Komis *et al.*, 2018). After development of fluorescent recombinant proteins technology (such as GFP, YFP, RFP and other), fluorescence microscopy exploded in further development. Traditionally, the most frequently used are techniques of confocal laser scanning microscopy (CLSM) and spinning-disk microscopy (SD) that were among the first techniques capturing cells localized mostly on the surface of living or fixed plant samples (Berthet and Maizel, 2016).

Plants are very sensitive to changes in external environmental conditions. Therefore, the live cell imaging by conventional microscopy methods with traditional

sample preparation approaches may often generate some artefacts. This is mainly caused by enclosing plants to small observation chambers that are exposed to high laser light intensity, which often leads to temperature and photo-oxidation far from ideal (Reddy *et al.*, 2007). Hence, a compromise between achieving conditions allowing the observation of biological processes at the appropriate spatial and temporal resolution and maintaining conditions as close to natural as possible for the sample is a goal of advanced microscopic methods in live cell imaging (Stelzer, 2015). The presented Ph.D. thesis was elaborated by utilization of several microscopy methods. From conventional microscopy, we used confocal laser scanning microscope (CLSM) and spinning-disk microscope (SD), and from advanced microscopy methods Airyscan confocal laser scanning microscope (ACLSM) and light-sheet fluorescence microscope (LSFM) were employed. The basic principles of each individual microscopy method are depicted in Figure 13.

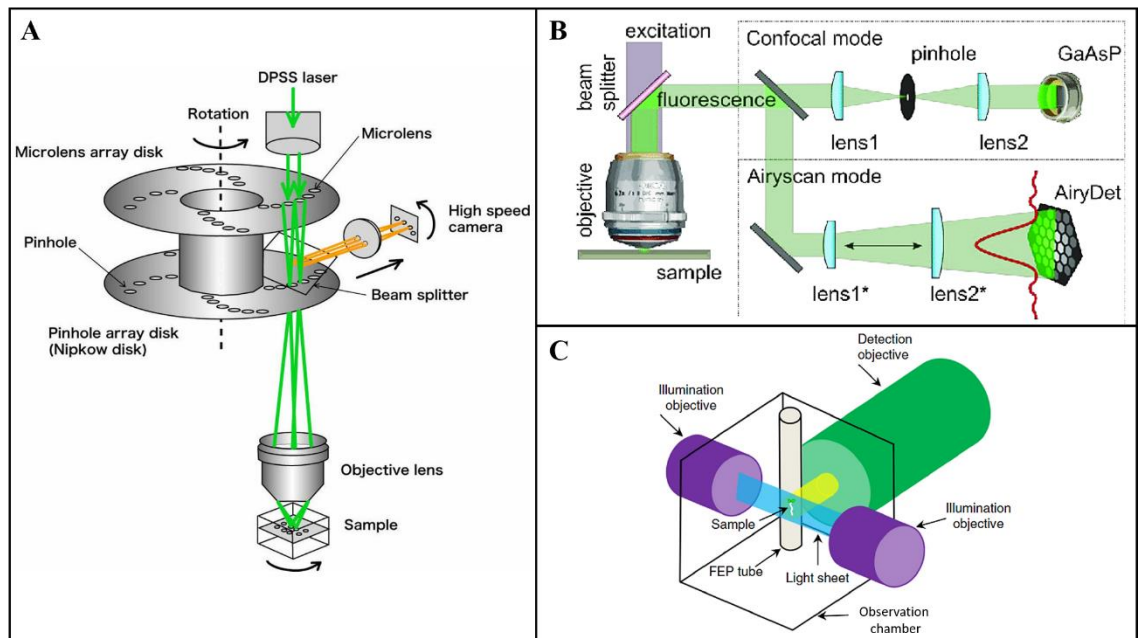


**Figure 13: Schematic representation of the principles and configuration of various microscopy methods.** (A) Spinning-disk microscopy with double spinning disk. Adapted from Lima *et al.*, 2006. (B) Airyscan CLSM with two different detection paths. Adapted from Korobchevskaya *et al.*, 2017. (C) LSFM with two illumination objectives and one detection objective. Adapted from Ovečka *et al.*, 2015.

### 2.5.1 Confocal laser scanning microscopy (CLSM)

CLSM belongs to conventional fluorescence methods utilizing a laser as a light source. Laser is monochromatic source of light with one, few, or a range of wavelengths. Classic wide-field fluorescence microscopy uses fluorescence lamps, which generates discontinues light. Required wavelength for excitation is selected by excitation filters.

The resulting fluorescence light is reflected from the dichroic mirror (beam splitter) to illuminate the whole specimen. The emitted light passing through the dichroic mirror and emission filter into the detector results, due to out-of-focus fluorescence collection, in a blurred image (Wright and Wright, 2002; Tichá *et al.*, 2020). CLSM is point-based imaging system, scanning specimen sequentially spot by spot, but eliminating out-of-focus light by the means of the pinhole (Figure 13B). The pinhole physically blocks less intense areas of the excitation and emission fluorescence light, letting to pass primarily in-focus emitted light only (Wright *et al.*, 1993; Mauko *et al.*, 2009). It secures high signal-to-noise ratio (SNR) and micrographs with good resolution. Improved axial resolution and high SNR, however, is consequence by reduced imaging speed (Girkin and Carvalho, 2018). Volumetric 3-D data are obtained from repetitional sequential scanning of 2-D optical slices in z-dimension (Girkin and McConnell, 2005). It may lead to high doses of fluorescence light loading, which leads to high sample photo-damage and photobleaching of fluorophore. For these reasons, CLSM is not always usable for imaging of very dynamic processes in cells and limitations are related also to range of imaging depth (Girkin and McConnell, 2005; Wang *et al.*, 2005).

### **2.5.2 Spinning-disk microscopy (SD)**

SD is conventional microscopy method, which is based on a different principle as compared to CLSM. It is based on the presence of two rotating disks (Figure 13A). Nipkow (pinhole) disk with 20.000 perforations arranged apart in a helical pattern, but covering only a part of the disk, rotates rapidly during imaging, creating thus thousand light spots that illuminate uniformly specimen without stripes. Each point is illuminated several hundred times during acquisition, and the image is the result of many short exposures at low excitation light intensity. The limitation is that pinhole disk blocks a large portion of excitation light, so the sample is illuminated insufficiently. This problem was solved by the second disk with microlenses, which is positioned towards the pinhole disk (Inoué and Inoué, 2002; Stehbens *et al.*, 2012). The positions of pinholes and microlenses are synchronized during imaging, securing that the fraction of excitation light transmitted by pinhole disk raised from about 1% to 40% (Tanaami *et al.*, 2002). Pinhole disk also reduces the out-of-focus emission fluorescence light. Together with highly efficient camera systems, such as low-light electron multiplication CCD (EMCCD) or complementary metal-oxide-semiconductor (sCMOS), SD is very fast imaging microscopy methods with sufficient resolution. Accordingly, the imaging speed

(high temporal resolution) is the highest advantage of SD, reaching the frequency up to 360 frames per second (Gräf *et al.*, 2005). SD is therefore a suitable method for the observation of very dynamic processes in living cells. Likewise, this method has also some disadvantages. First, samples with a low fluorescence yield require an increase of the light illumination energy, leading to a higher level of phototoxicity and photobleaching. The other limitation is related to thicker samples, as higher background noise is generated and only lower axial resolution can be achieved (Wang *et al.*, 2005; Stehbens *et al.*, 2012).

### **2.5.3 Airyscan confocal laser scanning microscopy (ACLSM)**

Airyscan CLSM is a system that combines super-resolution microscopy with conventional CLSM (Korobchevskaya *et al.*, 2017). Super-resolution microscopy methods have been developed and successfully used to study nano-sized objects at a subcellular level, however, mostly applied in fixed samples or samples mounted in a toxic and oxygen-free imaging buffers (Rust *et al.*, 2006). Consequently, super-resolution microscopy has some limitations for live-cell imaging. On the other hand, some methods like SIM (structured illumination microscopy) and STED (stimulated emission depletion microscopy) were adapted for live-cell super-resolution imaging (Komis *et al.*, 2018), although inducing a high dose of photo-toxicity (Wang, 2016).

Airyscan consists special 32-channel GaAsP (gallium arsenide phosphide) PMT array of detectors arranged in planar orientation (Figure 13B). Each unit of the array equivalent to a point detector with a sampling capacity of a 0.2 Airy Unit (AU) pinhole, support a total projecting efficiency equivalent to 1.25 AU (Engelmann and Weissart, 2014; Huff, 2015). Such increase in spatial resolution is related to a simultaneous enhancement of a signal-to-noise ratio without increasing the excitation power and acquisition time (Korobchevskaya *et al.*, 2017). Standard confocal microscopy operates with the pinhole opening corresponding to 1 AU (Snyman *et al.*, 1999), as the best setting to collect 80% of the light from a pixel location. In this case, the main factor is a numerical aperture (NA) of the objective used, and spectral properties of the fluorophore (Snyman *et al.*, 1999; Jonkman and Brown, 2015). However, still some amount of the emitted light is lost. In contrast, all emitted light is collected by the virtual pinhole of the 32 unit-detector of ACLSM. A further increase in resolution is obtained by the deconvolution of the acquired data (Korobchevskaya *et al.*, 2017). All mentioned properties, such as combination of confocal microscopy with enhanced spatial resolution, and increased

sensitivity to given fluorescence signal suggest that ACLSM is reasonable method for improved dynamic live-cell imaging (Sivaguru *et al.*, 2016).

#### **2.5.4 Light-sheet fluorescence microscopy (LSFM)**

LSFM is innovative and conceptually new method. A very thin light beam modulated to a „light-sheet”, which passes through the sample in one focal plane, is generated by two illumination objectives facing each other. The excitation and detection way are physically separated meaning that detection objective is oriented perpendicular to the illumination objectives (Figure 13C; Girkin and Carvalho, 2018; Ovečka *et al.*, 2018). The arrangement of individual objectives ensures that the excitation of the fluorophores in the sample is limited to the illuminated plane, and no emission away of the illuminated plane ensures no out-of-focus fluorescence. Simultaneously, it protects adjacent parts of the sample from photobleaching (Girkin and Carvalho, 2018). Position of the illumination plane at the sample fits perfectly to focal plane of the detection objective (Ovečka *et al.*, 2015). Hence, LSFM generate only a low photo-toxicity level and offers fast recording rate of optical sections. It is well suited for long-term live cell imaging (Reynaud *et al.*, 2015; Stelzer, 2015). Long-term imaging is also supported by the fact that sample mounting and orientation in the microscope chamber are similar to natural conditions (Maizel *et al.*, 2011; von Wangenheim *et al.*, 2016a). Traditionally prepared plant samples for conventional microscopes are placed between microscopic slide and the coverslip horizontally positioned in microscope stages, which limits growth, medium and oxygen exchange (Ovečka *et al.*, 2005; 2015). In contrast, plant samples are inserted into the observation chamber in a vertical position in LSFM. Whole plants are mounted in the FEP (fluorinated ethylene propylene) tube, allowing leaves and green part of plants to be exposed to air, while roots are growing in transparent solidified medium suitable for imaging. The rest of the imaging chamber is filled with a liquid medium (Figure 12C). In this way, inserted plants can grow along natural gravity vector supplied with enough space and nutrients (Ovečka *et al.*, 2015). Once inserted, the whole volume of the specimen can be imaged by acquiring optical sections in full range of x-, y- and z- dimensions, different angles and undetermined time. The obtained multidimensional data can be processed for 3-D rendering in time (Huisken *et al.*, 2004; Verveer *et al.*, 2007; Holekamp *et al.*, 2008; Reynaud *et al.*, 2015).

Light-sheet microscopy is the best among methods for long-term imaging of whole living specimens, which is mainly utilized in development studies. Important to



note is the fact that subsequent processing of the obtained data is time-consuming and their amount is in the order of gigabytes and terabytes (Dunsby, 2008; Huisken *et al.*, 2004; Maizel *et al.* 2011; Ovečka *et al.*, 2015).

### **3.6 Post-acquisition image processing and quantitative analysis of single particle dynamics**

Obtaining images from microscopic imaging is not the last step in the evaluation procedure. First step is a deconvolution process, which is useable for images from high-resolution advanced microscopical methods. Deconvolution is an iterative mathematical process to improve the contrast and resolution of a three-dimensional image by extrapolation of an experimental point spread function (PSF) by employing various algorithms. PSF is the 3D reconstructed image of a sub-diffraction spherical point emitter. Assuming that the acquisition of the PSF and microscope image are performed under similar conditions, the final processed image will be close to the real object (Komis *et al.*, 2015b; Shaw, 2006). For example, Airyscan CLSM uses the Weiner deconvolution filter, which is a non-iterative linear algorithm approach to minimise the impact of frequencies with low SNRs on the reconstructed images (Korobchevskaya *et al.*, 2017). This technique combines confocal imaging with the 32 detector units of 0.2 AU in diameter per unit, deconvolution and the pixel-reassignment principle in order to enhance both the spatial resolution and SNR. Images from the individual detector are part of the deconvolution process leading to preservation of information about lateral and axial resolution (Huff *et al.*, 2017; Korobchevskaya *et al.*, 2017).

The next step is quantitative analysis of microscopic data. In the Ph.D. thesis, we utilized single-particle tracking (SPT), which is a powerful tool in the quest for quantitative analysis of intracellular dynamic processes (such as trajectories, speeds, and size of particles). A particle can mean most things, from a single molecule to a macromolecular complex, organelle, virus or microsphere (Saxton, 2008). The SPT is challenging, because manually detecting and following large numbers of individual particles is not feasible, and therefore automated computational methods were developing rapidly (Chenourd *et al.*, 2014). The image analysis procedure of SPT is divided into two steps: (1) particle identification (the spatial aspect), their separation from the background, and estimating of coordination in every frame (the segmentation step); (2) the linking step (or the temporal aspect), when segmented objects are connected from frame to frame (Meijering *et al.*, 2012). Over the years, many methods have been developed for each of

these steps, often originating from other research areas of data analysis, which are summarized in Meijering *et al.*, 2012 and Chenourd *et al.*, 2014. Most of used ones are plugins of Fiji (ImageJ) or the Matlab software. The difference in use also depends on image dimensions in 2D or 3D, and mode of manual or automatic segmentation (Meijering *et al.*, 2012).

Frequently used programs for tracking of endosomes and vesicles are Motion Track (Gasman *et al.*, 2003), PolyParticleTracker (Flores-Rodriguez *et al.*, 2011), ImageJ plugins (Toshima *et al.*, 2006; Ohashi *et al.*, 2011; Li *et al.*, 2012), or DiaTrack (Trejo *et al.*, 2010). All of them use individual algorithms to recognize and follow the particles. Two independent studies analysed early endosomal/TGN compartments in growing RHs. By MultipleKymograph plugin for ImageJ software was shown that GFP-RabA1d vesicles moved with an average speed of about  $8.7 \mu\text{m}\cdot\text{s}^{-1}$  (Berson *et al.*, 2014; von Wangenheim *et al.*, 2016b). On the other hand, late endosomes in RHs visualized by fluorescence markers, such as YFP-RabF2a, YFP-RabF2b, GFP-2xFYVE, had lower value of average speed (around  $6 \mu\text{m}\cdot\text{s}^{-1}$ ; von Wangenheim *et al.*, 2016b). Measurements of early endosomes (GFP-Rab5) movement in HeLa cells using PolyParticleTracker software, likewise showed similar values (Flores-Rodriguez *et al.*, 2011). In summary, there are many evaluation tools, and the choice depends mainly on the origin of the data and the kind of quantitative parameters under analysis.

### 3. Materials and methods

#### 3.1 Plant material and growth conditions

*Arabidopsis thaliana* (L.) Heynh. plants of the Columbia (Col-0) and C24 ecotypes were used as a wild-type. All mutant plants and their transgenic or crossed lines are summarized in Table 1. Seeds were surface sterilized in 70% ethanol for 2 min, in 1% sodium hypochlorite with 0.01% Tween 20 for 8 min, and finally washed three times in sterile distilled water.

**Table 1: List of mutant and transgenic lines used in this study**

<b>Mutant/transgenic plants</b>	<b>Description</b>	<b>Origin/source</b>
<i>der1-3</i> ( <i>deformed root hairs</i> )	Single-point mutation in <i>ACT2</i> (C24 background; At3g18780)	Ringli <i>et al.</i> , 2002
<i>rhd2-1</i> ( <i>root hair defective</i> )	Single-point mutation in <i>RHD2</i> (Col-0 background; At5g51060)	Foreman <i>et al.</i> , 2003
mCherry-RabF2b (W2R)	<i>UBQ10::mCherry:RabF2</i> (Col-0 background; At4g19640)	Geldner <i>et al.</i> , 2009
mCherry-VTI12 (W13R)	<i>UBQ10::mCherry:VTI12</i> (Col-0 background; At1g26670)	Geldner <i>et al.</i> , 2009
<b>Background line</b>	<b>Donor construct/line</b>	<b>Preparation method</b>
C24 or <i>der1-3</i> ( <i>deformed root hairs</i> )	<i>pro35S::GFP:FABD2</i> (Voigt <i>et al.</i> , 2005b; At4g26700)	transformation
C24 or <i>der1-3</i> ( <i>deformed root hairs</i> )	<i>pro35S::GFP:MBD</i> (Marc <i>et al.</i> , 1998; MT-binding domain of human <i>MAP4</i> )	transformation

<i>rhd2-1</i> (root hair defective)	35S:: <i>GFP:RabA1d</i> in Col-0 (Ovečka <i>et al.</i> , 2010; At4g18800)	crossing
<i>rhd2-1</i> (root hair defective)	35S:: <i>RabF2a:YFP</i> in Col-0 (Voigt <i>et al.</i> , 2005a; At5g45130)	crossing
GFP-RHD2 in Col-0 (Takeda <i>et al.</i> , 2008; At5g51060)	mCherry-VTI12 in Col-0	crossing
	mCherry-RabF2b in Col-0	crossing

Sterilized seeds were planted into ½ (half-strength) MS (Murashige & Skoog, 1962) medium without vitamins, supplemented with 1% sucrose and solidified with 0.6 % (w/v) Gellan gum (Alfa Aesar, ThermoFisher Scientific, Waltham, MA, USA). Petri dishes containing seeds were stratified at 4 °C for 3 days. After stratification, plates with seeds were cultivated vertically in a growth chamber at 21 °C at 70 % humidity with a 16/8 h light/dark photoperiod (*in vitro* conditions). The illumination intensity was 130  $\mu\text{mol m}^{-2}\text{s}^{-1}$ .

### 3.2 Transformation and crossing

*Arabidopsis thaliana* plants of ecotype C24 and *der1-3* mutant were transformed with *Agrobacterium tumefaciens* strain GV3101 carrying a construct *pro35S::GFP:FABD2*, coding for F-actin binding domain 2 of *Arabidopsis* FIMBRIN 1 (FABD2) fused to green fluorescent protein (GFP; Voigt *et al.*, 2005b) or with a construct *pro35S::GFP:MBD* coding for the microtubule-binding domain (MBD) of the mammalian MICROTUBULE-ASSOCIATED PROTEIN 4 (MAP4) fused to GFP (Marc *et al.*, 1998). Both constructs were driven by the constitutive 35S promoter and N-terminal GFP fusion with rifampicin and kanamycin resistance. Constructs were prepared by a classical cloning method in *pCB302* vector with an N-terminal GFP fusion with rifampicin and kanamycin resistance and with the herbicide phosphinothricin as the selection marker *in planta*. Stable plant transformation was performed according to Clough and Bent (1998). Inflorescences of 3-4 weeks old plants were soaked in *Agrobacterium tumefaciens* cultures for 10 s and were stabilized in the dark overnight. After that, plants were cultivated in a culture chamber at 24 °C, 60% humidity, 16/8 h light/dark photoperiod. Transformation was repeated after one week. For T<sub>1</sub> seeds

generation, a selection culture medium containing phosphinothricin ( $50 \text{ mg.ml}^{-1}$ ) was used. In addition, stable transformed lines were selected according to the phenotype expected. The RH phenotype of transgenic *der1-3* plants was visually selected using a stereomicroscope and the presence of GFP fusion protein marker was detected and confirmed using an epifluorescence stereomicroscope Axio Zoom.V16 (Carl Zeiss, Germany). Seeds of the stable T<sub>3</sub> generation were used for experiments.

Crossing was performed with plants of the *rhd2-1* mutant as female donors, that were crossed with transgenic plants bearing fluorescent markers for early endosomes/TGN, GFP-RabA1d (Ovečka *et al.*, 2010), or late endosomes, RabF2a-YFP (Voigt *et al.*, 2005a), which were used as male donors. Transgenic plants with N-terminal fusion of RHD2 with GFP under the control of the RHD2 promoter (GFP-RHD2 line in the Col-0 background; Takeda *et al.*, 2008), were crossed with transgenic plants carrying fluorescent markers of endosomal compartments (Wave line W2R producing mCherry-RabF2b for late endosomes Geldner *et al.*, 2009; and Wave line W13R producing mCherry-VTI12 for early endosomes/TGN; Geldner *et al.*, 2009). Transgenic plants with GFP-RHD2 were used as female donors in crossings. The progeny of the F<sub>1</sub> generation was selected according to fluorescence signals using an Axio Zoom.V16 fluorescence stereomicroscope (Carl Zeiss, Germany), and plants of the F<sub>2</sub> or F<sub>3</sub> generations were used for experiments.

### 3.3 Application of stress factors

The response of C24, C24 bearing GFP-FABD2 (C24 GFP-FABD2), *der1-3*, and *der1-3* bearing GFP-FABD2 (*der1-3* GFP-FABD2) plants to oxidative stress was tested with three different concentrations (0.1; 0.2 and  $0.5 \mu\text{mol.l}^{-1}$ ) of paraquat (PQ; methyl viologen), and four different concentrations of H<sub>2</sub>O<sub>2</sub> (0.5; 1; 1.5 and  $3 \text{ mmol.l}^{-1}$ ). Stress-inducing compounds were added directly to ½ MS culture medium after autoclaving (summarized in Table 2). Seeds were planted either directly on ½ MS media containing different concentrations of PQ, or 3-day-old plants germinated and growing on the control ½ MS media were transferred to media containing different concentrations of PQ or H<sub>2</sub>O<sub>2</sub>.

**Table 2: Effective concentrations and volumes of chemicals used in the culture medium for induction of oxidative stress.**

<b>Chemical</b>	<b>Effective concentration</b>	<b>Volume in 250 ml ½ MS medium</b>
<b>Paraquat (PQ)</b>	0.1 $\mu\text{mol.l}^{-1}$	25 $\mu\text{l}$
	0.2 $\mu\text{mol.l}^{-1}$	50 $\mu\text{l}$
	0.5 $\mu\text{mol.l}^{-1}$	125 $\mu\text{l}$
<b>Hydrogen peroxide (H<sub>2</sub>O<sub>2</sub>)</b>	0.5 $\text{mmol.l}^{-1}$	7.5 $\mu\text{l}$
	1 $\text{mmol.l}^{-1}$	15 $\mu\text{l}$
	1.5 $\text{mmol.l}^{-1}$	22.5 $\mu\text{l}$
	3 $\text{mmol.l}^{-1}$	45 $\mu\text{l}$

### 3.4 Phenotypic analysis

#### 3.4.1 Phenotype, growth and biomass production of *der1-3* mutant plants

Plants (C24 wild-type and *der1-3* mutant) cultured *in vitro* were scanned for phenotype directly on Petri plates every 24 h for 5 days after germination. Pictures from a scanner (Image Scanner III, GE Healthcare, Chicago, IL, USA) were used for measurements of primary root length in ImageJ software (<http://rsb.info.nih.gov/ij/>). Phenotypes of 18-days old plants *in vitro*, morphology of rosettes of 19-days old plants growing *in vivo* and the size of individual leaves were documented using a Nikon 7000 camera equipped with macro-objective (50 mm, 2.8; Sigma). The phenotypes of entire roots and root tips of 5-days old plants *in vitro* were recorded with an M165FC stereo microscope equipped with LAS V 4.0 software (Leica).

#### 3.4.2 Oxidative stress

C24, C24 GFP-FABD2, *der1-3*, and *der1-3* GFP-FABD2 plants were scanned directly on plates every 24 h for 11 days from the day of germination. This was done for plants of both germinating and growing *in vitro* on the control media, or on media containing different concentrations of PQ. Plants germinating on the control media and transferred to stress conditions (plates containing PQ or H<sub>2</sub>O<sub>2</sub>) were scanned on plates every 24 h for an additional 4 days after their transfer. The measurement of the primary root length was done from scanner images (Image Scanner III, GE Healthcare, Chicago, IL, USA). The root length was measured in ImageJ software (<http://rsb.info.nih.gov/ij/>). A Nikon 7000 camera equipped with a macro objective Sigma 50 mm (2.8 focal distance)

was used for documenting the phenotype of plants growing in plates. Fresh weights of shoots and roots separately were measured from 18-days old plants growing on media containing PQ.

### **3.5 Immunolabelling of microtubules by the whole-mount method**

Whole-mount immunofluorescence labelling was prepared from 3-days old C24 and *der1-3* mutant roots germinating in control half-strength MS medium according to a standard protocol (Beck *et al.*, 2010; Šamajová *et al.*, 2014) with some modifications. Samples were fixed at room temperature for 1 h or at 4 °C overnight. After aldehyde reduction samples were washed five times for 10 min and washing after cell wall digestion was done three times for 10 min. In addition, 5 % (w/v) bovine serum albumin (BSA) in phosphate-buffered saline (PBS) was used for blocking. YOL1/34 (Bio-Rad) diluted in 3 % (w/v) BSA was used as the primary anti- $\alpha$  tubulin rat monoclonal antibody. Thorough washing after incubating with the primary antibody was done 12 times for 10 min with 3 % (w/v) BSA in PBS. Subsequently, a secondary Alexa Fluor 488-conjugated anti-rat IgG antibody (Molecular Probes), appropriately diluted in 3 % (w/v) BSA, was applied. Incubation was done at 37 °C for 3 h followed by incubation at 4 °C overnight. Nuclear DNA was counterstained with 4',6-diamidino-2-phenylindole (DAPI; Sigma Aldrich). Immunolabelled samples were examined using a confocal laser scanning microscope (CLSM) LSM 710 (Carl Zeiss, Germany).

### **3.6 Histochemical detection of $O_2^{\cdot-}$ and $H_2O_2$ production**

C24 and *der1-3* mutant plants (3-days old) were transferred from the control media to media containing  $0.1 \mu\text{mol.l}^{-1}$  of PQ and  $3 \text{ mmol.l}^{-1}$  of  $H_2O_2$ . We have chosen these concentrations of PQ and  $H_2O_2$  based on preliminary growth response and phenotypical analyses. Histochemical detection of ROS was performed 11 days after the transfer (plants were 14-days old). Superoxide ( $O_2^{\cdot-}$ ) was detected by NBT (nitrotetrazolium blue) staining according to Ramel *et al.* (2009).  $H_2O_2$  detection was performed with DAB (diaminobenzidine) staining according to Daudi *et al.* (2012). After staining, plants were mounted into slides and imaged with Axio Zoom.V16 (Carl Zeiss, Germany). Staining intensity mean values from selected areas in cotyledons and leaves were measured and quantified in ZEN 2 software (blue edition; Carl Zeiss, Germany).

### 3.7 Modelling of ACTIN2 protein structure

A phenol/chloroform/isoamylalcohol protocol (Pallotta *et al.*, 2000) was used for isolation of genomic DNA from the *der1-3* mutant plants (from three different samples). Isolated genomic DNA samples were subjected to sequencing (SeqMe, Dobříš, Czech Republic). In Nucleotide BLAST database (BLAST, U.S. National Library of Medicine, National Center for Biotechnology Information; [https://blast.ncbi.nlm.nih.gov/Blast.cgi?PROGRAM=blastn&PAGE\\_TYPE=BlastSearch&LINK\\_LOC=blasthome](https://blast.ncbi.nlm.nih.gov/Blast.cgi?PROGRAM=blastn&PAGE_TYPE=BlastSearch&LINK_LOC=blasthome)), we compared acquired sequences with control *ACTIN2* genomic DNA sequence. Sequences (both control and mutated) were translated to protein sequences in the application available at <http://bio.lundberg.gu.se> (University of Gothenburg, Sweden; <http://bio.lundberg.gu.se/edu/translat.html?fbclid=IwAR3var5FJ8CB14QqNe4Yic8NVz0TvWRd0TrFuGUo6Nk6idLQxy2HvQqPEU>). Only one single point mutation found (in position 1114 C-T) changed the protein sequence at the position 97 (Arg97-Cys97) accordingly. Protein sequences were used for protein structure modelling using the application SWISS-MODEL (Biozentrum, University of Basel, Switzerland; <https://swissmodel.expasy.org/interactive?fbclid=IwAR1V9lhUgjiR1kUwFLd8ojFftkHpKZwxIoT6mnEVulEC2cPSYQov2twoE>). The representative images were generated in the same application.

### 3.8 Preparation of samples for microscopy

All lines under study were prepared for microscopy. Plants 2- to 3-days old were transferred to microscopy chambers containing liquid modified MS medium according to Ovečka *et al.* (2005, 2014). The composition of the liquid modified MS medium (annotated as ARA medium) is summarized in the Table 3. After manipulation with plants during sample preparation, the subsequent stabilization period for 24 h allowed undisturbed growth of the root and the formation of new RHs.



**Table 3: Composition of liquid (ARA) medium for microscopic preparations**

Component	Value or amount in 50 ml medium
<b>Macroelements - 10x diluted</b> (KNO <sub>3</sub> , KH <sub>2</sub> PO <sub>4</sub> , MgSO <sub>4</sub> .7H <sub>2</sub> O, Ca (NO <sub>3</sub> ) <sub>2</sub> .4 H <sub>2</sub> O)	5 ml
<b>Microelements (added after autoclaving)</b>	
<b>- 1000x diluted</b> (H <sub>3</sub> BO <sub>3</sub> , MnCl <sub>2</sub> .4 H <sub>2</sub> O, CuSO <sub>4</sub> .5 H <sub>2</sub> O, Na <sub>2</sub> MoO <sub>4</sub> .2 H <sub>2</sub> O, NaCl, ZnSO <sub>4</sub> .7 H <sub>2</sub> O, CoCl <sub>2</sub> .6 H <sub>2</sub> O)	0.05 ml
<b>Iron - 100x diluted</b> (Na <sub>2</sub> EDTA, FeSO <sub>4</sub> .7 H <sub>2</sub> O)	0.5 ml
<b>Sucrose</b>	0.5 g
<b>CaCl<sub>2</sub></b>	5.5 mg
<b>MiliQ water</b>	44 ml
<b>Total volume</b>	50 ml, adjust to pH 5.7-5.8 (with 0.1 M KOH)

### 3.9 Application of stress factors directly at the microscope stage

Application of oxidative stress was induced in the liquid culture medium (ARA medium) containing 0.1  $\mu\text{mol.l}^{-1}$  of PQ. The C24 ecotype and *der1-3* mutant expressing a construct *pro35S::GFP:FABD2* were observed under the microscope under the control conditions for 30 min first, and then the medium containing PQ was applied using perfusion of the microscopy chamber. The medium was applied sequentially 10 times 10  $\mu\text{l}$ , therefore the total volume applied reached 100  $\mu\text{l}$ . After perfusion, hypocotyls and cotyledons out of the coverslip were carefully covered with parafilm and samples were scanned in the microscope every 30 s for a further 30 min. These samples were used for live cell imaging of the actin cytoskeleton in hypocotyl epidermal cells and observed in a spinning disk microscope Cell Observer SD Axio Observer Z1 (Carl Zeiss, Germany).

### 3.10 FM4-64 and phalloidin staining

The FM4-64 dye was used as a marker for PM and vesicular compartments in root cells and in RHs. Experiments were done in 3-days old seedlings of *A. thaliana* ecotype

C24 and *der1-3* mutant. Plants were placed in a drop of half-strength MS culture medium supplemented with 4  $\mu\text{mol.l}^{-1}$  FM4-64 (Thermo Fisher Scientific, Waltham, MA, USA) on a microscope slide for 30 min in darkness and at constantly high humidity. After staining, excess of FM4-64 was carefully washed out from the slide using fresh culture medium, and samples after closing with coverslip were directly observed in a spinning disk (SD) microscope.

For the FM4-64 labelling of RHs, 3- to 4-days old plants (GFP-RHD2, GFP RabA1d and RabF2a-YFP) were used after 24 h stabilization in microscopy chamber with liquid ARA medium. FM4-64 (4  $\mu\text{mol.l}^{-1}$ ) in liquid ARA medium were individually applied by perfusion directly to the microscopy chamber. The total volume of the modified liquid ARA medium with FM4-64 applied was 100  $\mu\text{l}$ , added in 10 separate steps consisting of 10  $\mu\text{l}$  each for 10 min. After perfusion, the plants were directly observed using a SD microscope.

Visualization of F-actin using phalloidin was performed in 3-days old plants of *A. thaliana* ecotype C24 and *der1-3* mutant according to Panteris *et al.* (2006). After fixation, F-actin was labelled with Alexa Fluor 488-phalloidin (Invitrogen). Samples were observed with a confocal laser scanning microscope (CLSM) LSM 710, Carl Zeiss, Germany.

### **3.11 Filipin III and auxinole application**

Filipin III (Sigma-Aldrich, St Louis, MO, USA) was used as a vital probe for the PM structural sterols, allowing the formation of filipin-sterol complexes in RHs at higher concentrations. GFP-RHD2, GFP-RabA1d, RabF2a-YFP and GFP-RHD2  $\times$  mCherry-RabF2b plants were used for filipin III labelling. Auxinole (MedChemExpress, Monmouth Junction, NJ, USA), a potent auxin antagonist, was used for arresting RH tip growth of GFP-RHD2 plants. Filipin III (10  $\mu\text{g.ml}^{-1}$ ) and auxinole (20  $\mu\text{mol.l}^{-1}$ ) in modified liquid ARA medium were individually applied by perfusion directly to the microscopy chamber. The total volume of the modified liquid ARA medium with filipin III or auxinole applied was 100  $\mu\text{l}$ , added in 10 separate steps of 10  $\mu\text{l}$  each for 10 min. After perfusion, the plants were directly observed using a SD microscope.

### **3.12 Microscopic imaging**

#### **3.12.1 Epifluorescence microscopy**

An epifluorescence microscope Zeiss Axio Imager M2 equipped with DIC optics and epifluorescence metal halide source illuminator HXP 120 V (Zeiss, Oberkochen, Germany), and analysed using Zeiss ZEN 2012 Blue software (Zeiss, Germany) was used for time-lapse documenting of RHs growth after filipin III or auxinole treatments. Two to three-days-old plants were transferred to microscopy chambers containing liquid modified ARA medium according to Ovečka *et al.* (2005, 2014). Plants after preparation required 24 h stabilization in a glass cuvette in an environmental chamber allowed the continuation of root growth and the formation of new RHs. Growing RHs (n = 3-5 RHs from five plants) were recorded at 1 min intervals for 5 min before the application, then for another 5 min throughout the application of mock, or 10  $\mu\text{g}\cdot\text{ml}^{-1}$  filipin III, or 20  $\text{mmol}\cdot\text{l}^{-1}$  auxinole in modified liquid ARA medium, respectively, and 5 min after application. Mock treatment represented modified ARA medium without inhibitors. Applied solutions (control medium, filipin III, and auxinole) were added sequentially in five separate steps of 10  $\mu\text{l}$  each, making a total volume of 50  $\mu\text{l}$ . Gentle application by perfusion was performed directly at the microscope stage in the sample chambers at the respective time points of acquisition. Imaging was performed with a Plan-Neofluar 40x/0.75 NA dry objective and documented with a Zeiss AxioCam ICm1 camera. A filter set providing a wavelength of 450-490 nm for the excitation and 515-565 nm for the emission at 400 ms exposure time was used to visualize the GFP signal. For the filipin III signal, the filter set provided an excitation wavelength of 335-383 nm and an emission wavelength of 420-470 nm was used. The exposure time was 200 ms for both filipin III and DIC channel acquisitions. The image scaling for both channels was  $0.116 \times 0.116$  mm in  $x \times y$  dimensions, and with the  $z$  dimension 1.65 mm for the filipin III channel, and 1.81 mm for the GFP channel.

#### **3.12.2 Spinning disk microscopy (SD)**

A spinning-disk microscope (Cell Observer Z.1; Carl Zeiss, Germany), equipped with EC Plan-Neofluar 40x/1.3 NA oil immersion objective, Plan-Apochromat 63x/1.4 NA oil immersion objective, and alpha Plan-Apochromat 100x/1.57 NA DIC Korr oil immersion objective was used for different live-cell imaging, namely for visualization of the cytoskeleton, FM4-64-labelled samples, and for colocalization studies.

### 3.12.2.1 Visualization of cytoskeleton and FM4-64 in living plants

Plants of C24 ecotype and *der1-3* mutant expressing *pro35S::GFP:FABD2* (actin cytoskeleton) and *pro35S::GFP:MBD* (microtubules) constructs were scanned in a Z-stack mode in a time range of every 30 s for 30 min. For these experiments were used EC Plan-Neofluar 40x/1.3 NA and Plan-Apochromat 63x/1.4 NA oil immersion objectives. Images were recorded with a high-resolution Evolve 512 back-thinned EM-CCD camera (Photometrics) with the exposure time 500-750 ms per optical section. The samples were imaged with a 488 nm excitation laser line and BP525/50 emission filter for detection of GFP fluorescence and with a 514 nm excitation laser line and emission filter BP690/50 for detection of FM4-64 fluorescence. The excitation laser power level for all lasers used was set up to 50%.

#### 3.12.2.1.1 Quantification of cytoskeleton and FM4-64 in living plants

Parameters tested, such as orientation of the cell division plane CDP, actin cytoskeleton skewness (an extent of AF bundling) and AF fluorescence integrated density (representing a percentage of occupancy), were measured in ImageJ software (<http://rsb.info.nih.gov/ij/>). Orthogonal projections of 6 to 10 optical sections from Z-stacks (in C24 GFP-FABD2 and *der1-3* GFP-FABD2 lines) were used for the preparation of videos and measurement of AF skewness and occupancy. Quantitative analysis of AF angular distribution was done with CytoSpectre Version 1.2 software using the cell axis as a reference (Kartasalo *et al.*, 2015). Analysis showed the degree of AF arrangement with respect to transverse (defined as perpendicular to the cell axis at an angle of 0° or 180°), longitudinal (parallel to the cell axis at an angle of 90° or 270°) or random (an angle between 0° and 180°) orientations. Semiquantitative analysis of AF dynamics in hypocotyl epidermal cells were presented by pseudocolouring displacement analysis. Images recorded at the beginning, after 15 min, and after 30 min of the time-point scanning were individually coloured red, green, and blue, respectively, and merged. Overlay of all three colours creating a white one indicated lowering, or eventually stopping, active actin rearrangements.

FM4-64 labelled roots of C24 wild-type and *der1-3* mutant plants were used for quantification of CDP orientation. The angular positioning of cross-walls with respect to the longitudinal root axis was measured from microscopic images of root cells stained with FM4-64. The obtained data were divided into three categories according to the recorded angles: cross-walls at right angles ( $90^\circ \pm 5\%$ ), cross-walls at acute angles ( $<85^\circ$ )

and cross-walls with obtuse angles ( $>95^\circ$ ). Angles were measured in root epidermal and cortical cells of C24 wild-type and *der1-3* mutant plants.

### **3.12.2.2 Colocalization studies in root hairs**

The colocalization of fluorescence signals was analysed using simultaneous signal acquisition with two independent Evolve 512 EMCCD cameras (Photometrics). After camera calibration for proper alignment, the fluorescence signals of the two markers were imaged and recorded using a camera streaming mode. The samples were imaged using an excitation laser line of 405 nm and emission filter BP450/50 for filipin III signal detection, excitation laser line of 488 nm and emission filter BP525/50 for GFP signal detection, excitation laser line of 514 nm, and emission filter BP535/30 for YFP signal detection, excitation laser line of 514 nm and emission filter BP690/50 for FM4-64 signal detection, and excitation laser line of 561 nm and emission filter BP629/62 for the mCherry signal detection. The excitation laser power level for all lasers used was set up to 50%, and the samples were scanned every 731 ms using a camera-streaming mode. Semi-quantitative signal intensity analysis of double transgenic lines GFP-RHD2  $\times$  mCherry-VTI12 and GFP-RHD2  $\times$  mCherry-RabF2b were done from one selected Z-stack of the scanned area. Similarly, the fluorescence intensity was determined in single transgenic lines GFP-RHD2, GFP-RabA1d, and RabF2a-YFP labelled with FM4-64. Profiles for quantitative signal intensity distribution and colocalization were generated using Zen Blue 2014 software (Carl Zeiss, Germany). Quantitative colocalization analysis of vesicular compartments was performed from 75 measurements of each individual line. It represents three different ROIs from five individual RHs at five different time points. Colocalization analysis was also performed on PM from five individual RHs at five different time points, in total 25 measurements. For the measurement, a particular ROI covering the selected PM area of each respective time point was indicated. Pearson's correlation coefficient according to Costes *et al.* (2004) was used as the parameter for quantitative colocalization analysis from selected ROIs of vesicles and PMs of double transgenic lines (GFP-RHD2 GFP-RHD2  $\times$  mCherry-VTI12 and GFP-RHD2  $\times$  mCherry-RabF2b) and FM4-64 staining of GFP-RHD2, GFP-RabA1d, and RabF2a-YFP lines.

### **3.12.3 Confocal laser scanning microscopy (CLSM)**

Fixed plant samples for phalloidin staining and for whole-mount immunolabelling were examined with a confocal laser scanning microscope (LSM 710; Carl Zeiss, Germany) equipped with a Plan-Apochromat 40x/1.4 numerical aperture (NA) oil

immersion objective. Samples labelled with phalloidin and Alexa Fluor 488 immunolabelled roots were imaged using a 488-nm laser excitation line and emission spectrum 493-630 nm and DAPI fluorescence detection was done with a 405-nm excitation laser line and emission spectrum 410-495 nm. Laser excitation intensity did not exceed 2 % of the laser intensity range available. The range of the Z-stack was always set to 0.61  $\mu\text{m}$ .

#### **3.12.4. Airyscan confocal laser scanning microscopy (Airyscan CLSM)**

Confocal laser scanning microscope LSM 880 equipped with Airyscan (Carl Zeiss, Germany) was used for qualitative and quantitative characterization of GFP-RHD2-positive compartments during RH development and growth. Plants 2- to 3-days old were transferred to microscopy chambers containing liquid modified ARA medium according to Ovečka *et al.* (2005, 2014). After manipulation with plants during sample preparation, the subsequent stabilization period for 24 h allowed undisturbed growth of the root and the formation of new RHs. In total, we used more than 10 individual plants to analyse the development and growth of RHs. Image acquisition was performed with a 20x/0.8 NA dry Plan-Apochromat objective (Carl Zeiss, Germany). The samples were imaged with an excitation laser line of 488 nm and BP420-480 + BP495-550 emission filters for GFP detection. The laser power did not exceed 0.8% of the available laser intensity range. The samples were scanned every 706 ms with 700 ms of exposure time using a 32 GaAsP detector. Pixel dwell time was set up to 1.98 ms, and with default settings of the gain level the image scaling was set up to  $0.074 \times 0.074 \times 0.397$  mm (x  $\times$  y  $\times$  z).

##### **3.12.4.1 Single-particle tracking of compartments containing GFP-RHD2**

Quantitative tracking of the GFP-RHD2 compartments was performed in Arivis Vision4D program, version 3.1.4. (Arivis AG, Germany). Data from 3-days old plants imaged by Airyscan CLSM were used for measurements. Different stages of RH development were selected, and one particular Z-stack of the representative field of view was imaged for 60 s. Acquired data were processed and quantified using the Tracked cells function of the Arivis software. Before analysis, the following conditions were set up for normalization: (1) the highest and lowest fluorescence intensity thresholds were set to 30 and 410, respectively; (2) the distance of compartment movement recorded during one time period should not exceed 5 mm; (3) accepted compartments did not disappear from the image plane for more than two time periods during acquisition; and (4) the accepted compartment surface area was always in the range of 0.5-3  $\text{mm}^2$ . GFP-RHD2

compartments moving in different stages of RH development, namely in the early bulges, late bulges, short growing RHs, and longer growing RHs were characterized by minimum, maximum, average speed, and the distance parameters. The analysed compartments were divided into the following subgroups: moving to and contacting the apical PM (red group), moving in the cytoplasm without any contact with the PM (blue group), and contacting the PM and moving back to the cytoplasm (cyan group). A comparison was made between compartments moving outside the bulging domain in trichoblasts and those moving in atrichoblasts. Fluorescence intensity profiles in the 2.5-D dimension was also done in Arivis software.

### **3.12.5 Light-sheet fluorescence microscopy (LSFM)**

Live-cell imaging of whole roots was done with a light-sheet fluorescence microscope (Lightsheet Z.1; Carl Zeiss, Germany) equipped with a W Plan-Apochromat 20x/1.0 NA water immersion detection objective and two LSFM 10x/0.2 NA illumination objectives. Samples were prepared in an open system according to Ovečka *et al.* (2015). Sterilized seeds of C24 and the *der1-3* mutant, both expressing *pro35S::GFP:FABD2* construct and Col-0 GFP-RHD2 were plated on half-strength MS medium and stratified at 4 °C for 5 days. After rupture of the testa, seeds were transferred to culture medium solidified with 0.5 % (w/v) Gellan gum on Petri plates and left to germinate horizontally in a growth chamber. Three-day-old plants were inserted into the fluorinated ethylene propylene (FEP) tubes with an inner diameter of 2.8 mm and wall thickness of 0.2 mm (Wolf-Technik, Germany) with the solidified medium surrounding the root (root was embedded in the medium, and the upper green part of plants was exposed to air). The FEP tube with one seedling was carefully pulled away from the Petri dish. The samples were transferred to a pre-tempered (22°C) observation chamber of the LSFM filled with a modified liquid ARA medium. The agar block with the plant was partially pushed out from the FEP tube into the liquid medium for imaging of the root tip not surrounded by FEP tube walls. Imaging was carried out using dual-side illumination and pivot scan mode with a light-sheet thickness of 4.52 µm and with a 488 nm excitation line and BP505-545 emission filter. Laser excitation intensity did not exceed 3% of the laser intensity range available. Image acquisition was done every 5 min in Z-stack mode for 10-15 h. Scaling of images in the x, y and z dimensions was  $0.228 \times 0.228 \times 0.477$  µm, encompassing the volume of  $438.69 \times 438.69 \times 229.79$  mm (x × y × z). Images were recorded with the PCO

Edge sCMOS camera (PCO AG, Germany) with an exposure time of 40 to 50 ms per optical section.

#### **3.12.5.1 3D rendering of GFP-RHD2 distribution**

Data obtained by LSFM time-lapse imaging from growing primary roots and RHs of the GFP-RHD2 line were subjected to 3D rendering. In Zen 2014 software, black edition (Carl Zeiss, Germany), a subset of selected time-points (lasting for 4 h and 25 min of imaging) was created from the whole volume of the root (containing 483 Z stacks). The subsets were selected to capture the different developmental stages of RH formation in the root differentiation zone. The output data were imported into Arivis Vision4D version 2.12.6 software (Arivis AG, Rostock, Germany) and automatically converted to the \*.sis file. Subsequently, data were visualized as 3D objects by activating the 4D viewer in the Viewer Types Panel. 3D objects were rendered in the maximum intensity mode. The colour scale was switched to rainbow colouring to enhance the contrast visibility of the fluorescence signal intensities and distribution. The lowest and highest saturation points were adjusted to 219 (black) and 427 (red), respectively. For 3D visualizations of primary root cross-sections, clipping around a region of interest was adjusted using a 4D clipping panel and ROI tab. Videos were configured by arranging keyframes and rendered as movies for export in the storyboard extension. Animations were prepared by clipping the 3D model against the y- and z-planes in a 4D clipping panel and using rotation and zoom tools (done with the help of Michaela Tichá).

#### **3.12.6 Data acquisition and analysis**

Microscopic data were processed and evaluated in Zen 2014 software, black and blue editions (Carl Zeiss, Germany). Kymographs were generated from time-lapsed images acquired by SD, Airyscan CLSM and LSFM using the appropriate plugin of Zen software (Blue version). ImageJ software (<http://rsb.info.nih.gov/ij/>) was used for analysis of root growth rate, CDP orientation, skewness, and integrated density of cytoskeletal components. All graphical plots were prepared in Microsoft Excel software and statistical analyses were performed using the STATISTICA 12 (StatSoft, TIBCO Software Inc., Palo Alto, CA, USA) by analysis of variance (ANOVA) and subsequent Fisher's least significant difference (LSD) tests ( $p < 0.05$ ).



## 4. Results

### 4.1 Single-point *ACT2* gene mutation in the *Arabidopsis* root hair mutant *der1-3* affects overall actin organization, root growth and plant development

**Vaškebová L**, Šamaj J, Ovečka M (2018). Single-point *ACT2* gene mutation in the *Arabidopsis* root hair mutant *der1-3* affects overall actin organization, root growth and plant development. *Annals of Botany* 122: 889-901. doi: 10.1093/aob/mcx180

**LV** performed all experiments included in the paper, namely the preparation of stable transgenic lines, immunolabelling and phalloidin staining of the cytoskeleton, phenotypic and microscopic analyses, data acquisition and their quantitative evaluation. **LV** also participated in writing of the manuscript.

Actin cytoskeleton forms dynamic network in plant cells, regulating cellular and developmental processes like cell division, growth, intracellular signalling and transport. *ACTIN* genes expressed in plants are divided into two groups - encoding for vegetative and reproductive actin classes. A major actin in vegetative tissues is encoded by *ACT2* gene. Single-point mutation in the *DER1* (*deformed root hairs1*) locus encoding *ACTIN2* in *A. thaliana*, generates mutant plants with short RHs, with so called “short root hair phenotype”. Originally, only impaired in RH development has been ascribed to *der1* mutations without any other obvious defects in plant growth and development. However, our thorough plant phenotyping, organ-specific and cellular analyses revealed differences in the growth and development of *der1* mutants in comparison to control wild-type plants. The phenotypical analyses revealed that the speed of germination, plant fresh weight, and total leaf area were significantly reduced in the *der1-3* mutant, while number of true leaves was increased in *der1-3* mutant and the root growth rate was not altered. Obvious phenotypical aspect characteristic for *der1-3* mutant was wavy growth pattern of the main root. Using three independent methods, such as FM4-64 vital staining, live cell imaging by light-sheet microscopy of *der1-3* mutant lines carrying GFP-FABD2 fusion protein, and whole-mount immunolabelling of MTs, we consistently found higher frequencies of shifted cell division planes (CDPs) in the root epidermal and cortical cells of the mutant, which was much less frequent in the control C24 ecotype. Waving root growth pattern connected with alterations in CPD orientation may indicate changes in the actin cytoskeleton organization. Therefore, live-cell imaging experiments with transgenic lines

carrying GFP-FABD2 fusion protein, together with actin visualization using phalloidin labelling in fixed plant samples revealed morphological differences in the actin cytoskeleton between *der1-3* mutant and control C24 ecotype. Quantitative evaluation measurements from two independent studies in hypocotyl epidermal cells and roots proved that AFs in the cells of *der1-3* mutant were shorter, thinner, and arranged in more random orientations. It indicates, that *ACT2* mutation in the *der1-3* mutant does not influence solely RH formation process, but it has more general effects on overall plant growth and development.

PART OF A SPECIAL ISSUE ON FUNCTIONAL–DEVELOPMENTAL PLANT CELL BIOLOGY  
**Single-point *ACT2* gene mutation in the *Arabidopsis* root hair mutant *der1-3* affects overall actin organization, root growth and plant development**

L. Vaškebová, J. Šamaj and M. Ovečka\*

Department of Cell Biology, Centre of the Region Haná for Biotechnological and Agricultural Research, Palacký University Olomouc, Olomouc 783 71, Czech Republic

\*For correspondence. E-mail [miroslav.ovecka@upol.cz](mailto:miroslav.ovecka@upol.cz)

Received: 1 September 2017 Returned for revision: 9 October 2017 Editorial decision: 24 October 2017 Accepted: 20 November 2017  
Published electronically 27 December 2017

- **Background and Aims** The actin cytoskeleton forms a dynamic network in plant cells. A single-point mutation in the *DER1* (*deformed root hairs 1*) locus located in the sequence of *ACTIN2*, a gene for major actin in vegetative tissues of *Arabidopsis thaliana*, leads to impaired root hair development (Ringli C, Baumberger N, Diet A, Frey B, Keller B. 2002. *ACTIN2* is essential for bulge site selection and tip growth during root hair development of *Arabidopsis*. *Plant Physiology* **129**: 1464–1472). Only root hair phenotypes have been described so far in *der1* mutants, but here we demonstrate obvious aberrations in the organization of the actin cytoskeleton and overall plant development.
- **Methods** Organization of the actin cytoskeleton in epidermal cells of cotyledons, hypocotyls and roots was studied qualitatively and quantitatively by live-cell imaging of transgenic lines carrying the GFP-FABD2 fusion protein and in fixed cells after phalloidin labelling. Patterns of root growth were characterized by FM4-64 vital staining, light-sheet microscopy imaging and microtubule immunolabelling. Plant phenotyping included analyses of germination, root growth and plant biomass.
- **Key Results** Speed of germination, plant fresh weight and total leaf area were significantly reduced in the *der1-3* mutant in comparison with the C24 wild-type. Actin filaments in root, hypocotyl and cotyledon epidermal cells of the *der1-3* mutant were shorter, thinner and arranged in more random orientations, while actin bundles were shorter and had altered orientations. The wavy pattern of root growth in *der1-3* mutant was connected with higher frequencies of shifted cell division planes (CDPs) in root cells, which was consistent with the shifted positioning of microtubule-based preprophase bands and phragmoplasts. The organization of cortical microtubules in the root cells of the *der1-3* mutant, however, was not altered.
- **Conclusions** Root growth rate of the *der1-3* mutant is not reduced, but changes in the actin cytoskeleton organization can induce a wavy root growth pattern through deregulation of CDP orientation. The results suggest that the *der1-3* mutation in the *ACT2* gene does not influence solely root hair formation process, but also has more general effects on the actin cytoskeleton, plant growth and development.

**Key words:** *ACTIN2* gene, actin cytoskeleton, *Arabidopsis thaliana*, cell division plane orientation, *der1-3* mutant, GFP-FABD2, live-cell imaging, microscopy, microtubules, phenotype, plant development, root growth.

## INTRODUCTION

The plant cytoskeleton, consisting of actin filaments (AFs) and microtubules, represents a dynamic supramolecular structure with many cellular functions. The actin cytoskeleton plays crucial roles in the establishment of cell polarity, in the positional control and progression of cell division, and it is involved in diffuse and polar cell elongation (Volkman and Baluška, 1999; Baluška *et al.*, 2000b; Barlow and Baluška, 2000; Meagher and Fechheimer, 2003; Šamaj *et al.*, 2004; Henty-Ridilla *et al.*, 2013). The genome of *Arabidopsis thaliana* contains two major classes of actin genes, encoding vegetative and reproductive actin isoforms. The vegetative group of actin genes includes *ACT2*, *ACT7* and *ACT8*, which are typically expressed in all vegetative tissues. The reproductive class of actin genes consists of *ACT1*, *ACT3*, *ACT4*, *ACT11* and *ACT12*. They are expressed mainly in pollen tubes and ovules (Meagher *et al.*, 1999; Kandasamy *et al.*, 2007). Vegetative actin isoforms have

specific expression patterns. The *ACT2* gene is expressed in young and old vegetative tissues, in flowers, leaves, stems and roots. The *ACT8* gene has expression patterns similar to those of the *ACT2* gene while the *ACT7* gene is expressed mainly in young expanding vegetative tissues (Meagher *et al.*, 1999). Importantly, the overproduction of *ACT1* caused the formation of sheet- or star-like aberrant actin structures in vegetative cells, leading to different thickness and orientation of actin filaments in comparison with control cells (Kandasamy *et al.*, 2002). On the other hand, overexpression of *ACT2* in vegetative tissues has little effect on plant morphology and the structure of actin filaments (Kandasamy *et al.*, 2002). Although the vegetative actins differ from the reproductive ones only by 4–7 % at the amino acid sequence level, their expression patterns and functions are different (Kandasamy *et al.*, 2007).

Some vegetative plant organs contain up to 50 % of *ACT2* mRNA out of the total actin mRNA amount, suggesting that the

*ACT2* gene is highly expressed among actin genes in *Arabidopsis* (McDowell et al., 1996). An expression study of *proACT2::GUS* and *proACT8::GUS* constructs revealed that the *ACT2* promoter is the stronger (An et al., 1996). Its expression was found in nearly all vegetative tissues of young seedlings and juvenile and mature plants, and persisted in older plant tissues. No or little expression has been found in the seed coat, hypocotyl, gynoceum or pollen sac (An et al., 1996). Hence, the *ACT2* isoform has attracted more interest than other isoforms in plant biology studies. Mutational studies of the *ACT2* gene generated several interesting mutants. Classical mutagenesis approaches based on ethyl methanesulphonate (EMS) or X-rays, inducing randomly generated single-point mutations, led to the isolation of a series of *der* mutants (*der1-der9*; *deformed root hair*) (Ringli et al., 2002, 2005). Three *der1* allelic mutants isolated after EMS mutagenesis in the C24 ecotype background were identified based on the root hair phenotype. Among them, the strongest phenotypic effect has been described in *der1-2* and *der1-3* mutants (Ringli et al., 2002). The root hair phenotype of the *der1-3* mutant was characterized by wrong selection of the root hair initiation site in the trichoblast and impairment of root hair elongation after bulge establishment. Therefore, *der1-3* mutant plants show a phenotype of very short root hairs (Ringli et al., 2002). It has been concluded that *ACT2* is involved mainly in the tip growth of root hairs, since no other obvious aberrations of overall development and phenotype of *der1* mutant plants have been detected (Ringli et al., 2002). Another mutant produced by EMS mutagenesis in the *Ler* ecotype background, *act2-2D*, is not able to form root hairs. In this mutant, bulges are not developed on trichoblasts (root hair-forming cells) and bundles of actin filaments in the root epidermal cells of *act2-2D* mutant are shorter than in wild-type plants (Nishimura et al., 2003). T-DNA insertional loss-of-function mutants in *ACT2*, *act2-1* (Gilliland et al., 2002) and *act2-3* (Nishimura et al., 2003) show very similar root hair phenotypes. The length of root hairs of the *act2-1* mutant was 10–70 % of that of wild-type root hairs (Gilliland et al., 2002). Root hair initiation is not impaired in the *act2-3* mutant, but mature root hairs of this mutant are shorter than wild-type root hairs (Nishimura et al., 2003). These data support the role of AFs in the process of root hair initiation and in their tip growth (Braun et al., 1999; Baluška et al., 2000a; Pei et al., 2012). The phenotype of the *act2-5* mutant is a bit more complex, showing a wavy shape of the main root and altered structure of the actin cytoskeleton (Lanza et al., 2012). Single mutants for the vegetative actin genes *ACT2*, *ACT7* and *ACT8* revealed only mild phenotypes, but double mutants were much more affected. They exhibited dwarf phenotypes, defects in cell and organ morphology and aberrant actin cytoskeleton organization (in *act2-1 act7-4* and *act8-2 act7-4*) or totally missing root hairs (*act2-1 act8-2*) (Kandasamy et al., 2009). This study revealed that *ACT7* is involved in root growth, epidermal cell specification, cell division and root architecture, while *ACT2* and *ACT8* are essential for root hair tip growth. Nevertheless, all mutants for single vegetative actin genes were fully fertile (Gilliland et al., 1998).

The plant cytoskeleton plays important roles during cell division, a fundamental process for plant morphogenesis and development. Plant cells are delineated by rigid cell walls and therefore the orientation of the cell division plane (CDP) during cell division is a basic determinant of plant anatomy and development (Müller, 2012; Smolarkiewicz and Dhonukshe,

2013; Zhang et al., 2016). Plant cell division is controlled by specific arrangements of mitotic microtubules organized in distinct arrays. The microtubule preprophase band (PPB), formed at preprophase and early prophase, predicts the future cell division site. The mitotic spindle is a major mitotic microtubule structure formed at prophase, which positions and segregates sister chromatids through the successive stages of metaphase, anaphase and telophase. The phragmoplast is a specialized microtubule array formed during cytokinesis, delivering vesicles to the nascent cell plate and expanding centrifugally to meet the cortical domain predetermined by the PPB (Fowler and Quatrano, 1997; Rasmussen et al., 2013; de Keijzer et al., 2014). The indispensable role of microtubules in the determination of CDP orientation of dividing cells has been proved in many studies after pharmacological treatments or in appropriate mutants (Palevitz, 1987; Mineyuki et al., 1991; Komis et al., 2017; reviewed in Rasmussen et al., 2013).

The actin cytoskeleton also contributes to the correct progression of cell division, although AFs differ from microtubules in spatial and temporal distribution. Actin filaments contribute to early stages of PPB formation, but are less abundant in the PPB at later stages (Takeuchi et al., 2016), while their occurrence in the mitotic spindle is obscure, forming a surrounding cage around the spindle to maintain its position during mitosis (Lloyd and Traas, 1988; Katsuta et al., 1990). Later, AFs are abundant in the phragmoplast during cytokinesis. Not surprisingly, disorientation of the CDP in tobacco BY-2 cells has been induced after application of actin-depolymerizing or actin-stabilizing drugs during early stages of mitosis (Sano et al., 2005; Kojo et al., 2013, 2014). These data suggest that both microtubules and AFs may functionally cooperate during PPB and phragmoplast formation, the establishment of the CDP and the correct deposition of the cell plate. Reciprocity between microtubule and AF organization was shown through the partial damage of the fine transversely oriented cortical AFs after microtubule depolymerization in *A. thaliana* and carrot interphase cells. Vice versa, pharmacological disruption of AFs led to the reorganization of microtubules (Sampathkumar et al., 2011). These data strongly indicate that AFs may play a key role not only in the assembly but also in the positioning of the PPB in the cell. It is not clear, however, how the process of microtubule–AF interaction during the regulation of cell division is affected in *ACTIN* mutants.

So far, only the root hair phenotype has been described in *der1* mutants without any obvious aberrations in plant development. In the present study, we provide thorough plant phenotyping and characterization of the actin cytoskeleton in *der1-3* mutant plants. The changed organization and arrangement of AFs in cell types other than root hairs, the phenotypical differences in root development related to the deregulated CDP during cell division and the changed leaf phenotype indicate that the *der1-3* mutation in the *ACT2* gene has effects additional to those on root hair formation.

## MATERIALS AND METHODS

### *Plant material and growth conditions*

Seeds of *Arabidopsis thaliana* (L.) Heynh. ecotype C24 and the *der1-3* (*deformed root hairs1*) mutant (Ringli et al., 2002)

were surface-sterilized and placed on half-strength Murashige and Skoog (MS) medium without vitamins solidified with 0.6 % w/v Phytigel. Petri dishes containing seeds were stratified at 4 °C for 3 d. After stratification, seeds were cultivated vertically in a growth chamber at 21 °C at 70 % humidity with a 16/8 h light/dark photoperiod (*in vitro* conditions). For experiments *in vivo*, seeds were imbibed overnight in sterile tap water at room temperature. Seeds were transferred to small flowerpots with soil containing Careo (pesticide). Plants were cultured in a growth chamber at 24 °C at 60 % humidity with a 16/8 h light/dark photoperiod.

#### Stable plant transformation

Stable plant transformation was performed according to Clough and Bent (1998). *Arabidopsis thaliana* (ecotype C24 and *der1-3* mutant) plants were transformed with *Agrobacterium tumefaciens* strain GV3101 carrying a construct *pro35S::GFP:FABD2*, coding for F-actin binding domain 2 of *Arabidopsis* FIMBRIN 1 (FABD2) fused to green fluorescent protein (GFP; Voigt et al., 2005) or with a construct *pro35S::GFP:MBD* coding for the microtubule-binding domain (MBD) of the mammalian MICROTUBULE-ASSOCIATED PROTEIN 4 (MAP4) fused to GFP (Marc et al., 1998). Both constructs were driven by the constitutive 35S promoter. An N-terminal GFP fusion with rifampicin and kanamycin resistance was prepared by a classical cloning method in pCB302 vector with the herbicide phosphinothricin as the selection marker *in planta*. Seeds of the  $T_1$  generation were plated on the selection culture medium with phosphinothricin (50 mg mL<sup>-1</sup>). The root hair phenotype of transgenic *der1-3* plants was visually selected (using a stereomicroscope) and the presence of marker GFP fusion proteins was confirmed using a fluorescence microscope. Seeds of the  $T_3$  generation were used for experiments.

#### FM4-64 and phalloidin staining

The FM4-64 dye was used as a plasma membrane marker of root cells. Three-day-old seedlings of *A. thaliana* ecotype C24 and *der1-3* mutant were placed in a drop of half-strength MS culture medium supplemented with 4 μM FM4-64 (Invitrogen) on a microscope slide for 30 min in darkness and at constant humidity. After staining, excess FM4-64 was carefully washed from the slide using culture medium, and samples were then directly observed in a spinning-disk microscope.

Visualization of F-actin using phalloidin was performed in 3-d-old plants of *A. thaliana* ecotype C24 and *der1-3* mutant according to Panteris et al. (2006). After fixation, F-actin was labelled with Alexa Fluor 488-phalloidin (Invitrogen). Samples were observed with a confocal laser scanning microscope.

#### Immunolabelling of microtubules using a whole-mount method

Three-day-old seedlings of C24 and *der1-3* mutant cultivated on half-strength MS medium were prepared for whole-mount immunofluorescence labelling of roots according to a standard

protocol (Beck et al., 2010; Šamajová et al., 2014) with some modifications. Samples were fixed at room temperature for 1 h or at 4 °C overnight. Washing of samples after aldehyde reduction was done five times for 10 min and washing after cell wall digestion was done three times for 10 min. For blocking we used 5 % w/v bovine serum albumin (BSA) in phosphate-buffered saline (PBS). As the primary anti- $\alpha$  tubulin rat monoclonal antibody we used clone YOL1/34 (Bio-Rad) diluted in 3 % w/v BSA, and thorough washing after incubating with the primary antibody was done 12 times for 10 min with 3 % w/v BSA in PBS. Subsequently, a secondary Alexa Fluor 488-conjugated anti-rat IgG antibody (Molecular Probes), appropriately diluted in 3 % w/v BSA, was applied and incubation was done at 37 °C for 3 h followed by incubation at 4 °C overnight. Nuclear DNA was counterstained with 4',6-diamidino-2-phenylindole (DAPI; Sigma Aldrich). Samples were examined with a confocal laser scanning microscope.

#### Microscopy

**Confocal laser scanning microscopy.** Fixed plant samples for phalloidin staining and for whole-mount immunolabelling were examined with a confocal laser scanning microscope (LSM 710; Carl Zeiss, Germany) equipped with a Plan-Apochromat  $\times 40/1.4$  numerical aperture (NA) oil immersion objective. Samples labelled with phalloidin were imaged using a 488-nm laser excitation line and emission spectrum 493–630 nm. Laser excitation intensity did not exceed 2 % of the laser intensity range available. The range of the Z-stack was always set to 0.61 μm. Immunolabelled roots were imaged using a 488-nm excitation laser line and emission spectrum 493–630 nm for Alexa Fluor 488 fluorescence detection and with a 405-nm excitation laser line and emission spectrum 410–495 nm for DAPI fluorescence detection.

**Spinning disk microscopy.** Live-cell imaging of the cytoskeleton and FM4-64-labelled samples was performed with a spinning-disk microscope (Cell Observer Z.1; Carl Zeiss, Germany), equipped with an EC Plan-Neofluar  $\times 40/1.3$  NA oil immersion objective and Plan-Apochromat  $\times 63/1.4$  NA oil immersion objective. Samples were imaged with a 488-nm excitation laser line and BP525/50 emission filter for detection of GFP fluorescence and emission filter BP690/50 for detection of FM4-64 fluorescence. Living samples expressing *pro35S::GFP:FABD2* and *pro35S::GFP:MBD* constructs were scanned every 30 s for 30 min. Images were recorded with a high-resolution Evolve 512 back-thinned EM-CCD camera (Photometrics) with the exposure time 500–750 ms per optical section.

**Light-sheet microscopy.** Live-cell imaging of whole roots was done with a light-sheet fluorescence microscope (Lightsheet Z.1; Carl Zeiss, Germany) equipped with a W Plan-Apochromat  $\times 20/1.0$  NA water immersion detection objective and two LSFM  $\times 10/0.2$  NA illumination objectives. Samples were imaged using dual-side illumination with a light sheet modulated in pivot scan mode, with a 488-nm excitation line and BP505-545 emission filter. Laser excitation intensity did not exceed 3 % of the laser intensity range available. Image acquisition was done every 5 min in Z-stack mode for 10–15 h. Scaling of images in the x, y and z dimensions was 0.228

$\times 0.228 \times 0.477 \mu\text{m}$ . Images were recorded with a PCO.Edge camera (PCO AG) with an exposure time of 50 ms per optical section. Samples were prepared in an open system according to Ovečka et al. (2015). Sterilized seeds of C24 and the *der1-3* mutant expressing *pro35S::GFP:FABD2* construct were plated on half-strength MS medium and stratified at 4 °C for 5 d. After rupture of the testa, seeds were transferred to culture medium on Petri plates and left to germinate horizontally in a growth chamber. After germination, a piece of fluorinated ethylene propylene (FEP) tube with an inner diameter of 2.8 mm and wall thickness of 0.2 mm (Wolf-Technik, Germany) was inserted in the medium, enclosing the seedling. The FEP tube, filled with a cylinder of solidified culture medium and one seedling, was carefully pulled away from the Petri dish. Roots of the examined plant grew inside the culture medium and leaves were in open space and in contact with the air. The FEP tube was then attached to a glass capillary with inner diameter 2.5 mm serving as a sample holder and placed in the light-sheet microscope.

#### Measurements and quantitative and statistical analyses

Plants cultured *in vitro* were scanned directly on Petri plates every 24 h for 5 d from the day of germination. Pictures from a scanner (Image Scanner III, EpsonScan) were used for measurements of primary root length. Phenotypes of 18-d-old plants *in vitro*, rosettes of 19-d-old plants growing *in vivo* and the sizes of individual leaves were documented using a Nikon 7000 camera equipped with macro-objective (50 mm, 2.8; Sigma). The phenotypes of entire roots and root tips of 5-d-old plants *in vitro* were recorded with an M165FC stereo microscope equipped with LAS V 4.0 software (Leica). Microscopic data were processed and evaluated in Zen 2014 software, black and blue editions (Carl Zeiss, Germany). Root growth, orientation of the CDP and cytoskeletal skewness (a measure of microtubule bundling) parameters were measured in ImageJ software. Quantification of CDP orientation was performed from roots of C24 wild-type and *der1-3* mutant plants after FM4-64 staining. The angular positioning of cross-walls with respect to the root axis was measured on microscopic images of root cells labelled with FM4-64. The data obtained were divided into three categories according to the recorded angles: cross-walls at right angles ( $90^\circ \pm 5^\circ$ ), cross-walls at acute angles ( $<85^\circ$ ) and cross-walls with obtuse angles ( $>95^\circ$ ). Angles were measured in root epidermal and cortical cell files of C24 wild-type and *der1-3* mutant plants. Graphs depicting relative frequencies of angle distributions were produced in Microsoft Excel software. Quantitative analysis of actin filament angular distribution was done with CytoSpectre Version 1.2 software using the cell axis as a reference (Kartasalo et al., 2015). Analysis showed the degree of actin filament arrangement with respect to transverse (defined as perpendicular to the cell axis at an angle of  $0^\circ$  or  $180^\circ$ ), longitudinal (parallel to the cell axis at an angle of  $90^\circ$  or  $270^\circ$ ) or random (an angle between  $0^\circ$  and  $180^\circ$ ) orientations. All graphical plots were prepared in Microsoft Excel software and statistical analyses were done using STATISTICA 12 (StatSoft) software using analysis

of variance (ANOVA) and subsequent Fisher's LSD tests ( $P < 0.05$ ).

## RESULTS

### Phenotype, growth and biomass production of *der1-3* mutant plants

A single-point mutation in the *DER1* (*deformed root hairs1*) locus within the *ACTIN2* gene in *A. thaliana* produced by EMS-based mutagenesis leads to a mutant phenotype with impaired root hair development (Ringli et al., 2002). The process of root hair formation is affected after root hair initiation and root hair tip growth. Among three allelic mutations originally identified, *der1-3* shows the strongest phenotype (Ringli et al., 2002). Direct comparison revealed that root hairs of the *der1-3* mutant were much shorter than in the C24 wild-type (Fig. 1A, B). They showed arrested development mainly after bulge formation, confirming the root hair phenotype of this mutant described earlier (Ringli et al., 2002, 2005).

Further morphological analysis evaluated potential differences in the phenotype, growth and development of whole roots and entire plants between control C24 wild-type and *der1-3* mutant. Our phenotypic studies comprised seed germination tests, evaluation of the root growth rate of young seedlings and biomass quantification in more advanced plants under *in vitro* and *in vivo* conditions. Survival and progress of early plant growth and development are highly dependent on the efficiency and speed of seed germination. For this reason we analysed germination rates of seeds that were surface-sterilized at a dry stage, thoroughly washed, primed at 4 °C for 2 d and aseptically cultured on Phytigel-solidified medium in a vertical position under controlled conditions. Importantly, the germination rate of *der1-3* mutant seeds was considerably slower compared with wild-type (Fig. 1C). Although all seeds were treated similarly and the germination efficiency was eventually 100 %, seeds of the *der1-3* mutant germinated significantly later in comparison with control C24 wild-type seeds. Within the first 24 h after placing of seeds in the growing chamber,  $95 \pm 0.05$  % of the C24 wild-type seeds germinated, while only  $55 \pm 0.05$  % of *der1-3* mutant seeds started germination in same time period (Fig. 1D).

Size comparison of 18-d-old entire plants revealed visually smaller green aerial parts (Fig. 1E, F) and a less developed root system (Fig. 1F) of *der1* mutants. However, measurement of root growth rates within the first 5 d after germination showed no significant difference between C24 wild-type and *der1-3* mutant plants (Fig. 1G). Similar results were found in a comparison of average root growth per 24 h measured within the first 5 d after germination, with no significant difference between C24 wild-type and *der1-3* mutant plants (Fig. 1H). These data indicate that the visually shorter roots of *der1-3* mutant plants are attributable to delays in seed germination (Fig. 1C, D) rather than to a slower root growth rate (Fig. 1G, H).

Nevertheless, the pattern of root growth in the *der1-3* mutant displayed some alterations, leading to changes in phenotype of the whole root system. In comparison with C24 wild-type, where primary roots developed in a straight direction along a longitudinal vector (Fig. 2A, C), primary roots of *der1-3* mutant showed a more irregular and wavy growth pattern (Fig. 2B, D). A similar trend was observed in lateral roots of

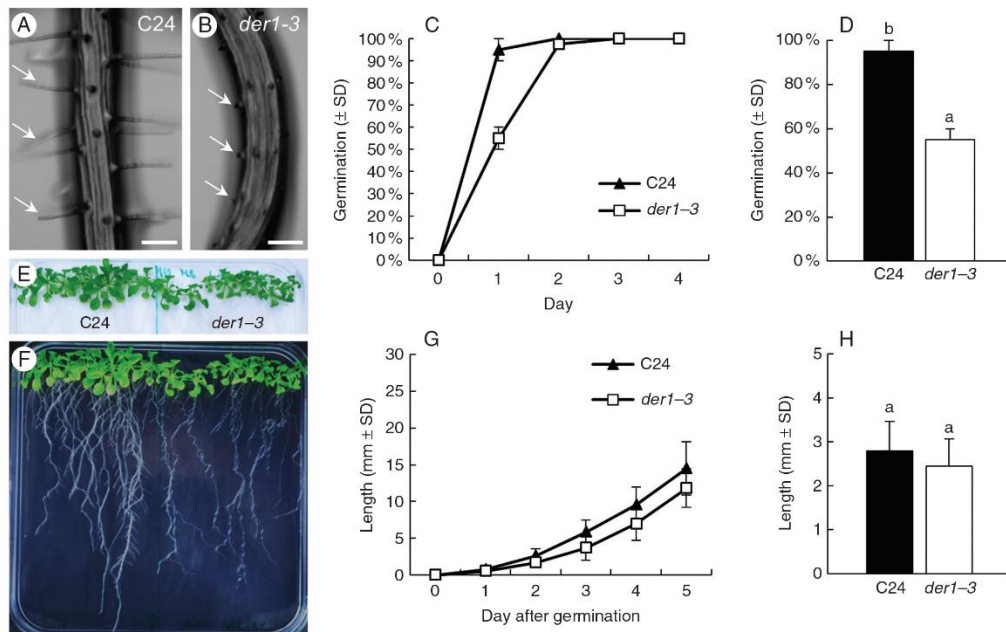


FIG. 1. Germination, root growth and phenotype overview of *der1-3* mutant. (A, B) Mature part of the root of 5-d-old seedlings showing normal long root hairs in C24 wild-type (A, arrows) and much shorter root hairs arrested at the bulge stage in *der1-3* mutant (B, arrows). (C, D) Germination of C24 and *der1-3* seeds. Efficiency of seed germination within first 4 d after placing seeds on Phytigel-solidified culture medium (C) and average germination rate within the first 24 h (D). Experiments were performed twice with 20 seeds per line. (E, F) Size and phenotype of green aerial parts (E) and entire 18-d-old plants (F) grown on Phytigel-solidified culture medium *in vitro*. (G, H). Time course of root growth of plants cultured on Phytigel-solidified culture medium *in vitro* within the first 5 d after germination (G) and average root growth per 24 h (H). Experiments were performed twice with eight plants per line. Different letters above bars represent statistical significance at  $P < 0.05$  (one-way ANOVA). Scale bars (A, B) = 100  $\mu$ m.

the *der1-3* mutant (Fig. 2B), which are normally straight in the C24 wild-type (Fig. 2A). To decipher the role of actin in root waving during growth, we analysed AF organization in the apex of primary roots during the root growth of C24 and *der1-3* seedlings stably expressing a *35S::GFP-FABD2* actin marker. In order to maintain intact living plants in near-environmental conditions and avoid any artefacts in the speed and directionality of root growth induced by prolonged irradiation during imaging, we utilized light-sheet microscopy. This method provides an optimal approach for long-term developmental microscopy imaging of intact plants with minimal fluorophore photobleaching and phototoxicity. The actin cytoskeleton was visualized in cells of the whole root apex of transgenic C24 (Fig. 2E) and *der1-3* mutant (Fig. 2F) plants. Detailed images of the root apex revealed boundaries between individual cells at their cross-walls in cell files. The planes of these cross-walls in non-dividing cells corresponded to CDP orientation during cell division. Cross-walls between individual cells were predominantly transverse in cell files of C24 control (Fig. 2E, G). In contrast, many cross-walls between individual cells were obliquely oriented in cell files of *der1-3* mutant root (Fig. 2F, H). In order to quantify cross-wall orientation differences between C24 and *der1-3* seedlings, roots were stained with FM4-64 and examined by spinning-disk fluorescence microscopy. Inspection of

C24 wild-type roots confirmed the preferential perpendicular orientation of the cross-walls of cell files with respect to the longitudinal root axis (Fig. 2I), and the frequent presence of oblique orientation of the cross-walls in cell files of *der1-3* mutant roots (Fig. 2J).

Quantitative evaluation of cross wall orientations between neighbouring cells in cell files was performed in FM4-64-labelled roots by measuring the angle between the cross and the longitudinal wall of the same cell. CDP orientations of measured cells were scored into three categories: close to right angle ( $90^\circ \pm 5^\circ$ ), with acute angles ( $<85^\circ$ ) and with obtuse angles ( $>95^\circ$ ). Data were collected from cells in cell files of root epidermis and cortex. To exclude the possible influence of GFP-FABD2 overexpression on CDP orientation, the same measurements were done in both transgenic and non-transformed C24 and *der1-3* seedlings. Such measurements confirmed the prevalence of transverse CDP orientation in the epidermis and the cortex of C24 wild-type roots (Fig. 3A, B). In contrast, a significantly lower number of perpendicular CDP orientations was present in the epidermis and cortex of *der1-3* mutant roots, while oblique CDP orientations increased (Fig. 3A, B). A proportionally lower number of perpendicular CDP orientations was found in epidermal and cortical cell files of transgenic C24 and *der1-3* mutant lines harbouring

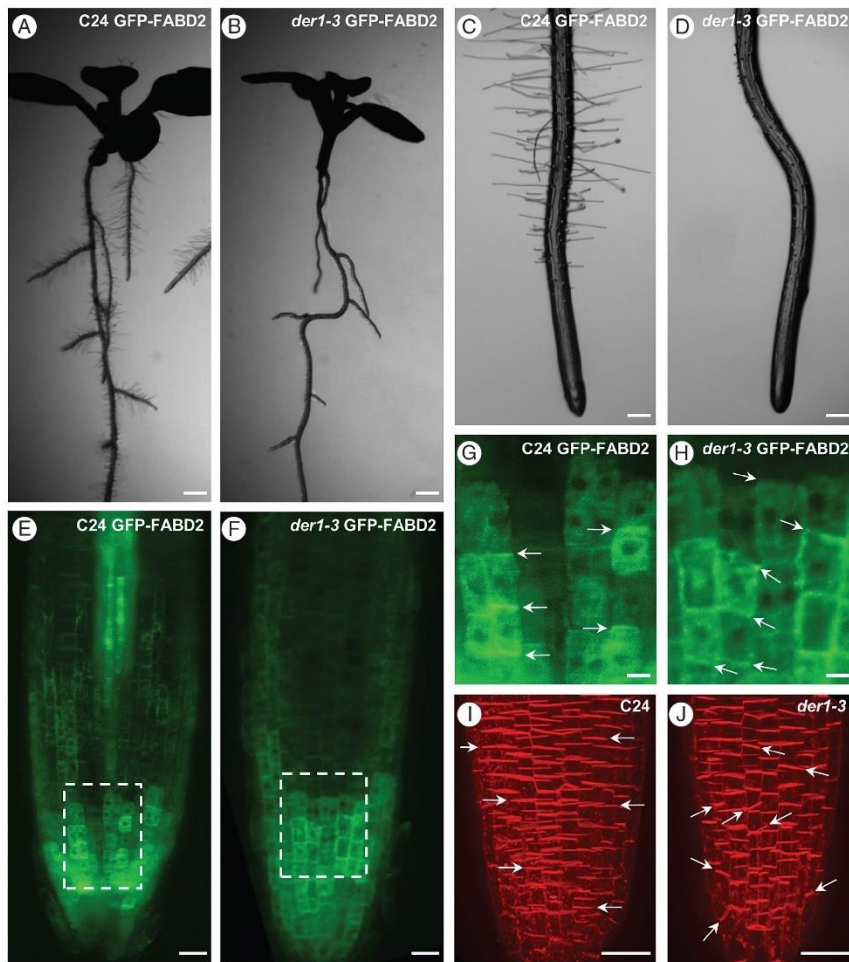


FIG. 2. Root phenotype and pattern of root growth in *der1-3* mutant. (A, B) Root morphology of 8-d-old seedlings of C24 wild-type (A) and *der1-3* mutant (B) grown on Phytigel-solidified culture medium *in vitro*. (C, D) Root tip morphology of 5-d-old seedlings documenting straight shape of the root in C24 wild-type (C) and wavy shape of the root in *der1-3* mutant (D). (E–H) Light-sheet fluorescence microscopy imaging of transgenic *Arabidopsis* lines harbouring the actin filament fluorescent marker GFP-FABD2. (E, F) Overview of GFP-FABD2 expression in root apex cells of C24 wild-type (E) and *der1-3* mutant (F). (G, H) Detailed images of cell files in the root apex of C24 (G, magnified inset from E) and *der1-3* mutant (H, magnified inset from F) harbouring the GFP-FABD2 marker. Cell boundaries within the cell files at cross-walls defining orientation of cell division planes during cell division are marked by arrows. (I, J) Vital labelling of root apices using the fluorescent membrane marker FM4-64. There is prominent FM4-64 labelling of plasma membranes at the cross-walls of C24 wild-type (I) and *der1-3* mutant (J) root cells. Arrows indicate orientation of cell division planes during cell division. Scale bars (A, B) = 400  $\mu\text{m}$ ; (C, D) = 200  $\mu\text{m}$ ; (E, F, I, J) = 20  $\mu\text{m}$ ; (G, H) = 5  $\mu\text{m}$ .

GFP-FABD2 compared with control non-transgenic C24 wild-type and *der1-3* mutant lines (Fig. 3C, D). Nevertheless, a significantly lower number of perpendicular CDP orientations was present in *der1-3* GFP-FABD2 mutant roots, while the number of oblique CDP orientations was increased in both cell layers (Fig. 3C, D). These results clearly indicate that the wavy pattern of root growth in the *der1-3* mutant is somehow

related to alterations in CDP orientations during cell division in the root meristem.

To reveal whether the development of green aerial parts (Fig. 1E, F) could also be significantly affected by delay in seed germination in the *der1-3* mutant, we compared quantitative parameters of shoots and leaves. Shoot and root fresh weights of 19-d-old plants cultured *in vitro* were significantly higher in the



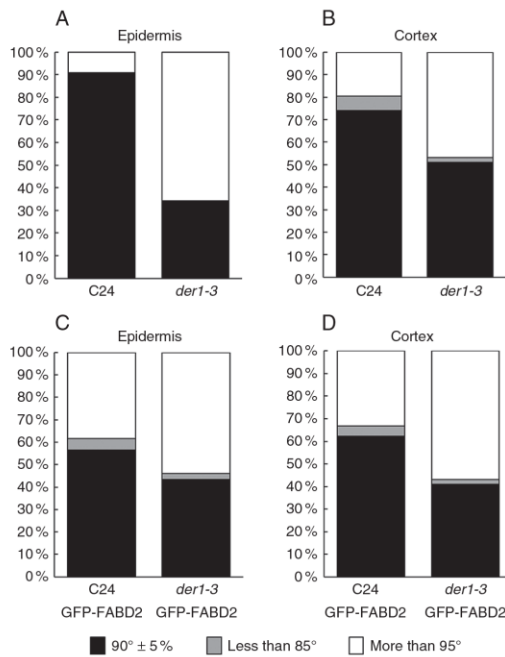


Fig. 3. Quantitative evaluation of cross-wall orientation between neighbouring cells in root cell files, indicating orientation of cell division planes. Data were collected from roots labelled with FM4-64. Angles between the cross cell wall and the longitudinal cell wall of measured cells were scored into three categories: right angle ( $90^\circ \pm 5\%$ ); acute angle ( $<85^\circ$ ); and obtuse angle ( $>95^\circ$ ). (A, B) Relative frequencies of angle distributions in epidermal and cortical cell files of C24 wild-type and *der1-3* mutant plants. (C, D) Relative frequencies of angle distributions in epidermal and cortical cell files of transgenic C24 and *der1-3* plants harbouring the actin filament fluorescent marker GFP-FABD2. Experiments were performed three times with 10–17 cells from three plants per line.

control C24 wild-type plants than in the *der1-3* mutant (Fig. 4A). Nevertheless, average fresh weight of all true leaves (Fig. 4B), average leaf area (Fig. 4C), size of leaf rosettes (Fig. 4E, F) and size of individual leaves (Fig. 4G, H) in plants cultured *in vivo* suggested that the reduced development of the *der1-3* mutant might not be related to delay in germination. This suggestion was supported by the higher average number of leaves in 19-d-old *der1-3* mutant plants (Fig. 4D), which may functionally compensate for the suppressed development of green aerial part in *der1-3* mutants.

#### Organization of the actin cytoskeleton

We performed detailed qualitative and quantitative analyses of the actin cytoskeleton in the *der1-3* mutant in order to see how the *ACT2* mutation could be involved in the phenotypical and developmental changes of this mutant. The AFs were visualized in hypocotyls and cotyledons of fixed and fluorescent

phalloidin-labelled 3-d-old seedlings. This was followed by live-cell imaging in hypocotyl and root epidermal cells of transgenic lines expressing the GFP-FABD2 marker for AFs. These microscopic observations were supported by quantitative analysis of AF angular distribution in transverse (defined as perpendicular to the cell axis at an angle of  $0^\circ$  or  $180^\circ$ ), longitudinal (parallel to the cell axis at an angle of  $90^\circ$  or  $270^\circ$ ) or random (angles between  $0^\circ$  and  $180^\circ$ ) orientations (Kartasalo *et al.*, 2015).

Actin visualization using Alexa Fluor 488–phalloidin labelling in hypocotyl epidermal cells revealed the presence of long AFs and actin bundles, arranged mostly in longitudinal or slightly oblique orientations in C24 plants (Fig. 5A). Quantification of angular distribution confirmed a rather uniform longitudinal orientation of AFs in these cells (Fig. 5B). In cotyledon epidermal cells of C24 plants AFs were arranged in long, interconnected and curled cables (Fig. 5C), longitudinally and randomly spanning whole cells (Fig. 5D). In contrast, hypocotyl epidermal cells of the *der1-3* mutant contained thinner and shorter AFs and actin bundles (Fig. 5E), which were less pronounced and reorganized in comparison with the C24 control plants (Fig. 5A). In addition, the angular distribution of AFs in the mutant revealed more random AF orientation compared with the C24 control plants (Fig. 5F). Cotyledon epidermal cells of the *der1-3* mutant contained predominantly fragmented AFs and short actin bundles (Fig. 5G), arranged loosely along the longitudinal axes of these cells (Fig. 5H).

Live-cell imaging of the actin cytoskeleton in epidermal hypocotyl cells of transgenic C24 lines carrying the GFP-FABD2 molecular marker revealed actin bundles spanning these cells longitudinally as well as longitudinally, and obliquely oriented fine AFs forming a dense meshwork (Fig. 5I). Thus, quantification of angular distribution revealed a high degree of longitudinal orientation of AFs (Fig. 5J). Organization of the actin cytoskeleton in post-mitotic elongating cells of root epidermis showed typical AFs and actin bundles interconnected into a dense network. Long actin cables formed typical bending structures in the vicinity of cross-walls (Fig. 5K). The angularity of such an arrangement was thus characterized by regular distribution of AFs with prevalent longitudinal orientation (Fig. 5L). The actin cytoskeleton in hypocotyl epidermal cells of the *der1-3* mutant carrying the GFP-FABD2 molecular marker consisted of very short AFs arranged in a random and loose network. In addition, thick and rather short actin cables were oriented preferentially in oblique orientation with respect to the longitudinal axis of the hypocotyl epidermal cells (Fig. 5M). Quantification of AF angularity confirmed random and oblique orientation of AFs (Fig. 5N). The actin cytoskeleton in post-mitotic elongating root epidermal cells of the *der1-3* mutant carrying the GFP-FABD2 molecular marker showed dense arrangements of very short filaments and spot-like structures. The network of AFs was disorganized and actin cables were short and sometimes fragmented (Fig. 5O). Quantitative evaluation of angularity clearly revealed the random orientation of the actin cytoskeleton (Fig. 5P). These data conclusively confirmed marked alterations in the organization of the actin cytoskeleton in cells of different tissues and organs of *der1-3* mutant plants caused by mutation of *ACT2*.

Altogether, the results described above indicate that the wavy pattern of root growth in the *der1-3* mutant is most probably

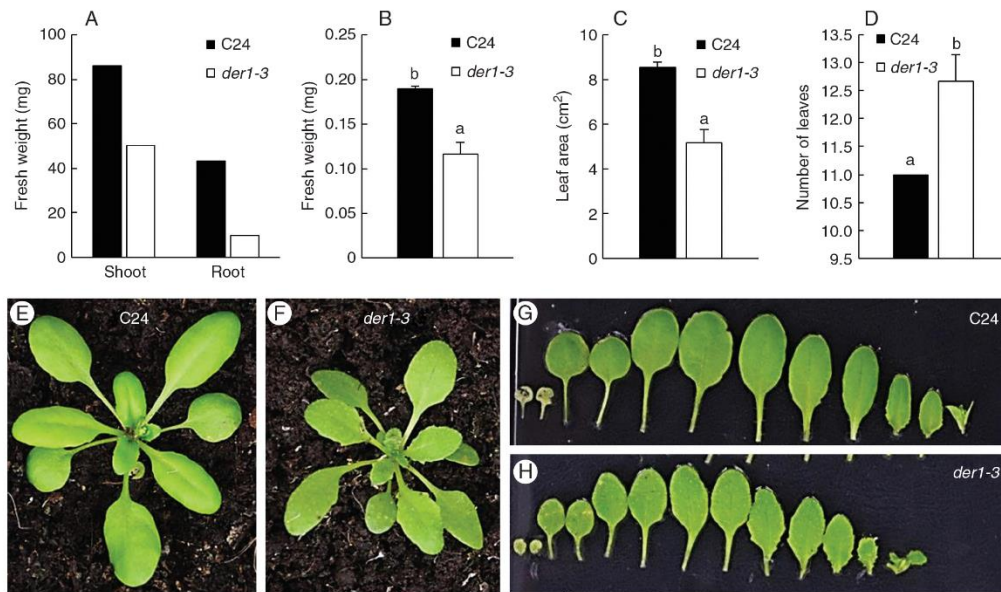


FIG. 4. Development and phenotype of shoots in *der1-3* mutant. (A) Average fresh weight of shoots and roots of 19-d-old C24 wild-type and *der1-3* mutant plants grown on Phytigel-solidified culture medium *in vitro*. Shoots and roots were collected separately from ten plants and weighed together. The experiment was performed three times. (B–D) Quantitative parameters of shoots of 19-d-old C24 wild-type and *der1-3* mutant plants grown in pots (*in vivo*): fresh weight of green aerial plant parts (B), total area of true leaves per plant (C) and number of true leaves per plant (D). Data were collected from three plants. (E–H) Comparison of leaf rosettes and individual true leaves in 19-d-old plants grown in pots (*in vivo*). Size of the leaf rosette in C24 wild-type plants (E) and *der1-3* mutant plants (F). Number and size of individual true leaves in C24 wild-type plants (G) and *der1-3* mutant plants (H). Different letters above bars represent statistical significance at  $P < 0.05$  (one-way ANOVA).

caused by deregulation of CDP orientation (Figs 2 and 3) depending on altered organization of the actin cytoskeleton (Fig. 5). To provide a more complex overview of the cytoskeleton-regulating phenotype of the *der1-3* mutant, we also characterized the organization of microtubules. Cortical and mitotic microtubules in root cells of C24 wild-type and the *der1-3* mutant were visualized *in situ* by immunofluorescence localization using an anti-tubulin antibody. In addition, transgenic C24 and *der1-3* mutant plants carrying the microtubule fluorescent marker GFP-MBD were used for live-cell imaging of microtubules in root cells. The CDP is clearly defined by the positioning of the PPB during preprophase and prophase and by the orientation of the phragmoplast during telophase and subsequent cytokinesis. Most cell divisions in the root meristem are proliferative and contribute to the increasing number of successive cells in single cell files, where the CDP is oriented transversely to the main root axis. Thus, we observed regular transverse orientation of the CDP in dividing root cells of the C24 wild-type (Fig. 6A). On the other hand, we observed frequent deviation of the CDP from its expected transverse orientation in root meristematic cells of the *der1-3* mutant (Fig. 6B). Importantly, the organization of cortical (Fig. 6C) and mitotic (Fig. 6D) microtubules in root epidermal cells of control C24 did not differ significantly from that in root epidermal cells of the *der1-3* mutant, as revealed by live-cell imaging (Fig.

6E–G). Determination of the CDP was apparent in dividing cells of control C24, showing coordinated orientation of the PPB, the equatorial plane of the mitotic spindle and the phragmoplast. All of these were transversely oriented to the axis of root cell files (Fig. 6D). On the other hand, the CDP orientation of the dividing cells was not so strictly determined in the *der1-3* mutant as it was frequently observed in oblique orientation with respect to the axis of root cell files (Fig. 6F, G). Because quantitative analysis of cortical microtubule angular distribution in root epidermal cells of control C24 (Fig. 6H) and *der1-3* mutant (Fig. 6I) did not reveal significant differences and no significant differences were found in skewness, the degree of cortical microtubule bundling in root epidermal cells between control C24 and *der1-3* mutant (Fig. 6J), we can conclude that the point mutation of *ACT2* in the *der1-3* mutant does not have a considerable influence on the organization of the microtubule cytoskeleton in root cells.

#### DISCUSSION

A single-point mutation in the locus *DER1* (*deformed root hairs1*) leads to the generation of mutant plants impaired in root hair development. The root hair initiation site is not typically positioned on the outer tangential cell wall of the trichoblast

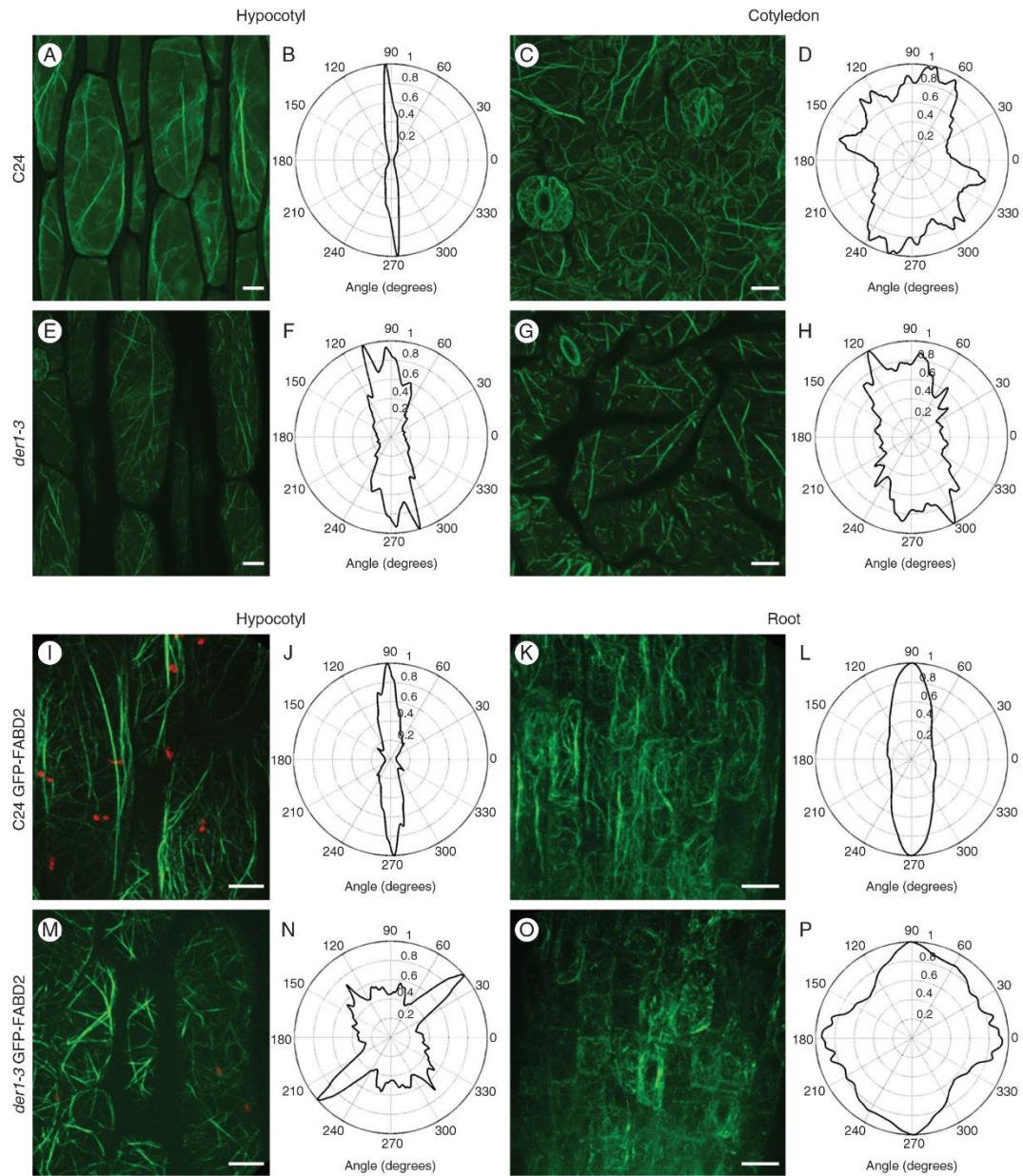


FIG. 5. Organization of the actin cytoskeleton in C24 wild-type and *der1-3* mutant plants. (A–H) Microscopic observations (A, C, E, G) and quantitative analysis (B, D, F, H) of actin filament angular distribution in hypocotyl epidermal cells (A, B, E, F) and cotyledon epidermal cells (C, D, G, H) of 3-d-old C24 wild-type and *der1-3* mutant plants after Alexa Fluor 488–phalloidin labelling of actin filaments. (I–P) Microscopic observations (I, K, M, O) and quantitative analysis of actin filament angular distribution (J, L, N, P) in hypocotyl epidermal cells (I, J, M, N) and in root epidermal cells (K, L, O, P) of 3-d-old C24 wild-type and *der1-3* mutant transgenic plants harbouring the actin filament fluorescent marker GFP-FABD2. Quantitative analysis of actin filament angular distribution was performed for three independent microscopic images of examined cell types from three to five plants. Scale bars = 10 μm.

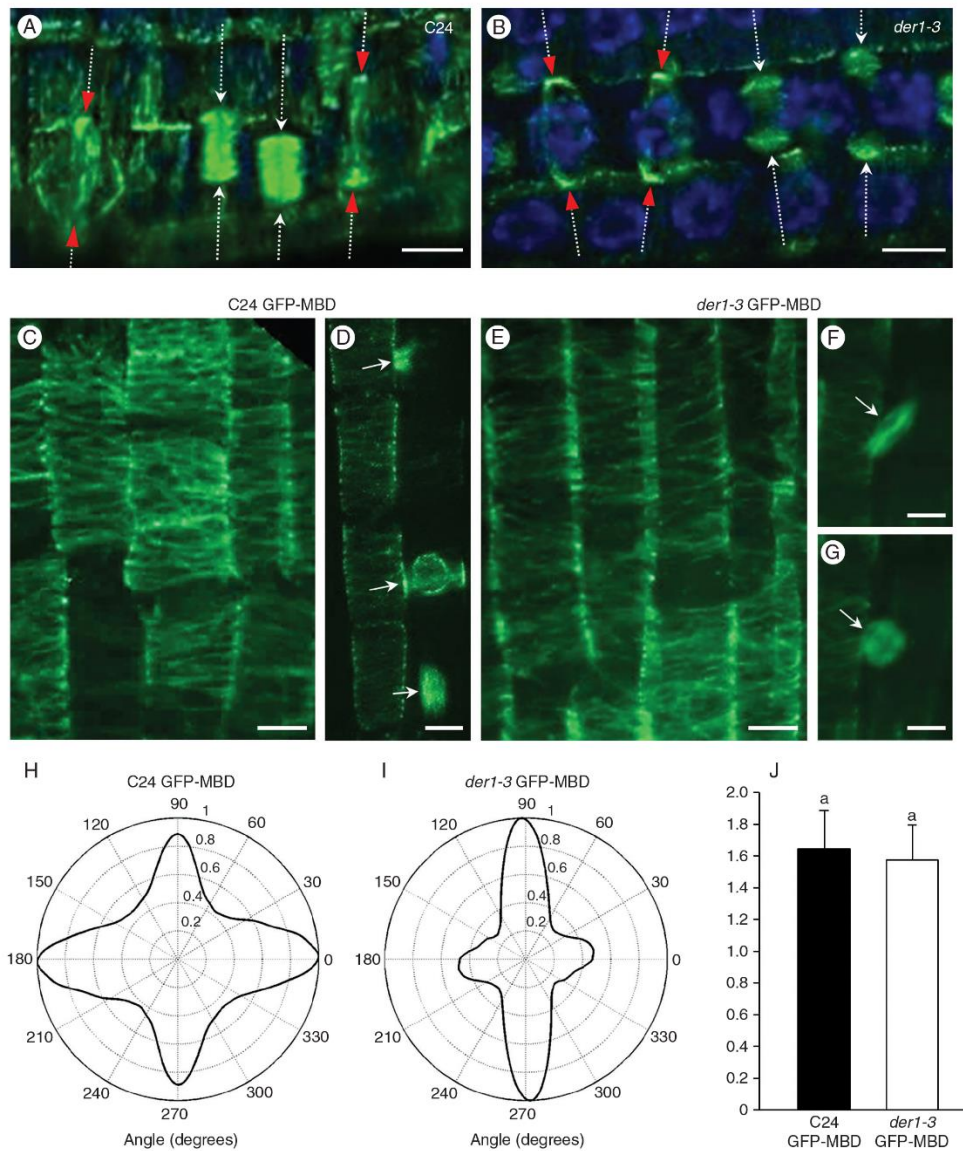


FIG. 6. Microtubule organization in root cells of C24 wild-type and *der1-3* mutant plants. (A, B) Microscopic documentation of cortical and mitotic microtubules in root cells of C24 wild-type and *der1-3* mutant after immunofluorescence localization with anti-tubulin antibody. Positions of PPBs in prophase cells are indicated by red arrowheads while positions of phragmoplasts in telophase and during the cytokinesis are indicated by white arrows. All arrows indicate orientations of CDPs. DNA in nuclei is counterstained with DAPI. (C–G) Microscopic documentation of cortical and mitotic microtubules in root cells of living transgenic C24 wild-type and *der1-3* mutant plants harbouring the microtubule fluorescent marker GFP-MBD. Cortical microtubules in root epidermal cells of C24 wild-type (C) and *der1-3* mutant (E) and mitotic microtubules in dividing root epidermal cells of C24 wild-type (D) and *der1-3* mutant (F, G). The same dividing cell in the anaphase stage with a mitotic spindle (F) and in the subsequent telophase with an early phragmoplast (G) is shown in a *der1-3* mutant. Arrows indicate orientation of the PPB in prophase (D), the equatorial plane of the mitotic spindle (D, F) and the midzone of the phragmoplast (D, G). (H, I) Quantitative analysis of cortical microtubule angular distribution in root epidermal cells of C24 wild-type (H, analysed microtubules from C) and in root epidermal cells of *der1-3* mutant (I, analysed microtubules from E). (J) Skewness of cortical microtubules in root epidermal cells of living transgenic C24 wild-type and *der1-3* mutant plants harbouring the microtubule fluorescent marker GFP-MBD. Data are from four or five cells of five or six plants. Scale bars = 5  $\mu$ m.

and after bulge formation the growth of the root hair tip is abolished. As a result, root hairs of *der1* mutant plants are very short (Ringli et al., 2002). The mutated locus is localized in the sequence of the *ACTIN2* gene, encoding a major vegetative actin in *A. thaliana*. Until now, only the root hair phenotype has been described in *der1* mutants showing no obvious aberrations in plant development (Ringli et al., 2002). The root hair phenotype of the *der1-3* mutant was also confirmed in our study. However, our thorough plant phenotyping and cellular analysis of the cytoskeleton in different cell types revealed that this single-point mutation in the *ACTIN2* gene had a more general influence on plant growth and development.

The first apparent developmental difference was delay in germination of the *der1-3* seeds. During the first 24 h after imbibition only around 50 % of *der1-3* seeds were germinated in comparison with almost 100 % germinating C24 wild-type seeds. Due to this delay in germination, seedlings of *der1-3* mutant were visually smaller, but parameters of average root growth of the *der1-3* mutant were similar to those of control C24 wild-type roots. Similar results were reported for the homozygous *act7-1* mutant, which is defective in the expression of another vegetative actin gene, *ACT7*. Seed germination of the *act7-1* mutant was also about 24 h delayed in comparison with the control wild-type seeds, although without any other changes in growth and further development of germinated seedlings (Gilliland et al., 2003). Slower germination of seeds can significantly influence further seedling development, but it remains to be determined how genetically disturbed organization and dynamics of the actin cytoskeleton are involved in the delay in the seed germination process.

In order to characterize the organization of the actin cytoskeleton, we prepared transgenic C24 and *der1-3* mutant lines carrying GFP-FABD2, a molecular marker for the actin cytoskeleton. Expression of GFP-FABD2 in transgenic plants does not cause detectable adverse effects on plant morphology or development and thus it is generally accepted as a vital marker for the visualization and characterization of the actin cytoskeleton in plants (Voigt et al., 2005; Wang et al., 2008). In general, the actin cytoskeleton in plant cells consists of individual AFs and actin bundles. The network of individual AFs is randomly dispersed in the cortical cytoplasm and, although they are dynamic, they have a shorter lifetime, while actin bundles are mostly oriented longitudinally along the cell's longer axis; they are less dynamic but have a longer lifetime (Henty-Ridilla et al., 2013). The organization of AFs in cells of the *der1-3* mutant displayed some considerable alterations in comparison with control cells. Individual AFs were shorter in the *der1-3* mutant. More importantly, however, actin bundles were also shorter and thicker than in the control and did not span the entire length of the epidermal cells in cotyledons, hypocotyls and roots. Analysis of actin cytoskeleton organization in living plants harbouring the fluorescent marker GFP-FABD2 was validated by an alternative method of actin labelling in fixed cells using Alexa-phalloidin staining. Both independent methods confirmed the altered configuration of the actin cytoskeleton in different cell types of the *der1-3* mutant. Quantitative determination of actin cytoskeleton orientation demonstrated considerable differences between the *der1-3* mutant and the control C24. Cells of C24 plants contained especially longitudinally oriented actin bundles, while these were mostly obliquely and

sometimes transversely oriented in cells of the *der1-3* mutant. Analogous orientations of AFs have been reported in the *act2-1* mutant. Root hairs of the *act2-1* mutant often contained transversely oriented AFs, in contrast to the longitudinally oriented AFs in wild-type plants (Kandasamy et al., 2009). Moreover, similar results have also been published for *act2-2D* and *act2-5* mutants. For example, the *act2-2D* mutant (single-point mutation) had shorter actin bundles in root epidermal cells and showed defects in actin polymerization (Nishimura et al., 2003). The T-DNA insertional mutant *act2-5* showed a modified actin cytoskeleton pattern, where AFs were shorter and unbundled (Lanza et al., 2012). Our data are consistent with these studies and suggest that changes in the organization of the actin cytoskeleton are typical of various mutations in the *ACT2* gene, including *der1-3*. This clearly indicates an important function of ACT2 in the establishment and maintenance of the correct organization of the actin cytoskeleton during plant growth and development.

In general, involvement of ACT2 has been considered mainly in the two major cellular functions, namely root hair formation and cell elongation (e.g. Ringli et al., 2002; Nishimura et al., 2003). Our analysis revealed that, although root growth rate does not differ from the C24 wild-type, roots of the *der1-3* mutant show a wavy growth pattern. Therefore, we documented root growth using different microscopic methods in order to reveal the main reason for root waving. Based on live-cell imaging of transgenic *der1-3* plants harbouring the actin cytoskeleton marker GFP-FABD2, vital labelling of cell membranes using FM4-64 and immunofluorescence whole-mount labelling of microtubules, we confirmed alterations in the cell division pattern in the root meristem. The root meristematic zone of the *der1-3* mutant regularly contained a significantly higher number of shifted cell division planes in comparison with the control C24 plant. The significantly higher number of oblique CDPs deviating from transverse orientation (with respect to the longitudinal root axis) at  $<90^\circ$  (therefore not assuming longitudinal orientation) could generate random and asymmetrical forces within the root that lead to a wavy root growth pattern.

However, immunolocalization and live-cell imaging of microtubules revealed that the organization of both cortical and mitotic microtubules in root cells of the *der1-3* mutant does not show any considerable alterations from the normal microtubule organization in root cells of control C24 plants. What was clearly evident, however, was a higher number of shifted CDPs and accordingly tilted mitotic microtubule systems (PPBs, spindles and phragmoplasts) in dividing root meristematic cells of the *der1-3* mutant compared with control C24 plants. The data presented here thus suggest that the actin cytoskeleton plays an important role in the proper determination of the CDP. Microtubules have been reported to associate with AFs during the formation of the PPB already in the prophase stage of cell division (Takeuchi et al., 2016). In subsequent stages of cell division, cortical AFs are less abundant in the future cortical division site, forming the so called actin-depleted zone (Hoshino et al., 2003), but are further involved in the progression of cytokinesis within the expanding phragmoplast. Therefore, the actin cytoskeleton plays relevant roles in cell division and in CDP determination in both asymmetrically and symmetrically dividing cells (Van Damme et al., 2007; Rasmussen et al., 2013; Kojo et al., 2013, 2014). Involvement of the actin cytoskeleton

in the determination of CDP orientation has also been tested by application of actin-depolymerizing drugs during preprophase and prophase, leading to misorientation of the CDP in dividing tobacco BY-2 cells (Sano et al., 2005). Finally, defects in CDP orientation were also encountered in plants with reduced expression of *ACT7*, a gene encoding an actin isoform highly expressed during mitosis (Gilliland et al., 2003).

In conclusion, the wavy pattern of root growth, changes in the phenotype of mutant plants and the altered organization of the actin cytoskeleton in different cell types of *der1-3* mutant plants indicate that mutation in the *DER1* gene locus of *ACTIN2* has a more general influence on plant morphology, growth and development than only interference with root hair formation. The changes in mutant plants described here are mediated through alterations of the actin cytoskeleton. Better understanding of the molecular mechanisms of how the actin cytoskeleton contributes to the proper orientation of cell division and what is the role of *ACTIN2* isoforms in this process will require more detailed analysis in future studies.

#### ACKNOWLEDGEMENTS

We cordially acknowledge George Komis for critical reading of the manuscript and anonymous referees for their valuable comments. This work was funded by grant No. LO1204 (Sustainable development of research in the Centre of the Region Haná) from the National Program of Sustainability I, the Ministry of Education, Youth and Sports, Czech Republic and by student project IGA\_PrF\_2017\_026 from PU Olomouc. The authors declare no conflict of interests.

#### LITERATURE CITED

- An Y-Q, McDowell JM, Huang S, McKinney EC, Chambliss S, Meagher RB. 1996. Strong, constitutive expression of the *Arabidopsis* *ACT2/ACT8* actin subclass in vegetative tissues. *Plant Journal* **10**: 107–121.
- Baluška F, Salaj J, Mathur J, et al. 2000a. Root hair formation: F-actin-dependent tip growth is initiated by local assembly of profilin-supported F-actin meshworks accumulated within expansin-enriched bulges. *Developmental Biology* **227**: 618–632.
- Baluška F, Volkmann D, Barlow PW. 2000b. Actin-based domains of the 'cell periphery complex' and their associations with polarized 'cell bodies' in higher plants. *Plant Biology* **2**: 253–267.
- Barlow PW, Baluška F. 2000. Cytoskeletal perspectives on root growth and morphogenesis. *Annual Review of Plant Physiology and Plant Molecular Biology* **51**: 289–322.
- Beck M, Komis G, Müller J, Menzel D, Šamaj J. 2010. *Arabidopsis* homologs of nucleus- and phragmoplast-localized kinase 2 and 3 and mitogen-activated protein kinase 4 are essential for microtubule organization. *Plant Cell* **22**: 755–771.
- Braun M, Baluška F, von Witsch M, Menzel D. 1999. Redistribution of actin, profilin and phosphatidylinositol-4,5-bisphosphate (PIP<sub>2</sub>) in growing and maturing root hairs. *Planta* **209**: 435–443.
- Clough SJ, Bent AF. 1998. Floral dip: a simplified method for *Agrobacterium*-mediated transformation of *Arabidopsis thaliana*. *Plant Journal* **16**: 735–743.
- Van Damme D, Vanstraelen M, Geelen D. 2007. Cortical division zone establishment in plant cells. *Trends in Plant Science* **12**: 458–464.
- Fowler JE, Quatrano RS. 1997. Plant cell morphogenesis: plasma membrane interactions with the cytoskeleton and cell wall. *Annual Review of Cell and Developmental Biology* **13**: 697–743.
- Gilliland LU, McKinney EC, Asmussen MA, Meagher RB. 1998. Detection of deleterious genotypes in multigenerational studies. I. Disruptions in individual *Arabidopsis* actin genes. *Genetics* **149**: 717–725.
- Gilliland LU, Kandasamy MK, Pawloski LC, Meagher RB. 2002. Both vegetative and reproductive actin isoforms complement the stunted root hair phenotype of the *Arabidopsis* *act2-1* mutation. *Plant Physiology* **130**: 2199–2209.
- Gilliland LU, Pawloski LC, Kandasamy MK, Meagher RB. 2003. *Arabidopsis* actin gene *ACT7* plays an essential role in germination and root growth. *Plant Journal* **33**: 319–328.
- Henty-Ridilla JL, Li J, Blanchoin L, Staiger CJ. 2013. Actin dynamics in the cortical array of plant cells. *Current Opinion in Plant Biology* **16**: 678–687.
- Hoshino H, Yoneda A, Kumagai F, Hasezawa S. 2003. Roles of actin-depleted zone and preprophase band in determining the division site of higher-plant cells, a tobacco BY-2 cell line expressing GFP-tubulin. *Protoplasma* **222**: 157–165.
- Kandasamy MK, McKinney EC, Meagher RB. 2002. Functional nonequivalency of actin isoforms in *Arabidopsis*. *Molecular Biology of the Cell* **13**: 251–261.
- Kandasamy MK, Burgos-Rivera B, McKinney EC, Ruzicka DR, Meagher RB. 2007. Class-specific interaction of profilin and ADF isoforms with actin in the regulation of plant development. *Plant Cell* **19**: 3111–3126.
- Kandasamy MK, McKinney EC, Meagher RB. 2009. A single vegetative actin isoform overexpressed under the control of multiple regulatory sequences is sufficient for normal *Arabidopsis* development. *Plant Cell* **21**: 701–718.
- Kartasalo K, Pölonen R-P, Ojala M, et al. 2015. CytoSpectre: a tool for spectral analysis of oriented structures on cellular and subcellular levels. *BMC Bioinformatics* **16**: 344. doi: 10.1186/s12859-015-0782-y.
- Katsuta J, Hashiguchi Y, Shibaoka H. 1990. The role of the cytoskeleton in positioning of the nucleus in premitotic tobacco BY-2 cells. *Journal of Cell Science* **95**: 413–422.
- de Keijzer J, Mulder BM, Janson ME. 2014. Microtubule networks for plant cell division. *Systems and Synthetic Biology* **8**: 187–194.
- Kojo KH, Higaki T, Kutsuna N, Yoshida Y, Yasuhara H, Hasezawa S. 2013. Roles of cortical actin microfilament patterning in division plane orientation in plants. *Plant & Cell Physiology* **54**: 1491–1503.
- Kojo KH, Yasuhara H, Hasezawa S. 2014. Time-sequential observation of spindle and phragmoplast orientation in BY-2 cells with altered cortical actin microfilament patterning. *Plant Signaling & Behavior* **9**: e29579.
- Komis G, Luptovčiak I, Ovečka M, Samakovli D, Šamajová O, Šamaj J. 2017. Katanin effects on dynamics of cortical microtubules and mitotic arrays in *Arabidopsis thaliana* revealed by advanced live-cell imaging. *Frontiers in Plant Science* **8**: 866. doi: 10.3389/fpls.2017.00866.
- Lanza M, Garcia-Ponce B, Castrillo G, et al. 2012. Role of actin cytoskeleton in brassinosteroid signaling and in its integration with the auxin response in plants. *Developmental Cell* **22**: 1275–1285.
- Lloyd CW, Traas JA. 1988. The role of F-actin in determining the division plane of carrot suspension cells. *Development* **102**: 211–221.
- Marc J, Granger CL, Brincat J, et al. 1998. A GFP-MAP4 reporter gene for visualizing cortical microtubule rearrangements in living epidermal cells. *Plant Cell* **10**: 1927–1939.
- McDowell JM, An Y-Q, Huang S, McKinney EC, Meagher RB. 1996. The *Arabidopsis* *ACT7* actin gene is expressed in rapidly developing tissues and responds to several external stimuli. *Plant Physiology* **111**: 699–711.
- Meagher RB, Fehcheimer M. 2003. The *Arabidopsis* cytoskeletal genome. *Arabidopsis Book*. e0096. doi: 10.1199/tab.0096.
- Meagher RB, McKinney EC, Vitale AV. 1999. The evolution of new structures: clues from plant cytoskeletal genes. *Trends in Genetics* **15**: 278–284.
- Mineyuki Y, Murata T, Wada M. 1991. Experimental obliteration of the preprophase band alters the sites of cell division, cell plate orientation and phragmoplast expansion in *Adiantum protonemata*. *Journal of Cell Science* **100**: 551–557.
- Müller S. 2012. Universal rules for division plane selection in plants. *Protoplasma* **249**: 239–253.
- Nishimura T, Yokota E, Wada T, Shimmen T, Okada K. 2003. An *Arabidopsis* *ACT2* dominant-negative mutation, which disturbs F-actin polymerization, reveals its distinctive function in root development. *Plant & Cell Physiology* **44**: 1131–1140.
- Ovečka M, Vaškebová L, Komis G, Luptovčiak I, Smertenko A, Šamaj J. 2015. Preparation of plants for developmental and cellular imaging by light-sheet microscopy. *Nature Protocols* **10**: 1234–1247.
- Palevitz BA. 1987. Actin in the preprophase band of *Allium cepa*. *Journal of Cell Biology* **104**: 1515–1519.
- Panteris E, Apostolakos P, Galatis B. 2006. Cytoskeletal asymmetry in *Zea mays* subsidiary cell mother cells: a monopolar prophase microtubule

- half-spindle anchors the nucleus to its polar position. *Cell Motility and the Cytoskeleton* **63**: 696–709.
- Pei W, Du F, Zhang Y, He T, Ren H. 2012.** Control of the actin cytoskeleton in root hair development. *Plant Science* **187**: 10–18.
- Rasmussen CG, Wright AJ, Müller S. 2013.** The role of the cytoskeleton and associated proteins in determination of the plant cell division plane. *Plant Journal* **75**: 258–269.
- Ringli C, Baumberger N, Diet A, Frey B, Keller B. 2002.** ACTIN2 is essential for bulge site selection and tip growth during root hair development of *Arabidopsis*. *Plant Physiology* **129**: 1464–1472.
- Ringli C, Baumberger N, Keller B. 2005.** The *Arabidopsis* root hair mutants *der2–der9* are affected at different stages of root hair development. *Plant & Cell Physiology* **46**: 1046–1053.
- Šamaj J, Baluška F, Voigt B, Schlicht M, Volkmann D, Menzel D. 2004.** Endocytosis, actin cytoskeleton and signalling. *Plant Physiology* **135**: 1150–1161.
- Šamajová O, Komis G, Šamaj J. 2014.** Immunofluorescent localization of MAPKs and colocalization with microtubules in *Arabidopsis* seedling whole-mount probes. *Methods in Molecular Biology* **1171**: 107–115.
- Sampathkumar A, Lindeboom JJ, Debolt S, et al. 2011.** Live-cell imaging reveals structural associations between the actin and microtubule cytoskeleton in *Arabidopsis*. *Plant Cell* **23**: 2302–2313.
- Sano T, Higaki T, Oda Y, Hayashi T, Hasezawa S. 2005.** Appearance of actin microfilament 'twin peaks' in mitosis and their function in cell plate formation, as visualized in tobacco BY-2 cells expressing GFP-fimbrin. *Plant Journal* **44**: 595–605.
- Smolarkiewicz M, Dhonukshe P. 2013.** Formative cell divisions: principal determinants of plant morphogenesis. *Plant Cell Physiology* **54**: 333–342.
- Takeuchi M, Karahara I, Kajimura N, et al. 2016.** Single microfilaments mediate the early steps of microtubule bundling during preprophase band formation in onion cotyledon epidermal cells. *Molecular Biology of the Cell* **27**: 1809–1820.
- Voigt B, Timmers ACJ, Šamaj J, Müller J, Baluška F, Menzel D. 2005.** GFP-FABD2 fusion construct allows *in vivo* visualization of the dynamic actin cytoskeleton in all cells of *Arabidopsis* seedlings. *European Journal of Cell Biology* **84**: 595–608.
- Volkmann D, Baluška F. 1999.** The actin cytoskeleton in plants: from transport networks to signaling networks. *Microscopy Research and Technique* **47**: 135–154.
- Wang Y-S, Yoo C-M, Blancaflor EB. 2008.** Improved imaging of actin filaments in transgenic *Arabidopsis* plants expressing a green fluorescent protein fusion to the C- and N-termini of the fimbrin actin-binding domain 2. *New Phytologist* **177**: 525–536.
- Zhang Y, Iakovidis M, Costa S. 2016.** Control of patterns of symmetric cell division in the epidermal and cortical tissues of the *Arabidopsis* root. *Development* **143**: 978–982.

#### 4.2 Single amino acid exchange in ACTIN2 confers increased tolerance to oxidative stress in Arabidopsis *der1-3* mutant

**Kuběnová L**, Takáč T, Šamaj J, Ovečka M (2021). Single amino acid exchange in ACTIN2 confers increased tolerance to oxidative stress in Arabidopsis *der1-3* mutant. *International Journal of Molecular Sciences* 22: 1879. doi: 10.3390/ijms22041879

**LK** performed the modelling of the ACTIN2 protein structure, phenotypic and microscopic analyses, histochemical detection of ROS, data processing and statistical evaluation. **LK** participated in writing the manuscript.



Our previous study showed, that mutation in *ACTIN2* gene of the *der1-3* mutant affects not only RH development, but has more general effects on overall plant growth and development. In particular, *der1-3* mutant shows a wavy root growth pattern caused by higher frequencies of shifted cell division planes (CDPs) in dividing root cells. In addition, *der1-3* mutant displayed differences in actin cytoskeleton structure and organization compared to C24 control plants. We found out in this following study, that *der1-3* mutant has increased tolerance to the oxidative stress. Even though the actin cytoskeleton is included in the plant defense against the oxidative stress, the complete mechanism how altered organization and dynamics of AFs may protect plants was not clear. Phenotypic analyses of C24 control and *der1-3* mutant plants under the oxidative stress revealed that *der1-3* mutant possess better growth parameters, such as root growth and plant biomass production, especially fresh weight of leaves after prolonged exposure of oxidative stress-inducing compounds. We tested plants either germinated on control media and transferred to the oxidative stress conditions, or germinated directly on media containing different concentrations of PQ or H<sub>2</sub>O<sub>2</sub>. After documentation of the phenotypes, we characterized the structure and dynamic properties of the actin cytoskeleton after application of oxidative stress. Live-cell imaging by spinning-disk fluorescence microscope of *der1-3* mutant carrying *pro35S::GFP:FABD2* construct showed a lower bundling rate and higher dynamicity of actin cytoskeleton after 0.1 μmol.l<sup>-1</sup> PQ treatment compared to C24 GFP-FABD2 plants. To support and understand *der1-3* mutant resistance to oxidative stress in more detail, biochemical analyses of selected proteins for estimation of lipid peroxidation and antioxidant capacity were performed. In particular, *der1-3* mutant exhibited a lower degree of lipid peroxidation after oxidative stress, which is important aspect of its enhanced antioxidant defense



capacity. Plants of *der1-3* mutant also showed an elevated capacity to decompose superoxide and hydrogen peroxide, which was supported by increased abundance and activity of several antioxidant enzymes, such as iron superoxide dismutase 1 (FeSOD1), copper-zinc superoxide dismutase isoforms (CuZnSOD1 and CuZnSOD2), and peroxiredoxin Q (PrxQ). Therefore, higher capacity to decompose ROS and enhanced cellular redox regulation might represent the other main factors determining an increased tolerance of the *der1-3* mutant to oxidative stress. This is further supported by the fact that single-point mutation in *ACT2* leading to single change at the position 97 (Arg97 to Cys97) did not change the tertiary protein structure of ACTIN2. However, this change is located in the subdomain 1 and topologically present on the protein surface. Since the mutated ACTIN2 protein has one additional Cys, we assume that this change could lead to enhanced redox-mediated post-translational modifications, accelerating further the antioxidant capacity through PrxQ and thioredoxins in the *der1-3* mutant. Described single-point mutation in the *der1-3* mutant also led to increased sensitivity to reducing agent dithiothreitol (DTT), which might influence biochemical properties of the ACTIN2. Putting all data together, alterations in the actin cytoskeleton, enhanced protection of membrane integrity, higher activity of antioxidant enzymes, and increased capacity for redox modifications lead to enhanced resistance of *der1-3* mutant to mild and severe oxidative stress induced by PQ or H<sub>2</sub>O<sub>2</sub> in the culture medium.

Article

# Single Amino Acid Exchange in ACTIN2 Confers Increased Tolerance to Oxidative Stress in Arabidopsis *der1–3* Mutant

Lenka Kuběnová, Tomáš Takáč , Jozef Šamaj and Miroslav Ovečka \* 

Department of Cell Biology, Centre of the Region Haná for Biotechnological and Agricultural Research, Faculty of Science, Palacký University Olomouc, Šlechtitelů 27, 783 71 Olomouc, Czech Republic; lenka.kubanova@upol.cz (L.K.); tomas.takac@upol.cz (T.T.); jozef.samaj@upol.cz (J.Š.)

\* Correspondence: miroslav.ovecka@upol.cz; Tel.: +420-585-634-734

**Abstract:** Single-point mutation in the *ACTIN2* gene of the *der1–3* mutant revealed that *ACTIN2* is an essential actin isoform required for root hair tip growth, and leads to shorter, thinner and more randomly oriented actin filaments in comparison to the wild-type C24 genotype. The actin cytoskeleton has been linked to plant defense against oxidative stress, but it is not clear how altered structural organization and dynamics of actin filaments may help plants to cope with oxidative stress. In this study, we characterized root growth, plant biomass, actin organization and antioxidant activity of the *der1–3* mutant under oxidative stress induced by paraquat and H<sub>2</sub>O<sub>2</sub>. Under these conditions, plant growth was better in the *der1–3* mutant, while the actin cytoskeleton in the *der1–3* carrying *pro35S::GFP:FABD2* construct showed a lower bundling rate and higher dynamicity. Biochemical analyses documented a lower degree of lipid peroxidation, and an elevated capacity to decompose superoxide and hydrogen peroxide. These results support the view that the *der1–3* mutant is more resistant to oxidative stress. We propose that alterations in the actin cytoskeleton, increased sensitivity of *ACTIN* to reducing agent dithiothreitol (DTT), along with the increased capacity to decompose reactive oxygen species encourage the enhanced tolerance of this mutant against oxidative stress.



**Citation:** Kuběnová, L.; Takáč, T.; Šamaj, J.; Ovečka, M. Single Amino Acid Exchange in *ACTIN2* Confers Increased Tolerance to Oxidative Stress in Arabidopsis *der1–3* Mutant. *Int. J. Mol. Sci.* **2021**, *22*, 1879. <https://doi.org/10.3390/ijms22041879>

Academic Editor: Staffan Persson  
Received: 7 January 2021  
Accepted: 10 February 2021  
Published: 13 February 2021

**Publisher's Note:** MDPI stays neutral with regard to jurisdictional claims in published maps and institutional affiliations.



**Copyright:** © 2021 by the authors. Licensee MDPI, Basel, Switzerland. This article is an open access article distributed under the terms and conditions of the Creative Commons Attribution (CC BY) license (<https://creativecommons.org/licenses/by/4.0/>).

**Keywords:** *ACTIN2*; actin cytoskeleton; antioxidant capacity; Arabidopsis; *der1–3* mutant; lipid peroxidation; oxidative stress; root hairs; single amino acid exchange

## 1. Introduction

Plants are continuously exposed to fluctuating environmental conditions, including adverse biotic and abiotic stressors. Oxidative stress, alone or in combination with other stress factors, may disrupt the cellular homeostasis in plants. Oxidative stress significantly increases symplastic and apoplastic amounts of reactive oxygen species (ROS) such as superoxide (O<sub>2</sub><sup>•−</sup>), hydrogen peroxide (H<sub>2</sub>O<sub>2</sub>), hydroxyl radical (OH<sup>•</sup>) and singlet oxygen (<sup>1</sup>O<sub>2</sub>). Although ROS also serve as signaling molecules, playing important roles in the regulation of numerous plant developmental processes [1–3], they are generated as toxic by-products of the aerobic metabolism under stress conditions [4–8]. In general, the production of ROS with metabolic or stress-related origin, is controlled by components of redox signaling pathways. These maintain cellular ROS homeostasis, since both low and high ROS levels are undesirable for plant cells. Thus, an equilibrated threshold of ROS is maintained and controlled by the activity of antioxidant enzymes from the family of superoxide dismutases (SODs), catalases, peroxidases, glutathione peroxidases, iron uptake/storage regulating proteins, and a network of thio- and glutaredoxins [8–10].

A common approach in inducing oxidative stress in plants experimentally is based on the external application of paraquat (PQ, 1,1'-dimethyl-4,4'-bipyridinium chloride) and hydrogen peroxide (H<sub>2</sub>O<sub>2</sub>). PQ, or methyl viologen, is a widely used herbicide, which passes rapidly to the cells [11,12]. PQ is effective particularly in photosynthetically-active plant tissues [13]. Primary place of its activity is chloroplast, where PQ takes away electrons, probably from photosystem I and ferredoxin. This process leads to the formation of stable

reduced cationic radical, reacting rapidly with molecular oxygen to form  $O_2^{\bullet-}$  [14,15]. Superoxide anion interferes with antioxidant defense mechanisms, leading to the damage of cells due to numerous chain reactions [16]. Treatment of plants with PQ also affects gene expression. Alterations have been documented in the expression of numerous genes encoding different protein kinases such as receptor-like kinases (RLKs), mitogen-activated protein kinases (MAPKs) or calcium-dependent protein kinases (CDPKs), antioxidant enzymes such as ascorbate peroxidase, CuZn SOD (CSD), FeSOD (FSD), some transcription factors that contain typical DNA binding motifs such as MYB and MYC, or in genes securing cell structural integrity [17]. All these changes likewise lead to the significant oxidation of proteins or nucleic acids [18]. The typical phenotypical reaction of affected plants is wilting and chlorosis. Prolonged PQ exposure causes the browning of damaged tissues and severe chlorosis, leading to the leaves falling off [12].

$H_2O_2$  is generated in chloroplasts, mitochondria and peroxisomes as an inevitable by-product of aerobic metabolism, or it is produced under stress conditions (both biotic and abiotic); [19]. It is a relatively long-living molecule (up to 1 ms) with the ability to pass membranes either by diffusion or actively via aquaporins [20–23]. The biological activity of  $H_2O_2$  is mediated by its ability to oxidize free SH groups [22]. Excessive exogenous  $H_2O_2$  application induces rapid cell death and necrosis of plant cells, even without passing through the apoptotic stage [19,24,25]. The external application of  $H_2O_2$  can stimulate some morphogenetic events in plants, such as adventitious root initiation in flax hypocotyls [26].  $H_2O_2$ , particularly at higher concentrations, affects the expression pattern of genes involved in diverse plant defense responses. It can be exemplified by changing expression patterns of genes encoding biosynthetic enzymes of phenylpropanoids, lignin and salicylic acid [27,28], as well as enzymes protecting against oxidative stress, such as glutathione S-transferase (GST) [29] and anthranilate synthase (ASA1), which is required for the biosynthesis of the phytoalexin camalexin [30]. The excessive formation of  $H_2O_2$  also causes oxidative impairments of photosynthetic apparatus [22,31,32].

Actin filaments are essential cytoskeletal components, playing important roles in cellular (e.g., cytoplasmic streaming, organelle movement, vesicular trafficking) and developmental processes (e.g., establishment and maintenance of cell polarity and shape, cell division plane determination, tip growth). A typical feature of the actin cytoskeleton is its ability to perform dynamic structural reorganizations [33,34]. The actin cytoskeleton is also involved in signaling events triggered by diverse external stimuli. Among others, actin cytoskeleton remodeling is part of abiotic stress response mechanisms in plants [35]. Interestingly, dysfunctional ACTIN2 isoform or destabilization of actin microfilaments using cytochalasin D alters the localization of Respiratory burst oxidase homolog protein C (RbohC) during root hair development in Arabidopsis [36]. The connection between the intracellular distribution pattern of NDC1 (NAD(P)H dehydrogenases type II), and its ability to reduce mitochondrial ROS production and ACTIN2 was also revealed [37]. These data suggest a supporting role of actin filaments in the mediation of both short- and long-term plant responses to oxidative stress conditions. The dependence between changing dynamics of the actin cytoskeleton and elevated ROS level was described in Arabidopsis root tip cells under salt stress. Treatment with NADPH oxidase inhibitor diphenyleneiodonium prevented a salt stress-induced ROS increase, but treatment with actin inhibitors latrunculin B or jaspilakinolide caused an enhanced ROS accumulation in salt stress-treated root cells [38]. Actin microfilaments play an important role in vesicular trafficking, which is linking ROS signaling with auxin transport [39]. In the proposed model, oxidative stress caused by  $H_2O_2$  affects the dynamics of the actin cytoskeleton, which subsequently interferes with the ADP-ribosylation factor guaninenucleotide exchange factor (ARF-GEF)-dependent trafficking of PIN2 from the plasma membrane to early endosomes [39]. However, the complete mechanism regulating the structural and dynamic properties of the actin cytoskeleton under oxidative stress in plants is not fully understood yet.

The actin cytoskeleton is essential for the tip growth of root hairs. Indispensable functions of actin in growing root hairs were documented by pharmacological [40] and genetic [41,42] means. Evolution of land plants brought a diversification into reproductive and vegetative classes of actin, later ones represented by ACTIN2, ACTIN7 and ACTIN8 [43,44]. Genetic approaches using chemically-induced single-point mutation [42] or insertional knockout mutation [41] revealed that ACTIN2 is essential for proper root hair tip growth. Expression level of the ACTIN2 gene is not affected by the single point mutations in the DER1 (DEFORMED ROOT HAIRS 1) locus and wild-type levels of ACTIN2 expression has been documented in the *der1* (*deformed root hairs1*) mutants [42]. Nevertheless, the palette of received mutants (*der1-1*, *der1-2*, *der1-3*) showed different degrees of the mutant root hair phenotype [42]. It provides an opportunity to characterize the involvement of ACTIN2, altered by single-point mutations in *der1* mutants [42], in different aspects of their development [45]. In this study, we describe growth and developmental parameters of the *der1-3* mutant, bearing a strong ACTIN2 mutation phenotype [42], under oxidative stress caused by PQ and H<sub>2</sub>O<sub>2</sub>. In comparison to plants of the wild-type (C24 ecotype), post-germination root growth, biomass production, antioxidant activity and the prevention of lipid peroxidation were more effective in the *der1-3* mutant. Considering the lower bundling rate and higher dynamicity of the actin cytoskeleton, together with the increased capacity of ACTIN for redox modifications caused by reducing agent dithiothreitol (DTT), we conclude that *der1-3* mutant plants are more resistant to mild and severe oxidative stress induced by PQ or H<sub>2</sub>O<sub>2</sub> in the culture medium.

## 2. Results

### 2.1. Impact of the *der1-3* Mutation and Its Topology on Protein Tertiary Structure

*Arabidopsis thaliana* mutant *der1-3* has been produced in the C24 ecotype background by an ethylmethanesulfonic acid-induced mutagenesis in the DER1 locus, leading to a single-point mutation in the ACTIN2 gene [42]. In general, *der1* mutants were selected according to disturbed root hair development phenotypes [42,46], and subsequent complementation analysis rescuing the normal root hair phenotype through expression of the ACTIN2 cDNA under the control of ACTIN2 or root hair-specific CHIMERIC LEUCINE-RICH REPEAT/EXTENSIN1 (LRX1) promoters, confirming mutations in the ACTIN2 gene [42]. Single-point mutation in the genomic DNA sequence of the gene was determined at the position 1114 (changing cytosine to thymine), leading to an altered protein sequence exchanging Arg97 to Cys97 in the *der1-3* mutant [42]. We translated a nucleotide sequence, both in a natural and mutated variant, to a primary protein sequence and we prepared a model of a tertiary protein structure. We found that this position, both in the natural (Figure 1A) and mutated (Figure 1B) ACTIN2 protein is placed in a loop located at the protein periphery (Videos S1 and S2). Importantly, based on the 3D model, the mutation does not alter the overall tertiary structure of the protein (Figure 1A,B), while this single amino acid exchange is topologically exposed to the protein surface (Figure 1C,D). This analysis indicates that single-point mutation exchanging Arg to Cys at the position 97 in the ACTIN2 protein of the *der1-3* mutant might rather influence its biochemical properties.

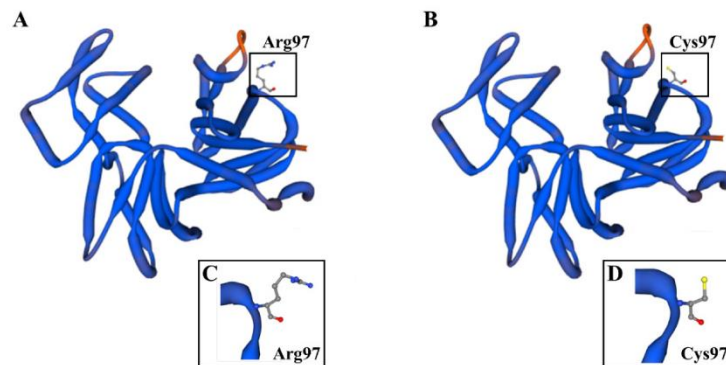


**Figure 1.** Model of the natural ACTIN2 protein structure and its mutated version in *der1-3* mutant. (A,B) SWISS model of the tertiary protein structure of ACTIN2 based on the wild-type gene sequence (A) or on the gene sequence altered by single-point mutation in the *der1-3* mutant (B). Topological location of arginine in the position 97 of the natural ACTIN2 (A) and substituted cysteine in the position 97 of the mutated ACTIN2 (B) of the *der1-3* mutant are showed in boxes. (C,D) Detailed structure of spatial arrangements of Arg97 (C) and Cys97 (D) from the boxed area in (A,B), respectively. 3D rotational models of protein structures are presented in Videos S1 and S2. Models of protein structures were produced in the application SWISS-MODEL (Biozentrum, University of Basel, Switzerland).

## 2.2. Influence of Oxidative Stress on Post-Germination Root Growth

In order to characterize the responses of the *der1-3* mutant to oxidative stress, we analyzed several phenotypical parameters. Apart from the obvious phenotype of root hairs that arrested their tip growth after bulge formation [42], mutant plants are also affected in other developmental aspects. Among them, seeds of the *der1-3* mutant germinate later than the C24 wild-type seeds, and primary roots show a more irregular and wavy growth pattern, due to obvious changes in the cell division plane orientation [45]. Analysis of the primary root growth of seedlings within the first 5 days after germination on the control media revealed a slightly lower elongation rate of the *der1-3* roots in comparison to the C24 (Figure 2A), however, the differences in average root growth per 24 h were insignificant (Figure 2I). We also found the same root growth rate in the transgenic *der1-3* mutant line carrying *pro35S::GFP:FABD2* (designated as *der1-3* GFP-FABD2; Figure 2I), but interestingly, the average root growth rate per 24 h of the transgenic C24 line carrying *pro35S::GFP:FABD2* (designated as C24 GFP-FABD2) on the control media was significantly higher (Figure 2E,I). Thus, seedlings of the transgenic C24 GFP-FABD2 line showed a more effective root growth rate than the C24 wild-type seedlings (Figure S1A), while there were no differences in this parameter between seedlings of the *der1-3* and transgenic *der1-3* GFP-FABD2 line in control conditions (Figure S1B).

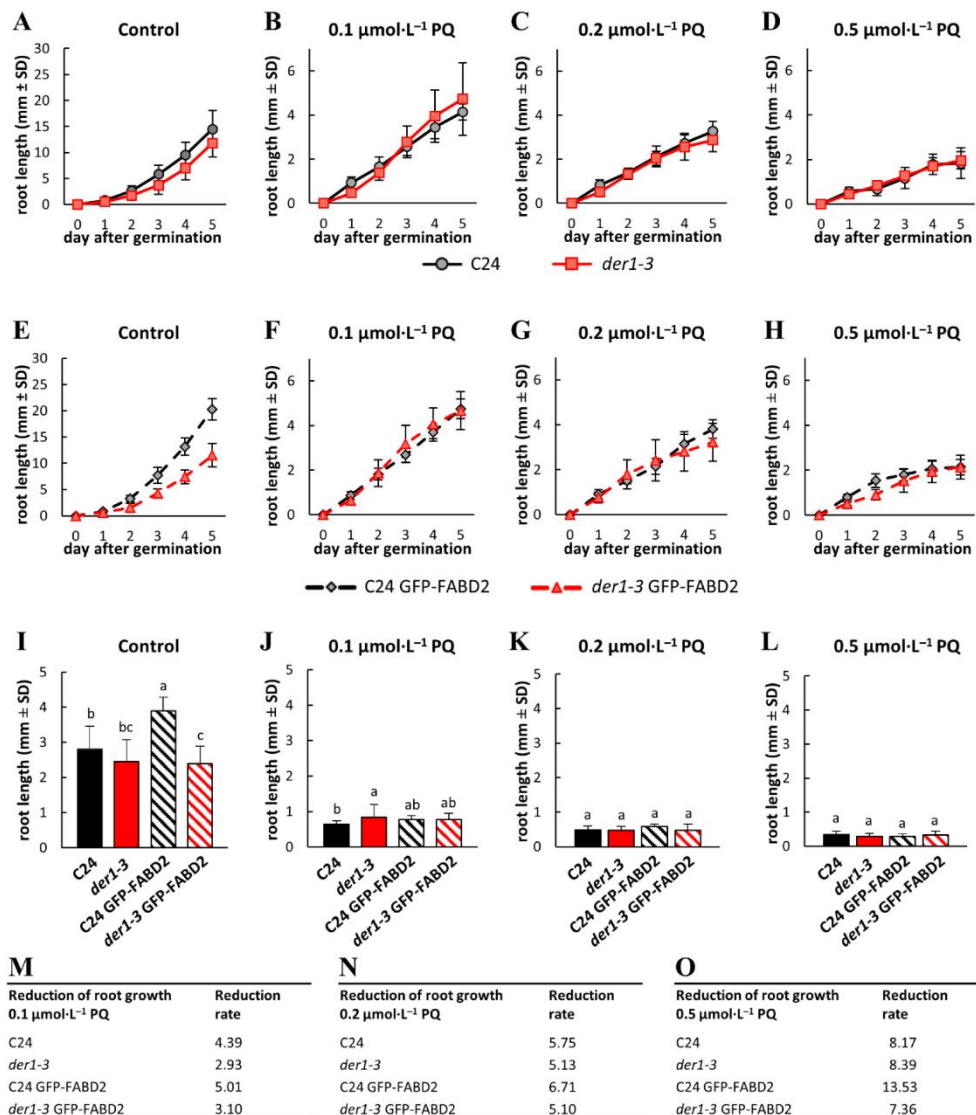


**Figure 2.** Root growth rate in plants of the control C24, *der1-3* mutant and transgenic C24 and *der1-3* lines expressing *pro35S::GFP:FABD2* after germination in paraquat (PQ)-containing media. (A–D) Root growth rate within the first 5 days after germination of the control C24 and *der1-3* mutant plants on the control media (A) and on media containing 0.1 (B), 0.2 (C) and 0.5 (D)  $\mu\text{mol}\cdot\text{L}^{-1}$  of PQ. (E–H) Root growth rate within the first 5 days after germination of the transgenic C24 line carrying GFP-FABD2 and transgenic *der1-3* line carrying GFP-FABD2 on the control media (E) and on media containing 0.1 (F), 0.2 (G) and 0.5 (H)  $\mu\text{mol}\cdot\text{L}^{-1}$  of PQ. (I–L) Average root growth per 24 h on the control media (I) and on media containing 0.1 (J), 0.2 (K) and 0.5 (L)  $\mu\text{mol}\cdot\text{L}^{-1}$  of PQ. (M–O) Reduction ratio (fold change in respect to control) of average root growth in respective lines on media containing 0.1 (M), 0.2 (N) and 0.5 (O)  $\mu\text{mol}\cdot\text{L}^{-1}$  of PQ. Experiments were repeated two times with 16 plants per line (control) and 12 plants per line (PQ). Different lowercase letters above the bars (I–L) represent statistical significance according to one-way ANOVA and subsequent LSD test at  $p$  value < 0.05.

Seedlings of all tested lines germinating and growing on PQ-containing media within the first 5 days after germination showed a reduction in primary root growth, which was dependent on PQ concentration (Figure S1C–F). Together with the flattening of the root growth rate curves, there was also the apparent PQ dose-dependent unification of the root growth rate between the C24 wild-type and *der1-3* mutant seedlings (Figure 2B–D), and also between the C24 GFP-FABD2 and *der1-3* GFP-FABD2 seedlings (Figure 2F–H). A dose-dependent reduction in average root growth per 24 h was apparent in seedlings germinating and growing on media containing 0.1, 0.2 and 0.5  $\mu\text{mol}\cdot\text{L}^{-1}$  of PQ (Figure 2J–L). Although the root growth rate of the *der1-3* mutant was always similar or lower in comparison to the C24 wild-type under control conditions (Figure 2A,I; Figure S1A,B), the roots of the *der1-3* mutant germinating and growing in the presence of 0.1  $\mu\text{mol}\cdot\text{L}^{-1}$  of PQ showed better growth than the C24 wild-type (Figure 2J). The average root growth rate per 24 h was considerably reduced on media containing 0.2 and 0.5  $\mu\text{mol}\cdot\text{L}^{-1}$  of PQ (Figure 2K,L) without any differences among all tested lines. However, when differences were evaluated as a reduction ratio in respect to control values, the fold change in average root growth rate on media containing 0.1  $\mu\text{mol}\cdot\text{L}^{-1}$  of PQ was 4.39 and 5.01 in the C24 wild-type and C24 GFP-FABD2, respectively, but only 2.93 and 3.10 in the *der1-3* mutant and *der1-3* GFP-FABD2, respectively (Figure 2M). Although the fold change in average root growth rate between the C24 and *der1-3* mutant genotypes were less obvious on media containing 0.2 and 0.5  $\mu\text{mol}\cdot\text{L}^{-1}$  of PQ, the reduction rate was similar or slightly lower in the *der1-3* mutant (Figure 2N,O). These data clearly indicate that the root growth of both the *der1-3* mutant and the *der1-3* GFP-FABD2 transgenic line is less affected by mild and severe oxidative stress induced by PQ presence in the culture medium.

The effectivity of the root growth rate under oxidative stress in analyzed lines was also determined by the measurement of the distance between the first root hair and the root tip. In roots of 5-day-old plants growing in control conditions, this distance was significantly longer in C24 wild-type in comparison to *der1-3* (Figure S2A). The same tendency showing a significantly longer distance between the first root hair and the root tip was also observed in the transgenic C24 GFP-FABD2 line in comparison to the transgenic *der1-3* GFP-FABD2 line (Figure S2A). Interestingly, both transgenic lines (C24 GFP-FABD2 and *der1-3* GFP-FABD2) had this measured distance significantly longer in comparison to the control C24 and *der1-3* plants, respectively (Figure S2A). Such differences between the C24 and *der1-3* mutant were reduced considerably, or disappeared completely, in seedlings germinating and growing on media containing 0.1, 0.2 and 0.5  $\mu\text{mol}\cdot\text{L}^{-1}$  of PQ (Figure S2B–D). This represented another indication of differential responses to oxidative stress of the analyzed lines, showing the significantly higher tolerance of the transgenic *der1-3* mutant line.

Plants monitored for 11 days after germination showed apparent time-dependent acceleration of root growth in control conditions (Figure S3A) with no obvious differences between the C24 wild-type and *der1-3* mutant (Figure S3E). However, root growth of the C24 GFP-FABD2 line was faster, particularly in the later stages of development (Figure S3A), leading to a significant increase in the average root growth per 24 h (Figure S3E). Monitoring root growth rate upon prolonged PQ treatment showed a clearly different trend of response between the control C24 lines and *der1-3* mutant lines. On media containing 0.1 and 0.2  $\mu\text{mol}\cdot\text{L}^{-1}$  of PQ, both the *der1-3* mutant and *der1-3* GFP-FABD2 line showed better average root growth per 24 h than the C24 wild-type and C24 GFP-FABD2 line (Figure S3F,G). Continuous monitoring of root growth rate revealed that it was higher in the *der1-3* mutant and *der1-3* GFP-FABD2 line than in the C24 wild-type and C24 GFP-FABD2 line from 8th to 11th day after germination (Figure S3B,C), and it was opposite to the control conditions (Figure S3A). The root growth of plants on media containing 0.5  $\mu\text{mol}\cdot\text{L}^{-1}$  of PQ was considerably reduced with minimal increase in length per day (Figure S3D), showing very similar average root growth per 24 h in all the examined lines (Figure S3H). This analysis confirmed that, unlike the wild-type lines, root growth and development of the *der1-3* mutant and *der1-3* GFP-FABD2 line is better adapted to the mild oxidative stress.

### 2.3. Biomass Production Affected by Oxidative Stress

Shoot and root fresh weights analyzed 18 days after germination of plants growing on the control media revealed a considerably higher biomass production in the C24 wild-type and C24 GFP-FABD2 line. Conversely, shoot and root biomass productions in the *der1-3* mutant and *der1-3* GFP-FABD2 line were seemingly lower (Figure S4A). In plants germinating and growing for 18 days on media containing PQ, both shoot and root biomass production declined, but not uniformly among the tested lines. While plants of the C24 wild-type and C24 GFP-FABD2 line reacted to increasing concentrations of PQ by drastic reduction of both shoot and root biomass, it was not so dramatically reduced in the *der1-3* mutant and *der1-3* GFP-FABD2 line. Already on media containing 0.1 and 0.2  $\mu\text{mol}\cdot\text{L}^{-1}$  of PQ (Figure S4B,C) biomass weights of the *der1-3* mutant and *der1-3* GFP-FABD2 line were similar or even higher as in C24 wild-type and C24 GFP-FABD2 line. Media with 0.5  $\mu\text{mol}\cdot\text{L}^{-1}$  of PQ massively hindered root development, but shoot biomass production and development was clearly better in *der1-3* mutant and *der1-3* GFP-FABD2 line (Figure S4D). Calculation of the biomass production as a reduction ratio in the fold change in respect to the control revealed minimal change in both shoot and root biomass in the *der1-3* mutant and *der1-3* GFP-FABD2 line on media containing 0.1  $\mu\text{mol}\cdot\text{L}^{-1}$  of PQ in comparison to the C24 wild-type and C24 GFP-FABD2 line (Figure S4E). On media containing 0.2 and 0.5  $\mu\text{mol}\cdot\text{L}^{-1}$  of PQ (Figure S4F,G), we found higher biomass production (in the fold change) in the *der1-3* mutant and *der1-3* GFP-FABD2 line when compared to the C24 wild-type and C24 GFP-FABD2 line. This analysis clearly revealed the physiological resistance of the *der1-3* mutant against mild and severe oxidative stress.

### 2.4. Plant Developmental Responses to Oxidative Stress

In order to characterize solely oxidative stress-related inhibition of root growth, we performed seed germination on the control media and after that, we transferred 3-day-old seedlings to a culture media containing different concentrations of PQ. Comparison of the root growth rate within 4 days after transfer showed that it is very similar for the C24 wild-type and *der1-3* mutant on the control media (Figure 3A,I). After the transfer of seedlings of transgenic lines, root growth rate on the control media of the C24 GFP-FABD2 line was significantly higher in comparison to the *der1-3* GFP-FABD2 line (Figure 3E). Actually, it was the highest among all tested lines (Figure 3I). Root growth rate of the C24 GFP-FABD2 line was higher as in C24 wild-type (Figure S5A), while there was no difference between the *der1-3* mutant and *der1-3* GFP-FABD2 line (Figure S5B). Transfer of the C24 wild-type and *der1-3* mutant seedlings germinated on the control media to media containing 0.1, 0.2 and 0.5  $\mu\text{mol}\cdot\text{L}^{-1}$  of PQ led to a similarly decreased root growth rate (Figure 3B–D). We also found a similar reaction in seedlings of the C24 GFP-FABD2 and *der1-3* GFP-FABD2 lines germinated on the control media and transferred to media containing the same concentrations of PQ (Figure 3F–H). Although the absolute root length of the *der1-3* mutant and *der1-3* GFP-FABD2 line was lower on media containing 0.2 and 0.5  $\mu\text{mol}\cdot\text{L}^{-1}$  of PQ (Figure 3C,D,G,H), the average root growth rate was not considerably different (Figure 3K,L). However, the reaction of seedlings to 0.1  $\mu\text{mol}\cdot\text{L}^{-1}$  of PQ revealed a much better tolerance of the *der1-3* mutant and *der1-3* GFP-FABD2 line, as their average root growth rate was significantly higher than in the C24 wild-type and C24 GFP-FABD2 line, respectively (Figure 3J). Different modes of seedling reaction after transfer to media with 0.1  $\mu\text{mol}\cdot\text{L}^{-1}$  of PQ was revealed. There was a rather uniform reduction of the root growth rate on PQ-containing media in the C24 wild-type and C24 GFP-FABD2 line (Figure S5C,D), while root growth rate much less affected by 0.1  $\mu\text{mol}\cdot\text{L}^{-1}$  of PQ was clearly documented in the *der1-3* mutant and *der1-3* GFP-FABD2 line (Figure S5E,F). These observations were corroborated by the quantitative characterization of differences in average root growth rate by a reduction ratio between the control and PQ-containing media in the fold changes. The root growth reduction ratio caused by 0.1  $\mu\text{mol}\cdot\text{L}^{-1}$  of PQ was lower in seedlings of the *der1-3* mutant and *der1-3* GFP-FABD2 line (Figure 3M). Using 0.2  $\mu\text{mol}\cdot\text{L}^{-1}$  of PQ, the differences between C24-related and *der1-3* mutant-related lines were lower in the *der1-3*



GFP-FABD2 line, while the reduction was stronger in the *der1-3* mutant than in the C24 wild-type (Figure 3N). Differences between the lines transferred to  $0.5 \mu\text{mol}\cdot\text{L}^{-1}$  of PQ were negligible (Figure 3O).

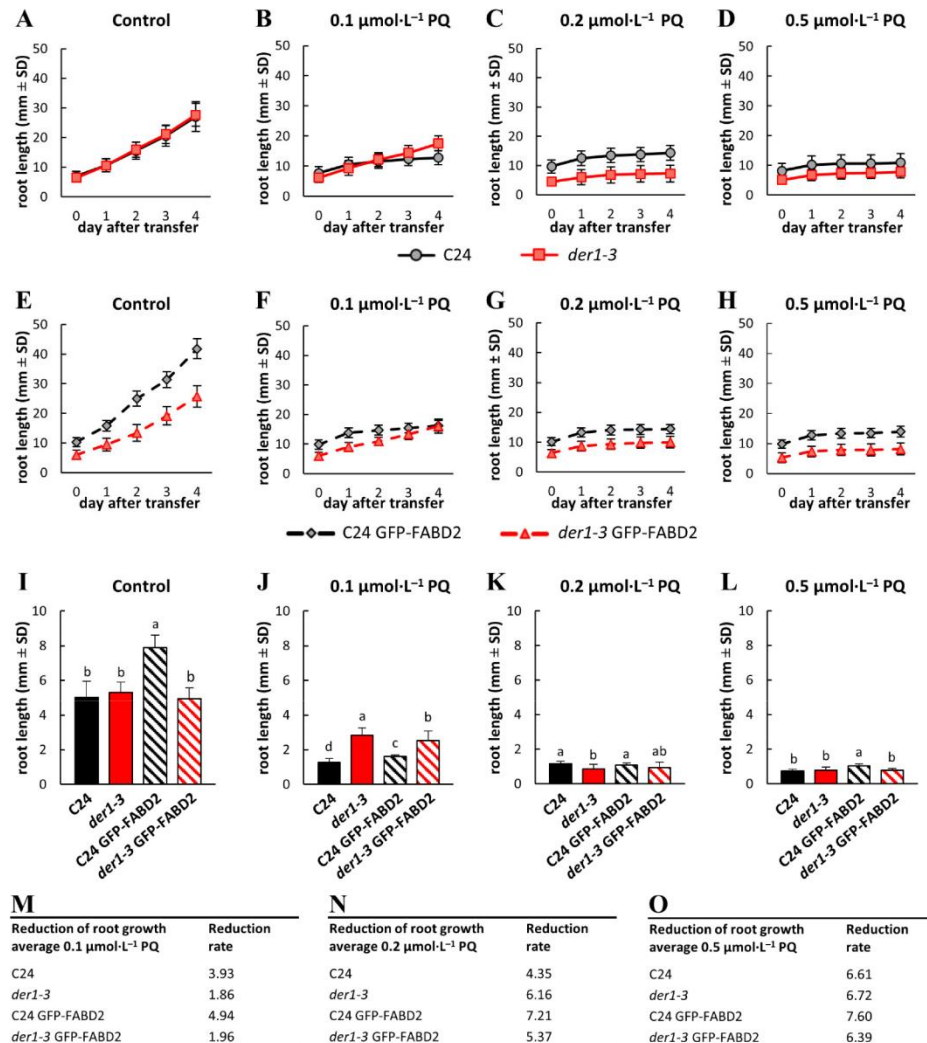


**Figure 3.** Root growth rate in plants of the control C24, *der1-3* mutant and transgenic C24 and *der1-3* lines expressing *pro35S::GFP:FABD2* after their transfer to PQ-containing media. 3-day-old plants germinated on the control media were transferred to PQ-containing media and the root growth rate was analyzed within the subsequent 4 days. (A–D) Root growth rate of the control C24 and *der1-3* mutant plants on the control media (A) and on media containing 0.1 (B), 0.2 (C) and 0.5 (D)  $\mu\text{mol}\cdot\text{L}^{-1}$  of PQ. (E–H) Root growth rate of the transgenic C24 line carrying GFP-FABD2 and the transgenic *der1-3* line carrying GFP-FABD2 on the control media (E) and on media containing 0.1 (F), 0.2 (G) and 0.5 (H)  $\mu\text{mol}\cdot\text{L}^{-1}$  of PQ. (I–L) Average root growth per 24 h on the control media (I) and on media containing 0.1 (J), 0.2 (K) and 0.5 (L)  $\mu\text{mol}\cdot\text{L}^{-1}$  of PQ. (M–O) Reduction ratio (fold change in respect to control) of the average root growth in the respective lines on media containing 0.1 (M), 0.2 (N) and 0.5 (O)  $\mu\text{mol}\cdot\text{L}^{-1}$  of PQ. Experiments were repeated two times with 16 plants per line (control) and 12 plants per line (PQ). Different lowercase letters above the bars (I–L) represent statistical significance according to one-way ANOVA and subsequent LSD test at  $p$  value  $< 0.05$ .

The phenotype of plants germinated and grown on the control media for 20 days confirmed smaller aboveground parts and a more irregular and wavy root growth pattern of the *der1-3* mutant (Figure S6A), in comparison to the C24 wild-type (Figure S6B). Transgenic plants of C24 GFP-FABD2 and *der1-3* GFP-FABD2 grown on the control media were bigger, but similar phenotypes, namely smaller aboveground parts and more irregular and wavy root growth pattern of *der1-3* GFP-FABD2 line, were still apparent (Figure S6C,D). However, plants transferred from the control to PQ-containing culture media revealed a better development of the *der1-3* mutant in comparison to the C24 wild-type (Figure 4A–C) and *der1-3* GFP-FABD2 line in comparison to the C24 GFP-FABD2 line (Figure 4D–F). In all concentrations of PQ tested, the aboveground parts of the *der1-3* mutant and *der1-3* GFP-FABD2 plants were much better developed (Figure 4). In addition, considering purple pigmentation and arrested leaf enlargement, plants of the *der1-3* mutant and *der1-3* GFP-FABD2 were much less affected in media containing  $0.2 \mu\text{mol}\cdot\text{L}^{-1}$  of PQ (Figure 4B,E) and  $0.5 \mu\text{mol}\cdot\text{L}^{-1}$  of PQ (Figure 4C,F). In media containing  $0.1 \mu\text{mol}\cdot\text{L}^{-1}$  of PQ, plants of the *der1-3* mutant and *der1-3* GFP-FABD2 line did not show such a strong stress reaction and developmental arrest (Figure 4A,D). Root development tested at the same conditions showed a clear genotype-dependent response to PQ-induced oxidative stress. Plants (3 days-old) transferred from control to PQ-containing plates and photographed 17 days after transfer showed that the *der1-3* mutant and *der1-3* GFP-FABD2 line are much less sensitive to  $0.1 \mu\text{mol}\cdot\text{L}^{-1}$  of PQ than the C24 wild-type and C24 GFP-FABD2 line, respectively (Figure 4A,D). The root system of the *der1-3* mutant (Figure 4A) and *der1-3* GFP-FABD2 line (Figure 4D) maintained the ability to grow and develop. Although  $0.2 \mu\text{mol}\cdot\text{L}^{-1}$  of PQ considerably reduced root development, the growing and branching capacity of the *der1-3* mutant (Figure 4B) and *der1-3* GFP-FABD2 line (Figure 4E) were higher in comparison to the C24 wild-type and C24 GFP-FABD2 line. Adding  $0.5 \mu\text{mol}\cdot\text{L}^{-1}$  of PQ to the culture medium dramatically reduced the root development of all the tested lines (Figure 4C,F), which was also apparent from the root growth rate (Figure 3L) and root fresh weight (Figure S4D) analyses. Putting together analyses of post-germination root growth and plant development after transfer to PQ-containing media from control conditions confirmed that plants of the *der1-3* mutant and *der1-3* GFP-FABD2 line are more tolerant, particularly to the mild oxidative stress.

Taking into account the inhibitory effects of PQ in photosynthetically active plant tissues, we also employed a  $\text{H}_2\text{O}_2$  treatment, as an alternative oxidative stress-inducing agent that directly affects the root system and its development. Four different concentrations of  $\text{H}_2\text{O}_2$  ( $0.5$ ;  $1$ ;  $1.5$  and  $3 \text{ mmol}\cdot\text{L}^{-1}$ ) were tested in post-germination root growth rate analysis within 4 days after the transfer of 3-day-old seedlings germinated on the control media. We observed a  $\text{H}_2\text{O}_2$  dose-dependent response in the inhibition of root elongation (Figure 5A–D). The average root length of both compared lines was gradually reduced by the presence of  $0.5$ ,  $1$ ,  $1.5$  and  $3 \text{ mmol}\cdot\text{L}^{-1}$  of  $\text{H}_2\text{O}_2$  (Figure 5A–E) in the culture medium. We observed significantly longer roots of the C24 wild-type plants than the *der1-3* mutant plants within the testing period in control conditions, and on media containing  $0.5$  and  $1 \text{ mmol}\cdot\text{L}^{-1}$  of  $\text{H}_2\text{O}_2$ , however, there was no statistically significant difference in the root length on media containing  $1.5 \text{ mmol}\cdot\text{L}^{-1}$  of  $\text{H}_2\text{O}_2$  (Figure 5E). Interestingly, the stronger concentration of  $\text{H}_2\text{O}_2$  ( $3 \text{ mmol}\cdot\text{L}^{-1}$ ) inhibited root elongation in the C24 wild-type significantly more than in the *der1-3* mutant plants (Figure 5E).

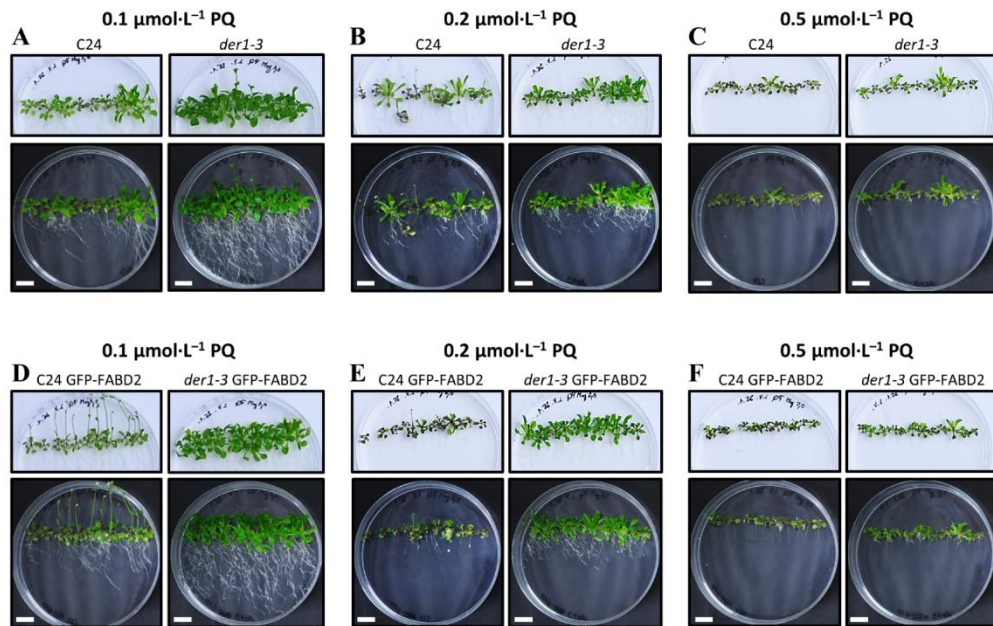


**Figure 4.** Plant phenotype of the control C24, *der1-3* mutant and transgenic C24 and *der1-3* lines expressing *pro35S::GFP-FABD2* after their transfer to PQ-containing media. 3-day-old plants germinated on the control media were transferred to PQ-containing media and photographed 17 days after transfer. (A–C) Plants of the control C24 and *der1-3* mutant growing on media containing 0.1 (A), 0.2 (B) and 0.5 (C)  $\mu\text{mol}\cdot\text{L}^{-1}$  of PQ. (D–F) Plants of the transgenic C24 line carrying GFP-FABD2 and transgenic *der1-3* line carrying GFP-FABD2 growing on media containing 0.1 (D), 0.2 (E) and 0.5 (F)  $\mu\text{mol}\cdot\text{L}^{-1}$  of PQ. Aboveground parts of plants were photographed on a white background (upper row of images), and whole plants including roots were documented on a black background (lower row of images). Plants grown on the control media are documented in Figure S6. Scale bar = 1 cm.

The quantitative characterization of differences in the average root growth rate presented as a reduction ratio between the control and  $\text{H}_2\text{O}_2$ -containing media showed no differences between the C24 wild-type and *der1-3* mutant on media containing 0.5 and 1  $\text{mmol}\cdot\text{L}^{-1}$  of  $\text{H}_2\text{O}_2$  (Figure 5F). However, a moderate difference caused by 1.5  $\text{mmol}\cdot\text{L}^{-1}$  of  $\text{H}_2\text{O}_2$  and a considerably increased difference induced by 3  $\text{mmol}\cdot\text{L}^{-1}$  of  $\text{H}_2\text{O}_2$  (Figure 5F) suggested that root growth and development of the *der1-3* mutant plants are substantially more resistant to moderate and severe oxidative stress than of the C24 wild-type plants. It can be further documented also by the phenotype of whole plants. Together with the root system that was severely reduced by increasing the concentration of  $\text{H}_2\text{O}_2$  in the C24 wild-type plants, a reduction in the development of their aboveground parts was also obvious (Figure S7A). In comparison, although the development of the root system of the *der1-3* mutant plants was also reduced by increasing the concentration of  $\text{H}_2\text{O}_2$ , the development of their aboveground parts was less affected (Figure S7B). The overall data of phenotypical analyses thus indicate that the *der1-3* mutant and transgenic plants in the *der1-3* mutant background maintain growth and development because they are better protected against PQ- or  $\text{H}_2\text{O}_2$ -induced oxidative stress.

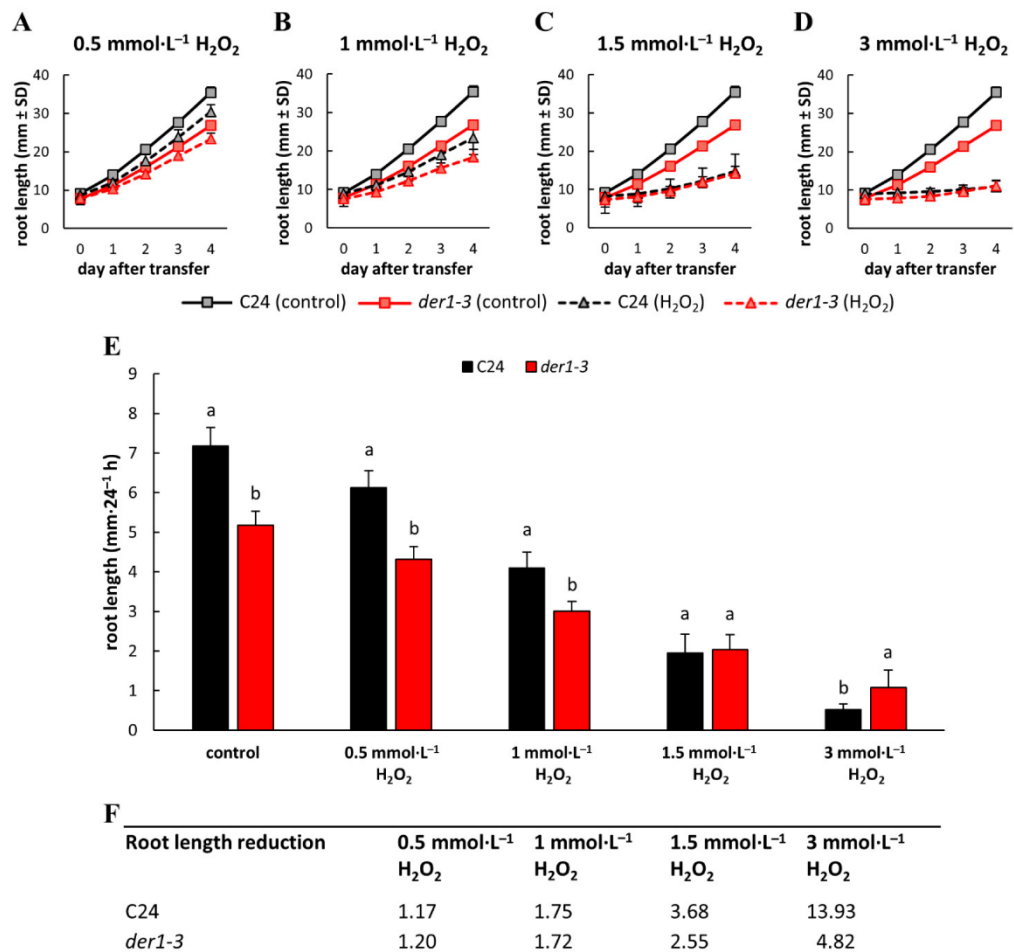


**Figure 5.** Root growth rate of the control C24 and *der1-3* mutant plants after their transfer to H<sub>2</sub>O<sub>2</sub>-containing media. 3-day-old plants germinated on the control media were transferred to a H<sub>2</sub>O<sub>2</sub>-containing media and root growth rate was analyzed within the subsequent 4 days. (A–D) Root growth rate of the control C24 and *der1-3* mutant plants on media containing 0.5 (A), 1 (B), 1.5 (C) and 3 (D) mmol·L<sup>-1</sup> of H<sub>2</sub>O<sub>2</sub>. (E) Average root growth per 24 h on the control media and on media containing indicated concentrations of H<sub>2</sub>O<sub>2</sub>. (F) Reduction ratio (fold change in respect to control) of average root growth in the control C24 and *der1-3* mutant plants on media containing 0.5 (A), 1 (B), 1.5 (C) and 3 (D) mmol·L<sup>-1</sup> of H<sub>2</sub>O<sub>2</sub>. Experiments were repeated two times with 10 plants per line. Different lowercase letters above the bars (E) represent statistical significance according to one-way ANOVA and subsequent LSD test at *p* value < 0.05.

### 2.5. Oxidative Stress and Response of the Actin Cytoskeleton

In order to characterize the organization and dynamic properties of the actin cytoskeleton under PQ-induced oxidative stress, we utilized transgenic C24 and *der1-3* lines expressing *pro35S::GFP:FABD2* construct. In hypocotyl epidermal cells of 3-day-old plants of the C24 GFP-FABD2 line in control conditions, actin filaments were arranged in an extensive, well-organized and dynamic network (Video S3). However, we observed massive bundling, particularly in cortical layers of the cell after treatment with 0.1 μmol·L<sup>-1</sup> of PQ for 30 min (Figure 6A; Video S4). The semi-quantitative evaluation of actin filament

skewness, determining a degree of actin filament bundling, showed increased values after application of oxidative stress (Figure 6B). The semi-quantitative evaluation of integrated density, determining fluorescence signal intensity per  $1 \mu\text{m}^2$ , was also significantly increased after PQ treatment (Figure 6C). Actin filament organization was slightly different in hypocotyl epidermal cells of 3-day-old *der1-3* GFP-FABD2 plants in control conditions, showing mainly thinner, less organized, but dynamic actin filaments in cell cortex (Video S5). Treatment with  $0.1 \mu\text{mol}\cdot\text{L}^{-1}$  of PQ for 30 min induced partial bundling of actin filaments, but overall changes in their organization and dynamics were not so dramatic (Figure 6D; Video S6). As a result, both actin filament skewness (Figure 6E) and integrated density, determining mean fluorescence signal intensity (Figure 6F), were not significantly affected by oxidative stress.

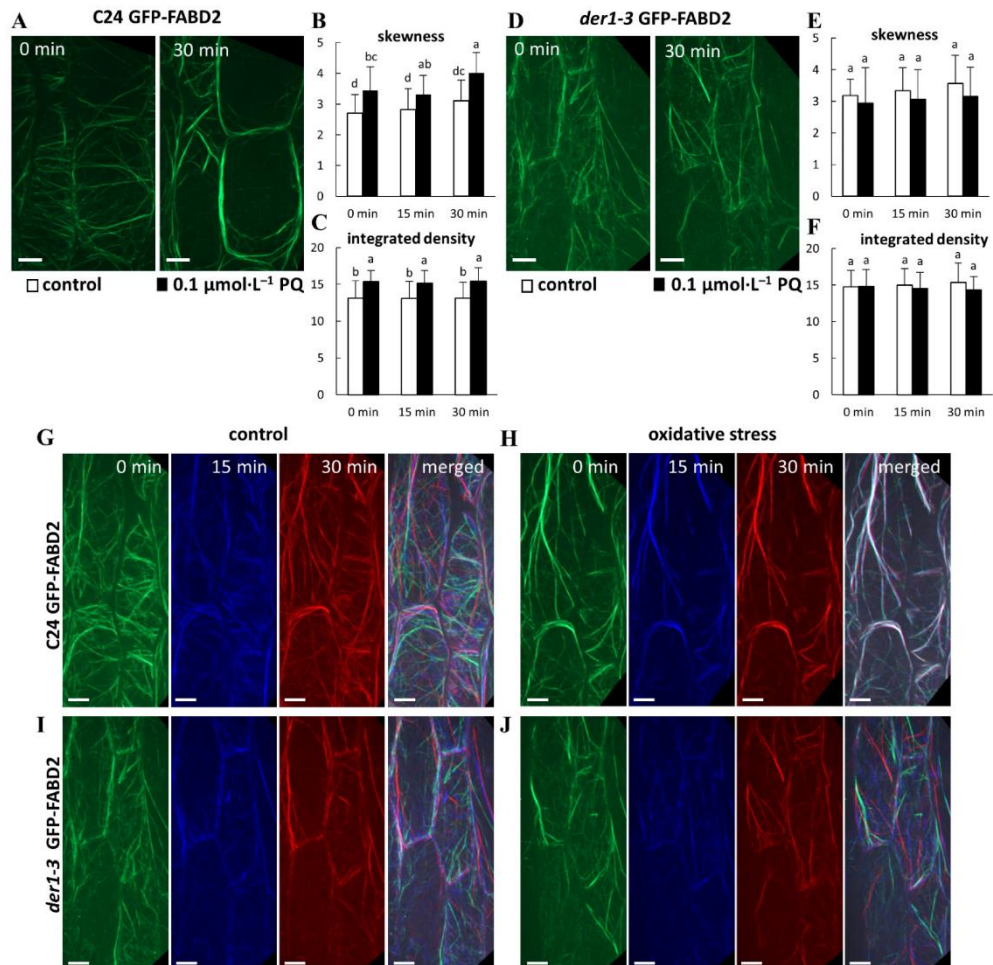


**Figure 6.** Organization and dynamics of actin filaments in the hypocotyl epidermal cells of transgenic C24 and *der1-3* lines expressing *pro355::GFP:FABD2* under PQ-induced oxidative stress. (A–C) Actin filaments in hypocotyl epidermal cells of 3-day-old plants of the C24 GFP-FABD2 line in control conditions and after treatment with  $0.1 \mu\text{mol}\cdot\text{L}^{-1}$  of PQ for 30 min (A). Quantitative analysis of the actin filament bundling extent (skewness, B) and the actin filament density (percentage of occupancy, C) in control conditions and after the application of  $0.1 \mu\text{mol}\cdot\text{L}^{-1}$  of PQ. (D–F) Actin filaments in the hypocotyl epidermal cells of 3-day-old plants of the *der1-3* GFP-FABD2 line in control conditions and after treatment with  $0.1 \mu\text{mol}\cdot\text{L}^{-1}$

of PQ for 30 min (D). Quantitative analysis of the actin filament bundling extent (skewness, E) and the actin filament density (percentage of occupancy, F) in control conditions and after the application of  $0.1 \mu\text{mol}\cdot\text{L}^{-1}$  of PQ. Data were analyzed on images collected from hypocotyl epidermal cells within 0, 15 and 30 min time-points of scanning. (G–J) Semiquantitative analysis of actin filament dynamics in hypocotyl epidermal cells presented by pseudocoloring displacement analysis. Dynamic properties of actin filaments in the C24 GFP-FABD2 line in control conditions (G) and after the application of  $0.1 \mu\text{mol}\cdot\text{L}^{-1}$  of PQ (H). Dynamic properties of the actin filaments in the *der1-3* GFP-FABD2 line in control conditions (I) and after the application of  $0.1 \mu\text{mol}\cdot\text{L}^{-1}$  of PQ (J). Images acquired at the beginning, after 15 min and after 30 min of time-point scanning were colored red, green, and blue, respectively, and merged. A white color indicates lowering (eventually stopping) of the actin dynamic activity. Experiments were repeated 5–6 times with 4–5 cells per plant in each line. Different lowercase letters above the bars (B,C,E,F) represent statistical significance according to one-way ANOVA and subsequent LSD test at  $p$  value  $< 0.05$ . Scale bar =  $10 \mu\text{m}$ .

Next, dynamic properties of the actin cytoskeleton in hypocotyl epidermal cells were analyzed by sequential imaging of actin filaments within 30 min (by acquiring 0, 15 and 30 min time-points), followed by pseudocolor-based evaluation of their lateral displacement. In control conditions, dynamic changes of the actin filament network in cells of both C24 GFP-FABD2 (Figure 6G; Video S3) and *der1-3* GFP-FABD2 (Figure 6I; Video S5) lines were determined by the minimal overlay of sequential colored scans in merged images. After the application of  $0.1 \mu\text{mol}\cdot\text{L}^{-1}$  of PQ, the same analysis revealed the formation of excessive actin bundles with minimal dynamic changes in structure and organization in cells of the C24 GFP-FABD2 line (Figure 6H; Video S4), while far fewer bundles were formed in cells of the *der1-3* GFP-FABD2 line. In addition, the overlay of sequential colored scans revealed unchanged dynamic properties that were still high, particularly in fine actin filaments (Figure 6J; Video S6). This analysis showing alterations in structure and dynamic properties of the actin cytoskeleton in the *der1-3* GFP-FABD2 line, that were not considerably affected by PQ treatment, may significantly support observed physiological resistance of the *der1-3* mutant and the related transgenic *der1-3* GFP-FABD2 line against oxidative stress.

#### 2.6. ROS Production, Lipid Peroxidation and Antioxidant Activity

The relative levels of ROS were determined by the histochemical ROS detection in the cotyledons and leaves of seedlings under control and oxidative stress-inducing conditions. Visualization was performed using NBT (nitrotetrazolium blue) staining of  $\text{O}_2^{\bullet-}$  production and DAB (diaminobenzidine) staining of  $\text{H}_2\text{O}_2$  production, respectively. Semi-quantitative evaluation of the mean staining intensity revealed that both in cotyledons (Figure S8A) and leaves (Figure S8B) of plants treated for 7 days, there was no difference in  $\text{O}_2^{\bullet-}$  production upon PQ and  $\text{H}_2\text{O}_2$  treatments between the C24 wild-type and the *der1-3* mutant. The ability of  $\text{H}_2\text{O}_2$  production visualized by DAB staining was lower in the *der1-3* mutant than in the C24 wild-type in control conditions, both in cotyledons (Figure S8C) and leaves (Figure S8D). Interestingly, upon PQ and  $\text{H}_2\text{O}_2$  treatments, the level of  $\text{H}_2\text{O}_2$  production in the *der1-3* mutant was increased to the C24 wild-type level, both in cotyledons and leaves (Figure S8C,D).

Based on observed phenotypical differences, we aimed to provide evidence about the biochemical mechanisms underlying an increased tolerance of the *der1-3* mutant to oxidative stress. Our analyses showed that the *der1-3* mutant exhibited a lower degree of lipid peroxidation after long-term PQ treatment compared to the C24 wild-type, while cultivation on  $\text{H}_2\text{O}_2$ -containing media did not cause lipid peroxidation in any examined line (Figure 7A). This indicated that PQ treatment was less damaging to the *der1-3* mutant compared to C24 in terms of membrane integrity. Next, we also examined activities of important antioxidant enzymes in the *der1-3* mutant and C24 wild-type. We found the elevated capacity to decompose  $\text{O}_2^{\bullet-}$  in the *der1-3* mutant, as manifested by a more intensive activation of iron superoxide dismutase 1 (FeSOD1) in these plants when exposed to both PQ and  $\text{H}_2\text{O}_2$ , compared to the C24 wild-type (Figure 7B,C). Both treatments substantially decreased the activity of copper-zinc superoxide dismutase (CuZnSOD) isoforms in both

the *der1-3* mutant and the C24 wild-type, while this reduction was less pronounced in the *der1-3* mutant (Figure 7B,C). This was also observed on protein abundance levels, as shown by immunoblotting (Figure 7D,E). In addition, we also encountered a substantially increased abundance of chloroplastic PEROXIREDOXIN Q (PrxQ), a H<sub>2</sub>O<sub>2</sub> decomposing enzyme, in the *der1-3* mutant in response to both PQ and H<sub>2</sub>O<sub>2</sub> treatments, while a slight increase (in the case of PQ), or unchanged abundance (in the case of H<sub>2</sub>O<sub>2</sub>), were observed in the C24 wild-type (Figure 7F,G). Altogether, these results showed that an increased tolerance of the *der1-3* mutant plants to oxidative stress is determined by an elevated enzymatic capacity to decompose ROS.

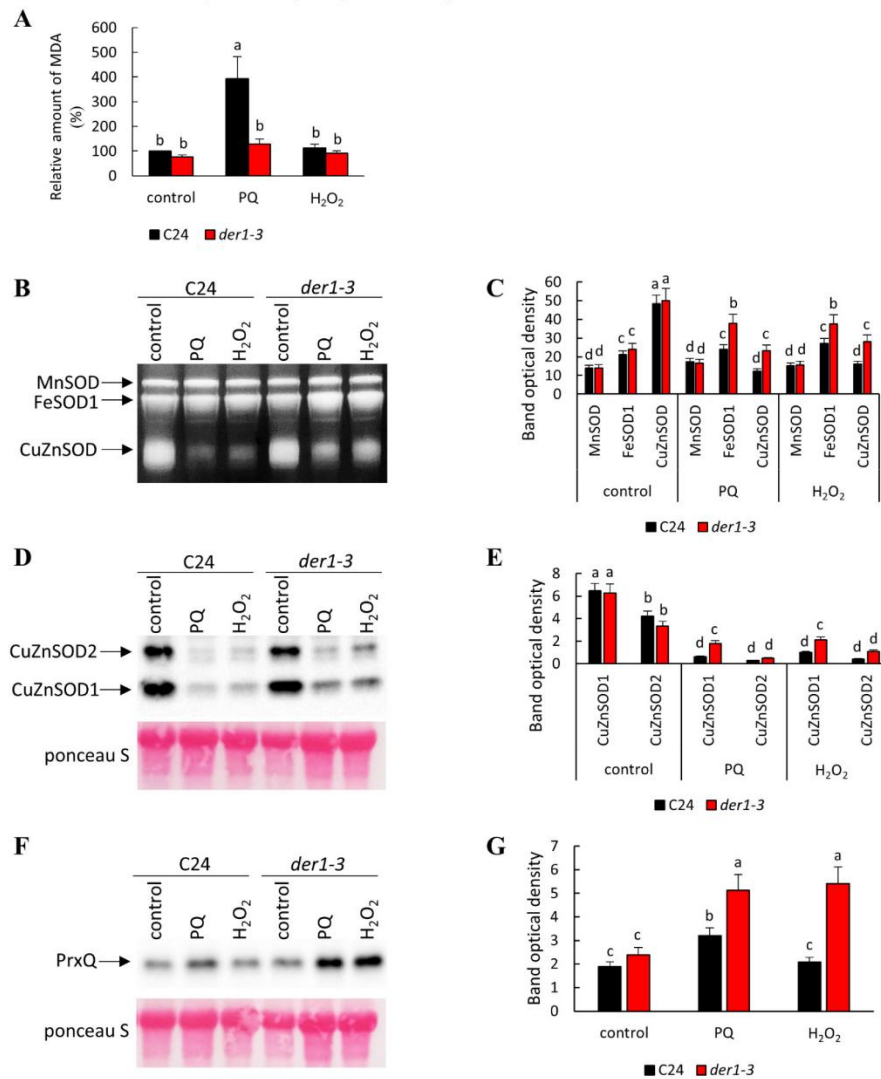


**Figure 7.** Estimation of lipid peroxidation and antioxidant capacity in plants of C24 wild-type and *der1-3* mutant. 3-day-old plants germinated on the control media were transferred to 0.1  $\mu\text{mol}\cdot\text{L}^{-1}$  of PQ- and 3  $\text{mmol}\cdot\text{L}^{-1}$  of H<sub>2</sub>O<sub>2</sub>-containing media and biochemical analysis was performed 11 days after the transfer (plants were 14 days old). (A) Relative quantification of malondialdehyde content. (B,C) Visualization of superoxide dismutase (SOD) isoforms activity (B) and quantification of

individual band densities (C) on native polyacrylamide gels. (D,E) Immunoblot of CuZnSOD1 and CuZnSOD2 isoforms (D) and quantification of band densities (E). (F,G) Immunoblot of peroxiredoxin Q abundance (F) and quantification of band densities (G). Different lowercase letters above the bars (A,C,E,G) represent statistical significance between treatments according to *t*-Test at *p* value < 0.05. Uncropped, full original images of immunoblots are provided in Figures S9 and S10.

The altered ROS metabolism in the *der1-3* mutant implies that point mutation exchanging Arg97 to Cys97 makes ACTIN2 in the *der1-3* mutant more prone to oxidative modifications. This might be supported also by the fact that Cys is one of the two amino acids undergoing oxidative posttranslational modifications. To test this, we monitored ACTIN protein(s) using extraction in the presence of the reducing agent dithiothreitol (DTT) and immunoblots on C24 and the *der1-3* mutant. We found that 0.1 mmol·L<sup>-1</sup> of DTT induced an additional band of 30 kDa along with the specific band (45 kDa) corresponding to the ACTIN 2, 8 and 11 isoforms recognized by the specific monoclonal anti-ACTIN antibody (Figure 8A,B). Considering that ACTIN 11 is expressed only in reproductive organs, the immunoreactive bands (Figure 8A,B) likely reflect the relative abundance of ACTIN 2 and ACTIN 8 isoforms. The 30 kDa band showed higher DTT-induced abundance in the *der1-3* mutant (Figure 8D) compared to the C24 line (Figure 8C). Thus, ACTIN in the *der1-3* mutant shows increased sensitivity to DTT, indicating an amended capacity for redox modifications.

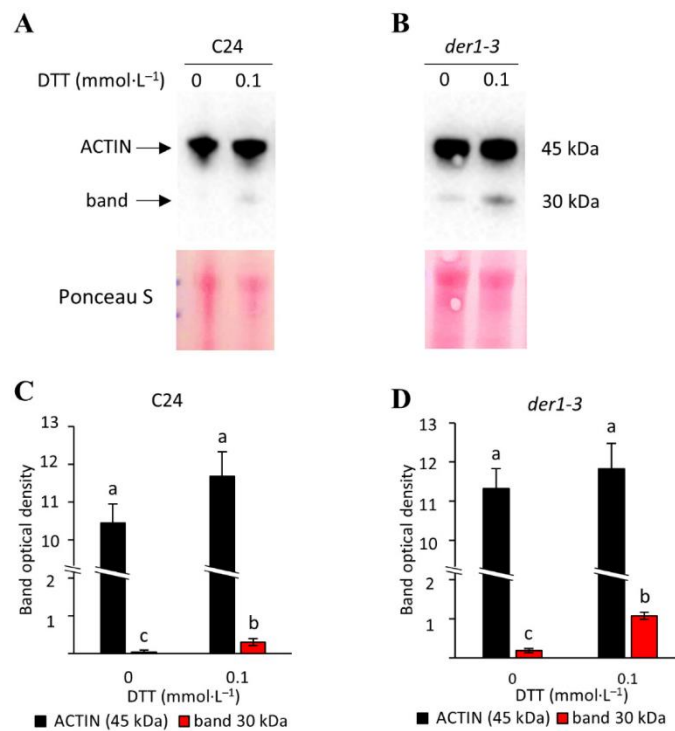


**Figure 8.** Examination of ACTIN sensitivity to dithiothreitol (DTT) in the C24 wild-type and *der1-3* mutant. (A–B) Immunoblots of ACTIN prepared by using anti-ACTIN 2, 8, 11 primary antibody in the C24 wild-type (A) and *der1-3* mutant (B). (C,D) Quantification of band densities in (A,B), respectively. Different lowercase letters above the bars (C,D) represent statistical significance between treatments according to *t*-Test at *p* value < 0.05. Uncropped, full original images of immunoblots are provided in Figure S11.



### 3. Discussion

The random mutagenesis approach in *Arabidopsis thaliana* led to the isolation of *der1* mutants, bearing a single-point mutation in the *DER1* locus. It was demonstrated that these mutants (*der1-1*, *der1-2*, *der1-3*) are compromised in root hair development after the bulge initiation, showing typical “short root hair” phenotypes [42]. The map-based cloning of the *DER1* locus revealed mutation in the *ACTIN2* gene [42]. Locations of these mutations to the *ACTIN2* confirmed the essential role of the actin cytoskeleton in the root hair development [42,46]. Further phenotypical, developmental and microscopic analyses of *der1-3* mutant plants revealed that due to changes in the cell division plane orientation, primary roots showed an irregular and wavy pattern while actin filaments in epidermal cells of different plant organs (roots, hypocotyls and cotyledons) were shorter, thinner and arranged in more random orientations [45]. Thus, the *der1-3* mutant was affected in a broader range of morphological and developmental aspects, related to alterations of the actin cytoskeleton and its organization at a cellular level. It is not clear how structural and dynamic properties of the actin cytoskeleton may support plant reactions to oxidative stress, therefore we addressed this in the present study. We induced conditions of mild and severe oxidative stress by supplementing PQ or H<sub>2</sub>O<sub>2</sub> to the culture medium and characterized diverse parameters such as root growth, development and biomass production in the *der1-3* mutant and C24 wild-type plants. Analyses were performed on plants germinating directly on such oxidative stress-inducing media or on seedlings germinated on the control media first and subsequently transferred to PQ- or H<sub>2</sub>O<sub>2</sub>-containing plates.

We found that oxidative stress induced by three different concentrations of PQ has a clear negative effect on the root growth of the C24 plants and *der1-3* mutant. We prepared transgenic lines of C24 and *der1-3* expressing *pro35S::GFP:FABD2* construct in order to perform live-cell microscopic characterization of the actin cytoskeleton, its organization and dynamic properties in these lines. We also characterized the root growth rate in all above-mentioned lines. Interestingly, root growth of both the *der1-3* mutant and the *der1-3* GFP-FABD2 transgenic line was much less affected by mild and severe PQ-induced oxidative stress as in the control C24, particularly at the concentration 0.1 μmol·L<sup>-1</sup> of PQ in the culture medium. Consequently, the reduction ratio in average root growth quantified as a fold change in respect to the C24 control was several orders lower in the *der1-3* mutant (Figures 2M, 3M and 5F). We found a similar tendency in the reduction of biomass production by the PQ treatment, which was several orders stronger in the C24 wild-type than in the *der1-3* mutant. This trend was documented in both root and shoot biomass production and recorded in all PQ concentrations tested (Figure S4E–G). All data from analyses of post-germination root growth and plant development, both germinating on PQ-containing media and after the transfer of non-treated seedlings to PQ-containing media, indicate that plants of the *der1-3* mutant and *der1-3* GFP-FABD2 line are more tolerant, particularly to the mild oxidative stress.

The observed changes of phenotypical parameters distinguishing the C24 wild-type from the *der1-3* mutant indicate different sensitivities to oxidative stress. In addition, we performed several supporting biochemical experiments. The estimation of lipid peroxidation based on the relative quantification of malondialdehyde content revealed that the *der1-3* mutant exhibits a lower degree of lipid peroxidation after long-term PQ treatment compared to the C24 wild-type. Thus, an important aspect of antioxidant defense in plants, namely membrane integrity, was better protected in the *der1-3* mutant. Better tolerance of the *der1-3* mutant against oxidative stress was also supported by the abundance and activity of antioxidant enzymes such as iron superoxide dismutase 1 (FeSOD1) and two copper-zinc superoxide dismutase isoforms (CuZnSOD1 and CuZnSOD2). Elevated levels of FeSOD1 (activity) and CuZnSOD1/2 (activity and abundance) in the *der1-3* mutant after long-term PQ and H<sub>2</sub>O<sub>2</sub> exposure point to the higher capacity of the mutant to decompose O<sub>2</sub><sup>•-</sup> compared to the C24 wild-type. CuZnSOD1/2 and FeSOD1 are proposed as important determinants of oxidative stress tolerance [47,48]. The *der1-3* mutant also showed increased H<sub>2</sub>O<sub>2</sub> decomposing efficiency which is executed by PrxQ. Nevertheless,

other mechanisms of H<sub>2</sub>O<sub>2</sub> removal cannot be excluded. PrxQ is an atypical 2-cys peroxiredoxin which uses (and interacts with) thioredoxin as an electron donor to decompose H<sub>2</sub>O<sub>2</sub> [49,50]. Peroxiredoxins and thioredoxins as redox buffering proteins, may also modulate intracellular signaling related to ROS [51]. Thus, we propose that the higher capacity to decompose ROS and enhanced cellular redox regulation might represent main factors determining an increased tolerance of the *der1-3* mutant to oxidative stress.

The next task was to reveal how the structure and organization of the actin cytoskeleton in *der1-3* may support increased tolerance of this mutant to oxidative stress. Previous studies reported that the *der1-3* mutant does not show solely root hair phenotype, but the actin cytoskeleton was altered and also affected root growth and development. Actin filaments in cells of the *der1-3* mutant were shorter, thinner and arranged in more random orientations [45]. Oxidative stress caused by application of 0.1 µmol·L<sup>-1</sup> of PQ for 30 min induced massive bundling of actin filaments in cells of the C24 GFP-FABD2 line. The actin cytoskeleton in cells of the *der1-3* GFP-FABD2 line was arranged in an extensive network, although actin filaments were thinner and less organized. However, this organization was virtually insensitive to the 0.1 µmol·L<sup>-1</sup> of PQ applied for 30 min. A higher protection of the actin fine network in the *der1-3* GFP-FABD2 line was accompanied by roughly unchanged dynamic properties under PQ treatment. Thus, higher resistance of the actin cytoskeleton against the deteriorating effects of oxidative stress may be one of the main molecular mechanisms supporting the higher tolerance of the *der1-3* mutant to this type of stress. This can be related to the proposed role of the actin cytoskeleton in the adaptation of Arabidopsis root meristem cells to oxidative stress through protecting PIN2 auxin efflux carrier trafficking to the plasma membrane, which is controlled by auxin levels. Since auxin levels were disturbed by generated ROS, the abundance of PIN2 at the plasma membrane decreased. The role of the actin cytoskeleton lies on keeping the PIN2 intracellular trafficking, which requires the function of the ADP-ribosylation factor (ARF)-guanine nucleotide exchange factor (GEF) BEN1, an actin-associated regulator [39]. However, it is not known how this, and similar functions can be affected by altered structural and dynamic properties of the actin cytoskeleton in the *der1-3* mutant. It was proposed that PIN2 intracellular trafficking was reduced because H<sub>2</sub>O<sub>2</sub> treatment affected actin dynamics [39]. A reduction in actin filament bundling can be directly associated with increased actin filament dynamics [34]. Similarly, the treatment of Arabidopsis plants with strigolactones reduces bundling of actin filaments with their simultaneously increasing dynamics, however, *der1-2* and *der1-3* mutants were much less sensitive to strigolactone analogue GR24 [52]. Collectively, these data support our conclusion that the actin filament arrangement is less prone to bundling and staying dynamic is critical for actin properties in the *der1-3* mutant, significantly contributing also to higher tolerance of this mutant against oxidative stress.

The position of the mutated amino acid Arg-97 in the ACTIN2 sequence is located in the subdomain 1 on the protein surface ([42,53,54]; Figure 1A; Video S1). The topology of this modification might have an impact on the biochemical properties of ACTIN2 in the *der1-3* mutant. There are some supporting facts for this. BEN1, a guanine exchange factor for ARF, regulating the actin filament-based intracellular trafficking of PIN2 during adaptation to oxidative stress, contains highly conserved cysteine residues [39,55] that could be modified by H<sub>2</sub>O<sub>2</sub> treatment. Increased redox status upon the accumulation of H<sub>2</sub>O<sub>2</sub> can initiate the oxidation of cysteine sulfhydryl groups in actins [56]. As mutated ACTIN2 protein in the *der1-3* mutant contains additional Cys compared to the native one, we hypothesize that ACTIN2 in *der1-3* might undergo redox-mediated posttranslational modifications accelerating the antioxidant capacity in the *der1-3* mutant via PrxQ and thioredoxins.

The actin cytoskeleton is recognized as a part of the plant stress sensing machinery and contributes to abiotic and biotic stress responses [57]. For example, actin depolymerization induces the salicylic acid signaling pathway [58], also having an impact on the abundance of proteins involved in abscisic acid signaling [59]. The actin nucleating com-

plex containing actin-related proteins 2 and 3 (ARP2/3) is necessary for H<sub>2</sub>O<sub>2</sub>-dependent stomatal closure in *Arabidopsis* [60]. During elicitation by diverse plant pathogen elicitors, the actin cytoskeleton is rapidly remodeled through the activation of respiratory burst oxidase homolog protein D (RbohD)-dependent ROS production. This ROS signal is transduced to the actin cytoskeleton by heterodimeric capping protein [61]. In addition, there is evidence about direct oxidative posttranslational modifications of ACTIN in mammalian cells, including oxidation [62], glutathionylation [63] or S-sulfhydration [64]. These modifications affect ACTIN depolymerization [62] and dynamics [65,66]. In this study, we provide biochemical evidence that ACTIN might be more prone to undergo redox posttranslational modifications in the *der1-3* mutant. Redox modification by DTT resulted in higher abundance of a band with 30 kDa, which resembles an actin fragment produced by actin cleavage in mammalian cells [67,68]. Thus, our results indicate that ACTIN redox modifications might influence its biochemical properties, which is likely associated with the modified oxidative stress response in the *der1-3* mutant.

Putting together, our data indicate that a topologically important change in ACTIN2 in the *der1-3* mutant is linked to a better tolerance to mild and severe oxidative stress, increased capacity to decompose ROS and higher dynamicity of the actin cytoskeleton.

#### 4. Materials and Methods

##### 4.1. Plant Material and Cultivation In Vitro

Seeds of *Arabidopsis thaliana* (L.) Heynh., ecotype C24, *der1-3* mutant (kindly provided by Christoph Ringli, [42]) and transgenic lines expressing markers for visualization of the actin cytoskeleton were surface sterilized and planted into  $\frac{1}{2}$  Murasighe and Skoog medium without vitamins solidified with 0.6% (*w/v*) Gellan gum (Alfa Aesar, ThermoFisher Scientific, Waltham, MA, USA). Seeds on medium in Petri dishes were stratified at 4 °C for 3 days for synchronized germination. After stratification, seeds on plates were cultivated *in vitro* vertically in a culture chamber at 21 °C, 70% humidity, and 16/8 h light/dark cycle. The level of photosynthetically active radiation (PAR) source was 120  $\mu\text{mol}\cdot\text{m}^{-2}\cdot\text{s}^{-1}$  (400–700 nm), provided by cool white fluorescent linear tube light sources (Philips Master TL-D Reflex 36W, light flow 3350 lm, light efficiency 93  $\text{lm}\cdot\text{W}^{-1}$ ).

##### 4.2. Transgenic Lines and Transformation Method

Plants of *Arabidopsis thaliana* (L.) Heynh. ecotype C24 [69] and the *der1-3* mutant [42] were transformed with *Agrobacterium tumefaciens* strain GV3101 carrying a construct *pro35S::GFP:FABD2*, coding for F-actin binding domain 2 of *Arabidopsis* FIMBRIN 1 (FABD2) fused to green fluorescent protein (GFP); [70]. These lines were used for fluorescent visualization of actin filaments [45]. Briefly, this construct was prepared in a pCB302 vector with rifampicin and kanamycin resistance by the classical cloning method with herbicide phosphinothricin as the selection marker *in planta*. Stable transformation was used according to [71]. Plants (3–4 weeks old) were soaked in *Agrobacterium tumefaciens* cultures for 10 s and were stabilized in the dark overnight. After that, plants were cultivated in a culture chamber at 24 °C, 60% humidity, 16/8 h light/dark photoperiod. Transformation was repeated after one week. Seeds of T<sub>1</sub> generation were planted for selection on  $\frac{1}{2}$  MS media with phosphinothricin (50  $\text{mg}\cdot\text{mL}^{-1}$ ). Transgenic plants were selected for the presence of GFP fusion proteins using an epifluorescence zoom microscope Axio Zoom.V16 (Carl Zeiss, Germany). For further experiments, seeds of T<sub>3</sub> generation were used.

##### 4.3. Application of Stress Factors

Oxidative stress was induced by adding three different concentrations of PQ (0.1; 0.2 and 0.5  $\mu\text{mol}\cdot\text{L}^{-1}$ ), and four different concentrations of H<sub>2</sub>O<sub>2</sub> (0.5; 1; 1.5 and 3  $\text{mmol}\cdot\text{L}^{-1}$ ) to the culture medium. Either seeds were planted directly on  $\frac{1}{2}$  MS media containing different concentrations of PQ, or 3-day-old plants germinated on the control media were transferred to media containing different concentrations of PQ or H<sub>2</sub>O<sub>2</sub>.

#### 4.4. Phenotypical Analysis

Plants germinating and growing *in vitro* on the control media, or on media containing different concentrations of PQ, were scanned directly on plates every 24 h for 11 days from the day of germination. Plants germinating on the control media and transferred to stress conditions were scanned on plates every 24 h for an additional 4 days after their transfer. Images from the scanner (Image Scanner III, GE Healthcare, Chicago, IL, USA) were used for the measurement of the primary root length. Images documenting the phenotype of plants growing in plates were prepared with a Nikon 7000 camera equipped with a macro-objective Sigma 50 mm (2.8 focal distance) in time points indicated in the corresponding figure captions. Fresh weights of separated shoots and roots were measured from 18-day-old plants growing on media containing PQ.

#### 4.5. Sample Preparation and Microscopic Analysis

Samples for microscopic analysis were prepared in microscopic chambers filled with the liquid culture medium according to [72]. Oxidative stress was induced using the liquid culture medium containing  $0.1 \mu\text{mol}\cdot\text{L}^{-1}$  of PQ. Samples were firstly observed under the microscope in the control medium for 30 min and then the medium containing PQ was applied using perfusion of the microscopic chamber. The total volume of the medium applied was  $100 \mu\text{L}$ , added by perfusion sequentially 10 times with  $10 \mu\text{L}$ . After perfusion, hypocotyl and cotyledon above the coverslip was carefully covered with parafilm and samples were scanned in the microscope every 30 s for a further 30 min. Live cell imaging of the actin cytoskeleton in hypocotyl epidermal cells of the C24 ecotype and *der1-3* mutant expressing a construct *pro35S::GFP:FABD2* was performed in a fast scanning mode using a spinning disk microscope Cell Observer SD Axio Observer Z1 (Carl Zeiss, Germany), equipped with EC Plan-Neofluar  $40\times/1.3$  NA oil immersion objective (Carl Zeiss, Germany) and Plan-Apochromat  $63\times/1.4$  NA oil immersion objective (Carl Zeiss, Germany). Samples were imaged with an excitation laser line 488 nm and emission filter BP525/50. Laser power was set up not to exceed 50% of the laser intensity range available. Samples were scanned in a Z-stack mode in a time range of every 30 s for 30 min. Images were acquired with the Evolve 512 EM CCD camera with the exposure time 500–750 ms per optical section. Orthogonal projections of 6 to 10 optical sections from Z-stacks were used for the preparation of videos and measurement of actin filament skewness and occupancy. Semiquantitative analysis of actin filament dynamics in hypocotyl epidermal cells was presented by pseudocoloring displacement analysis. Images were acquired at the beginning, after 15 min and after 30 min of time-point scanning, individually colored red, green, and blue, respectively, and merged. Overlay of all three colors creating a white one indicated lowering, or eventually stopping, of the actin dynamic activity.

#### 4.6. Histochemical Detection of $\text{O}_2^{\bullet-}$ and $\text{H}_2\text{O}_2$ Production

Plants (3 days old) were transferred from the control media to media containing  $0.1 \mu\text{mol}\cdot\text{L}^{-1}$  of PQ and  $3 \text{mmol}\cdot\text{L}^{-1}$  of  $\text{H}_2\text{O}_2$  and histochemical detection of ROS was performed 11 days after the transfer (plants were 14 days old). Superoxide ( $\text{O}_2^{\bullet-}$ ) was detected by NBT (nitrotetrazolium blue) staining according to [73].  $\text{H}_2\text{O}_2$  detection was performed with DAB (diaminobenzidine) staining according to [74]. After staining, plants were mounted and imaged in Axio Zoom.V16 (Carl Zeiss, Germany). Staining intensity mean values in cotyledons and leaves were measured and quantified in ZEN 2 (blue edition; Carl Zeiss, Germany) software.

#### 4.7. Analysis of Enzymatic Activity and Immunoblotting

The plant material for enzyme analyses was prepared as described in Section 4.6. For superoxide dismutase (SOD) activity examination, proteins were extracted using a Na-phosphate extraction buffer containing  $50 \text{mmol}\cdot\text{L}^{-1}$  of Na-phosphate buffer (pH 7.8),  $2 \text{mmol}\cdot\text{L}^{-1}$  of EDTA,  $2 \text{mmol}\cdot\text{L}^{-1}$  of ascorbic acid and 10% (*v/v*) glycerol. SOD activities were visualized on native PAGE gels as described in [75]. For the immunoblotting of CSD

and PrxQ, the enzyme extracts were enriched with a 4× Laemmli SDS buffer (to reach a final concentration of 10% (v/v) glycerol, 60 mmol·L<sup>-1</sup> of Tris/HCl pH 6.8, 2% (w/v) SDS, 0.002% (w/v) bromophenol blue and 5% (v/v) β-mercaptoethanol). Afterwards, the samples were boiled at 95 °C for 5 min. To evaluate the response of ACTIN to DTT, proteins were extracted from 14 day-old C24 wild-type and *der1-3* plants ground to fine powder using liquid nitrogen as described in [76] with modifications. Homogenates were incubated for 1 h at RT in 62.5 mmol·L<sup>-1</sup> of Tris-HCl buffer (pH 6.8) supplemented with 2% (w/v) SDS, 7.5% (v/v) glycerol, 0.01% (w/v) bromophenol blue, complete EDTA-free protease inhibitor cocktail (Roche Life Science, Penzberg, Germany), and without or with 0.1 mmol·L<sup>-1</sup> of DTT. Subsequently, the extracts were boiled at 95 °C for 8 min and cleared by centrifugation at 13,000× g at room temperature for 20 min. Equal amounts of proteins (15 µg) were loaded on 10% SDS PAGE gels. Immunoblotting analysis and chemiluminescence signal development were carried out according to [77]. As primary antibodies, anti-CSD2, anti-PrxQ, anti-ACTIN 2, 8 and 11; all from Agrisera (Vännäs, Sweden) were used diluted 1:3000, 1:1000 and 1:5000, respectively, in Tris-buffered saline containing 0.1% (v/v) Tween-20. The band optical densities were quantified using Image J. Analyses were performed in three biological replicates.

#### 4.8. TBARS Assay

The plant material for TBARS assay was prepared as described in Section 4.6. In this analysis, lipid peroxidation was assayed using the TBARS (thiobarbituric acid reactive substances) assay as described in [78].

#### 4.9. Modelling of ACTIN2 Protein Structure

Samples of genomic DNA from the *der1-3* mutant plants (from three different samples) were isolated using a phenol/chloroform/isoamylalcohol protocol [79]. Isolated genomic DNA samples were subjected to sequencing (SeqMe, Dobříš, Czech Republic). Acquired sequences were compared with control ACTIN2 genomic DNA sequence in Nucleotide BLAST database (BLAST, U.S. National Library of Medicine, National Center for Biotechnology Information; [https://blast.ncbi.nlm.nih.gov/Blast.cgi?PROGRAM=blastn&PAGE\\_TYPE=BlastSearch&LINK\\_LOC=blasthome](https://blast.ncbi.nlm.nih.gov/Blast.cgi?PROGRAM=blastn&PAGE_TYPE=BlastSearch&LINK_LOC=blasthome), accessed on 12 February 2021). Sequences (both control and mutated) were translated to protein sequences in the application available at <http://bio.lundberg.gu.se>, accessed on 12 February 2021, (University of Gothenburg, Sweden; <http://bio.lundberg.gu.se/edu/translat.html?fbclid=IwAR3var5FJ8CBl4QqNe4Yic8NVz0TvWRd0TrFuGUo6Nk6idLQxy2HvQqPEU>, accessed on 12 February 2021). Only one single point mutation found (1114 C-T) changed the protein sequence (Arg97-Cys97) accordingly. Protein sequences were used for protein structure modelling using the application SWISS-MODEL (Biozentrum, University of Basel, Switzerland; <https://swissmodel.expasy.org/interactive?fbclid=IwAR1V9lhUgjiR1kUwFLd8ojFftkHpKZwxIoT6mnEVuIEC2cPSYQov2twoE>, accessed on 12 February 2021). The same application was used also for the generation and downloading of representative images and videos.

#### 4.10. Data Acquisition and Analysis

Evaluated parameters such as root growth, skewness (representing an extent of actin filament bundling) and actin filament fluorescence integrated density (representing a percentage of occupancy) were measured in ImageJ (<http://rsb.info.nih.gov/ij/>, accessed on 12 February 2021). Graphs were prepared in the Microsoft Excel program. Statistical significance between treatments at  $p < 0.05$  was performed using a *t*-Test in Microsoft Excel or in program the STATISTICA 12 (StatSoft, TIBCO Software Inc., Palo Alto, CA, USA) by ANOVA and subsequent Fisher's LSD test ( $p < 0.05$ ).

**Supplementary Materials:** The following materials are available online at <https://www.mdpi.com/1422-0067/22/4/1879/s1>, Figure S1: Impact of PQ treatment on the root growth rate in control and transgenic C24 and *der1-3* mutant lines, Figure S2: Effect of PQ treatment on the distance between the first root hair and the root tip in control and transgenic C24 and *der1-3* mutant lines, Figure S3: Root growth rate in plants of control C24, *der1-3* mutant and transgenic C24 and *der1-3* lines under prolonged PQ treatment, Figure S4: Shoot and root fresh weight in plants of control C24, *der1-3* mutant and transgenic C24 and *der1-3* lines expressing *pro35S::GFP:FABD2* after germination and growth in PQ-containing media, Figure S5: Root growth rate in control and transgenic C24 and *der1-3* mutant lines after their transfer to PQ-containing media, Figure S6: Plant phenotype of control and transgenic C24 and *der1-3* mutant lines on the control media, Figure S7: Phenotype of control C24 and *der1-3* mutant plants after their transfer to H<sub>2</sub>O<sub>2</sub>-containing media, Figure S8: Histochemical detection of O<sub>2</sub><sup>•−</sup> and H<sub>2</sub>O<sub>2</sub> production in the cotyledons and leaves of control C24 and *der1-3* mutant plants after their transfer to PQ- and H<sub>2</sub>O<sub>2</sub>-containing media, Figure S9: Full scan of the entire original gel stained for specific activity of superoxide dismutases presented in Figure 7B, Figure S10: Full scan of the entire original immunoblots presented in Figure 7, Figure S11: Full scans of the entire original immunoblots presented in Figure 8, Video S1: 3D rotational model of protein structure of the nature ACTIN2 protein, Video S2: 3D rotational model of protein structure of mutated version of ACTIN2 in *der1-3* mutant, Video S3: Actin filaments in hypocotyl epidermal cells of C24 GFP-FABD2 line recorded in 30 s intervals for 30 min in control conditions, Video S4: Actin filaments in hypocotyl epidermal cells of C24 GFP-FABD2 line recorded in 30 s intervals after treatment with 0.1 μmol·L<sup>−1</sup> of PQ for 30 min, Video S5: Actin filaments in hypocotyl epidermal cells of the *der1-3* GFP-FABD2 line recorded in 30 s intervals for 30 min in control conditions, Video S6: Actin filaments in hypocotyl epidermal cells of *der1-3* GFP-FABD2 line recorded in 30 s intervals after treatment with 0.1 μmol·L<sup>−1</sup> of PQ for 30 min.

**Author Contributions:** L.K. performed the phenotypical and microscopic analyses, data processing and statistical evaluation. T.T. performed the biochemical analyses. M.O. and L.K. wrote the manuscript with input from all co-authors. M.O. and J.Š. conceived the study, designed the experiments and made the final edits. J.Š. provided the infrastructure, coordinated the whole project and supervised the work. All authors have read and agreed to the published version of the manuscript.

**Funding:** The work was supported by the Czech Science Foundation GAČR, project Nr. 19-18675S and by ERDF project “Plants as a tool for sustainable global development” (No. CZ.02.1.01/0.0/0.0/16\_019/0000827).

**Institutional Review Board Statement:** Not applicable.

**Informed Consent Statement:** Not applicable.

**Data Availability Statement:** The data presented in this study are available in the article and supplementary material.

**Acknowledgments:** We thank Christoph Ringli (Institute of Plant and Microbial Biology, University of Zurich, Zurich, Switzerland) for seeds of the *der1-3* mutant.

**Conflicts of Interest:** The authors declare no conflict of interest.

## References

- Mittler, R.; Vanderauwera, S.; Suzuki, N.; Miller, G.; Tognetti, V.B.; Vandepoele, K.; Gollery, M.; Shulaev, V.; Van Breusegem, F. ROS signaling: The new wave? *Trends Plant Sci.* **2011**, *16*, 1360–1385. [[CrossRef](#)]
- Baxter, A.; Mittler, R.; Suzuki, N. ROS as key players in plant stress signalling. *J. Exp. Bot.* **2014**, *65*, 1229–1240. [[CrossRef](#)]
- Mhamdi, A.; Van Breusegem, F. Reactive oxygen species in plant development. *Development* **2018**, *145*, dev164376. [[CrossRef](#)]
- König, J.; Muthuramalingam, M.; Dietz, K.-J. Mechanisms and dynamics in the thiol/disulfide redox regulatory network: Transmitters, sensors and targets. *Curr. Opin. Plant Biol.* **2012**, *15*, 261–268. [[CrossRef](#)]
- Foyer, C.H.; Noctor, G. Redox signaling in plants. *Antioxid. Redox Signal.* **2013**, *18*, 2087–2090. [[CrossRef](#)] [[PubMed](#)]
- Vaahtera, L.; Brosché, M.; Wrzaczek, M.; Kangasjärvi, J. Specificity in ROS signaling and transcript signatures. *Antioxid. Redox Signal.* **2014**, *21*, 1422–1441. [[CrossRef](#)]
- Mignolet-Spruyt, L.; Xu, E.; Idänheimo, N.; Hoerberichts, F.A.; Mühlentock, P.; Brosché, M.; Van Breusegem, F.; Kangasjärvi, J. Spreading the news: Subcellular and organellar reactive oxygen species production and signalling. *J. Exp. Bot.* **2016**, *67*, 3831–3844. [[CrossRef](#)]
- Mittler, R. ROS are good. *Trends Plant Sci.* **2017**, *22*, 11–19. [[CrossRef](#)] [[PubMed](#)]

9. Vanderauwera, S.; Suzuki, N.; Miller, G.; van de Cotte, B.; Morsa, S.; Ravanat, J.-L.; Heggie, A.; Triantaphylidès, C.; Shulaev, V.; Van Montagu, M.C.E.; et al. Extranuclear protection of chromosomal DNA from oxidative stress. *Proc. Natl. Acad. Sci. USA* **2011**, *108*, 1711–1716. [[CrossRef](#)] [[PubMed](#)]
10. Dvořák, P.; Krasylenko, Y.; Zeiner, A.; Šamaj, J.; Takáč, T. Signaling Toward Reactive Oxygen Species-Scavenging Enzymes in Plants. *Front. Plant Sci.* **2021**, *11*, 618835. [[CrossRef](#)]
11. Riley, D.; Wilkinson, W.; Tucker, B.V. Biological unavailability of bound paraquat residues in soil. In *Bound and Conjugated Pesticide Residues*; Kaufmann, D., Still, G.G., Paulson, G.D., Bandal, S.K., Eds.; American Chemical Society: Washington, DC, USA, 1976; Volume 29, pp. 301–353.
12. Hawkes, T.R. Mechanisms of resistance to paraquat in plants. *Pest Manag. Sci.* **2014**, *70*, 1316–1323. [[CrossRef](#)]
13. Krieger-Liszka, A.; Kós, P.B.; Hideg, E. Superoxide anion radicals generated by methylviologen in photosystem I damage photosystem II. *Physiol. Plant.* **2011**, *142*, 17–25. [[CrossRef](#)]
14. Farrington, J.A.; Ebert, M.; Land, E.J.; Fletcher, K. Bipyridylium quaternary salts and related compounds. V. Pulse radiolysis studies of the reaction of paraquat radical with oxygen. Implications for the mode of action of bipyridyl herbicides. *Biochim. Biophys. Acta Bioenerg.* **1973**, *314*, 372–381. [[CrossRef](#)]
15. Bus, J.S.; Aust, S.D.; Gibson, J.E. Superoxide- and singlet oxygen-catalysed lipid peroxidation as a possible mechanism for paraquat (methyl viologen) toxicity. *Biochem. Biophys. Res. Commun.* **1974**, *58*, 749–755. [[CrossRef](#)]
16. Kunert, K.J.; Dodge, A.D. Herbicide-induced radical damage and antioxidative systems. In *Target Sites of Herbicide Action*, 1st ed.; Boger, P., Sandmann, G., Eds.; CRC Press: Boca Raton, FL, USA, 1989; pp. 49–63.
17. Han, H.J.; Peng, R.H.; Zhu, B.; Fu, X.Y.; Zhao, W.; Shi, B.; Yao, Q.H. Gene expression profiles of Arabidopsis under the stress of methyl viologen: A microarray analysis. *Mol. Biol. Rep.* **2014**, *41*, 7089–7102. [[CrossRef](#)] [[PubMed](#)]
18. Xiong, Y.; Contento, A.L.; Nguyen, P.Q.; Bassham, D.C. Degradation of oxidized proteins by autophagy during oxidative stress in Arabidopsis. *Plant Physiol.* **2007**, *143*, 291–299. [[CrossRef](#)] [[PubMed](#)]
19. Maurino, V.G.; Flügge, U.-I. Experimental systems to assess the effects of reactive oxygen species in plant tissues. *Plant Signal. Behav.* **2008**, *3*, 923–928. [[CrossRef](#)] [[PubMed](#)]
20. Levine, A.; Tenhaken, R.; Dixon, R.; Lamb, C. H<sub>2</sub>O<sub>2</sub> from the oxidative burst orchestrates the plant hypersensitive disease resistance response. *Cell* **1994**, *79*, 583–593. [[CrossRef](#)]
21. Willekens, H.; Chamnongpol, S.; Davey, M.; Schraudner, M.; Langebartels, C.; Van Montagu, M.; Inzé, D.; Van Camp, V. Catalase is a sink for H<sub>2</sub>O<sub>2</sub> and is indispensable for stress defence in C3 plants. *EMBO J.* **1997**, *16*, 4806–4816. [[CrossRef](#)]
22. Dat, J.; Vandenabeele, S.; Vranová, E.; Van Montagu, M.; Inzé, D.; Breusegem, F. Dual action of the active oxygen species during plant stress responses. *Cell. Mol. Life Sci.* **2000**, *57*, 779–795. [[CrossRef](#)] [[PubMed](#)]
23. Miller, E.W.; Dickinson, B.C.; Chang, C.J. Aquaporin-3 mediates hydrogen peroxide uptake to regulate downstream intracellular signaling. *Proc. Natl. Acad. Sci. USA* **2010**, *107*, 15681–15686. [[CrossRef](#)]
24. O'Brien, I.E.W.; Baguley, B.C.; Murray, B.G.; Morris, B.A.M.; Ferguson, I.B. Early stages of the apoptotic pathway in plant cells are reversible. *Plant J.* **1998**, *13*, 803–814. [[CrossRef](#)]
25. Yao, N.; Tada, Y.; Park, P.; Nakayashiki, H.; Tosa, Y.; Mayama, S. Novel evidence for apoptotic cell response and differential signals in chromatin condensation and DNA cleavage in victorin-treated oats. *Plant J.* **2001**, *28*, 13–26. [[CrossRef](#)]
26. Takáč, T.; Obert, B.; Rolčík, J.; Šamaj, J. Improvement of adventitious root formation in flax using hydrogen peroxide. *New Biotechnol.* **2016**, *33*, 728–734. [[CrossRef](#)] [[PubMed](#)]
27. Douglas, C.J. Phenylpropanoid metabolism and lignin biosynthesis: From weeds to trees. *Trends Plant Sci.* **1996**, *1*, 171–178. [[CrossRef](#)]
28. Mauch-Mani, B.; Slusarenko, A.J. Production of salicylic acid precursors is a major function of phenylalanine ammonia-lyase in the resistance of Arabidopsis to *Peronospora parasitica*. *Plant Cell* **1996**, *8*, 203–212. [[CrossRef](#)] [[PubMed](#)]
29. Pickett, C.B.; Lu, A.Y.H. Glutathione S-transferases: Gene structure, regulation, and biological function. *Annu. Rev. Biochem.* **1989**, *58*, 743–764. [[CrossRef](#)]
30. Desikan, R.; Reynolds, A.; Hancock, J.T.; Neill, S.J. Harpin and hydrogen peroxide both initiate programmed cell death but have differential effects on defence gene expression in Arabidopsis suspension cultures. *Biochem. J.* **1998**, *330*, 115–120. [[CrossRef](#)]
31. Park, H.-J.; Miura, Y.; Kawakita, K.; Yoshioka, H.; Doke, N. Physiological mechanisms of a sub-systemic oxidative burst triggered by elicitor-induced local oxidative burst in potato tuber slices. *Plant Cell Physiol.* **1998**, *39*, 1218–1225.
32. Rao, M.V.; Davis, K.R. Ozone-induced cell death occurs via two distinct mechanisms in Arabidopsis: The role of salicylic acid. *Plant J.* **1999**, *17*, 603–614. [[CrossRef](#)] [[PubMed](#)]
33. Wasteneys, G.O.; Galway, M.E. Remodeling the cytoskeleton for growth and form: An overview with some new views. *Annu. Rev. Plant Biol.* **2003**, *54*, 691–722. [[CrossRef](#)]
34. Staiger, C.J.; Blanchoin, L. Actin dynamics: Old friends with new stories. *Curr. Opin. Plant Biol.* **2006**, *9*, 554–562. [[CrossRef](#)] [[PubMed](#)]
35. Zhou, Y.; Yang, Z.; Guo, G.; Guo, Y. Microfilament dynamics is required for root growth under alkaline stress in Arabidopsis. *J. Integr. Plant Biol.* **2010**, *52*, 952–958. [[CrossRef](#)] [[PubMed](#)]
36. Takeda, S.; Gapper, C.; Kaya, H.; Bell, E.; Kuchitsu, K.; Dolan, L. Local positive feedback regulation determines cell shape in root hair cells. *Science* **2008**, *319*, 1241–1244. [[CrossRef](#)] [[PubMed](#)]

37. Wallström, S.V.; Aidemark, M.; Escobar, M.A.; Rasmusson, A.G. An alternatively spliced domain of the NDC1 NAD(P)H dehydrogenase gene strongly influences the expression of the ACTIN2 reference gene in *Arabidopsis thaliana*. *Plant Sci.* **2012**, *183*, 190–196. [[CrossRef](#)]
38. Liu, S.G.; Zhu, D.Z.; Chen, G.H.; Gao, X.-Q.; Zhang, X.S. Disrupted actin dynamics trigger an increment in the reactive oxygen species levels in the *Arabidopsis* root under salt stress. *Plant Cell Rep.* **2012**, *31*, 1219–1226. [[CrossRef](#)]
39. Zwiewka, M.; Bielach, A.; Tamizhselvan, P.; Madhavan, S.; Ryad, E.E.; Tan, S.; Hrtyan, M.; Dobrev, P.; Vanková, R.; Friml, J.; et al. Root adaptation to H<sub>2</sub>O<sub>2</sub>-induced oxidative stress by ARF-GEF BEN1- and cytoskeleton-mediated PIN2 trafficking. *Plant Cell Physiol.* **2019**, *60*, 255–273. [[CrossRef](#)]
40. Baluška, F.; Salaj, J.; Mathur, J.; Braun, M.; Jasper, F.; Šamaj, J.; Chua, N.H.; Barlow, P.W.; Volkmann, D. Root hair formation: F-actin-dependent tip growth is initiated by local assembly of profilin-supported F-actin meshworks accumulated within expansin-enriched bulges. *Dev. Biol.* **2000**, *227*, 618–632. [[CrossRef](#)]
41. Gilliland, L.U.; Kandasamy, M.K.; Pawloski, L.C.; Meagher, R.B. Both vegetative and reproductive actin isoforms complement the stunted root hair phenotype of the *Arabidopsis act2-1* mutation. *Plant Physiol.* **2002**, *130*, 2199–2209. [[CrossRef](#)]
42. Ringli, C.; Baumberger, N.; Diet, A.; Frey, B.; Keller, B. ACTIN2 is essential for bulge site selection and tip growth during root hair development of *Arabidopsis*. *Plant Physiol.* **2002**, *129*, 1464–1472. [[CrossRef](#)]
43. McDowell, J.M.; Huang, S.R.; McKinney, E.C.; An, Y.Q.; Meagher, R.B. Structure and evolution of the actin gene family in *Arabidopsis thaliana*. *Genetics* **1996**, *142*, 587–602. [[CrossRef](#)] [[PubMed](#)]
44. Meagher, R.B.; McKinney, E.C.; Vitale, A.V. The evolution of new structures: Clues from plant cytoskeletal genes. *Trends Genet.* **1999**, *15*, 278–284. [[CrossRef](#)]
45. Vaškebová, L.; Šamaj, J.; Ovečka, M. Single-point ACT2 gene mutation in the *Arabidopsis* root hair mutant *der1-3* affects overall actin organization, root growth and plant development. *Ann. Bot.* **2018**, *122*, 889–901. [[CrossRef](#)] [[PubMed](#)]
46. Ringli, C.; Baumberger, N.; Keller, B. The *Arabidopsis* root hair mutants *der2–der9* are affected at different stages of root hair development. *Plant Cell Physiol.* **2005**, *46*, 1046–1053. [[CrossRef](#)]
47. Sunkar, R.; Kapoor, A.; Zhu, J.-K. Posttranscriptional induction of two Cu/Zn superoxide dismutase gene in *Arabidopsis* is mediated by downregulation of miR398 and important for oxidative stress tolerance. *Plant Cell* **2006**, *18*, 2051–2065. [[CrossRef](#)]
48. Dvořák, P.; Krasylenko, Y.; Ovečka, M.; Basheer, J.; Zapletalová, V.; Šamaj, J.; Takáč, T. In vivo light-sheet microscopy resolves localisation patterns of FSD1, a superoxide dismutase with function in root development and osmoprotection. *Plant Cell Environ.* **2021**, *44*, 68–87.
49. Lamkemeyer, P.; Laxa, M.; Collin, V.; Li, W.; Finkemeier, I.; Schöttler, M.A.; Holtkamp, V.; Tognetti, V.B.; Issakidis-Bourguet, E.; Kandlbinder, A.; et al. Peroxiredoxin Q of *Arabidopsis thaliana* is attached to the thylakoids and functions in context of photosynthesis. *Plant J.* **2006**, *45*, 968–981. [[CrossRef](#)]
50. Yoshida, K.; Hara, S.; Hisabori, T. Thioredoxin selectivity for thiol-based redox regulation of target proteins in chloroplasts. *J. Biol. Chem.* **2015**, *290*, 14278–14288. [[CrossRef](#)]
51. Dietz, K.-J.; Jacob, S.; Oelze, M.-L.; Laxa, M.; Tognetti, V.; Nunes de Miranda, S.M.; Baier, M.; Finkemeier, I. The function of peroxiredoxins in plant organelle redox metabolism. *J. Exp. Bot.* **2006**, *57*, 1697–1709. [[CrossRef](#)]
52. Pandya-Kumar, N.; Shema, R.; Kumar, M.; Mayzlish-Gati, E.; Levy, D.; Zemach, H.; Belausov, E.; Winer, S.; Abu-Abied, M.; Kapulnik, Y.; et al. Strigolactone analog GR24 triggers changes in PIN2 polarity, vesicle trafficking and actin filament architecture. *New Phytol.* **2014**, *202*, 1184–1196. [[CrossRef](#)]
53. Diet, A.; Brunner, S.; Ringli, C. The *enl* mutants enhance the *lrx1* root hair mutant phenotype of *Arabidopsis thaliana*. *Plant Cell Physiol.* **2004**, *45*, 734–741. [[CrossRef](#)]
54. Kabsch, W.; Mannherz, H.G.; Suck, D.; Pai, E.F.; Holmes, K.C. Atomic structure of the actin: DNase-I complex. *Nature* **1990**, *347*, 37–44. [[CrossRef](#)] [[PubMed](#)]
55. Mouratou, B.; Biou, V.; Joubert, A.; Cohen, J.; Shields, D.J.; Geldner, N.; Jürgens, G.; Melançon, P.; Cherfils, J. The domain architecture of large guanine nucleotide exchange factors for the small GTP-binding protein Arf. *BMC Genom.* **2005**, *6*, 20. [[CrossRef](#)] [[PubMed](#)]
56. Wang, H.; Wang, S.; Lu, Y.; Alvarez, S.; Hicks, L.M.; Ge, X.; Xia, Y. Proteomic analysis of early-responsive redox-sensitive proteins in *Arabidopsis*. *J. Proteome Res.* **2012**, *11*, 412–424. [[CrossRef](#)]
57. Lian, N.; Wang, X.; Jing, Y.; Lin, J. Regulation of Cytoskeleton-associated Protein Activities: Linking Cellular Signals to Plant Cytoskeletal Function. *J. Integr. Plant Biol.* **2021**, *63*, 241–250. [[CrossRef](#)]
58. Matoušková, J.; Janda, M.; Fišer, R.; Šašek, V.; Kocourková, D.; Burketová, L.; Dušková, J.; Martinec, J.; Valentová, O. Changes in Actin Dynamics Are Involved in Salicylic Acid Signaling Pathway. *Plant Sci.* **2014**, *223*, 36–44. [[CrossRef](#)]
59. Takáč, T.; Bekešová, S.; Šamaj, J. Actin Depolymerization-Induced Changes in Proteome of *Arabidopsis* Roots. *J. Proteom.* **2017**, *153*, 89–99. [[CrossRef](#)] [[PubMed](#)]
60. Li, X.; Li, J.-H.; Wang, W.; Chen, N.-Z.; Ma, T.-S.; Xi, Y.-N.; Zhang, X.-L.; Lin, H.-F.; Bai, Y.; Huang, S.-J.; et al. ARP2/3 Complex-Mediated Actin Dynamics Is Required for Hydrogen Peroxide-Induced Stomatal Closure in *Arabidopsis*: H<sub>2</sub>O<sub>2</sub> and Actin Dynamics in ABA Signalling. *Plant Cell Environ.* **2014**, *37*, 1548–1560. [[CrossRef](#)]
61. Li, J.; Cao, L.; Staiger, C.J. Capping Protein Modulates Actin Remodeling in Response to Reactive Oxygen Species during Plant Innate Immunity. *Plant Physiol.* **2017**, *173*, 1125–1136. [[CrossRef](#)]



62. Frémont, S.; Hammich, H.; Bai, J.; Wioland, H.; Klinkert, K.; Rocancourt, M.; Kikuti, C.; Stroebel, D.; Romet-Lemonne, G.; Pylypenko, O.; et al. Oxidation of F-Actin Controls the Terminal Steps of Cytokinesis. *Nat. Commun.* **2017**, *8*, 14528. [[CrossRef](#)] [[PubMed](#)]
63. Sakai, J.; Li, J.; Subramanian, K.K.; Mondal, S.; Bajrami, B.; Hattori, H.; Jia, Y.; Dickinson, B.C.; Zhong, J.; Ye, K.; et al. Reactive Oxygen Species-Induced Actin Glutathionylation Controls Actin Dynamics in Neutrophils. *Immunity* **2012**, *37*, 1037–1049. [[CrossRef](#)]
64. Mustafa, A.K.; Gadalla, M.M.; Sen, N.; Kim, S.; Mu, W.; Gazi, S.K.; Barrow, R.K.; Yang, G.; Wang, R.; Snyder, S.H. H<sub>2</sub>S Signals Through Protein S-Sulfhydration. *Sci. Signal.* **2009**, *2*, ra72. [[CrossRef](#)] [[PubMed](#)]
65. Stojkov, D.; Amini, P.; Oberson, K.; Sokollik, C.; Duppenhaller, A.; Simon, H.-U.; Yousefi, S. ROS and Glutathionylation Balance Cytoskeletal Dynamics in Neutrophil Extracellular Trap Formation. *J. Cell Biol.* **2017**, *216*, 4073–4090. [[CrossRef](#)] [[PubMed](#)]
66. Gellert, M.; Hanschmann, E.-M.; Lepka, K.; Berndt, C.; Lillig, C.H. Redox Regulation of Cytoskeletal Dynamics during Differentiation and De-Differentiation. *Biochim. Biophys. Acta (BBA) Gen. Subj.* **2015**, *1850*, 1575–1587. [[CrossRef](#)]
67. Mashima, T.; Naito, M.; Noguchi, K.; Miller, D.K.; Nicholson, D.W.; Tsuruo, T. Actin Cleavage by CPP-32/Apopain during the Development of Apoptosis. *Oncogene* **1997**, *14*, 1007–1012. [[CrossRef](#)]
68. Mashima, T.; Naito, M.; Tsuruo, T. Caspase-Mediated Cleavage of Cytoskeletal Actin Plays a Positive Role in the Process of Morphological Apoptosis. *Oncogene* **1999**, *18*, 2423–2430. [[CrossRef](#)] [[PubMed](#)]
69. Beemster, G.T.S.; De Vusser, K.; De Tavernier, E.; De Bock, K.; Inze, D. Variation in growth rate between Arabidopsis ecotypes is correlated with cell division and A-type cyclin-dependent kinase activity1. *Plant Physiol.* **2002**, *129*, 854–864. [[CrossRef](#)]
70. Voigt, B.; Timmers, A.C.J.; Šamaj, J.; Müller, J.; Baluška, F.; Menzel, D. GFP-FABD2 fusion construct allows in vivo visualization of the dynamic actin cytoskeleton in all cells of Arabidopsis seedlings. *Eur. J. Cell Biol.* **2005**, *84*, 595–608. [[CrossRef](#)]
71. Clough, S.J.; Bent, A.F. Floral dip: A simplified method for *Agrobacterium*-mediated transformation of *Arabidopsis thaliana*. *Plant J.* **1998**, *16*, 735–743. [[CrossRef](#)]
72. Ovečka, M.; Lang, I.; Baluška, F.; Ismail, A.; Illeš, P.; Lichtscheidl, I.K. Endocytosis and vesicle trafficking during tip growth of root hairs. *Protoplasma* **2005**, *226*, 39–54. [[CrossRef](#)]
73. Ramel, F.; Sulmon, C.; Bogard, M.; Couée, I.; Gouesbet, G. Differential patterns of reactive oxygen species and antioxidative mechanisms during atrazine injury and sucrose-induced tolerance in *Arabidopsis thaliana* plantlets. *BMC Plant Biol.* **2009**, *9*, 28. [[CrossRef](#)] [[PubMed](#)]
74. Daudi, A.; Cheng, Z.; O'Brien, J.A.; Mammarella, N.; Khan, S.; Ausubel, F.M.; Bolwell, G.P. The apoplastic oxidative burst peroxidase in Arabidopsis is a major component of pattern-triggered immunity. *Plant Cell* **2012**, *24*, 275–287. [[CrossRef](#)] [[PubMed](#)]
75. Takáč, T.; Šamajová, O.; Vadovič, P.; Pechan, T.; Košútová, P.; Ovečka, M.; Husičková, A.; Komis, G.; Šamaj, J. Proteomic and biochemical analyses show a functional network of proteins involved in antioxidant defense of the *Arabidopsis anp2anp3* double mutant. *J. Proteome Res.* **2014**, *13*, 5347–5361.
76. Yoshida, K.; Hisabori, T. Two Distinct Redox Cascades Cooperatively Regulate Chloroplast Functions and Sustain Plant Viability. *Proc. Natl. Acad. Sci. USA* **2016**, *113*, E3967–E3976. [[CrossRef](#)]
77. Takáč, T.; Šamajová, O.; Luptovčíak, I.; Pechan, T.; Šamaj, J. Feedback microtubule control and microtubule-actin cross-talk in *Arabidopsis* revealed by integrative proteomic and cell biology analysis of *KATANIN 1* mutants. *Mol. Cell. Proteom.* **2017**, *16*, 1591–1609. [[CrossRef](#)]
78. Larkindale, J.; Knight, M.R. Protection against heat stress-induced oxidative damage in Arabidopsis involves calcium, abscisic acid, ethylene, and salicylic acid. *Plant Physiol.* **2002**, *128*, 682–695. [[CrossRef](#)]
79. Pallotta, M.A.; Graham, R.D.; Langridge, P.; Sparrow, D.H.B.; Barker, S.J. RFLP mapping of manganese efficiency in barley. *Theor. Appl. Genet.* **2000**, *101*, 1100–1108. [[CrossRef](#)]

## 4.2.1 Supplements

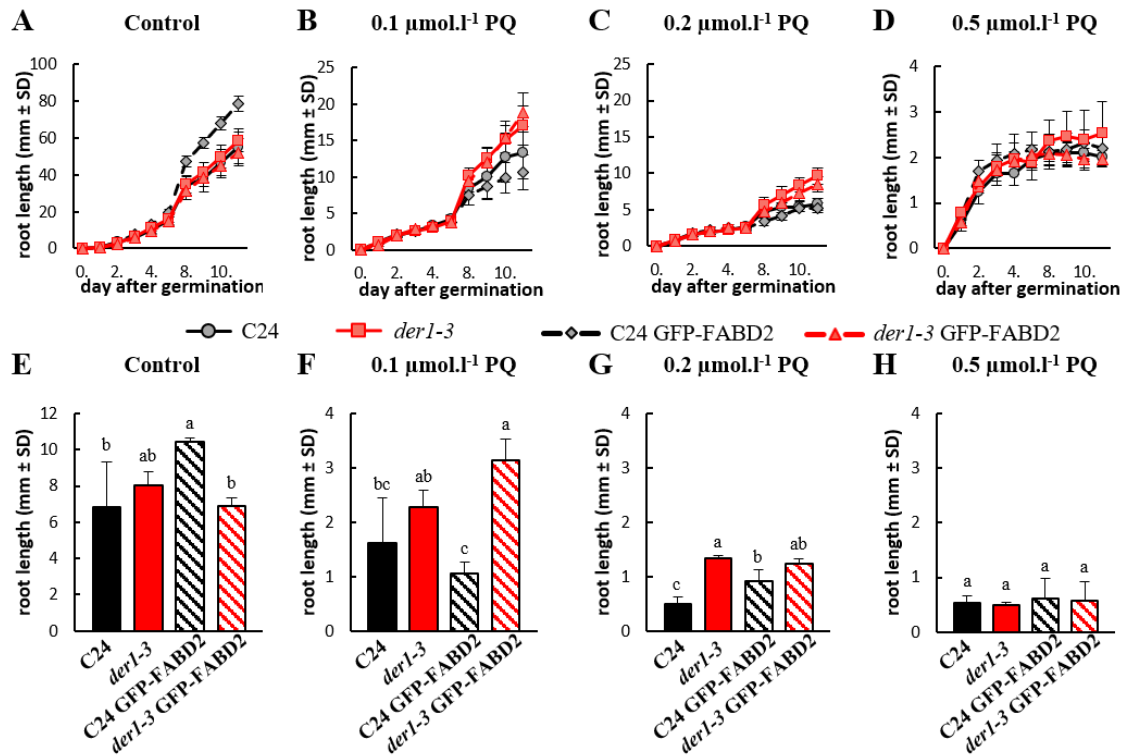


**Figure S1: Root growth rate in plants of control C24, *der1-3* mutant and transgenic C24 and *der1-3* lines under prolonged treatment with PQ.** Growth rate of the main root in plants of control C24, *der1-3* mutant, transgenic C24 line and *der1-3* line carrying GFP-FABD2 on control media (A) and on media containing 0.1 (B), 0.2 (C) and 0.5 (D)  $\mu\text{mol.l}^{-1}$  PQ within 11 days after germination. Average root growth per 24 h on the control media (E) and on media containing 0.1 (F), 0.2 (G) and 0.5 (H)  $\mu\text{mol.l}^{-1}$  PQ. N=15. Different lowercase letters above the bars (E-H) represent statistical significance according to one-way ANOVA and subsequent LSD test at p value < 0.05. Adapted from Kuběnová *et al.*, 2021.

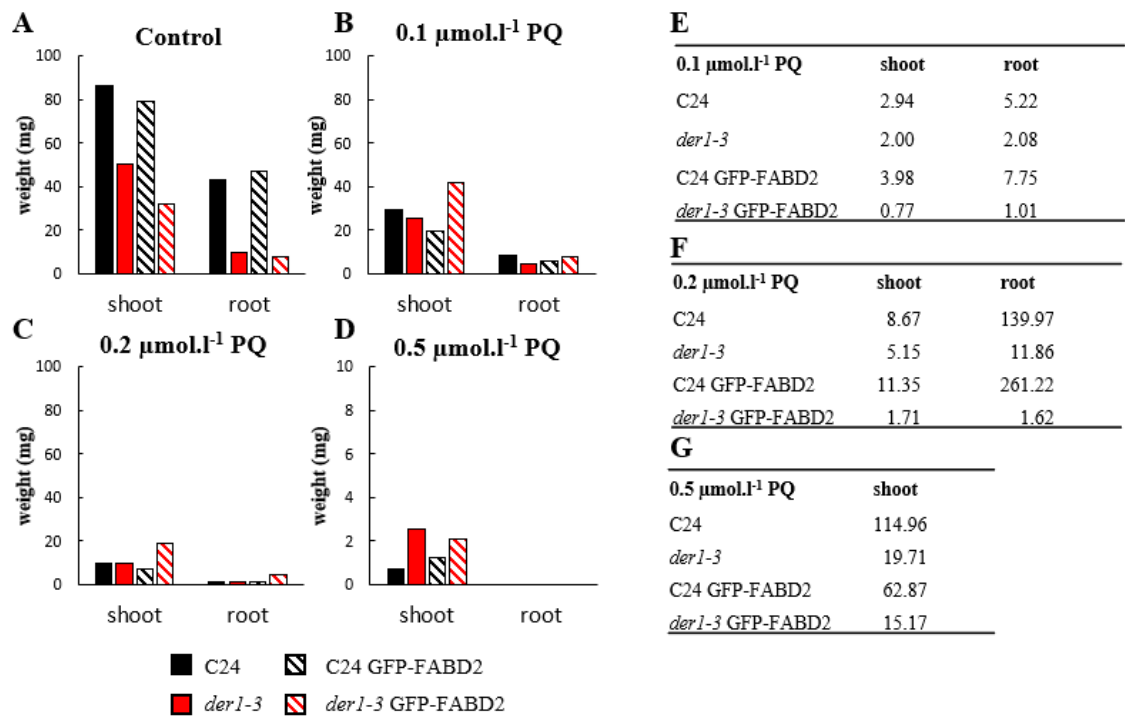


**Figure S2: Shoot and root fresh weight in plants of control C24, *der1-3* mutant and transgenic C24 and *der1-3* lines expressing *pro35S::GFP:FABD2* after germination and growth in PQ-containing media.** Fresh weight (pooled shoots and pooled roots, respectively) from plants of control C24, *der1-3* mutant, transgenic C24 line and *der1-3* line carrying GFP-FABD2 growing 18 days on control media (A) and on media containing 0.1 (B), 0.2 (C) and 0.5 (D)  $\mu\text{mol.l}^{-1}$  PQ. Reduction ratio (fold change in respect to control) of shoot and root fresh weight of respective lines growing on media containing 0.1 (E), 0.2 (F) and 0.5 (G)  $\mu\text{mol.l}^{-1}$  PQ. Experiments were repeated two times with 16 plants per line (control) and 12 plants per line (PQ). Adapted from Kuběnová *et al.*, 2021.

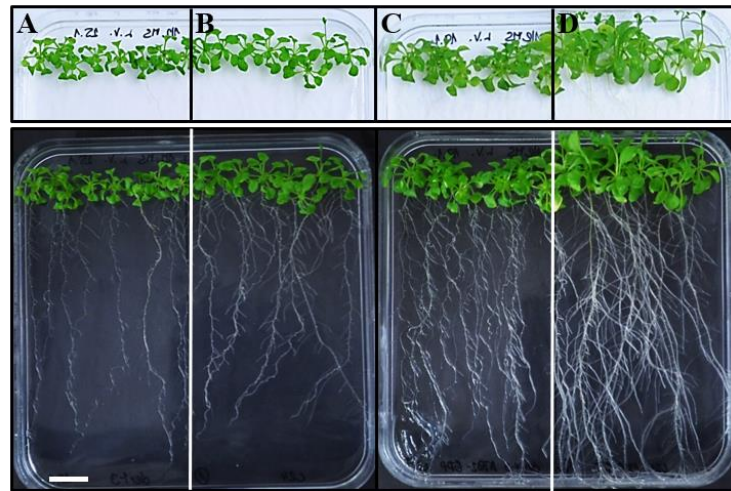


**Figure S3: Plant phenotype of control and transgenic C24 and *der1-3* mutant lines on control media.** Plants of *der1-3* mutant (A), control C24 (B), *der1-3* GFP-FABD2 line (C) and C24 GFP-FABD2 line (D). Aboveground parts of plants were photographed on white background (upper row of images), and whole plants including roots were documented on black background (lower row of images). Plants germinated and grown on control media for 20 days. Scale bar = 1 cm. Adapted from Kuběnová *et al.*, 2021.

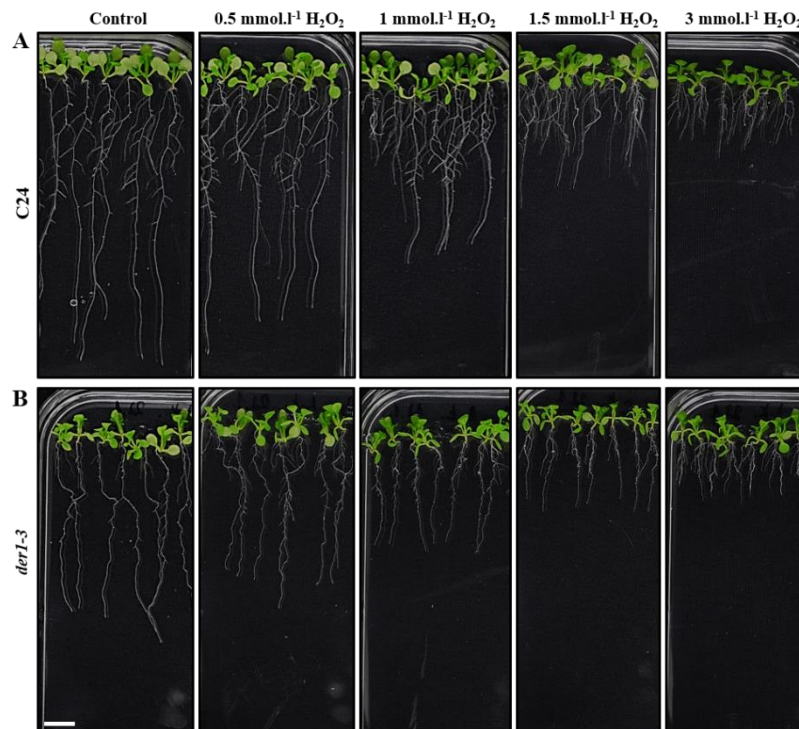


**Figure S4: Phenotype of control C24 and *der1-3* mutant plants after their transfer to H<sub>2</sub>O<sub>2</sub>-containing media.** Plants 3-days old germinated on control media were transferred to H<sub>2</sub>O<sub>2</sub>-containing media and photographed 8 days after transfer. (A-B) Plants of control C24 (A) and *der1-3* mutant (B) growing on media containing 0.5, 1, 1.5 and 3 mmol.l<sup>-1</sup> H<sub>2</sub>O<sub>2</sub>. Scale bar = 1 cm. Adapted from Kuběnová *et al.*, 2021.

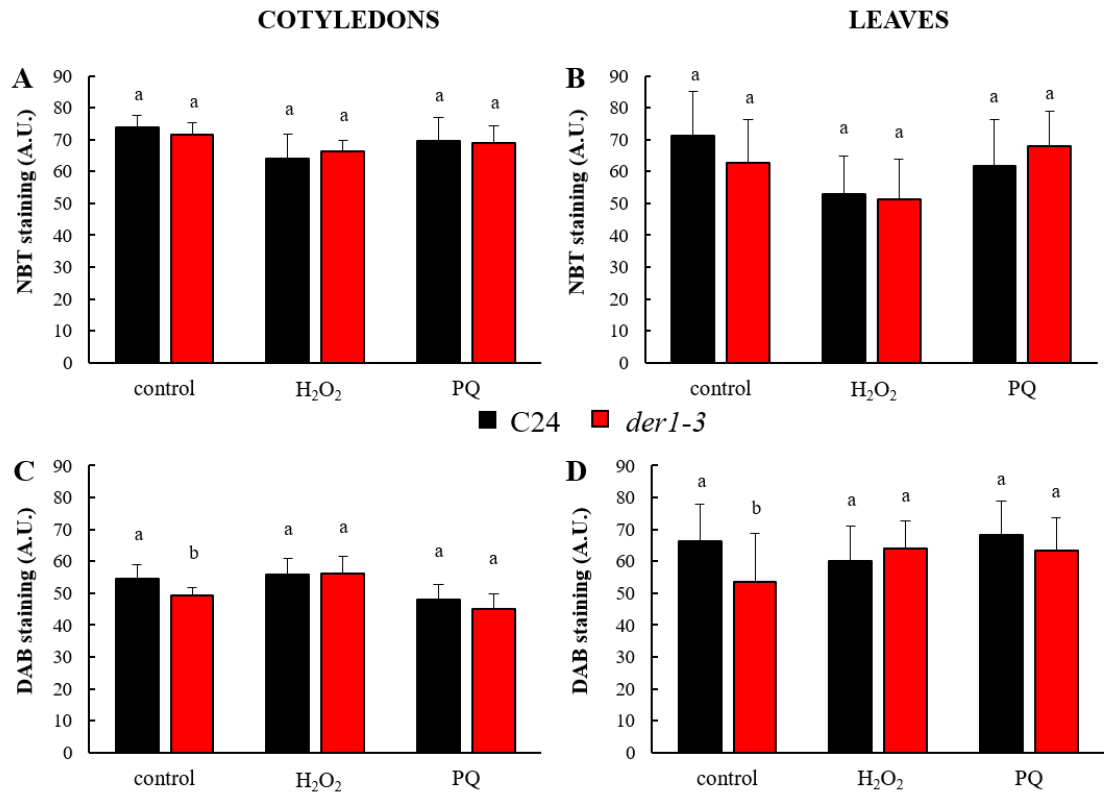


**Figure S5: Histochemical detection of  $O_2^{\cdot-}$  and  $H_2O_2$  production in cotyledons and leaves of control C24 and *der1-3* mutant plants after their transfer to PQ- and  $H_2O_2$ -containing media.** Plants 3-days old germinated on control media were transferred to PQ- and  $H_2O_2$ -containing media and analysed 11 days after transfer. Nitroblue tetrazolium (NBT) staining in cotyledons (A) and leaves (B). 3,3'-diaminobenzidine (DAB) staining in cotyledons (C) and leaves (D). Results are presented as mean intensity of the histochemical staining from plants transferred to media containing  $0.1 \mu\text{mol.l}^{-1}$  PQ and  $3 \text{mmol.l}^{-1}$   $H_2O_2$ . Adapted from Kuběnová *et al.*, 2021.

### **4.3 ROOT HAIR DEFECTIVE 2 vesicular delivery to the apical plasma membrane domain during Arabidopsis root hair development**

**Kuběnová L**, Tichá M, Šamaj J, Ovečka M (2022). ROOT HAIR DEFECTIVE 2 vesicular delivery to the apical plasma membrane domain during Arabidopsis root hair development. *Plant Physiology* 188: 1563-1585. doi: 10.1093/plphys/kiab595

**LK** performed the majority of experiments, namely preparation of stable transgenic plants by crossing, detailed microscopic analyses of compartments positive to GFP-RHD2, colocalization studies, quantitative evaluation of vesicle movements, filipin and auxinol treatments, processing and statistical evaluation of all microscopic and quantitative data. **LK** participated in writing the manuscript.

RHs are tubular extensions of epidermal cells called trichoblasts. RHs are important for increasing root surface area and efficiency of water and nutrient uptake. Arabidopsis RHs are excellent model for the study of polar tip growth. Gene *RHD2* (*ROOT HAIR DEFECTIVE2*) encodes NADPH oxidase AtRBOHC, which was localized in the apical part of the PM of growing RHs. The role of this NADPH oxidase in the tip of growing RHs is a production of ROS. Mutation in the *RHD2* gene leads to development of short RHs only that are lacking the gradients of ROS and Ca<sup>2+</sup> ions important for proper tip growth. However, the spatiotemporal subcellular redistribution and delivery to the PM in growing RHs are still unclear. Our detailed microscopic analyses using advanced microscopy methods revealed the localization pattern of GFP-RHD2 in bulges and tips of growing RHs. In this paper, we characterized distribution pattern of vesicular compartments containing GFP-RHD2 and their movements in developing bulges and growing RHs in transgenic plants where the fluorescence marker GFP-RHD2 was produced under the control of native promotor. The localization studies confirmed, that the distribution pattern of GFP-RHD2 was spatiotemporally related to the process of RH formation. The nature of compartments containing GFP-RHD2 was identified by colocalization studies with the selective membrane styryl dye (FM4-64) labelling early endosomal markers and with established fluorescent markers of early and late endosomal compartments. The colocalization results suggested that vesicular trafficking and targeted delivery of GFP-RHD2 during RH development seem to depend on early endosomal/TGN compartments. Next, quantitative particle tracking analysis characterizing movement parameters of GFP-RHD2 compartments allowed us to divide

them into the three independent groups. The first was a group of compartments moving to the apical PM and fusing with it. The second group consisted of compartments moving in the cytoplasm without any contact with the apical PM, and the third group contained compartments moving to and contacting the PM, but subsequently moving back to the cytoplasm. The tracking analysis provided quantitative data that showed different movement properties among compartments of three individual groups. In addition, the differences were also related to individual stages of RHs growth. Quantitative tracking analysis has also proven that movement of TGN/early endosomes, but not late endosomes, was more affected in the bulging domains of the *rh2-1* mutant. Finally, using specific filipin III labelling, we revealed that structural sterols might be involved in the accumulation, docking, and proper incorporation of TGN compartments containing GFP-RHD2 to the apical PM in growing RHs. Obtained results clarified the pattern of polarized AtRBOHC/RHD2 movement, targeting, maintenance, and recycling at the apical PM domain, and helped to better understanding how this pattern could be coordinated with different developmental stages of RH initiation and growth in Arabidopsis.



## ROOT HAIR DEFECTIVE 2 vesicular delivery to the apical plasma membrane domain during *Arabidopsis* root hair development

Lenka Kuběnová,<sup>1</sup> Michaela Tichá ,<sup>1</sup> Jozef Šamaj ,<sup>1</sup> and Miroslav Ovečka  <sup>1,\*†</sup>

<sup>1</sup> Department of Cell Biology, Centre of the Region Haná for Biotechnological and Agricultural Research, Faculty of Science, Palacký University Olomouc, Šlechtitelů 27, 783 71 Olomouc, Czech Republic

\*Author for communication: miroslav.ovecka@upol.cz

†Senior author

L.K. and M.T. performed experiments, M.O. evaluated data, L.K. and M.O. wrote the manuscript, and J.Š. edited the manuscript and provided infrastructure and funding.

The author responsible for distributing materials integral to the findings presented in this article according to the policy described in the Instructions for Authors (<https://academic.oup.com/plphys/pages/general-instructions>) is: Miroslav Ovečka (miroslav.ovecka@upol.cz).

### Abstract

*Arabidopsis* (*Arabidopsis thaliana*) root hairs develop as long tubular extensions from the rootward pole of trichoblasts and exert polarized tip growth. The establishment and maintenance of root hair polarity is a complex process involving the local apical production of reactive oxygen species generated by *A. thaliana* nicotinamide adenine dinucleotide phosphate (NADPH) oxidase respiratory burst oxidase homolog protein C/ROOT HAIR-DEFECTIVE 2 (AtRBOHC/RHD2). Loss-of-function *root hair defective 2* (*rhd2*) mutants have short root hairs that are unable to elongate by tip growth, and this phenotype is fully complemented by GREEN FLUORESCENT PROTEIN (GFP)-RHD2 expressed under the *RHD2* promoter. However, the spatiotemporal mechanism of AtRBOHC/RHD2 subcellular redistribution and delivery to the plasma membrane (PM) during root hair initiation and tip growth are still unclear. Here, we used advanced microscopy for detailed qualitative and quantitative analysis of vesicular compartments containing GFP-RHD2 and characterization of their movements in developing bulges and growing root hairs. These compartments, identified by an independent molecular marker mCherry-VTI12 as the trans-Golgi network (TGN), deliver GFP-RHD2 to the apical PM domain, the extent of which corresponds with the stage of root hair formation. Movements of TGN/early endosomes, but not late endosomes, were affected in the bulging domains of the *rhd2-1* mutant. Finally, we revealed that structural sterols might be involved in the accumulation, docking, and incorporation of TGN compartments containing GFP-RHD2 to the apical PM of root hairs. These results help in clarifying the mechanism of polarized AtRBOHC/RHD2 targeting, maintenance, and recycling at the apical PM domain, coordinated with different developmental stages of root hair initiation and growth.

### Introduction

Root hairs are specialized lateral tubular extensions of root epidermal cells called trichoblasts. Although their presence is dispensable for plant survival, they considerably increase root surface area, and are involved in effective water and

nutrient uptake, which is important for sustained plant growth. Moreover, root hairs represent an excellent and easily accessible model of polar cell expansion in plants because of their position at the root surface, simple structure, and fast growth. Root hair development starts with bulging at

Received September 13, 2021. Accepted November 26, 2021. Advance access publication January 5, 2022

© The Author(s) 2022. Published by Oxford University Press on behalf of American Society of Plant Biologists.

This is an Open Access article distributed under the terms of the Creative Commons Attribution-NonCommercial-NoDerivs licence (<https://creativecommons.org/licenses/by-nc-nd/4.0/>), which permits non-commercial reproduction and distribution of the work, in any medium, provided the original work is not altered or transformed in any way, and that the work is properly cited. For commercial re-use, please contact [journals.permissions@oup.com](mailto:journals.permissions@oup.com)

Open Access



the outer tangential cell wall/plasma membrane (PM) domain in the rootward pole of the trichoblasts, followed by a subsequent transition to tip growth, which is polar expansion at the tip, ensuring the formation of long tubular root hair (Carol and Dolan, 2002; Grierson and Schiefelbein, 2002).

Root hair tip growth is caused by the establishment and maintenance of cellular polarity since it requires polarization of the cytoskeleton, membrane trafficking, and localized cell wall deposition (Samaj et al., 2006). A tip-focused gradient of calcium ( $\text{Ca}^{2+}$ ) ions also plays a substantial role in all tip-growing cells, including root hairs. Hyperpolarization-activated cation channels maintain an increase in cytosolic  $\text{Ca}^{2+}$  concentration in the growing tip, transporting apoplastic  $\text{Ca}^{2+}$  ions inwardly across the PM (Kiegle et al., 2000; Véry and Davies, 2000; Miedema et al., 2001). This tip-focused cytosolic  $\text{Ca}^{2+}$  gradient is established upon root hair tip growth initiation and persists until its cessation (Dolan et al., 1994; Wymer et al., 1997; Foreman et al., 2003). Other components of the tip growth mechanism are reactive oxygen species (ROS), which are recognized by  $\text{Ca}^{2+}$  channels and gate their opening. These ROS are generated by the NADPH oxidase RESPIRATORY BURST OXIDASE HOMOLOG PROTEIN C (RBOHC), which is encoded by the *RBOHC/ROOT HAIR DEFECTIVE 2 (RHD2)* locus in *Arabidopsis thaliana* (Foreman et al., 2003). The genome of *A. thaliana* encodes 10 different RBOH members (RBOHA to RBOHJ; Torres et al., 2002; Sagi and Fluhr, 2006). Nevertheless, among all RBOH family members, only *AtRBOHC/RHD2* is required to regulate the early stages of root hair tip growth. Mutations in *RBOHH* and *RBOHJ* lead to defects in root hair elongation (Mangano et al., 2017). Although the root hairs of these mutants were shorter than those of the wild-type, they were considerably longer compared to loss-of-function mutants in *RBOHC*. Moreover, the most substantial defects in *rboh* and *rboh* mutants are caused by disturbed pollen tube elongation, leading to reduced mutant fertility (Kaya et al., 2019; Zhou et al., 2020).

*RHD2* transcription is activated in cells of the root epidermis of diverse root zones from the proximal meristem to the elongation zone (Foreman et al., 2003). Loss-of-function mutations in the *AtRBOHC/RHD2* locus in *rh**d2* mutants resulted in short root hairs with missing tip-focused ROS and  $\text{Ca}^{2+}$  gradients (Schiefelbein and Somerville, 1990; Foreman et al., 2003). Importantly, root hair tip growth of *rh**d2-1* mutant can be partly restored by external applications of ROS or by pH alkalization that reinstates the PM activity of  $\text{Ca}^{2+}$  channels (Monshausen et al., 2007). This indicates positive feedback between apical localization and activity of *RHD2*, ROS, and  $\text{Ca}^{2+}$  gradients, controlling root hair development (Foreman et al., 2003; Carol et al., 2005). A fully complemented phenotype of *rh**d2* mutants with rescued root hair development has been achieved after transformation with GREEN FLUORESCENT PROTEIN (GFP)-tagged functional *AtRBOHC (GFP-RHD2)* under the control of its native promoter (Takeda et al., 2008). Tissue- and cell-

specific localization studies revealed that GFP-RHD2 signals, particularly in trichoblasts, accumulate in the bulges and apices of growing root hairs (Takeda et al., 2008).

Root hair growth and development are supported by dynamic vesicular trafficking. The apical zone of growing root hairs is enriched with secretory and endocytic/recycling vesicles, balancing macromolecule supply, retrieval, and recycling (Cole and Fowler, 2006; Samaj et al., 2006; Campanoni and Blatt, 2007). Endosomal compartments represent endomembrane trafficking hubs categorized into early endosomes/trans-Golgi networks (TGNs) and late endosomes/multivesicular bodies (Reyes et al., 2011). Furthermore, early endosomal/TGN compartments merge secretory and endocytic pathways (Viotti et al., 2010; Contento and Bassham, 2012; Qi and Zheng, 2013), and late endosomes/multivesicular bodies are involved in transport pathways toward vacuoles (Bottanelli et al., 2011; Contento and Bassham, 2012). Rab guanosine triphosphatases (GTPases) in the clear zone of root hairs spatiotemporally organize vesicular trafficking, exocytosis, endocytosis, and membrane recycling (Voigt et al., 2005; Berson et al., 2014).

FM dyes allow the fluorescence labeling of PM, highly dynamic populations of early, recycling, and late endosomes in root hairs (Ovečka et al., 2005). Detailed analysis and characterization of distinct endosomal compartments have been achieved using protein markers translationally fused to fluorescent proteins; early endosomal/TGN compartments were specifically detected by Rab GTPase Homolog A1d (RabA1d) and Vesicle transport v-SNARE 12 (VT112), a Soluble N-ethylmaleimide-sensitive fusion protein Attachment protein REceptor (SNARE) protein (Sanderfoot et al., 2001; Uemura et al., 2004; Ovečka et al., 2010; Berson et al., 2014). A molecular marker based on the FYVE domain (a zinc finger domain named according to the four cysteine-rich proteins: Fab 1, yeast ortholog of PIKfyve, YOTB, Vac 1, vesicle transport protein, and EEA1, in which it has been found), specifically binding to phosphoinositol-3-phosphate, was used to detect late endosomes (Gillooly et al., 2001; Voigt et al., 2005). Members of the Rab-GTPase family, including RabF2a, RabF1 (Ueda et al., 2004; Voigt et al., 2005; Haas et al., 2007), and RabF2b (Geldner et al., 2009), have been verified as markers for late endosomal compartments and eventually colocalize with FYVE. The dynamic properties of early and late endosomes using molecular markers have been described in the growing root hairs of *Arabidopsis* (von Wangenheim et al., 2016).

Structural sterols modulate the permeability and fluidity of plant membranes and influence the physical and physiological properties of membrane proteins (Mukherjee and Maxfield, 2000; Clouse, 2002). They play important roles in vesicle trafficking and docking, signaling, and protein localization in membranes (Lindsey et al., 2003), particularly in root hairs (Ovečka et al., 2010) and pollen tubes (Liu et al., 2009). Sterols interact with phospholipids and create macromolecular nanodomains in the extracellular leaflet of the PM, so-called "lipid rafts" (Simons and Toomre, 2000).

Lipid rafts are involved in perceiving and transduction of signals associated with membrane receptors, selecting endocytic cargo molecules, and intracellular redistribution of sterols (Menon, 2002). Proteomic studies identified NADPH oxidases NtRBOHD, StRBOHB, and AtRBOHB with other PM proteins enriched in the detergent-resistant membrane fraction of suspension cells (Morel et al., 2006; Srivastava et al., 2013). Subcellular visualization revealed AtRBOHD localization to dynamic spots at the PM and its endocytosis induced by salt stress (Hao et al., 2014). Nevertheless, the spatiotemporal relationship between local arrangements of structural sterols and integral PM proteins such as AtRBOHC/RHD2 during root hair development is still unclear.

This study examined the qualitative and quantitative localization patterns of GFP-RHD2 during root hair formation in *Arabidopsis* using advanced microscopy methods. We revealed that incorporating GFP-RHD2 into the apical and subapical PM domains tightly corresponded with the establishment of the apical zone in bulges and growing root hairs. We documented the delivery of GFP-RHD2 to the apical zone during bulge formation and the apex of growing root hairs by dynamic vesicular compartments. These were identified as early endosomal/TGN compartments using colocalization analyses with reliable endosomal molecular markers. Single-particle tracking analysis revealed complex movement patterns of vesicular compartments containing GFP-RHD2 and identified their interactions with the apical PM during root hair formation. In addition, we revealed the possible involvement of structural sterols in the accumulation, docking, and incorporation of GFP-RHD2 vesicles at the apical PM domain of root hairs. Consequently, the genetic approach showed that early endosomal/TGN compartments were more seriously affected in their movements than late endosomes in the *rh2-1* mutant. This quantitative advanced microscopy study demonstrated the complex nature of GFP-RHD2 delivery, maintenance, and recycling at the apical PM, during root hair formation in *Arabidopsis*.

## Results

### Cell type-specific and subcellular distribution patterns of GFP-RHD2 in *Arabidopsis* root

Light-sheet fluorescence microscopy (LSFM) provided visualization for developmentally regulated and cell type-specific distribution patterns of GFP-RHD2 in growing *Arabidopsis* roots. The GFP-RHD2 signal was observed in epidermal cells in root hair formation zone, and was explicitly accumulated in the bulges and apices of developing root hairs (Figure 1A). Orthogonal projections from different root developmental zones confirmed GFP-RHD2 localization in the root epidermis, preferably in trichoblasts within the root differentiation and elongation zone (Figure 1B). Specifically, GFP-RHD2 accumulated at the tips of emerging (Figure 1, A and C) and growing (Figure 1, A and D) root hairs. This distribution and accumulation pattern of GFP-RHD2 was confirmed by a pseudo-color-coded, semi-quantitative

fluorescence intensity evaluation for maximum intensity projections of the whole root apex (Figure 1A; Supplemental Movie S1) and orthogonal projections of different root developmental zones (Figure 1, B–D). Advanced cellular and sub-cellular localization of GFP-RHD2 using Airyscan confocal laser scanning microscopy (CLSM) revealed a differential abundance of GFP-RHD2 in

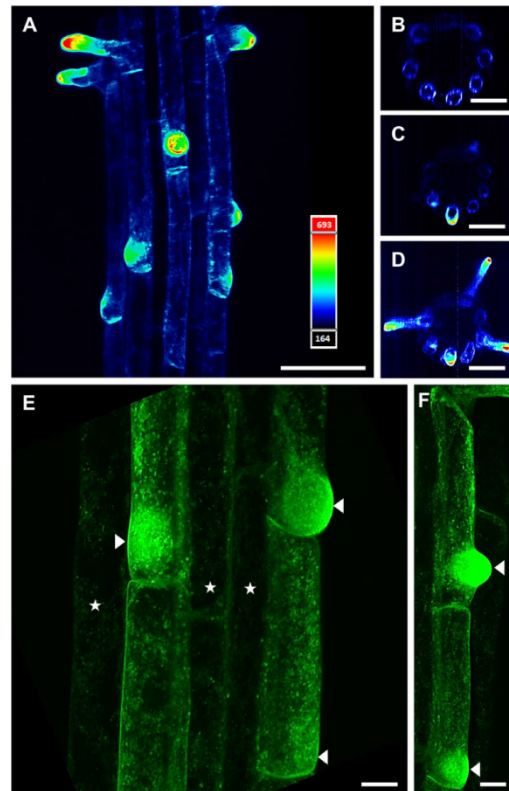


**Figure 1** Expression pattern and cell type-specific distribution of GFP-RHD2 in growing *Arabidopsis* root. A–D, Distribution pattern in root hair formation zone (A), where GFP-RHD2 was expressed mainly in trichoblasts (B) and accumulated at tips of emerging (C) and growing (D) root hairs. Maximum intensity projection of the root hair formation zone (A) and orthogonal projections at different developmental root zones (B–D) from LSFM imaging as visualized using semi-quantitative fluorescence intensity distribution and pseudo-color-coded scale, where dark blue represents minimal intensity (164 arbitrary units) and pale red represents maximum intensity (693 arbitrary units). Spatial overview of the maximum intensity projection from the root hair formation zone (A) is presented in Supplemental Movie S1. E and F, Detailed visualization of subcellular compartments containing GFP-RHD2 in trichoblasts and their progressive accumulation in developing bulges (arrowheads) using Airyscan CLSM. A substantially lower number of compartments with GFP-RHD2 was detected in atrichoblasts (asterisks). Scale bar = 50  $\mu\text{m}$  (A), 40  $\mu\text{m}$  (B–D), 10  $\mu\text{m}$  (E and F).

trichoblasts and atrichoblasts (Figure 1E) as well as specific enrichment in bulge selection sites and developing bulges of trichoblasts (Figure 1, E and F). Most importantly, Airyscan CLSM imaging revealed GFP-RHD2 presence in small motile compartments in the cytoplasm (Figure 1, E and F). Their number was considerably higher in trichoblasts (Figure 1E), and there was an apparent progressive accumulation in developing bulges (arrowhead in Figure 1, E and F). In addition to the visualization of GFP-RHD2 in small compartments in the cytoplasm, Airyscan CLSM revealed localization in the PM, particularly at bulging sites and apical domains of developing bulges (Figure 1, E and F).

We used time-lapse imaging of dynamic GFP-RHD2 localization and targeted accumulation during root hair formation to present the whole dynamic process in the form of a video. The localization pattern of GFP-RHD2 can be related to the root hair growth rate, which is known to change in diverse root hair developmental stages. Time-lapse recording (Supplemental Movie S2) allowed identification of particular stages from early bulges (Stage I; Figure 2A) to late bulges (Stage II; Figure 2B) at the beginning, followed by stages of accelerated root hair tip growth. Subsequent developmental stages were represented by short root hairs (Stage III; Figure 2C), a transition from short to long root hairs (Stages III and IV; Figure 2D), and long root hairs (Stage IV; Figure 2E). The pattern of the tip growth rate over the entire process was quantitatively analyzed using kymographs. In the long-term time-lapse acquisition set up, which was based on recording every 5 min (Figure 2, A–E; Supplemental Movie S2), we recorded a slow extension in early bulges (Stage I) and a faster extension in late bulges (Stage II; Supplemental Figure S1, A and B), followed by fast, smooth, and continuous tip growth of short and long root hairs (Stages III and IV; Supplemental Figure S1 C–F). Nongrowing root hairs (Supplemental Figure S1G) were also identified using this method (Supplemental Figure S1H). The slow mode of the bulge extension versus the fast mode of the root hair extension and particularly sustained regular mode of tip growth in short and long root hair stages were revealed (Figure 2F). Sub-cellular time-lapse imaging of GFP-RHD2 distribution at different stages of root hair initiation showed polarized accumulation at the bulging sites and emerging bulges. GFP-RHD2-positive compartments were mainly enriched in the cortical cytoplasm of the bulging domain and selectively targeted to the apical PM of the emerging bulge (Figure 2G). Polarized accumulation of GFP-RHD2 at the apical PM was documented in the late bulges (Figure 2, H and I; Supplemental Movie S3), short (Figure 2, J and K; Supplemental Movie S4), and long (Figure 2, L and M; Supplemental Movie S5) growing root hairs. GFP-RHD2 at the apical PM was also temporarily maintained in growth-terminating root hairs (Figure 2, N and O; Supplemental Movie S6). Importantly, GFP-RHD2 was present in the cortical cytoplasm of developing bulges (Figure 2, H and I; Supplemental Movie S3) and accumulated in the apical, vesicle-rich “clear” zone of tip-growing

root hairs (Figure 2, J–M; Supplemental Movies S4 and S5). Thus, GFP-RHD2 accumulation in PM was detected only in specific domains of the trichoblast, bulging out of the parental outer tangential PM during bulge formation (Figure 2, A and B) and in the apex of growing root hairs (Figure 2, C–E; Supplemental Movie S2). Live cell imaging revealed the presence of GFP-RHD2 in small compartments of the cortical cytoplasm (Figure 2G) and targeted GFP-RHD2 accumulation in the apical PM. Visualization of GFP-RHD2 distribution in growing root hairs, both at early (Figure 2, J and K) and later (Figure 2, L and M) stages, showed an accumulation of GFP-RHD2 in the apical PM, and in compartments in the clear zone, and subapical cytoplasm. Similarly, the PM specifically accumulated GFP-RHD2 only within the apical and subapical zones of root hairs (Figure 2, J–M; Supplemental Figure S1, C and E).

Localization analysis showed a different range of GFP-RHD2 specific targeting to the apical PM domain at distinct stages of root hair development. Therefore, we analyzed the range of PM decorated with GFP-RHD2 (Figure 3A). A quantitative evaluation revealed that the extent of the PM zone containing GFP-RHD2 increased progressively from early to late bulges. This zone was enlarged in short growing root hairs and reached a maximum in longer growing root hairs but declined considerably in nongrowing root hairs (Figure 3B). Thus, the distribution pattern of GFP-RHD2 at the apical PM was tightly associated with the individual developmental stages of root hairs (Figure 3, A and B). The GFP-RHD2 fluorescence signal intensity distribution further corroborated this finding. Visualization using the semi-quantitative 2.5-D rendering function demonstrated a gradual increase in GFP-RHD2 fluorescence signal intensity in successive root hair developmental stages, from the development of the early bulge up to fast-growing root hairs (Supplemental Figure S2).

Live cell imaging revealed targeted delivery of GFP-RHD2 in dynamic vesicular compartments to the cortical cytoplasm and apical PM of developing root hairs. Based on the nature of their movements, we determined three groups of vesicular compartments carrying GFP-RHD2. The first group was represented by compartments with targeted movement to the apical PM. The second group consisted of compartments moving in the cytoplasm without any contact with the apical PM. The third group of compartments moved toward the PM and subsequently moved back to the cytoplasm after making contact. The quantitative evaluation showed a high proportion of GFP-RHD2 vesicular compartments moving toward the apical PM. A low number of compartments moved without contact or moved back after contact with the PM in the early bulge stage (Figure 3C). However, this turned to a different pattern during root hair development. The proportions of compartments from the first group, with targeted movement to the apical PM, was relatively high in short- and longer growing root hairs, while the compartments from the third group, moving toward the PM and subsequently back to the cytoplasm after

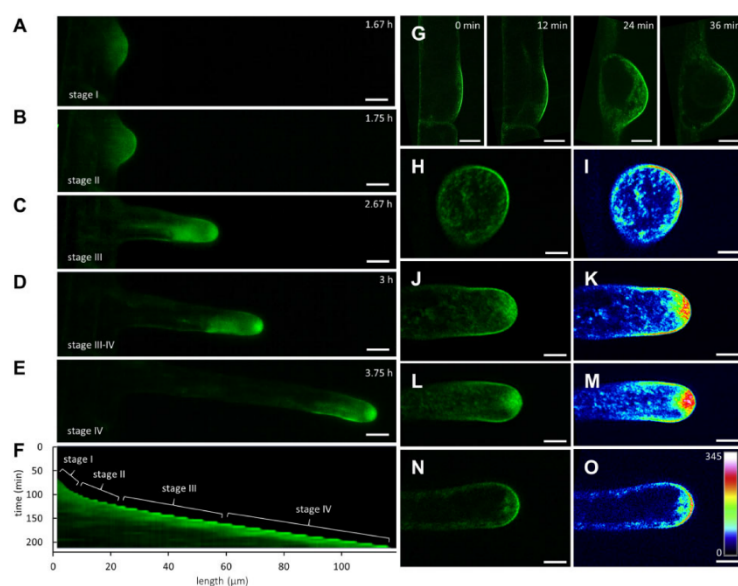


**Figure 2** Time-course imaging of GFP-RHD2 localization and accumulation during root hair formation. A–F, Localization pattern of GFP-RHD2 in different stages of root hair development and its relation to the particular root hair growth rate. Time-lapse recording of developing root hair showing stages of the early bulge (A; Stage I), late bulge (B; Stage II), short root hair (C; Stage III), the transition from short to long root hair (D; Stages III and IV), and long root hair (E; Stage IV). The whole process shown in [Supplemental Movie S2](#) is quantitatively presented in kymograph (F), representing the pattern and rate of the growth of this particular root hair, growing over the distance of 120  $\mu\text{m}$  within the time period of 220 min. Individual developmental stages presented in (A–E) are depicted in (F). G, Lateral view on the polarized accumulation of GFP-RHD2 at the PM domain and cortical cytoplasm of the bulging site and during the emerging of the bulge. H–O, The GFP-RHD2 distribution (H, J, L, and N) and a semi-quantitative signal intensity visualization using a pseudo-color-coded range (I, K, M, and O) of the polarized accumulation at the apical PM domain and cortical cytoplasm in the late bulge (H and I; [Supplemental Movie S3](#)), short (J and K; [Supplemental Movie S4](#)), and longer (L and M; [Supplemental Movie S5](#)) growing root hairs, and in nongrowing root hair (N and O; [Supplemental Movie S6](#)). The pseudo-color-coded scale ranges from dark blue representing minimal intensity (0 arbitrary units) to white representing maximum intensity (345 arbitrary units). Timing of the sequential imaging is indicated in hours (h) using light-sheet fluorescence microscopy (A–E) and in minutes (min) using Airyscan CLSM (G). Scale bar = 10  $\mu\text{m}$  (A–E), 5  $\mu\text{m}$  (G–O).

making contact, considerably increased ([Figure 3C](#)). With the cessation of tip growth, there was a considerable reduction in compartments moving to the apical PM ([Figure 3C](#)). This analysis showed that the extent of GFP-RHD2 specifically targeted to the apical PM corresponded with the stages of root hair formation. Importantly, this association was directly affected by the ratio between GFP-RHD2 vesicular compartments targeted to the apical PM and those moving back to the cytoplasm after contacting the PM.

#### Identification of GFP-RHD2-positive compartments

Next, we analyzed the nature of compartments containing GFP-RHD2 by colocalization with the selective membrane styryl dye FM4–64. In root hairs, the FM4–64 dye is able to stain the PM and early endocytotic/recycling vesicular compartments after a minute-long exposure period ([Ovečka et al., 2005](#)). After 10 min of application, FM4–64 colocalized with GFP-RHD2 at the PM and in motile vesicular compartments in the apical and subapical

zones of growing root hairs ([Figure 4A](#)). The colocalization at PM was semi-quantitatively documented by a cross-sectional fluorescence intensity profile measurement within the subapical zone of the root hair ([Figure 4B](#)). A high degree of colocalization in moving vesicular compartments within the subapical zone of growing root hairs ([Figure 4C](#)) was revealed by fluorescence intensity profile measurements ([Figure 4D](#)). Semi-quantitative measurement of fluorescence signal intensities of GFP-RHD2 and FM4–64 at the PM along the whole longitudinal root hair axis showed a stable level of FM4–64 fluorescence in the subapical and shank regions, but GFP-RHD2 fluorescence was specifically enriched only in the apical and subapical PM domains and gradually decreased in the shank region ([Figure 4E](#)). The quantitative colocalization analysis corroborated the results from semi-quantitative profile measurements showing a high degree of Pearson's correlation coefficients between FM4–64 and GFP-RHD2 in intracellular compartments ([Figure 4F](#); [Supplemental Figure S3, A and B](#)) and in the subapical PM ([Figure 4G](#);

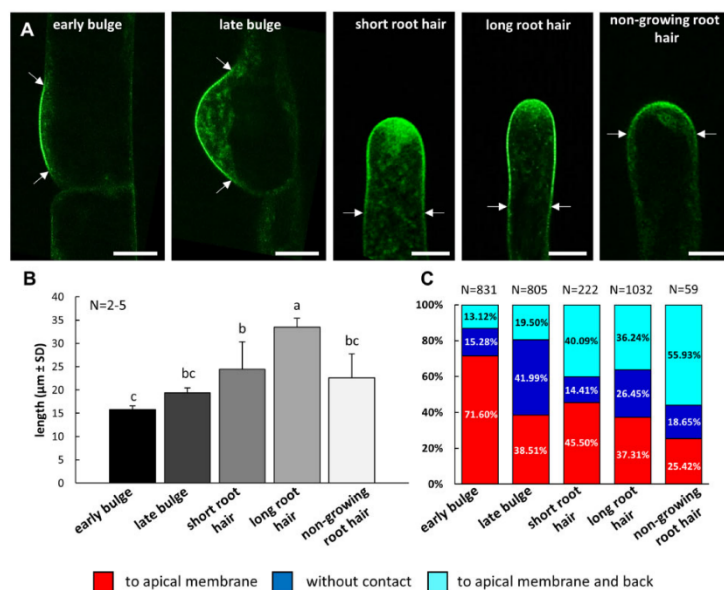


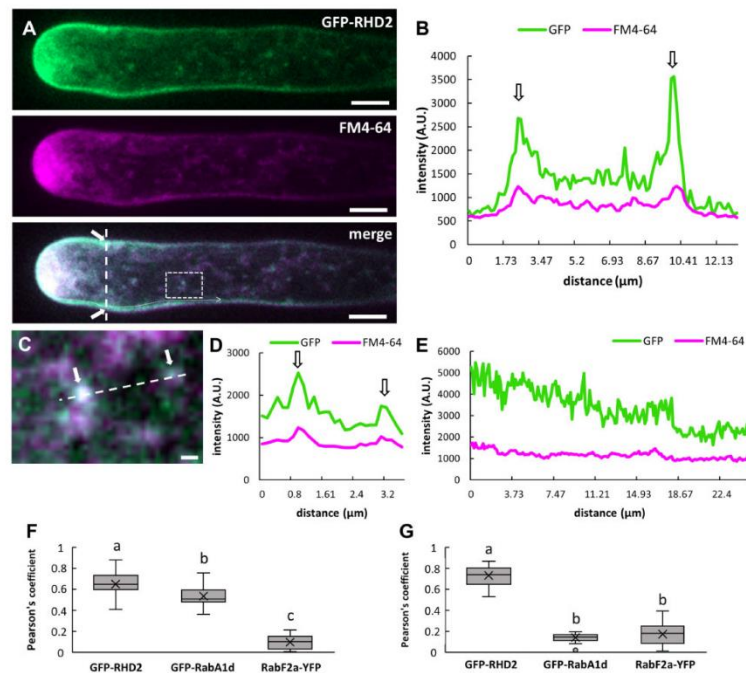
**Figure 3** Determination of GFP-RHD2 localization at the apical PM domain at different stages of root hair formation and growth. A, Delineation of the area (by two arrows) where GFP-RHD2 was specifically targeted to the apical PM domain at early and late bulging stage, in short and longer growing root hairs, and in nongrowing root hairs. B, Quantitative evaluation of the apical PM domain length decorated by GFP-RHD2 at different stages of root hair development. Measurement was done from 2 to 5 root hairs. Different lowercase letters indicate statistical significance between treatments according to one-way analysis of variance (ANOVA) and subsequent least significant difference (LSD) test ( $P < 0.05$ ). Error bars represent standard deviations. C, Quantitative determination of the ratio between the compartments containing GFP-RHD2 and showing targeted movement to the apical PM (red), moving in the cytoplasm without any contact with the apical PM (blue), or moving to and contacting the PM and subsequently moving back to the cytoplasm (cyan). The GFP-RHD2-positive compartments were tracked and analyzed at denoted stages of root hair development as depicted in (A). More than 59 compartments from 3 to 7 growing root hairs from individual plants were analyzed. Scale bar = 5 µm (A).

Supplemental Figure S3, C and D). This analysis suggests that vesicular compartments containing GFP-RHD2 might belong to the early endosome group.

Transgenic Arabidopsis line carrying GFP-RabA1d marker was used to visualize early endosomal/TGN compartments (Ovečka et al., 2010; Berson et al., 2014; von Wangenheim et al., 2016). Colocalization analysis of GFP-RabA1d with FM4-64 in growing root hairs revealed no overlap at the PM (Supplemental Figure S4, A and C). However, GFP-RabA1d colocalized with FM4-64 (applied for 10 min) in motile compartments (Supplemental Figure S4, E and F). This was corroborated by a quantitative colocalization analysis using Pearson's correlation coefficients, showing high values in intracellular compartments (Figure 4F; Supplemental Figure S5, A and B) and low values in the subapical PM (Figure 4G; Supplemental Figure S5, C and D). RabF2a-YFP is an appropriate marker of late endosomes (von Wangenheim et al., 2016) and colocalization analysis with FM4-64 (applied for 10 min) revealed no colocalization in growing root hairs both at the PM (Supplemental Figure S4, B and D) and in motile compartments (Supplemental Figure S4, G and H). Again, a quantitative colocalization analysis

using Pearson's correlation coefficients corroborated this observation, showing very low values both in intracellular compartments (Figure 4F; Supplemental Figure S6, A and B) and in the subapical PM (Figure 4G; Supplemental Figure S6, C and D).

Colocalization analysis using FM4-64 suggested that vesicular compartments delivering GFP-RHD2 toward the apical PM in growing root hairs are likely early endosomes/TGN. To confirm this suggestion, we prepared double transgenic lines carrying GFP-RHD2 together with the early endosomal/TGN marker, mCherry-VTI12, or with the late endosomal marker, mCherry-RabF2b. Markers mCherry-VTI12 and mCherry-RabF2b were not detected in the PM of growing root hairs (Supplemental Figure S7). Therefore, these two markers did not colocalize with GFP-RHD2 at the PM (Figure 5, A–D and J; Supplemental Figures S8, C and D and S9, C and D). However, the early endosomal/TGN marker mCherry-VTI12 showed colocalization with GFP-RHD2 in motile compartments (Figure 5, A and E); this was confirmed by fluorescence intensity profile quantification (Figure 5F) and a quantitative colocalization analysis using Pearson's correlation coefficients (Figure 5I; Supplemental



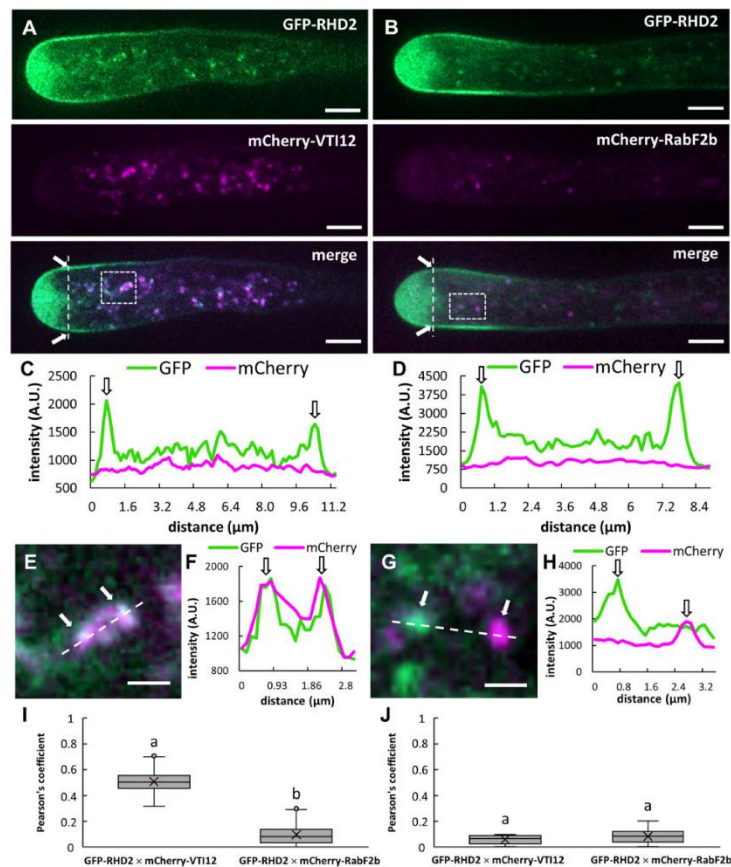
**Figure 4** Colocalization analysis of GFP-RHD2 with selective membrane styryl dye FM4-64 in growing root hairs. A, Localization pattern of GFP-RHD2 (green) in the apical PM domain, the cytoplasm of the apical and subapical zone, and in motile compartments of growing root hair co-labeled with membrane styryl dye FM4-64 (magenta). Colocalization analysis has been performed in the merged image along the cross-section profile marked by an interrupted white line (white arrows indicate the PM), in compartments within the white box, and along the white dotted line. B, Fluorescence intensity profile of the GFP and FM4-64 signal measured along the cross-section interrupted white line in (A). Arrows indicate the position of the PM. C, Detailed image of compartments containing GFP-RHD2 and FM4-64 within the white box depicted in (A). Arrows indicate the position of the compartments and the interrupted white line depicts the profile for fluorescence intensity quantification. D, Fluorescence intensity profile of the GFP and FM4-64 signal along the interrupted white line in (C). Arrows indicate the position of the compartments. E, Fluctuation of the GFP and FM4-64 fluorescence signal intensity at the PM along the longitudinal root hair axis from apex to the shank region measured along the white dotted line in (A). Note the stable level of FM4-64 fluorescence signal intensity at the PM in the subapical and shank region, while GFP-RHD2 fluorescence signal intensity was specifically enriched in the apical and subapical PM domains and gradually decreased within the shank region. F and G, Quantitative colocalization analysis using Pearson's correlation coefficients between FM4-64 and GFP-RHD2, early endosomal marker GFP-RabA1d (Supplemental Figure S4A), and late endosomal marker RabF2a-YFP (Supplemental Figure S4B) in intracellular compartments (F), and in subapical PM (G). Three independent ROIs from five individual root hairs at 5 different time points were selected, providing 75 measured vesicular compartments in total from each analyzed time point. Analogously, 25 measurements of PM in total from each time point originating from 5 individual root hairs were analyzed. Box plots display the first and third quartiles, split by the median; the crosses indicate the mean values; whiskers extend to include the max/min values. Different lowercase letters indicate statistical significance between lines according to one-way ANOVA and subsequent LSD test ( $P < 0.05$ ). Selections of ROIs and scatterplots of measurements are presented in Supplemental Figures S3, S5, and S6. Scale bar = 5  $\mu\text{m}$  (A), 1  $\mu\text{m}$  (C).

Figure S8, A and B). Topological colocalization analysis (Figure 5B), fluorescence intensity profile quantification (Figure 5, G and H), and quantitative colocalization analysis using Pearson's correlation coefficients (Figure 5I; Supplemental Figure S9, A and B) suggested no colocalization between GFP-RHD2 and mCherry-RabF2b, which represents marker for late endosomal compartments. Concluding from colocalization results with FM4-64 and endosomal markers, vesicular trafficking and targeted delivery of GFP-

RHD2 during root hair development seem to depend on early endosomal/TGN compartments.

#### Quantitative microscopic analysis of motile compartments containing GFP-RHD2 at different stages of root hair development

Live cell imaging of developing root hairs by advanced microscopy enabled the qualitative determination of



**Figure 5** Colocalization analysis of GFP-RHD2 with early and late endosomal markers in growing root hairs. A, Distribution of GFP-RHD2 in the apical PM domain, the clear zone, the cytoplasm of the subapical zone, and in moving compartments of growing root hair of Arabidopsis double transgenic line carrying both GFP-RHD2 (green) and the early endosomal/TGN marker mCherry-VTI12 (magenta). B, Distribution of GFP-RHD2 in the apical PM domain, the clear zone, the cytoplasm of the subapical zone, and in moving compartments of growing root hair of Arabidopsis double transgenic line bearing both GFP-RHD2 (green) and the late endosomal marker mCherry-RabF2b (magenta). In merged images of (A) and (B), an extent of fluorescence intensity colocalization has been analyzed along the cross-section profiles marked by interrupted white lines (white arrows indicate the PM) and in moving compartments within the white boxes. C, Fluorescence intensity profiles of GFP and mCherry signals along the cross-section interrupted the white line of the root hair shown in (A). D, Fluorescence intensity profiles of the GFP and mCherry signals along the cross-section interrupted the white line of the root hair shown in (B). Arrows in (C) and (D) indicate the position of the PM. E, Detailed image of compartments containing GFP-RHD2 and mCherry-VTI12 within the white box in (A). F, Fluorescence intensity profile of the GFP and mCherry-VTI12 signal along the interrupted white line in (E). G, Detailed image of compartments positive to GFP-RHD2 and mCherry-RabF2b within the white box in (B). H, Fluorescence intensity profile of the GFP and mCherry-RabF2b signal along the interrupted white line in (G). Arrows indicate the position of the compartments. I and J, Quantitative colocalization analysis using Pearson's correlation coefficients between GFP-RHD2 and the early endosomal/TGN marker mCherry-VTI12, and between GFP-RHD2 and the late endosomal marker mCherry-RabF2b, in intracellular compartments (I), and in the subapical PM (J). Three independent ROIs from five individual root hairs at five different time points were selected, providing 75 measured vesicular compartments in total per line from each analyzed time point. Analogously, 25 measurements of PM in total per line from each time point originating from five individual root hairs were analyzed. Box plots display the first and third quartiles, split by the median; the crosses indicate the mean values; whiskers extend to include the maximum/minimum values. Different lowercase letters indicate statistical significance between lines according to one-way ANOVA and subsequent LSD test ( $P < 0.05$ ). Selections of ROIs and scatter-plots of measurements are presented in [Supplemental Figures S8 and S9](#). Scale bar = 5 μm (A and B), 1 μm (E and G).

compartments containing GFP-RHD2. We analyzed the quantitative parameters of their movements in different stages of root hair formation using the particle-tracking method and characterized three independent groups of the GFP-RHD2 compartments. The first group was marked in red (compartments moving to the apical PM and fusing with it), the second group was marked in blue (compartments moving in the cytoplasm without any contact with the apical PM), and the third group was marked in cyan (compartments moving to and contacting the PM and subsequently moving back to the cytoplasm). Movement distances of GFP-RHD2 compartments during a 60 s period imaged by Airyscan CLSM were tracked using the “tracked cells function” of the ARIVIS Vision4D software. These trajectories were directly displayed in a color-coded mode in the image sequences of early (Figure 6A), and late (Figure 6C) bulges, as well as short (Figure 6E) and longer (Figure 6G) bulges, as well as short (Figure 6E) and longer

(Figure 6G) growing root hairs. In addition, the values of the maximum and the average speed of movement were analyzed.

Line tracking trajectories in different stages of root hair development clearly distinguished spatial separation of GFP-RHD2 compartments from different groups (Figure 6, A, C, E, and G). Compartments from the red group were located almost exclusively in the bulging site (Figure 6A) and the whole bulges (Figure 6C) as well as in the clear and subapical zones of growing root hairs (Figure 6, E and G). In contrast, GFP-RHD2 compartments from the cyan group were located mainly at the periphery of the bulging zone (Figure 6A) and developing bulging domains (Figure 6C). In growing root hairs, compartments from the cyan group moved preferably in the subapical and shank regions, contacting the lateral PM (Figure 6, E and G) exclusively. Differences in the spatial distribution of individual

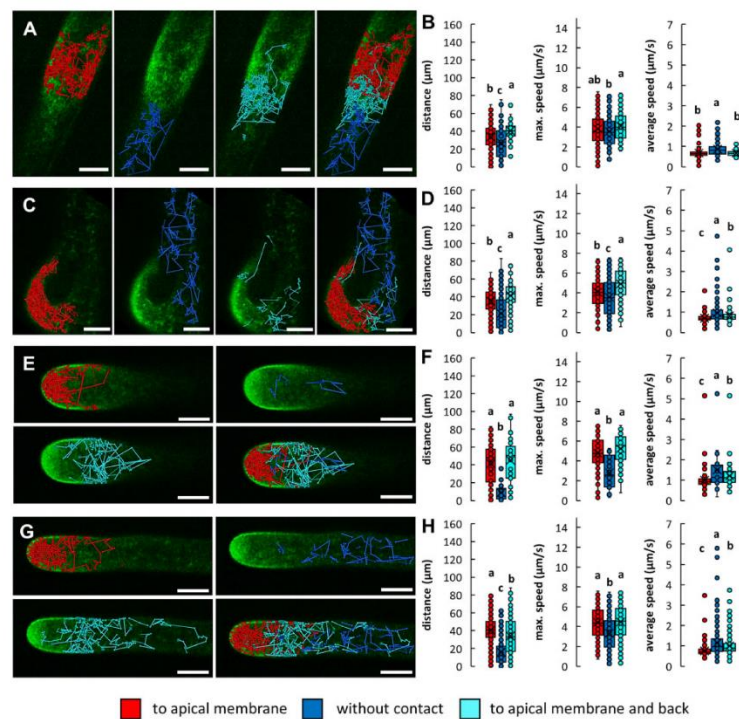


**Figure 6** Qualitative determination and quantitative tracking of moving compartments containing GFP-RHD2 at different stages of root hair development. A, C, E, and G, Line tracking of the compartments showing targeted movement to the apical PM (red), moving in the cytoplasm without any contact with the apical PM (blue), and moving to and contacting the PM and moving back to the cytoplasm (cyan), and merged images of all three types of tracks in the early bulge (A), late bulge (C), short (E), and longer (G) growing root hairs. B, D, F, and H, Quantitative determination of tracked distance of compartments, maximum and average speeds of their movements during tracking analysis, as compared separately for the compartments showing targeted movement to the apical PM (red), moving in the cytoplasm without any contact with the apical PM (blue), and moving to and contacting the PM and moving back to the cytoplasm (cyan) in the early bulge (B), late bulge (D), short (F), and longer (H) growing root hairs. More than 222 compartments from 3 to 7 growing root hairs from individual plants were analyzed. Box plots show the first and third quartiles, split by the median (line) and mean (cross). Whiskers extend to include the max/min values. Different lowercase letters indicate statistical significance between treatments according to one-way ANOVA and subsequent LSD test ( $P < 0.05$ ). Scale bar = 5  $\mu\text{m}$ .



compartments might be associated with the distance and speed of movement in different root hair developmental stages. Compartments from the blue group showed the shortest displacement distances in almost all cases (Figure 6, B, D, F, and H; Supplemental Figure S10), with the lowest values in maximum movement speed. However, the average speed of these compartments was the highest (with the highest variability) at all stages of root hair development (Figure 6, B, D, F, and H). Compartments from the red group moved along short distances in early and late bulging stages (Figure 6, B and D). These distances increased significantly during root hair tip growth compared to the cyan group (Figure 6, F and H). Compartments from the cyan group moved over the longest distance in early and late bulging stages (Figure 6, B and D), but these values decreased in the growing root hair stage (Figure 6, F and H; Supplemental Figure S10). The maximum movement speed was comparable between compartments from the red and cyan groups. Still, the average speed was significantly higher in compartments from the cyan group compared to the red group, particularly in growing root hairs (Figure 6, B, D, F, and H). The trend of faster movement of compartments from the cyan group was evident from the frequency distribution graphs. The curves for the maximum speed of cyan group compartments were right-shifted toward higher micrometer per second values (Supplemental Figure S10).

GFP-RHD2 was also localized to motile compartments in atrichoblasts. We carried out a comparative quantitative tracking analysis to characterize their properties with compartments from trichoblasts moving outside the bulging zone (Supplemental Figure S11, A and B). In principle, there were no significant differences in the average distance and minimum/maximum/average movement speed (Supplemental Figure S11, C and D). When the motions and dynamic behavior of compartments containing GFP-RHD2 were compared between tricho and atrichoblasts (Supplemental Figure S11, A and B), those in atrichoblasts showed more variable movement and dynamics. This trend was evident from the frequency distribution graphs, revealing a slightly shifted distribution to longer distances for GFP-RHD2 compartments in trichoblasts (Supplemental Figure S11E). However, the frequency distribution of maximum (Supplemental Figure S11F) and average (Supplemental Figure S11G) movement speed were very similar. These data indicate that trichoblast compartments with GFP-RHD2, which are not involved in root hair formation, move similarly to those from the atrichoblasts but distinctly from those from developing root hairs.

Live-cell imaging using Airyscan CSLM allowed the visualization of close contacts between motile compartments and the apical PM in the root hair and provided substantially improved spatial resolution. Time-course visualization of individual compartments containing GFP-RHD2 revealed direct contact with the PM enriched with GFP-RHD2 (Figure 7A;

Supplemental Movie S7). It was possible to document the full incorporation of these compartments into the apical PM by complete fusion (Figure 7, B and D; Supplemental Movie S8). Alternatively, we observed only temporal contacts of such compartments, lasting for ~30–50 s, but without full integration to the PM (Figure 7, C and E; Supplemental Movie S9). Such docking events without complete incorporation into the PM lasted longer than the total fusion events (cf. Figure 7, B and D to C and E).

#### Movements of early endosomes/TGN and late endosomes in *rhb2-1* mutant

Colocalization and common characteristics of compartments containing GFP-RHD2 and early endosomes/TGN but not late endosomes (Figures 4 and 5) raised the question of whether endosomal movements are affected in the *rhb2-1* mutant. To address this, we prepared transgenic *rhb2-1* lines carrying the early endosomal/TGN marker GFP-RabA1d and the late endosomal marker RabF2a-YFP. Since the *rhb2-1* mutant only produced short root hairs that were unable to grow, we performed quantitative tracking of endosomal compartments showing targeted movement to the bulge (red group), moving in the cytoplasm outside of the bulge (blue group), and moving toward the bulge and back (cyan group) during a 60 s imaging period. Quantitative determination of the ratio between individual groups revealed a higher proportion of early endosomes/TGN moving to the bulges in the *rhb2-1* mutant (Figure 8A). However, similar to the compartments moving to the bulge and back (the cyan group), the compartments from the red group moved over shorter distances compared to the control line (Figure 8, B–D). Characterization of movement parameters of GFP-RabA1d compartments in the control line by the frequency distribution diagram revealed different behaviors of individual groups (Figure 8, E and F). In particular, the curves for maximum speed were shifted differentially (Figure 8E). This indicates different properties of early endosomal/TGN compartments that participate in bulge formation. In contrast, frequency distribution analysis of the speed among all three different groups of GFP-RabA1d compartments in the *rhb2-1* mutant showed no differences (Figure 8, G and H). These data indicated that the movement of early endosomal/TGN compartments was partially affected in *rhb2-1*.

Late endosomal compartments did not accumulate in the apex of the growing root hairs (Figure 5, B and D; Supplemental Figures S4, B and S7, B). For this reason, we analyzed all late endosomes carrying RabF2a-YFP within one homogeneous group. Characterization of movement distances of RabF2a-YFP compartments in bulging trichoblasts showed only negligible differences between control and *rhb2-1* (Figure 8, I and J). In addition, the maximum and average movement speed measurements provided similar values (Figure 8, K and L). Thus, the movement of late endosomes seems to be unaffected in *rhb2-1*.

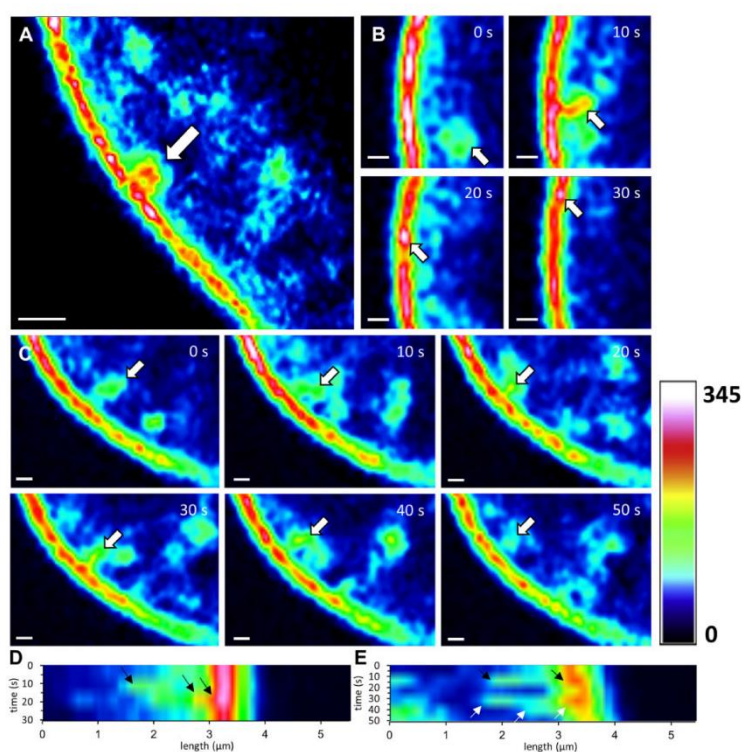


**Figure 7** Time-course visualization of close contacts between moving compartments containing GFP-RHD2 and the apical PM in the root hair apex. A, Round-shaped compartment (arrow) in direct contact with strong GFP-RHD2 fluorescence signal in the apical PM. B and C, Two events of interactions between the compartments and the apical PM (Supplemental Movie S7) showing fast full integration with the PM (arrows; B, Supplemental Movie S8) or temporal contact lasting 30 s (B) and 50 s (C). The time-lapse imaging encompassed 30 s (B) and 50 s (C). The fluorescence distribution is visualized through a semi-quantitative signal intensity using a pseudo-color-coded scale, where dark blue represents minimal intensity (0 arbitrary units) and white represents maximum intensity (345 arbitrary units). D and E, Kymographs showing interactions between the compartments and the apical PM either by full integration to the membrane (black arrows; D) or by approaching and a temporal contact with the PM (black arrows; E), but without fusion and followed by back movement to the cytoplasm (white arrows; E). Scale bar = 1  $\mu\text{m}$  (A and B), 500 nm (C).

### Distribution of GFP-RHD2 in root hairs after filipin III treatment

The delivery of compartments with GFP-RHD2 to the apical PM in bulges and growing root hairs requires physical interactions with the PM (Figure 7). Simultaneously, we identified and quantitatively characterized a sub-population of GFP-RHD2 compartments moving to and contacting the PM and subsequently moving back to the cytoplasm (Figures 6 and 7). Docking, eventual fusion, or recycling of these compartments back to the cytoplasm may require integral lipid membrane components. Structural sterols are integral components of plant membranes and are abundant in the apical PM of developing bulges and growing root hairs (Ovečka et al., 2010). In this study, we used filipin III, a vital probe for *in vivo* localization and sequestration of structural sterols (Grebe et al., 2003; Bonneau et al.,

2010) in a physiologically high concentration that causes the formation of filipin–sterol complexes at the PM (Milhaud et al., 1988; Bonneau et al., 2010; Ovečka et al., 2010) and a rapid arrest of root hair tip growth (Jones et al., 2006; Ovečka et al., 2010). First, roots of the GFP-RHD2 line were treated with  $10 \mu\text{g}\cdot\text{mL}^{-1}$  filipin III using gentle perfusion directly at the microscope stage, and plants were examined by time-lapse live-cell imaging. Growing root hairs were photographed to visualize the cytoarchitecture using differential interference contrast (DIC) optics. At the same time, epifluorescence illumination allowed the monitoring of GFP-RHD2 localization and filipin III-induced PM staining during perfusion. The stabilized position of the sample at the microscope stage during the perfusion and sequential image acquisition (Figure 9) and monitoring of GFP-RHD2 accumulation at the tip by measuring fluorescence

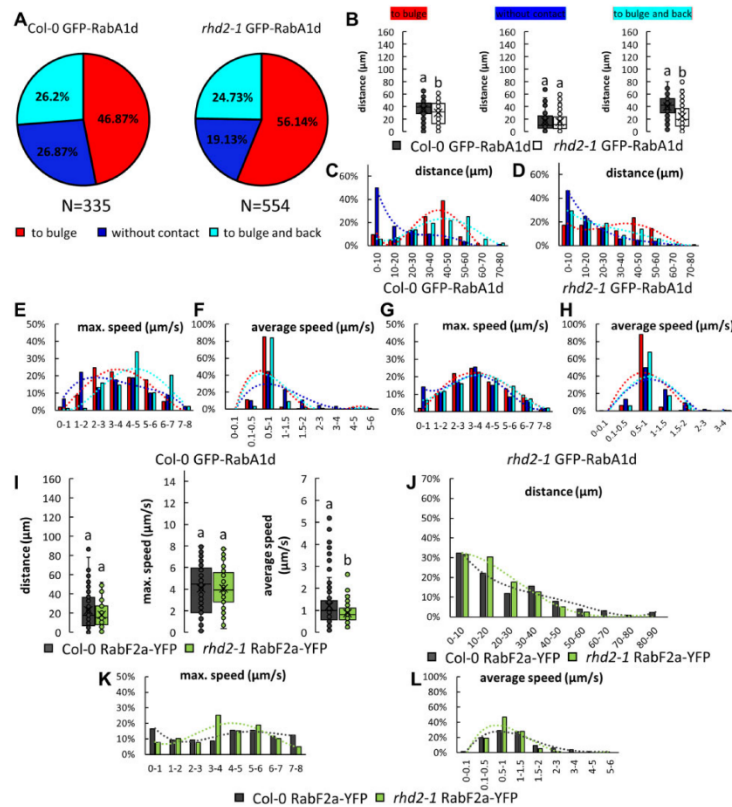


**Figure 8** Qualitative and quantitative evaluation of endosomal compartments movements in developing bulges during root hair formation in *Arabidopsis* control and *rhd2-1* mutant lines. A, Quantitative determination of the ratio between the compartments showing targeted movement to the bulge (red), moving in the cytoplasm outside of the bulge (blue), and moving to the bulge and back (cyan) in the control line (Col-0) and *rhd2-1* mutant bearing early endosomal marker GFP-RabA1d. B, Quantitative evaluation of tracking distance for compartments containing GFP-RabA1d and moving either to the bulge (red), in the cytoplasm outside of the bulge (blue), or to the bulge and back (cyan) in Col-0 control line and *rhd2-1* mutant. C and D, Frequency distributions of distances for tracked compartments moving either to the bulge (red), in the cytoplasm outside of the bulge (blue), or to the bulge and back (cyan) in Col-0 control line (C) and *rhd2-1* mutant (D) bearing GFP-RabA1d marker. E–H, Frequency distributions of the maximum (E and G) and average speed (F and H) of the tracked compartments moving either to the bulge (red), in the cytoplasm outside of the bulge (blue), or to the bulge and back (cyan) in Col-0 control line (E and F) and *rhd2-1* mutant (G and H) carrying GFP-RabA1d. More than 335 compartments from two to four bulges from individual plants were analyzed. I, Quantitative evaluation of compartment tracking distances, their maximum, and average movement speed in bulges of Col-0 and *rhd2-1* mutant bearing late endosomal marker RabF2a-YFP. J–L, Frequency distributions of the distance (J), maximum speed (K), and average speed (L) of the analyzed compartments moving in bulges of Col-0 control line and *rhd2-1* mutant bearing RabF2a-YFP. More than 127 compartments from two to four bulges from individual plants were analyzed. Box plots show the first and third quartiles, split by the median (line) and mean (cross). Whiskers extend to include the maximum/minimum values. Different lowercase letters indicate statistical significance according to one-way ANOVA and subsequent LSD test ( $P < 0.05$ ).

intensity profiles (Supplemental Figure S12) also provided the means for evaluation of the root hair tip growth. Root hairs before perfusion (time from 0 to 7 min) showed typical cytoarchitecture with tip-focused GFP-RHD2 localization (Figure 9, A and B). Analysis of the GFP fluorescence temporal distribution along a median profile in the form of a kymograph revealed continuous and sustained tip growth (Figure 9, C and D). To

avoid any misinterpretations caused by changes induced by mechanical and osmotic disturbances during the application, perfusion with the control medium (mock treatment) was applied to control root hairs (Figure 9A). The control medium application induced a transient movement of the vacuole closer to the tip, slightly reducing the cytoplasm amount in the apical and subapical root hair zone (Figure 9A; DIC, time from

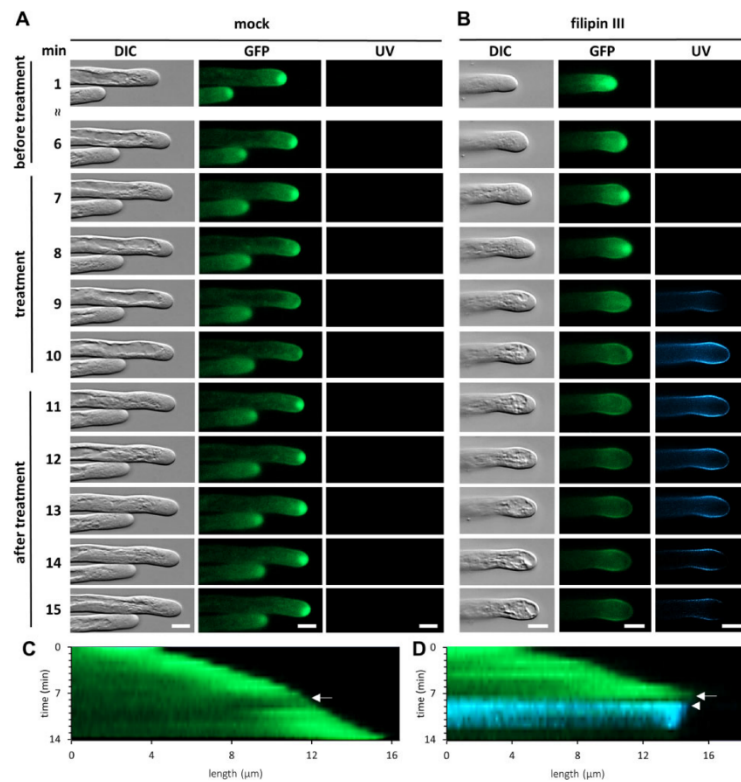


**Figure 9** Inhibition of growing root hairs and changes of GFP-RHD2 localization after filipin III application. A and B, Growing root hairs imaged either by DIC for cytoarchitecture visualization, blue excitation fluorescence light for GFP-RHD2 localization (GFP), or ultra-violet excitation fluorescence light for visualization of PM staining by filipin III (UV). Root hairs show normal cytoarchitecture, tip-focused GFP-RHD2 localization, no signal in UV light (A and B), and sustained tip growth (C and D) before treatment (time from 0 to 7 min). During perfusion mock treatment (A), there was a transient reduction of the cytoplasm at the subapical root hair zone (A; DIC, 8–10 min; [Supplemental Movie S10](#)) and transient reduction of GFP-RHD2 in the apex (A; GFP, 9–10 min; [Supplemental Movie S11](#); arrow in C), while it was reversibly restored and maintained up to the end of the experiments (up to 15 min; A and C). During perfusion filipin III treatment (B), root hairs stopped growth (arrow; D), their tips started to be invaded by round vacuoles (B; DIC, 9–10 min; [Supplemental Movie S12](#)), and GFP-RHD2 disappeared from the root hair apex (B; GFP, 9–10 min; [Supplemental Movie S13](#)). Simultaneously, filipin III-positive blue signal appeared at the PM (B; UV, 9–10 min; arrowhead in D). After a mock treatment (A), root hair cytoarchitecture (A; DIC, 11–15 min), tip-focused GFP-RHD2 localization (A; GFP, 11–15 min; [Supplemental Figure S12](#)), and root hair growth rate (C; 11–15 min) were regularly maintained and not disturbed. Root hair after filipin III treatment (B) showed disrupted cytoarchitecture such as vacuolated root hair apex (B; DIC, 11–15 min), lost GFP-RHD2 from the tip (B; GFP, 11–15 min; [Supplemental Figure S12](#)), filipin III-positive signal appeared at the PM (B; UV, 11–15 min), and completely blocked tip growth (D; 11–15 min). Acquisition of the GFP signal at 400 ms exposure time, and the filipin III signal at 200 ms exposure time was performed to gain optimal signal-to-noise ratio in GFP and UV channels (A and B). Reduction of filipin III-positive signal at the PM (B; UV, 11–15 min) was caused by bleaching induced by a wide-field epifluorescence illumination. Scale bar = 10  $\mu\text{m}$  (A and B).

8 to 10 min). The reaction of root hairs to mock treatment was connected with a transient reduction of GFP-RHD2 fluorescence in the apex (Figure 9A; GFP, time from 8 to 10 min; arrow in Figure 9C). However, both parameters were reversibly restored to normal and maintained until the end of the experiments (Figure 9A; DIC, GFP, time up to 15 min). Thus, after a mock treatment, root hair cytoarchitecture (Figure 9A; DIC, from 11 to 15 min; [Supplemental Movie S10](#)), tip-focused GFP-RHD2 localization (Figure 9A; GFP, from 11 to 15 min;

[Supplemental Figure S12A](#); [Supplemental Movie S11](#)), and root hair tip growth rate (Figure 9C; from 11 to 15 min) were maintained and not considerably disturbed. As expected, epifluorescence ultra-violet illumination for filipin III excitation produced no signal upon mock treatment (Figure 9A; UV, time from 0 to 15 min).

Perfusion with filipin III caused the arrest of root hair tip growth (Figure 9B; DIC, time from 7 to 8 min) and was documented in the related kymograph (Figure 9D, arrow). Consequently, root hair tips were invaded by round

articulated vacuoles that irreversibly persisted until the end of the experiments (Figure 9B; DIC, time from 9 to 15 min). As the tip growth was arresting, GFP-RHD2 disappeared irreversibly from the root hair apex (Figure 9B; DIC, time from 9 to 15 min). Alongside the loss of GFP-RHD2, a filipin III-positive blue signal appeared at the PM (Figure 9B; UV, time from 9 to 15 min; arrowhead in Figure 9D). Therefore, root hairs after filipin III treatment showed disrupted cytoarchitecture due to massive vacuolation of the root hair apex (Figure 9B; DIC, from 9 to 15 min; Supplemental Movie S12), a loss of GFP-RHD2 from the tip (Figure 9B; GFP, from 9 to 15 min; Supplemental Figure S12B; Supplemental Movie S13), and accumulated filipin III-positive signal at the PM (Figure 9B; UV, from 9 to 15 min), resulting in blocked tip growth (Figure 9D; from 8 to 15 min).

Next, the root hairs of the GFP-RHD2 line were treated with  $10 \mu\text{g}\cdot\text{mL}^{-1}$  filipin III for 10 min, and subcellular changes in GFP-RHD2 distribution were directly examined using a spinning disk microscope. The appearance of filipin III fluorescence in the PM of root hairs after application coincided with the tip growth arrest. Treatment with filipin III led to a layer-like accumulation of GFP-RHD2 closely associated with PM at the apex of root hairs (Figure 10, A and C). Because filipin III interacts specifically with sterols in the PM

(Milhaud et al., 1988; Bonneau et al., 2010), filipin III-positive blue staining served as a PM marker under these circumstances. Therefore, the layer-like accumulation of GFP-RHD2 beneath the PM suggests that GFP-RHD2 was prevented from incorporating into the PM after filipin III treatment. Consistent with the localization pattern of GFP-RHD2 in the apical and subapical PM domains in control growing root hairs (Figures 2, J–M, 3, A and B, 4, A and E, 5, A and B, and 6, E and G; Supplemental Figure S1, C and E), the extent of layer-like accumulation of GFP-RHD2 after filipin III treatment reached only PM at the apical and subapical domains of root hairs (Figure 10A; Supplemental Figures S13B). This localization pattern was unique because equivalent experiments on GFP-RabA1d root hairs treated with filipin III revealed accumulation of early endosomal/TGN compartments in the apical part of the root hairs but not in close contact with filipin III-positive apical PM (Figure 10, B and E). Semi-quantitative analysis of the fluorescence intensity distribution using a profile function across the root hair apex (Figure 10C) revealed a “basal” level of GFP-RHD2 in filipin III-positive PM but mostly accumulated in a thin layer beneath the PM (Figure 10D). Simultaneously, the clear zone was depleted of GFP-RHD2 fluorescence after filipin III treatment (Figure 10, C and D). The same pattern of layer-like accumulation of GFP-RHD2 beneath the PM has been

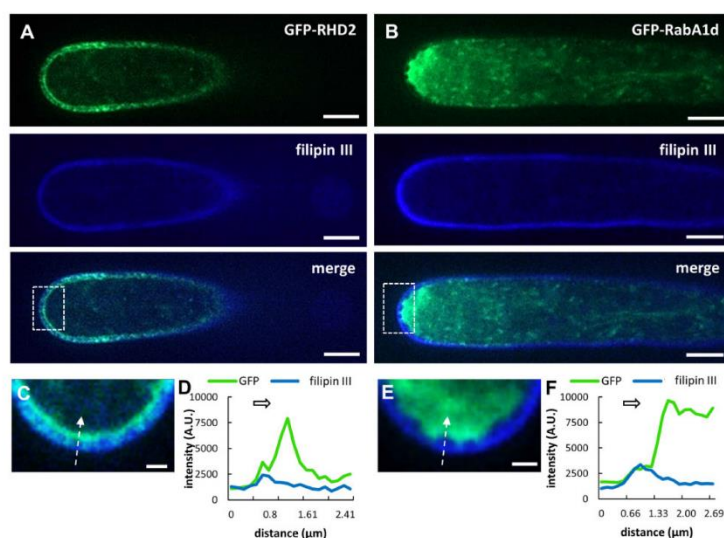


**Figure 10** Localization analysis of GFP-RHD2 and GFP-RabA1d in root hairs after treatment with filipin III. A, Localization of GFP-RHD2 (green) in the root hair, filipin III-positive signal (blue) at the PM, and merged image showing the distribution pattern of GFP-RHD2 after filipin III treatment for 10 min. B, Localization of early endosomal marker GFP-RabA1d (green) in the root hair, filipin III-positive signal (blue) at the PM, and merged image showing the distribution pattern of GFP-RabA1d after filipin III treatment for 10 min. C, Detailed image of the apical part of the root hair within the white box in (A). Arrow indicates the position and the direction of the fluorescence intensity profile measurement. D, Fluorescence intensity profile of the GFP-RHD2 and filipin III-positive signal along the arrow in (C). The arrow above the curves indicates the direction of the measurement. E, Detailed image of the apical part of the root hair within the white box in (B). Arrow indicates the position and the direction of the fluorescence intensity profile measurement. F, Fluorescence intensity profile of the GFP-RabA1d and filipin III-positive signal along the arrow in (E). The arrow above the curves indicates the direction of the measurement. Scale bar =  $5 \mu\text{m}$  (A and B),  $1 \mu\text{m}$  (C and E).

observed in emerged bulges and elongated root hairs (Supplemental Figure S13). Interestingly, GFP-RabA1d accumulation in the clear zone after filipin III treatment showed a different pattern (Figure 10E) because it was detached and did not show direct contact with the filipin III-positive PM (Figure 10, E and F). Different GFP-RHD2 and GFP-RabA1d localization patterns after filipin III treatment were repeatedly observed in the apical part of treated root hairs (Supplemental Figure S14). In contrast, treatment of root hairs with filipin III did not cause any changes in the subcellular localization pattern of late endosomes visualized by RabF2a-YFP in root hairs (Supplemental Figure S15). Although root hair tip growth was arrested by filipin III treatment, the distribution of late endosomal compartments carrying RabF2a-YFP resembled the situation under control conditions (Supplemental Figure S4B). Moreover, similar results were obtained in the root hairs of the double GFP-RHD2 × mCherry-RabF2b transgenic line treated with filipin III (Supplemental Figure S16A). GFP-RHD2 accumulated strictly in close association with the apical PM, but late endosomal compartments carrying mCherry-RabF2b were distributed along the whole root hairs (Supplemental Figure S16A). Semi-quantitative fluorescence intensity evaluation at the root hair apex confirmed the close association of GFP-RHD2 with the apical PM and the absence of late endosomal compartments carrying mCherry-RabF2b in the clear zone (Supplemental Figure S16, B and C).

These data might indicate that the change in the GFP-RHD2 distribution pattern and related inhibition of the root hair tip growth by filipin III, reveal a specific role of structural sterols in the physical interaction of vesicular compartments containing GFP-RHD2 with the apical PM. To clarify this question, we performed an alternative treatment of growing root hairs with another independent inhibitor arresting root hair tip growth. We have used  $\alpha$ -(2,4-dimethylphenylethyl-2-oxo)-IAA (auxinole), which is an auxin antagonist competing with auxin for binding sites on the auxin receptor TRANSPORT INHIBITOR RESPONSE 1 (TIR1), leading to the considerable reduction of root hair formation in *A. thaliana* (Smékalová et al., 2014). Root hairs after auxinole treatment rapidly arrested tip growth, which was not connected with considerable changes in the cytoarchitecture of root hair apex (Supplemental Figure S17). However, GFP-RHD2 gradually disappeared from the tip and the typical pattern of its distribution was lost. Only weak GFP-RHD2 signal remained at the PM (Supplemental Figure S17B). Detailed analysis confirmed the disappearance of GFP-RHD2 from the clear zone after auxinole treatment and revealed a localization of remaining GFP-RHD2 at the root hair periphery (Supplemental Figure S18, A–C). Staining of the PM with FM4–64 (Supplemental Figure S18D) confirmed the localization of remaining GFP-RHD2 in the PM, but not in a thin layer accumulated beneath the PM, typical for filipin III treatment. This was documented by both colocalization (Supplemental Figure S18E) and semi-quantitative analyses of the fluorescence intensity

distribution using a profile function across the root hair apex (Supplemental Figure S18F).

These experiments with filipin III suggest that structural sterols, abundant in the apical PM of growing root hairs (Ovečka et al., 2010), might be involved in the dynamic relocation of GFP-RHD2. Upon filipin III treatment, we did not observe incorporation of GFP-RHD2 into the apical PM and have concluded that it might be caused by GFP-RHD2 inability to physically integrate into the apical PM. Based on the fact that PM labeling by filipin III leads to a concentration-dependent formation of filipin–sterol complexes at the ultrastructural level in plant cells (Grebe et al., 2003; Bonneau et al., 2010), including growing root hairs (Ovečka et al., 2010), this treatment leads irreversibly to arrest of the root hair tip growth (Ovečka et al., 2010). These results indicate the dependence of growing root hairs on RHD2/AtRBOHC integration to the apical PM, which might be mediated by structural sterols.

## Discussion

The tip growth of root hairs is a highly polarized process depending on targeted vesicular transport, localized cell wall deposition, and PM extension at the growing tip. It is supported by tip-localized transmembrane gradients ( $\text{Ca}^{2+}$ , ROS, and pH) and by polarized organization and dynamics of the cytoskeleton (Šamaj et al., 2006). The establishment and maintenance of these gradients in root hairs are orchestrated by the NADPH oxidase AtRBOHC/RHD2 (Foreman et al., 2003) activated by Rop GTPases (Jones et al., 2007) accumulated at the site of future root hair initiation (Molendijk et al., 2001; Jones et al., 2002). Loss of AtRBOHC/RHD2 function in *rhd2* mutants leads to the interruption of root hair tip growth. Nevertheless, fully rescued root hair development has been achieved by transforming *rhd2* by GFP-tagged AtRBOHC/RHD2 under the control of the native promoter (Takeda et al., 2008). Cell type-specific and developmentally regulated localization of GFP-RHD2 in trichoblasts revealed its selective accumulation in bulges and tips of developing root hairs (Takeda et al., 2008). Using different advanced microscopy methods, we qualitatively and quantitatively characterized the subcellular localization of GFP-RHD2. We visualized dynamic vesicular compartments linked with the formation and maintenance of the apical PM domain during root hair development. In root development, these compartments appeared first in the epidermis of the root hair formation zone (the proximal part of the root elongation zone and in the differentiation zone). The number of compartments was substantially higher in the trichoblasts. This localization pattern, spatiotemporally related to root hair formation, is consistent with quantitative microarray analysis of roots, showing enhanced *RHD2* transcription in differentiation and elongation root zones, epidermal cells, and root hairs (Chapman et al., 2019). Next, we used a quantitative particle tracking approach to characterize the temporal and spatial GFP-RHD2 subcellular redistribution pattern during root hair initiation and growth. This analysis

revealed a mode of targeted GFP-RHD2 delivery to the apical PM domain of developing bulges and growing root hairs. Notably, the PM area containing GFP-RHD2 was restricted, and the range of this area corresponded with particular stages of root hair development.

Localized delivery of GFP-RHD2 and its incorporation into the PM by motile compartments raises questions about their molecular signatures. As expected, the membrane-specific dye FM4-64 colocalized with GFP-RHD2 at the PM of root hairs in the apical and subapical zones where GFP-RHD2 was restricted. In addition, labeling of growing root hairs with FM4-64 revealed a high degree of colocalization with GFP-RHD2 in compartments moving in the cytoplasm of root hairs. This unequivocally indicated their vesicular nature. The short incubation time of growing root hairs with FM4-64 serves to visualize early endocytic compartments (Ovečka et al., 2005). Colocalization studies with early endosomes/TGN (GFP-RabA1d; Ovečka et al., 2010; Berson et al., 2014) or late endosomes (RabF2a-YFP; Voigt et al., 2005; Berson et al., 2014) confirmed that a short FM4-64 application is suitable for the localization of early but not late endosomes. To corroborate these data, we analyzed colocalization in double transgenic lines carrying GFP-RHD2 together with mCherry-VTI12 (an early endosomal/TGN marker; Geldner et al., 2009) and mCherry-RabF2b (a late endosomal marker; Geldner et al., 2009). Using this approach, the colocalization of GFP-RHD2 with the early endosomal/TGN marker mCherry-VTI12 was confirmed in the cytoplasmic compartments of growing root hairs. The maximum speed of motile compartments containing GFP-RHD2 in root hairs was typically  $4\text{--}8\ \mu\text{m s}^{-1}$ . This is consistent with the dynamic properties of early endosomal compartments carrying molecular markers GFP-RabA1d and YFP-VTI12, with a maximal speed of  $6\text{--}9\ \mu\text{m s}^{-1}$  (von Wangenheim et al., 2016).

Notably, the spatial control of GFP-RHD2 incorporation into the apical PM was closely related to the nonuniform pattern of vesicular movements. The ratio of the compartments moving and fusing with the apical PM, those moving toward, contacting the PM, and subsequently moving back to the cytoplasm, or those moving in the cytoplasm without any contact with the apical PM, changed with different stages of root hair development. The particle tracking analysis provided quantitative parameters of these movements and their specific features, especially in compartments coming into contact with the PM. The enlargement of the bulging domain was tightly connected with the higher portion of compartments moving to the apical PM and fusing with it. This corresponded with the gradual enlargement of the apical PM area, incorporating and accumulating GFP-RHD2. In contrast, there was an increase in the fraction of compartments contacting the PM and subsequently moving back to the cytoplasm during the growth of root hairs. This likely represents the active recycling of GFP-RHD2 between the PM and motile vesicular compartments in the cytoplasm. These data also indicate that compartments containing GFP-RHD2 are

spatiotemporally specialized in particular stages of root hair formation. Consequently, the ratio between different compartment types responsible for the rate of GFP-RHD2 incorporation into the PM and/or recycling was regulated according to the developmental stage of the root hair.

We also tested a possible link between AtRBOHC/RHD2 and the movement of endosomal compartments through detailed quantitative characterization of early endosomes/TGN and late endosomes in the *rh2-1* mutant. We compared early endosomal/TGN compartments visualized by GFP-RabA1d in the control line, specifically those moving to the bulge or those moving to the bulge and back to the trichoblast, and found differences in their speed and trajectory values. The same comparison in the *rh2-1* mutant carrying GFP-RabA1d, however, revealed no differences. It seems that the loss of function of AtRBOHC/RHD2 in the *rh2-1* mutant influenced, at least partially, the dynamic behavior of early endosomes/TGN in bulges. Comparison with late endosomes visualized by RabF2a-YFP under the same circumstances revealed no differences between the control and *rh2-1* mutant. These results indicate that AtRBOHC/RHD2 loss-of-function mutation affects only early endosomal/TGN compartments, verifying the crucial role of early endosomal/TGN compartments in root hair formation and growth. Overall, live-cell localization during root hair initiation and growth by advanced microscopy indicated the involvement of GFP-RHD2 in the specialization and maintenance of apical PM domains in bulges and tip-growing root hairs and targeted delivery to the cortical cytoplasm and the clear zone in dynamic vesicular compartments.

Finally, we tested the possible role of structural sterols in docking and fusion of compartments containing GFP-RHD2 with the apical PM of growing root hairs. The subcellular localization of structural sterols can be performed using vital fluorescent probes. Filipin III is a polyene antibiotic fluorochrome suitable for the localization of structural sterols in animal (Nichols et al., 2001), yeast (Wachtler et al., 2003), and plant cells (Grebe et al., 2003; Boutté et al., 2009; Liu et al., 2009; Bonneau et al., 2010). Specific accumulation of filipin III signal was observed in the PM of the prebulging site, developing bulges, and at the tips of growing root hairs (Ovečka et al., 2010). At higher concentrations or after prolonged exposure, filipin III induced the formation of filipin-sterol complexes (Milhaud et al., 1988; Bonneau et al., 2010; Ovečka et al., 2010). This leads to PM damage and changes in physiological functions, and such treatments block root hair tip growth and affect vesicular trafficking (Ovečka et al., 2010). Treatment of root hairs with filipin III allowed us to visualize sterols in the PM of growing root hairs (Figure 9), which was inevitably connected with the arrest of tip growth. Detailed microscopic analysis revealed that filipin III might prevent the correct incorporation of GFP-RHD2 into the apical PM zone (Figure 10). Ultrastructural examination documented that concentrations of filipin III at and  $> 10\ \mu\text{g mL}^{-1}$  cause the formation of filipin-sterol complexes at the PM (Grebe et al., 2003; Bonneau et al., 2010;

Ovečka et al., 2010). The appearance of filipin–sterol complexes at the PM was immediately connected with PM rigidification. It triggered ion leakage, extracellular pH alkalization, and changes in signaling dependent on protein kinase-mediated phosphorylation (Bonneau et al., 2010). Thus, the formation of filipin III-induced complexes with sterols most likely inhibits sterol functions at the PM, possibly including the proper incorporation of GFP-RHD2 to the apical PM zone of growing root hairs. It was reported previously that treatment with the sterol-disrupting agent methyl- $\beta$ -cyclodextrin caused redistribution, clustering, and changes in the diffusion properties of GFP-RBOHD, a fluorescently tagged NADPH oxidase involved in plant defense within the PM of the hypocotyl epidermal cells (Hao et al., 2014). Defective localization of RHD2 NADPH oxidase in root hairs was observed in a sterol-deficient *drought hypersensitive/squalene epoxidase 1-5* mutant of *A. thaliana* (Posé et al., 2009; Sena et al., 2017). The link between structural sterols at the PM and root hair formation might be mediated by a regulatory role of Rho of plants (ROPs) such as ROP2, ROP4, and ROP6. ROPs are recruited at the site of future root hair initiation by RopGEF3 (Denninger et al., 2019) and accumulate in bulges and the apex of growing root hairs (Molendijk et al., 2001; Jones et al., 2002). ROP2 and ROP4 activate AtRBOHC/RHD2 for localized ROS production during root hair formation (Carol et al., 2005). ROPs activation leads to transient S-acylation, which is required for their functionality and stabilizes their interaction with the PM and accumulation in lipid rafts (Sorek et al., 2011, 2017). ROP2 and ROP6 colocalize with sterol-enriched PM domains at root hair formation sites and the tips of growing root hairs (Stanislas et al., 2015).

Surprisingly, unlike GFP-RabA1d, GFP-RHD2 in filipin III-treated root hairs accumulated within a thin layer closely associated with the inner cytoplasmic side of the apical PM, and the GFP-RHD2 signal was depleted in the clear zone. Independent treatment with auxinole, arresting similarly root hair tip growth, led to a different GFP-RHD2 distribution pattern, suggesting a specific role of structural sterols, targeted by filipin III. These data indicate that structural sterols, which are responsible for membrane fluidity and the formation of lipid nanodomains, might participate in the correct insertion of GFP-RHD2 to the apical PM in root hairs. Such layer-like accumulation of GFP-RHD2 beneath the apical PM might suggest that the physical incorporation is prevented, and the depletion of GFP-RHD2 compartments from the clear zone might indicate that recycling from the PM was inhibited. Although the complete functionality of the model includes the endogenous RHD2, which is still

present and functionally relevant in the examined transgenic line, this observation indicates that structural sterols might be involved in localized anchoring and maintenance of GFP-RHD2 in the apical PM zone of developing root hairs.

## Materials and methods

### Plant material preparation

Experiments were performed with plants of *Arabidopsis* (*A. thaliana*), wild-type of the Col-0 ecotype, *rhd2-1* (Foreman et al., 2003) mutant, and stably transformed *A. thaliana* plants (of Col-0 wild-type background) carrying constructs with GFP-RHD2 (Takeda et al., 2008) and fluorescent markers of endosomal compartments. Stable transgenic lines in the Col-0 background, bearing fluorescent markers of endosomal compartments, were prepared by crossing. Plants of the *rhd2-1* mutant, used as female donors, were crossed with transgenic plants bearing fluorescent markers for early endosomes/TGN, GFP-RabA1d (Ovečka et al., 2010), or late endosomes, RabF2a-YFP (Voigt et al., 2005). Transgenic plants bearing fluorescent markers of endosomal compartments were used as male donors. Transgenic plants with N-terminal fusion of RHD2 with GFP under the control of the *RHD2* promoter (GFP-RHD2 line in the Col-0 background; Takeda et al., 2008), were crossed with transgenic plants carrying fluorescent markers of endosomal compartments (Wave line W13R producing mCherry-VTI12 for early endosomes/TGN; Geldner et al., 2009, and Wave line W2R producing mCherry-RabF2b for late endosomes; Geldner et al., 2009). Transgenic plants with GFP-RHD2 were used as female donors in crossings. The progeny of the F1 generation was selected according to fluorescence signals using an Axio Zoom.V16 fluorescence stereomicroscope (Carl Zeiss, Germany), and plants of the F2 or F3 generations were used for experiments. We analyzed the transmission of the *GFP-RHD2* and red marker alleles in the F2 and F3 generations by phenotypical analysis. As expected, the progeny of heterozygous plants consisted of ~50% of the individuals simultaneously carrying GFP and red fluorescence. GFP fluorescence alone was detected in ~25% of plants, analogous to mCherry (Table 1). Lines showing both types of fluorescence with the wild-type root hair phenotype were used further for the colocalization studies.

### In vitro cultivation

Seeds of *A. thaliana* control, mutant, and transgenic lines were surface-sterilized and planted on 1/2 Murashige and Skoog (MS) medium (Murashige and

**Table 1** F2 progeny after the crossing of the transgenic lines bearing GFP-tagged RHD2 with mCherry-tagged endosomal markers

Crossed Lines	Phenotype (Fluorescence)				No. of Plants
	GFP + mCherry (%)	GFP (%)	mCherry (%)	None (%)	
<i>GFP-RHD2</i> × <i>mCherry-RabF2b</i>	49	25	21	5	118
<i>GFP-RHD2</i> × <i>mCherry-VTI12</i>	55	21	17	7	94



Skoog, 1962) without vitamins, solidified with 0.6% (w/v) Gellan gum (Alfa Aesar, Thermo Fisher Scientific, Heysham, UK). Petri dishes with seeds were stratified at 4°C for 3 d for synchronized germination. After stratification, seeds were cultivated vertically in an environmental chamber at 21°C, 70% humidity, and 16-h/8-h light/dark cycle. The illumination intensity was  $130 \mu\text{mol m}^{-2}\text{s}^{-1}$ .

#### LSFM

Samples for LSFM were prepared as described by Ovečka et al. (2015). Seeds of GFP-RHD2 line were surface sterilized and transferred to round  $90 \times 25$  mm Petri dishes filled with 80 mL of modified MS medium (Ovečka et al. 2014) at pH 5.7, solidified with 0.5% (w/v) Gellan gum. After germination, the roots began to grow into the medium gravitropically. Three-day-old plants were inserted into the fluorinated ethylene propylene (FEP) tubes with the medium surrounding the root (root was embedded in the medium, and the upper green part was exposed to air). The samples were transferred to a pretempered (22°C) observation chamber of the LSFM filled with a modified liquid MS medium. The agar block with the plant was partially pushed out from the FEP tube into the liquid medium for imaging of the root tip not surrounded by FEP tube walls. After 30 min of stabilization, plants were observed using a light-sheet Z.1 fluorescence microscope (Carl Zeiss, Germany) equipped with two LSFM  $10 \times /0.2$  NA illumination objectives (Carl Zeiss, Germany), Plan-Apochromat  $20 \times /1.0$  NA water immersion detection objective (Carl Zeiss, Germany), and the PCO Edge sCMOS camera (PCO AG, Germany) with an exposure time of 40 ms. Each individual plant represented an independent biological replicate, and  $>8$  plants were analyzed. Imaging was carried out using dual-side illumination and pivot scan mode with a light-sheet thickness of  $4.52 \mu\text{m}$ . GFP was excited at 488 nm using 2% of relative laser power level, and detected between 505 and 545 nm with BP505–545 emission filter. Images were acquired in three subsequent views aligned to each other in the root growth direction (along the  $y$  coordinate) at time points of every 5 min in Z-stack mode for 15 h. Image scaling in  $x$ ,  $y$ , and  $z$  was adjusted to  $0.228 \times 0.228 \times 0.477 \mu\text{m}$ , encompassing the volume of  $438.69 \times 438.69 \times 229.79 \mu\text{m}$  ( $x \times y \times z$ ).

#### Airyscan CLSM and spinning disk (SD) microscopy

Plants 2- to 3-day-old were transferred to microscopy chambers containing liquid modified MS medium according to Ovečka et al. (2005, 2014). After manipulation with plants during sample preparation, the subsequent stabilization period for 24 h allowed undisturbed growth of the root and the formation of new root hairs. The development of root hairs in more than 10 individual plants was observed using a confocal laser scanning microscope LSM880 equipped with Airyscan (Carl Zeiss, Germany) and a Cell Observer SD Axio Observer Z1 spinning disk microscope (Carl Zeiss, Germany). Airyscan CLSM was used for qualitative and quantitative characterization of GFP-RHD2-positive compartments during root hair development and growth. Image

acquisition was performed with a  $20 \times /0.8$  NA dry Plan-Apochromat objective (Carl Zeiss, Germany). The samples were imaged with an excitation laser line of 488 nm and BP420–480 + BP495–550 emission filters for GFP detection. The laser power did not exceed 0.8% of the available laser intensity range. The samples were scanned every 706 ms with 700 ms of exposure time using a 32 GaAsP detector. Pixel dwell time was set up to 1.98  $\mu\text{s}$ , and with default settings of the gain level the image scaling was set up to  $0.074 \times 0.074 \times 0.397 \mu\text{m}$  ( $x \times y \times z$ ). A spinning disk microscope equipped with alpha Plan-Apochromat  $100 \times /1.57$  NA DIC Korr oil immersion objective (Carl Zeiss, Germany) was used for colocalization analyses. The samples were imaged using an excitation laser line of 405 nm and emission filter BP450/50 for filipin III signal detection, excitation laser line of 488 nm and emission filter BP525/50 for GFP signal detection, excitation laser line of 514 nm, and emission filter BP535/30 for YFP signal detection, excitation laser line of 514 nm and emission filter BP690/50 for FM4-64 signal detection, and excitation laser line of 561 nm and emission filter BP629/62 for the mCherry signal detection. The excitation laser power level for all lasers used was set up to 50%, and the image scaling for all channels was  $0.133 \times 0.133 \mu\text{m}$  in  $x \times y$  dimensions, and with the  $z$  dimension  $0.52 \mu\text{m}$  for the filipin III channel,  $0.63 \mu\text{m}$  for the GFP channel,  $0.66 \mu\text{m}$  for the YFP channel,  $0.75 \mu\text{m}$  for the mCherry channel, and  $0.92 \mu\text{m}$  for the FM4-64 channel. Images were acquired sequentially or simultaneously with two Evolve 512 EMCCD cameras (Photometrics) with an exposure time of 700 ms. The samples were scanned every 731 ms using a camera-streaming mode.

#### FM4-64 staining, filipin III, and auxinole application

FM4-64 (Thermo Fisher Scientific, Waltham, MA, USA) was used as the PM and vesicular marker in the root hairs. Filipin III (Sigma-Aldrich, St Louis, MO, USA) was used as a vital probe for PM structural sterols, allowing the formation of filipin-sterol complexes in root hairs at higher concentrations. Auxinole (MedChemExpress, Monmouth Junction, NJ, USA), a potent auxin antagonist, was used for arresting root hair tip growth. In five independent plants per treatment, FM4-64 ( $4 \mu\text{mol.L}^{-1}$ ), filipin III ( $10 \mu\text{g.mL}^{-1}$ ), and auxinole ( $20 \mu\text{mol.L}^{-1}$ ) in modified liquid MS medium were individually applied by perfusion directly to the microscopy chamber. The total volume of the modified liquid MS medium with FM4-64, filipin III, or auxinole applied was  $100 \mu\text{L}$ , added in 10 separate steps of  $10 \mu\text{L}$  each for 10 min. After perfusion, the plants were directly observed using a spinning disk microscope.

#### Life imaging of GFP-RHD2 in root hairs after filipin III and auxinole application

Plants 2- to 3-day-old were transferred to microscopy chambers containing liquid modified MS medium according to Ovečka et al. (2005, 2014). Subsequent stabilization for 24 h in a glass cuvette in an environmental chamber allowed the continuation of root growth and the formation of new root

hairs. Growing root hairs ( $n = 3–5$  root hairs from five plants) were observed using an epifluorescence microscope Zeiss Axio Imager M2 equipped with DIC optics and epifluorescence metal halide source illuminator HXP 120 V (Zeiss, Oberkochen, Germany), and analyzed using Zeiss ZEN 2012 Blue software (Zeiss, Germany). Root hairs were recorded at 1 min intervals for 5 min before the application, then for another 5 min throughout the application of mock,  $10 \mu\text{g}\cdot\text{mL}^{-1}$  filipin III, or  $20 \mu\text{mol}\cdot\text{L}^{-1}$  auxinole in modified liquid MS medium, respectively, and 5 min after application. Modified MS medium without inhibitors was used as a mock treatment. The total volume of applied solutions (control medium, filipin III, and auxinole) was  $50 \mu\text{L}$ , added sequentially in five separate steps of  $10 \mu\text{L}$  each. Gentle application by perfusion was performed directly at the microscope stage in the sample chambers at the respective time points of acquisition. Imaging was performed with a Plan-Neofluar  $40\times/0.75$  NA dry objective and documented with a Zeiss AxioCam ICm1 camera. A filter set providing a wavelength of  $450–490 \text{ nm}$  for the excitation and  $515–565 \text{ nm}$  for the emission at  $400\text{-ms}$  exposure time was used to visualize the GFP signal. For the filipin III signal, the filter set provided an excitation wavelength of  $335–383 \text{ nm}$  and an emission wavelength of  $420–470 \text{ nm}$  was used. The exposure time was  $200 \text{ ms}$  for both filipin III and DIC channel acquisitions. The image scaling for both channels was  $0.116 \times 0.116 \mu\text{m}$  in  $x \times y$  dimensions, and with the  $z$  dimension  $1.65 \mu\text{m}$  for the filipin III channel, and  $1.81 \mu\text{m}$  for the GFP channel.

### Colocalization analysis

The colocalization of fluorescence signals was analyzed using a spinning disk microscope by simultaneous signal acquisition with two independent Evolve 512 EMCCD cameras. After camera calibration for proper alignment, the fluorescence signals of the two markers were imaged and recorded using a camera streaming mode. Semi-quantitative signal intensity analysis was performed on one selected Z-stack of the scanned area. The signal intensity and mode of colocalization were analyzed in double transgenic lines GFP-RHD2  $\times$  mCherry-VTI12 and GFP-RHD2  $\times$  mCherry-RabF2b. Similarly, the fluorescence intensity was determined in single transgenic lines GFP-RHD2, GFP-RabA1d, and RabF2a-YFP stained with FM4–64. Profiles for quantitative signal intensity distribution and colocalization were generated using Zen Blue 2014 software (Carl Zeiss, Germany) and graphically edited in Microsoft Excel. Quantitative colocalization analysis of vesicular compartments was conducted within selected ROIs from five individual root hairs at five different time points. Three ROIs selected at each analyzed time point led to 75 measurements of vesicular compartments performed in total. Analogously, colocalization analysis was performed on PMs from five individual root hairs at five different time points. A particular ROI covering the membrane area of each respective time point was selected, providing 25 measurements on PMs in total. Selected ROIs of vesicles and membranes of double lines (GFP-

RHD2  $\times$  mCherry-VTI12 and GFP-RHD2  $\times$  mCherry-RabF2b) and FM4–64 staining of GFP-RHD2, GFP-RabA1d, and RabF2a-YFP lines were subjected to quantitative colocalization analysis using Pearson's correlation coefficients according to Costes et al. (2004) in Zen Blue 2014 software (Carl Zeiss, Germany). The results were graphically edited using Microsoft Excel.

### 3D rendering of GFP-RHD2 distribution

Data obtained by LSFM time-lapse imaging from growing primary roots and root hairs of the GFP-RHD2 line were subjected to 3D rendering. In Zen 2014 software, black edition (Carl Zeiss, Germany), a subset of selected time-points (lasting for 4 h and 25 min of imaging) was created from the whole volume of the root (containing 483 Z-stacks). The subsets were selected to capture the different developmental stages of root hair formation in the root differentiation zone. The output data were imported into Arivis Vision4D version 2.12.6 software (Arivis AG, Rostock, Germany) and automatically converted to the \*.sis file. Subsequently, data were visualized as 3D objects by activating the 4D viewer in the Viewer Types Panel. 3D objects were rendered in the maximum intensity mode. The color scale was switched to rainbow coloring to enhance the contrast visibility of the fluorescence signal intensities and distribution. The lowest and highest saturation points were adjusted to 219 (black) and 427 (red), respectively. For 3D visualizations of primary root cross-sections, clipping around a region of interest was adjusted using a 4D clipping panel and ROI tab. Videos were configured by arranging keyframes and rendered as movies for export in the storyboard extension. Animations were prepared by clipping the 3D model against the  $y$ - and  $z$ -planes in a 4D clipping panel and using rotation and zoom tools.

### Single-particle tracking of compartments containing GFP-RHD2

Arivis Vision4D program, version 3.1.4. (Arivis AG, Germany) was used for quantitative tracking of the GFP-RHD2 compartments. Three-day-old plants were imaged using Airyscan CLSM. Different stages of root hair development were selected, and one particular Z-stack of the field of view was imaged for 60 s. Acquired data were processed and quantified using the Tracked cells function of the Arivis software. Before analysis, the following conditions were set up for normalization: (1) the highest and lowest fluorescence intensity thresholds were set to 30 and 410, respectively; (2) the distance of compartment movement recorded during one time period should not exceed  $5 \mu\text{m}$ ; (3) accepted compartments did not disappear from the image plane for more than two time periods during acquisition; and (4) the accepted compartment surface area was always in the range of  $0.5–3 \mu\text{m}^2$ . Characterized parameters were minimum, maximum, and average speed, the distance of GFP-RHD2 compartments moving in different stages of root hair development, namely in the early bulges, late bulges, short growing root hairs, and longer growing root hairs. The analyzed compartments were

divided into the following subgroups: moving to and contacting the apical PM, moving in the cytoplasm without any contact with the PM, and contacting the PM and moving back to the cytoplasm. A comparison was made between compartments moving outside the bulging domain in trichoblasts and those moving in atrichoblasts. The individual color-coded trajectories of the analyzed compartments were displayed directly in the images. Arivis software was also used to generate the 2.5D fluorescence intensity profiles.

#### Data analysis and graphical presentation

Kymographs were generated from time-lapsed images acquired by LSM, Airyscan CLSM, and SD using the appropriate plugin of Zen software (Blue version). All graphs were prepared using Microsoft Excel software. Statistical significance ( $P < 0.05$ ) was determined using the STATISTICA 12 (StatSoft, TIBCO Software Inc., Palo Alto, CA, USA) by analysis of variance (ANOVA) and subsequent Fisher's least significant difference (LSD) tests ( $P < 0.05$ ).

#### Accession numbers

Sequence data from this article can be found in the GenBank/EMBL/TAIR (<https://www.arabidopsis.org>) data libraries under accession numbers: AT5G51060 (*RHD2*), AT4G18800 (*RABA1D*), AT1G26670 (*VTI12*), AT5G45130 (*RABF2A*), and AT3G62980 (*TIR1*).

#### Supplemental data

The following materials are available in the online version of this article.

**Supplemental Figure S1.** Semi-quantitative analysis of root hair tip growth rate in individual developmental stages.

**Supplemental Figure S2.** Semi-quantitative analysis of the tip-focused GFP-RHD2 spatial signal intensity distribution obtained using the 2.5D rendering function in different stages of root hair development.

**Supplemental Figure S3.** Example of a quantitative colocalization analysis between FM4–64 and GFP-RHD2.

**Supplemental Figure S4.** Colocalization analysis of early and late endosomal markers with selective membrane styryl dye FM4–64 in growing root hairs.

**Supplemental Figure S5.** Example of a quantitative colocalization analysis between FM4–64 and early endosomal marker GFP-RabA1d.

**Supplemental Figure S6.** Example of a quantitative colocalization analysis between FM4–64 and late endosomal marker RabF2a-YFP.

**Supplemental Figure S7.** Localization of early and late endosomal markers in growing root hairs of control lines.

**Supplemental Figure S8.** Example of a quantitative colocalization analysis between GFP-RHD2 and early endosomal/TGN marker mCherry-VTI12.

**Supplemental Figure S9.** Example of a semi-quantitative colocalization analysis between GFP-RHD2 and late endosomal marker mCherry-RabF2b.

**Supplemental Figure S10.** Quantitative evaluation of the tracking parameters of compartments containing GFP-RHD2 in different stages of root hair development.

**Supplemental Figure S11.** Qualitative determination and quantitative tracking of moving compartments containing GFP-RHD2 in atrichoblasts and trichoblasts outside of the bulging zone.

**Supplemental Figure S12.** Changes of GFP-RHD2 localization in growing root hairs after filipin III application.

**Supplemental Figure S13.** Localization analysis of GFP-RHD2 in bulge and root hair after treatment with filipin III.

**Supplemental Figure S14.** Localization analysis of GFP-RHD2 and GFP-RabA1d in root hairs after treatment with filipin III.

**Supplemental Figure S15.** Localization analysis of RabF2a-YFP in root hairs after treatment with filipin III.

**Supplemental Figure S16.** Localization analysis of GFP-RHD2 and mCherry-RabF2b in root hairs after treatment with filipin III.

**Supplemental Figure S17.** Inhibition of growing root hairs and changes of GFP-RHD2 localization after auxinole application.

**Supplemental Figure S18.** Localization analysis of GFP-RHD2 in root hairs treated by auxinole.

**Supplemental Movie S1.** 3D maximum intensity projection and a volumetric rendering of a pseudo-color-coded semi-quantitative fluorescence intensity distribution of GFP-RHD2 in the root hair formation zone in Arabidopsis from LSM imaging.

**Supplemental Movie S2.** Time-lapse imaging of developing root hair in the root of transgenic Arabidopsis plant carrying GFP-RHD2 using LSM. Exposure time 40 ms, time point every 5 min, imaging time 220 min.

**Supplemental Movie S3.** Time-lapse imaging of developing late bulge using Airyscan CLSM showing polarized accumulation of GFP-RHD2 at the apical PM domain and cortical cytoplasm in a pseudo-color-coded semi-quantitative fluorescence intensity distribution. Exposure time 700 ms, time point every 9.8 s, imaging time 16 min.

**Supplemental Movie S4.** Time-lapse imaging of short growing root hair using Airyscan CLSM showing polarized accumulation of GFP-RHD2 at the apical PM domain and cortical cytoplasm in a pseudo-color-coded semi-quantitative fluorescence intensity distribution. Exposure time 700 ms, time point every 9.8 s, imaging time 8 min.

**Supplemental Movie S5.** Time-lapse imaging of long growing root hair using Airyscan CLSM showing polarized accumulation of GFP-RHD2 at the apical PM domain and cortical cytoplasm in a pseudo-color-coded semi-quantitative fluorescence intensity distribution. Exposure time 700 ms, time point every 9.8 s, imaging time 8 min.

**Supplemental Movie S6.** Time-lapse imaging of non-growing root hair using Airyscan CLSM showing polarized accumulation of GFP-RHD2 at the apical PM domain and cortical cytoplasm in a pseudo-color-coded semi-quantitative fluorescence intensity distribution.

Exposure time 700 ms, time point every 9.8 s, imaging time 3 min.

**Supplemental Movie S7.** Time-lapse imaging of close contacts (arrows) between moving compartments containing GFP-RHD2 and the apical PM in the apex of late bulge using Airyscan CLSM in a pseudo-color-coded semi-quantitative fluorescence intensity distribution. Exposure time 700 ms, time point every 9.8 s, imaging time 60 s, maximum intensity projections of two Z-stacks.

**Supplemental Movie S8.** Time-lapse imaging of contact between moving compartment containing GFP-RHD2 and the apical PM in the apex of a late bulge showing fast full integration. Imaging using Airyscan CLSM in a pseudo-color-coded semi-quantitative fluorescence intensity distribution. Exposure time 700 ms, time point every 9.8 s, imaging time 30 s, maximum intensity projections of two Z-stacks.

**Supplemental Movie S9.** Time-lapse imaging of contact between moving compartment containing GFP-RHD2 and the apical PM in the apex of a late bulge showing temporal contact without full integration. Imaging using Airyscan CLSM in a pseudo-color-coded semi-quantitative fluorescence intensity distribution. Exposure time 700 ms, time point every 9.8 s, imaging time 50 s, maximum intensity projections of two Z-stacks.

**Supplemental Movie S10.** Time-lapse imaging of growing root hair using DIC optics showing growth rate and cytoarchitecture during perfusion application of control medium. Exposure time 200 ms, time point every 1 min, imaging time 14 min.

**Supplemental Movie S11.** Time-lapse imaging of growing root hair using fluorescence excitation for localization of GFP-RHD2 during perfusion application of control medium. Exposure time 400 ms, time point every 1 min, imaging time 14 min.

**Supplemental Movie S12.** Time-lapse imaging of growing root hair using DIC optics showing growth rate and cytoarchitecture during perfusion application of filipin III. Exposure time 200 ms, time point every 1 min, imaging time 14 min.

**Supplemental Movie S13.** Time-lapse imaging of growing root hair using fluorescence excitation for localization of GFP-RHD2 during perfusion application of filipin III. Exposure time 400 ms, time point every 1 min, imaging time 14 min.

## Acknowledgments

We thank Liam Dolan for the seeds of the *rhd2-1* mutant and the GFP-RHD2 line. We would like to thank Editage ([www.editage.com](http://www.editage.com)) for English language editing.

## Funding

This work was supported by the Czech Science Foundation GAČR (project Nr. 19-18675S) and by the ERDF project “Plants as a tool for sustainable global development” (No. CZ.02.1.01/0.0/0.0/16\_019/0000827).

**Conflict of interest statement:** Authors declare that they have no conflicts of interests.

## References

- Berson T, Wangenheim D, Takáč T, Šamajová O, Rosero A, Ovečka M, Komis G, Stelzer EH, Šamaj J (2014) Trans-Golgi network localized small GTPase RabA1d is involved in cell plate formation and oscillatory root hair growth. *BMC Plant Biol* **14**: 252
- Bonneau L, Gerbeau-Pissot P, Thomas D, Der C, Lherminier J, Bourque S, Roche Y, Simon-Plas F (2010) Plasma membrane sterol complexation, generated by filipin, triggers signalling responses in tobacco cells. *Biochim Biophys Acta* **1798**: 2150–2159
- Bottanelli F, Foresti O, Hanton S, Denecke J (2011) Vacuolar transport in tobacco leaf epidermis cells involves a single route for soluble cargo and multiple routes for membrane cargo. *Plant Cell* **23**: 3007–3025
- Boutté Y, Frescatada-Rosa M, Men S, Chow C-M, Ebine K, Gustavsson A, Johansson L, Ueda T, Moore I, Jürgens G, et al. (2009) Endocytosis restricts Arabidopsis KNOLLE syntaxin to the cell division plane during late cytokinesis. *EMBO J* **29**: 546–558
- Campanoni P, Blatt MR (2007) Membrane trafficking and polar growth in root hairs and pollen tubes. *J Exp Bot* **58**: 65–74
- Carol RJ, Dolan L (2002) Building a hair: tip growth in *Arabidopsis thaliana* root hairs. *Phil Trans R Soc Lond B* **357**: 815–821
- Carol RJ, Takeda S, Linstead P, Durrant MC, Kakesova H, Derbyshire P, Drea S, Zarsky V, Dolan L (2005) A RhoGDP dissociation inhibitor spatially regulates growth in root hair cells. *Nature* **438**: 1013–1016
- Chapman JM, Muhlemann JK, Gayomba SR, Muday GK (2019) RBOH-dependent ROS synthesis and ROS scavenging by plant specialized metabolites to modulate plant development and stress responses. *Chem Res Toxicol* **32**: 370–396
- Clouse SD (2002) Arabidopsis mutants reveal multiple roles for sterols in plant development. *Plant Cell* **14**: 1995–2000
- Cole RA, Fowler JE (2006) Polarized growth: maintaining focus on the tip. *Curr Opin Plant Biol* **9**: 579–588
- Contento AL, Bassham DC (2012) Structure and function of endosomes in plant cells. *J Cell Sci* **125**: 3511–3518
- Costes SV, Daelemans D, Cho EH, Dobbin Z, Pavlakis G, Lockett S (2004) Automatic and quantitative measurement of protein-protein colocalization in live cells. *Biophys J* **86**: 3993–4003
- Denninger P, Reichelt A, Schmidt VAF, Mehlhorn DG, Asseck LY, Stanley CE, Keinath NF, Evers JF, Grefen C, Grossmann G (2019) Distinct RopGEFs successively drive polarization and outgrowth of root hairs. *Curr Biol* **29**: 1854–1865
- Dolan L, Duckett CM, Grierson C, Linstead P, Schneider K, Lawson E, Dean C, Poethig S, Roberts K (1994) Clonal relationships and cell patterning in the root epidermis of Arabidopsis. *Development* **120**: 2465–2474
- Foreman J, Demidchik V, Bothwell JH, Mylona P, Miedema H, Torres MA, Linstead P, Costa S, Brownlee C, Jones JD, et al. (2003) Reactive oxygen species produced by NADPH oxidase regulate plant cell growth. *Nature* **422**: 442–446
- Geldner N, Dénervaud-Tendon V, Hyman DL, Mayer U, Stierhof YD, Chory J (2009) Rapid, combinatorial analysis of membrane compartments in intact plants with a multicolor marker set. *Plant J* **59**: 169–178
- Grierson C, Schiefelbein J (2002) Root hairs. *Arabidopsis Book* **1**: e0060
- Gillooly DJ, Simonsen A, Stenmark H (2001) Cellular functions of phosphatidylinositol3-phosphate and FYVE domain proteins. *Biochem J* **355**: 249–258
- Grebe M, Xu J, Möbius W, Ueda T, Nakano A, Geuze HJ, Rook MB, Scheres B (2003) Arabidopsis sterol endocytosis involves

- actin-mediated trafficking via ARA6-positive early endosomes. *Curr Biol* **13**: 1378–1387
- Haas TJ, Sliwinski MK, Martínez DE, Preuss M, Ebine K, Ueda T, Nielsen E, Odorizzi G, Otegui MS** (2007) The Arabidopsis AAA ATPase SKD1 is involved in multi vesicular endosome function and interacts with its positive regulator LYST-INTERACTING PROTEIN 5. *Plant Cell* **19**: 1295–1312
- Hao H, Fan L, Chen T, Li R, Li X, He Q, Botella MA, Lin J** (2014) Clathrin and membrane microdomains cooperatively regulate RbohD dynamics and activity in Arabidopsis. *Plant Cell* **26**: 1729–1745
- Jones MA, Shen JJ, Fu Y, Li H, Yang Z, Grierson CS** (2002) The Arabidopsis Rop2 GTPase is a positive regulator of both root hair initiation and tip growth. *Plant Cell* **14**: 763–776
- Jones MA, Raymond MJ, Smirnov N** (2006) Analysis of the root-hair morphogenesis transcriptome reveals the molecular identity of six genes with roles in root-hair development in Arabidopsis. *Plant J* **45**: 83–100
- Jones MA, Raymond MJ, Yang Z, Smirnov N** (2007) NADPH oxidase-dependent reactive oxygen species formation required for root hair growth depends on ROP GTPase. *J Exp Bot* **58**: 1261–1270
- Kaya H, Takeda S, Kobayashi MJ, Kimura S, Iizuka A, Imai A, Hishinuma H, Kawarazaki T, Mori K, Yamamoto Y, et al.** (2019) Comparative analysis of the reactive oxygen species-producing enzymatic activity of Arabidopsis NADPH oxidases. *Plant J* **98**: 291–300
- Kiegle E, Gilliam M, Haselof, J, Tester M** (2000) Hyperpolarisation-activated calcium channels found only in cells from the elongation zone of *Arabidopsis thaliana* roots. *Plant J* **21**: 225–229
- Lindsey K, Pullen ML, Topping JF** (2003) Importance of plant sterols in pattern formation and hormone signalling. *Trends Plant Sci* **8**: 521–525
- Liu P, Zhang L, Li R, Wang Q, Niehaus K, Baluška F, Šamaj J, Lin J** (2009) Lipid microdomain polarization is required for NADPH oxidase-dependent ROS signaling in *Picea meyeri* pollen tube tip growth. *Plant J* **60**: 303–313
- Mangano S, Denita-Juarez SP, Choi HS, Marzol E, Hwang Y, Ranocha P, Velasquez SM, Borassi C, Barberini ML, Aptekmann AA, et al.** (2017) Molecular link between auxin and ROS-mediated polar growth. *Proc Natl Acad Sci USA* **114**: 5289–5294
- Menon AK** (2002) Lipid transport - an overview. *Semin Cell Dev Biol* **13**: 159–162
- Miedema H, Bothwell JHF, Brownlee C, Davies JM** (2001) Calcium uptake by plant cells—channels and pumps acting in concert. *Trends Plant Sci* **11**: 514–519
- Milhaud J, Hartmann MA, Bolard J** (1988) Interaction of the polyene antibiotic filipin with model and natural membranes containing plant sterols. *Biochim Biophys Acta* **943**: 315–325
- Molendijk AJ, Bischoff F, Rajendrakumar CS, Friml J, Braun M, Gilroy S, Palme K** (2001) *Arabidopsis thaliana* Rop GTPases are localized to tips of root hairs and control polar growth. *EMBO J* **20**: 2779–2788
- Monshausen GB, Bibikova TN, Messerli MA, Shi C, Gilroy S** (2007) Oscillations in extracellular pH and reactive oxygen species modulate tip growth of Arabidopsis root hairs. *Proc Natl Acad Sci USA* **104**: 20996–21001
- Morel J, Clavero S, Mongrand S, Furt F, Fromentin J, Bessoule J-J, Blein J-P, Simon-Plas F** (2006) Proteomics of plant detergent-resistant membranes. *Mol Cell Proteomics* **5**: 1396–1411
- Mukherjee S, Maxfield FR** (2000) Role of membrane organization and membrane domains in endocytic lipid trafficking. *Traffic* **1**: 203–211
- Murashige T, Skoog F** (1962) A Revised Medium for Rapid Growth and Bio Assays with Tobacco Tissue Cultures. *Physiol Plant* **15**: 473–497
- Nichols BJ, Kenworthy AK, Polishchuk RS, Lodge R, Roberts TH, Hirschberg K, Phair RD, Lippincott-Schwartz J** (2001) Rapid cycling of lipid raft markers between the cell surface and Golgi complex. *J Cell Biol* **153**: 529–542
- Ovečka M, Berson T, Beck M, Derksen J, Šamaj J, Baluška F, Lichtscheidl IK** (2010) Structural sterols are involved in both the initiation and tip growth of root hairs in *Arabidopsis thaliana*. *Plant Cell* **22**: 2999–3019
- Ovečka M, Lang I, Baluška F, Ismail A, Illés P, Lichtscheidl IK** (2005) Endocytosis and vesicle trafficking during tip growth of root hairs. *Protoplasma* **226**: 39–54
- Ovečka M, Lichtscheidl I, Šamaj J** (2014) Live microscopy analysis of endosomes and vesicles in tip-growing root hairs. *Methods Mol Biol* **1209**: 31–44
- Ovečka M, Vaskebová L, Komis G, Luptovciak I, Smertenko A, Šamaj J** (2015) Preparation of plants for developmental and cellular imaging by light-sheet microscopy. *Nat Protoc* **10**: 1234–1247
- Posé D, Castanedo I, Borsani O, Nieto B, Rosado A, Tacconat L, Ferrer A, Dolan L, Valpuesta V, Botella MA** (2009) Identification of the Arabidopsis *dry2/sqe1-5* mutant reveals a central role for sterols in drought tolerance and regulation of reactive oxygen species. *Plant J* **59**: 63–76
- Qi X, Zheng H** (2013) Rab-A1c GTPase defines a population of the trans-Golgi network that is sensitive to endosidin1 during cytokinesis in Arabidopsis. *Mol Plant* **6**: 847–859
- Reyes FC, Buono R, Otegui MS** (2011) Plant endosomal trafficking pathways. *Curr Opin Plant Biol* **14**: 666–673
- Sagi M, Fluhr R** (2006) Production of reactive oxygen species by plant NADPH oxidases. *Plant Physiol* **141**: 336–340
- Sanderfoot AA, Kovaleva V, Bassham DC, Raikhel NV** (2001) Interactions between syntaxins identify at least five SNARE complexes within the Golgi/prevacuolar system of the Arabidopsis cell. *Mol Biol Cell* **12**: 3733–3743
- Šamaj J, Müller J, Beck M, Böhm N, Menzel D** (2006) Vesicular trafficking, cytoskeleton and signalling in root hairs and pollen tubes. *Trends Plant Sci* **11**: 594–600
- Sena F, Sotelo-Silveira M, Astrada S, Botella MA, Malacrida L, Borsani O** (2017) Spectral phasor analysis reveals altered membrane order and function of root hair cells in Arabidopsis *dry2/sqe1-5* drought hypersensitive mutant. *Plant Physiol Biochem* **119**: 224–231
- Schiefelbein JW, Somerville C** (1990) Genetic control of root hair development in *Arabidopsis thaliana*. *Plant Cell* **2**: 235–243
- Simons K, Toomre D** (2000) Lipid rafts and signal transduction. *Nat Rev Mol Cell Biol* **1**: 31–39
- Směkalová V, Luptovciak I, Komis G, Šamajová O, Ovečka M, Doskočilová A, Takáč T, Vadovič P, Novák O, Pechan T, et al.** (2014) Involvement of YODA and mitogen activated protein kinase 6 in Arabidopsis post-embryonic root development through auxin up-regulation and cell division plane orientation. *New Phytol* **203**: 1175–1193
- Sorek N, Gutman O, Bar E, Abu-Abied M, Feng X, Running MP, Lewinsohn E, Ori N, Sadot E, Henis YI, et al.** (2011) Differential effects of prenylation and S-acylation on type I and II ROPS membrane interaction and function. *Plant Physiol* **155**: 706–720
- Sorek N, Poraty L, Sternberg H, Buriakovsky E, Bar E, Lewinsohn E, Yalovsky S** (2017) Activation status coupled transient S-acylation determines membrane partitioning of a plant Rho-related GTPase. *Mol Cell Biol* **37**: 2144–2154
- Srivastava V, Malm E, Sundqvist G, Bulone V** (2013) Quantitative proteomics reveals that plasma membrane microdomains from poplar cell suspension cultures are enriched in markers of signal transduction, molecular transport, and callose biosynthesis. *Mol Cell Proteomics* **12**: 3874–3885
- Stanislas T, Hüser A, Barbosa IC, Kiefer CS, Brackmann K, Pietra S, Gustavsson A, Zourelidou M, Schwechheimer C, Grebe M** (2015) Arabidopsis D6PK is a lipid domain-dependent mediator of root epidermal planar polarity. *Nat Plants* **1**: 15162

- Takeda S, Gapper C, Kaya H, Bell E, Kuchitsu K, Dolan L** (2008) Local positive feedback regulation determines cell shape in root hair cells. *Science* **319**: 1241–1244
- Torres MA, Dangel JL, Jones JD** (2002) Arabidopsis gp91phox homologues AtrbohD and AtrbohF are required for accumulation of reactive oxygen intermediates in the plant defence response. *Proc Natl Acad Sci USA* **99**: 517–522
- Ueda T, Uemura T, Sato MH, Nakano A** (2004) Functional differentiation of endosomes in Arabidopsis cells. *Plant J* **40**: 783–789
- Uemura T, Ueda T, Ohniwa RL, Nakano A, Takeyasu K, Sato MH** (2004) Systematic analysis of SNARE molecules in Arabidopsis: dissection of the post-Golgi network in plant cells. *Cell Struct Funct* **29**: 49–65
- Véry AA, Davies JM** (2000) Hyperpolarization-activated calcium channels at the tip of Arabidopsis root hairs. *Proc Natl Acad Sci USA* **97**: 9801–9806
- Viotti C, Bubeck J, Stierhof YD, Krebs M, Langhans M, van den Berg W, van Dongen W, Richter S, Geldner N, Takano J, et al.** (2010) Endocytic and secretory traffic in Arabidopsis merge in the trans-Golgi network/early endosome, an independent and highly dynamic organelle. *Plant Cell* **22**: 1344–1357
- Voigt B, Timmers A, Samaj J, Hlavacka A, Ueda T, Preuss M, Nielsen E, Mathur J, Emans N, Stenmark H, et al.** (2005) Actin-based motility of endosomes is linked to the polar tip growth of root hairs. *Eur J Cell Biol* **84**: 609–621
- von Wangenheim D, Rosero A, Komis G, Samajová O, Ovečka M, Voigt B, Samaj J** (2016) Endosomal interactions during root hair growth. *Front Plant Sci* **6**: 1262
- Wachtler V, Rajagopalan S, Balasubramanian MK** (2003) Sterol-rich plasma membrane domains in the fission yeast *Schizosaccharomyces pombe*. *J Cell Sci* **116**: 867–874
- Wymer CL, Bibikova TN, Gilroy S** (1997) Cytoplasmic free calcium distributions during the development of root hairs of *Arabidopsis thaliana*. *Plant J* **12**: 427–439
- Zhou X, Xiang Y, Li C, Yu G** (2020) Modulatory role of reactive oxygen species in root development in model plant of *Arabidopsis thaliana*. *Front Plant Sci* **11**: 485932

### 4.3.1 Supplements

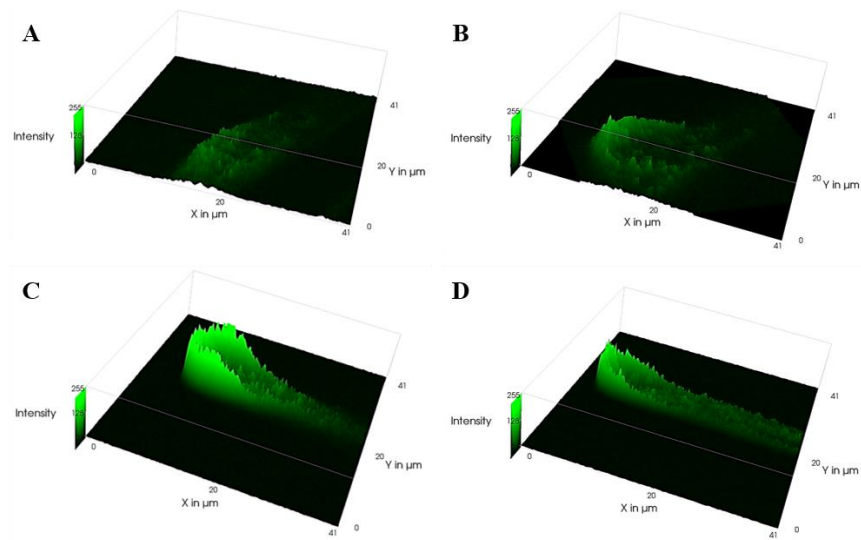


**Figure S1: Semi-quantitative analysis of the tip-focused GFP-RHD2 spatial signal intensity distribution obtained using the 2.5-D rendering function in different stages of root hair development. (A) early bulge, (B) late bulge, (C) short and (D) longer growing RHs. Adapted from Kuběnová *et al.*, 2022.**

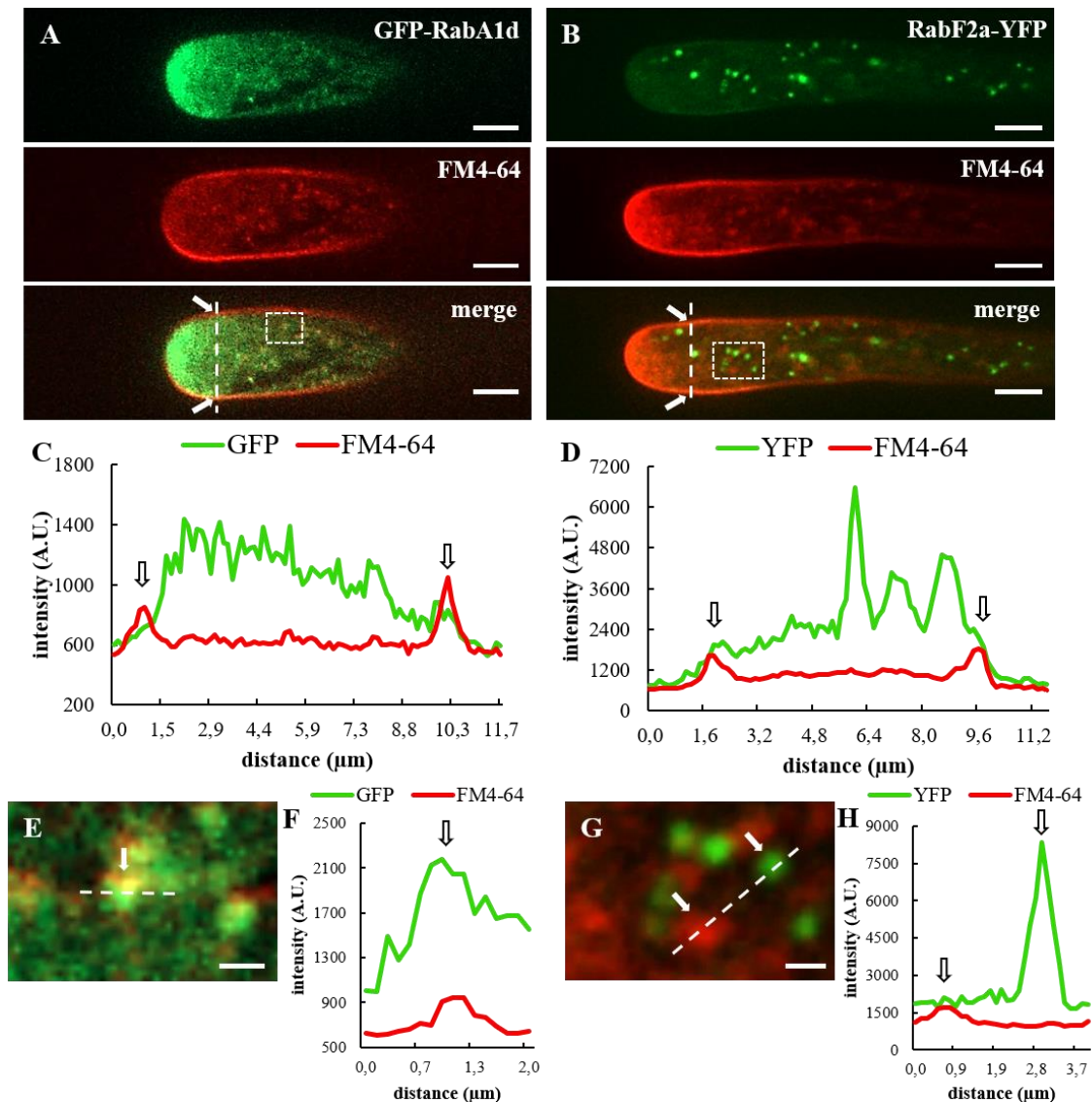


**Figure S2: Colocalization analysis of early and late endosomal markers with selective membrane styryl dye FM4-64 in growing root hairs.** Localization pattern of early endosomal marker GFP-RabA1d (**A**) or of late endosomal marker RabF2a-YFP (**B**) in the growing RH co-labelled with membrane styryl dye FM4-64. In merged image, an extend of fluorescence intensity colocalization has been analysed along the cross-section profile marked by interrupted white line (white arrows indicate the PM) and in moving compartments depicted by the white box. (**C**, **D**) Fluorescence intensity profiles of the GFP-RabA1d and FM4-64 signals (**C**) along the cross-section interrupted white line in (**A**) and fluorescence intensity profiles of the RabF2a-YFP and FM4-64 signals (**D**) along the cross-section interrupted white line in (**B**). Arrows indicate position of the PM. (**E**, **G**) Detailed image of compartments containing GFP-RabA1d and FM4-64 (**E**) within the white box in (**A**) and detailed image of compartments containing RabF2a-YFP and FM4-64 (**G**) within the white box in (**B**). Arrows indicate positions of the compartments and interrupted white lines depict the profile for fluorescence intensity quantification. (**F**, **H**) Fluorescence intensity profile of the RabA1d-GFP and FM4-64 signals (**F**) along the interrupted white line in (**E**) and fluorescence intensity profile of the RabF2a-YFP and FM4-64 signal (**H**) along the interrupted white line in (**G**). Arrows indicate position of the compartments. Scale bar = 5  $\mu\text{m}$  (**A**, **B**), 1  $\mu\text{m}$  (**E**, **G**). Adapted from Kuběnová *et al.*, 2022.



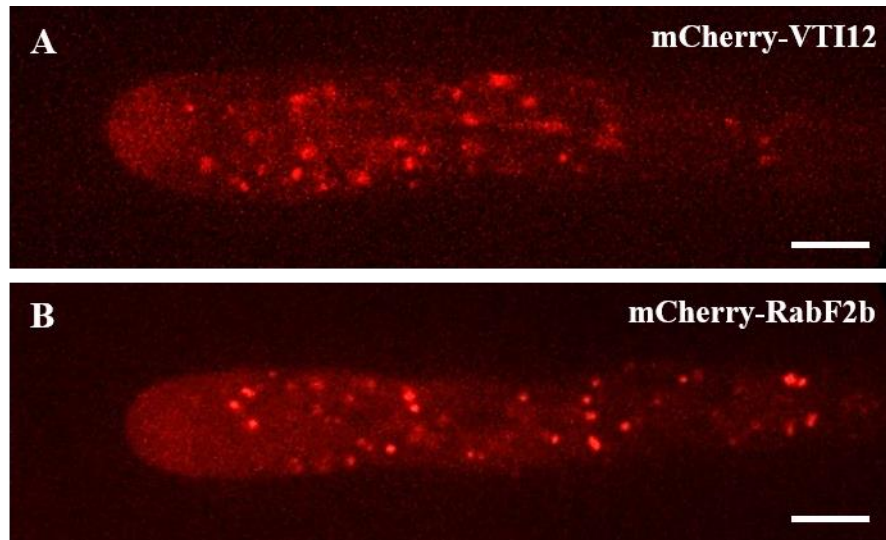


**Figure S3: Localization of early and late endosomal markers in growing root hairs of control lines.** (A) Localization of early endosomal/trans-Golgi marker mCherry-VTI12 in control (Col-0) line. (B) Localization of late endosomal marker mCherry-RabF2b in control (Col-0) line. Scale bar = 5 μm (A, B). Adapted from Kuběnová *et al.*, 2022.

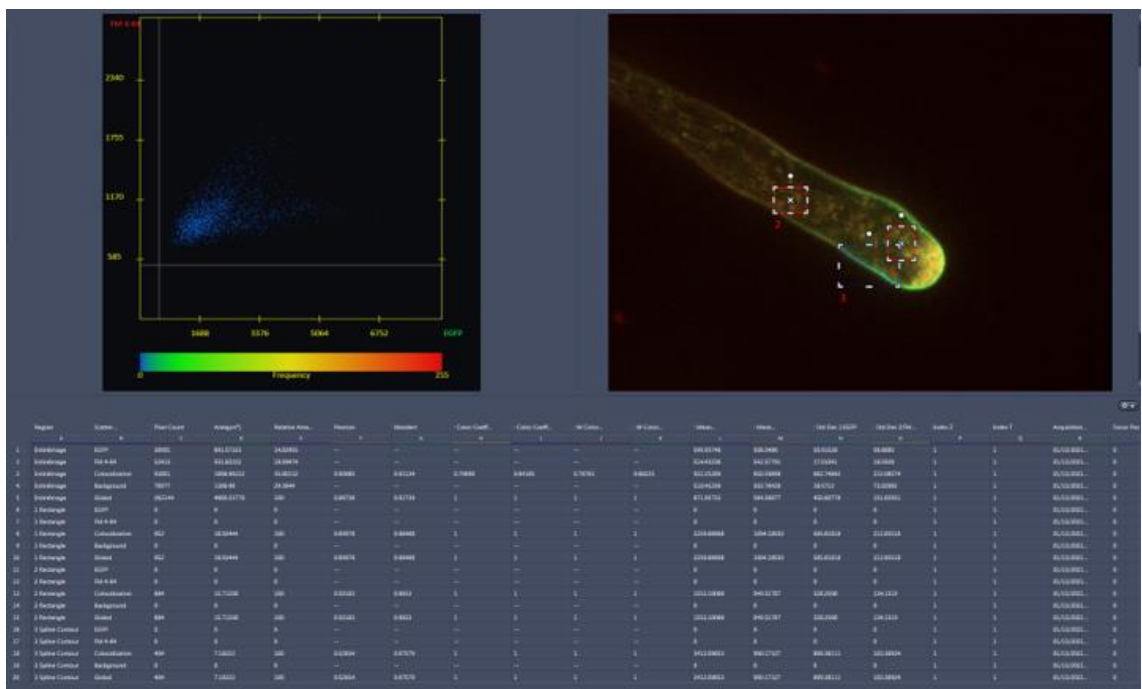


**Figure S4: Semi-quantitative colocalization analysis of GFP-RHD2 with FM4-64.** Adapted from Kuběnová *et al.*, 2022.

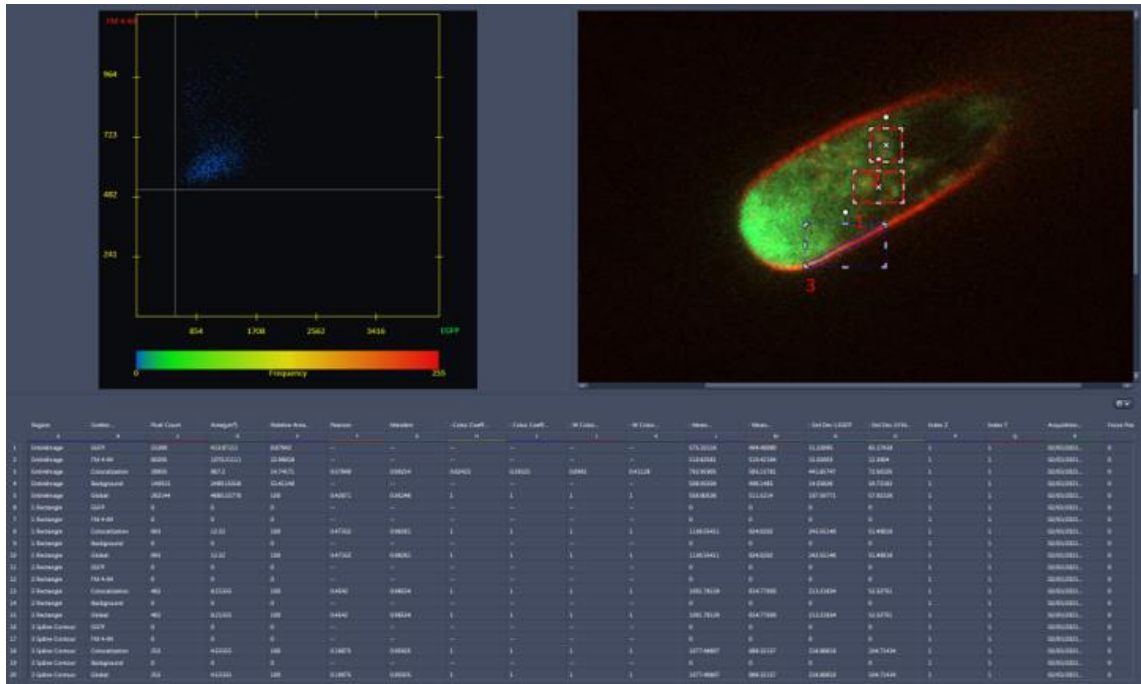


**Figure S5:** Semi-quantitative colocalization analysis of GFP-RabA1d with FM4-64. Adapted from Kuběnová *et al.*, 2022.

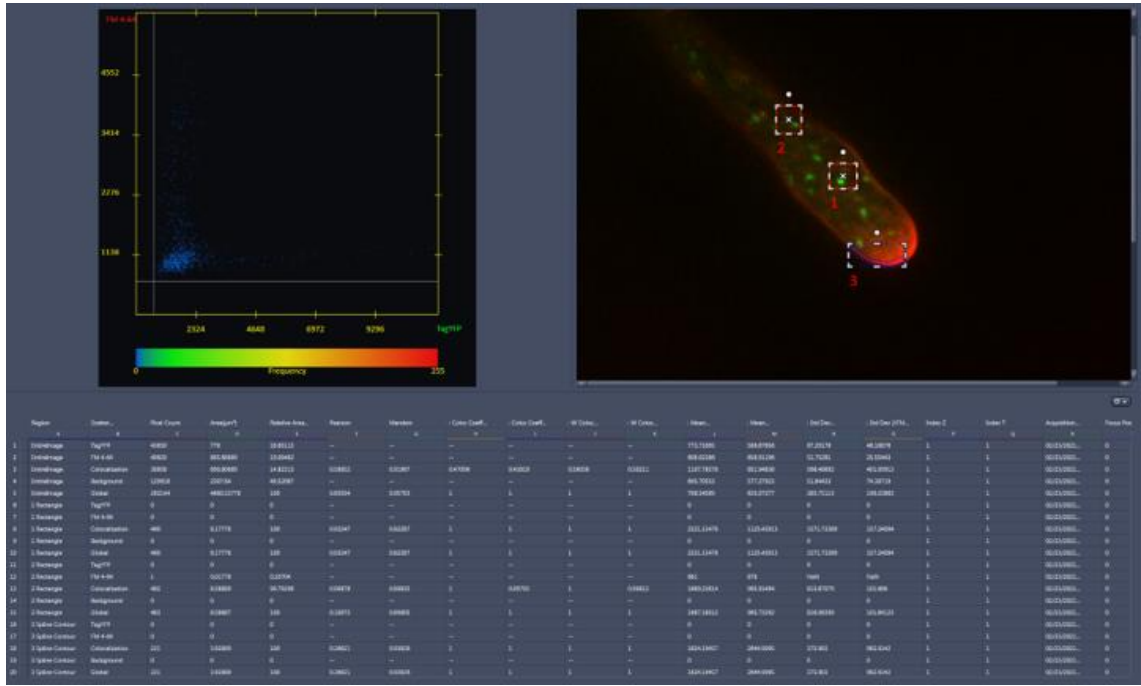


**Figure S6:** Semi-quantitative colocalization analysis of RabF2A-YFP with FM4-64. Kuběnová *et al.*, 2022.

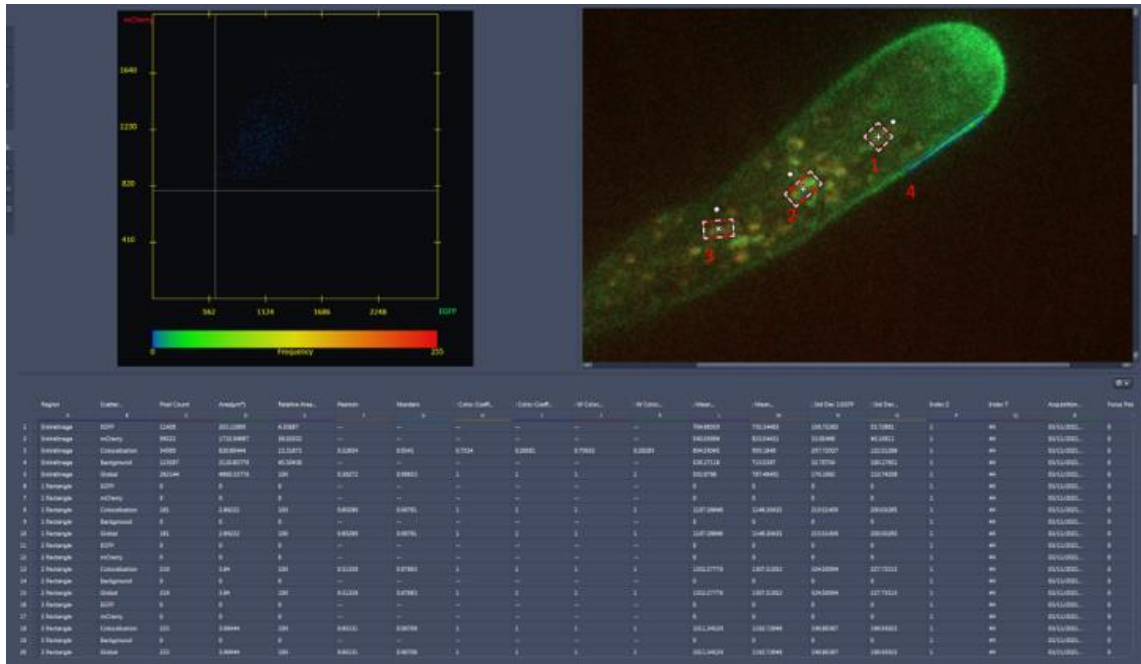


**Figure S7:** Semi-quantitative colocalization analysis of GFP-RHD2 with mCherry-VTI12. Adapted from Kuběnová *et al.*, 2022.

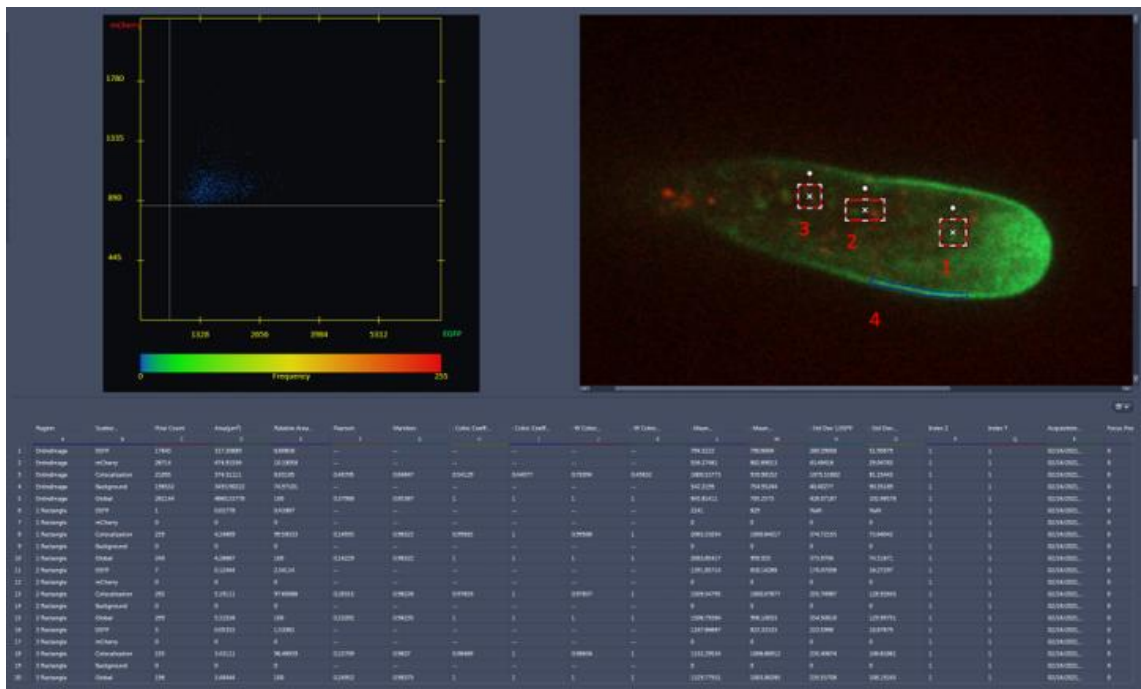


**Figure S8:** Semi-quantitative colocalization analysis of GFP-RHD2 with mCherry-RabF2b. Adapted from Kuběnová *et al.*, 2022.

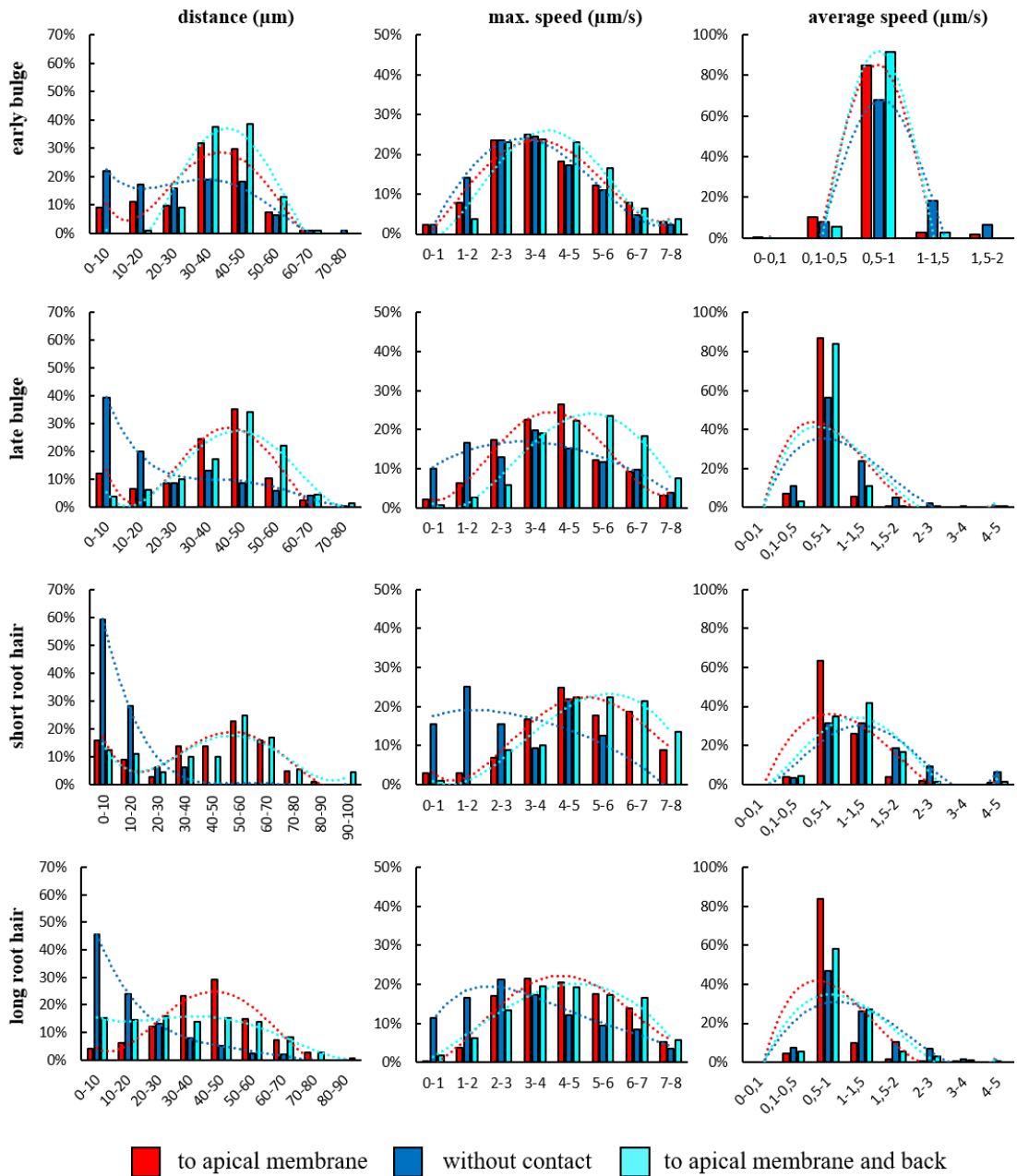


**Figure S9: Quantitative evaluation of the tracking parameters of compartments containing GFP-RHD2 in different stages of root hair development.** Distributions of distance frequencies, maximum and average speeds of analysed compartments moving to either the apical PM (red), in the cytoplasm without any contact with the apical plasma membrane (blue) or contacting the PM and moving back to the cytoplasm (cyan) in early bulge, late bulge, short and longer RHs. More than 59 compartments from 3 to 7 growing RHs from individual plants were analysed. Adapted from Kuběnová *et al.*, 2022.

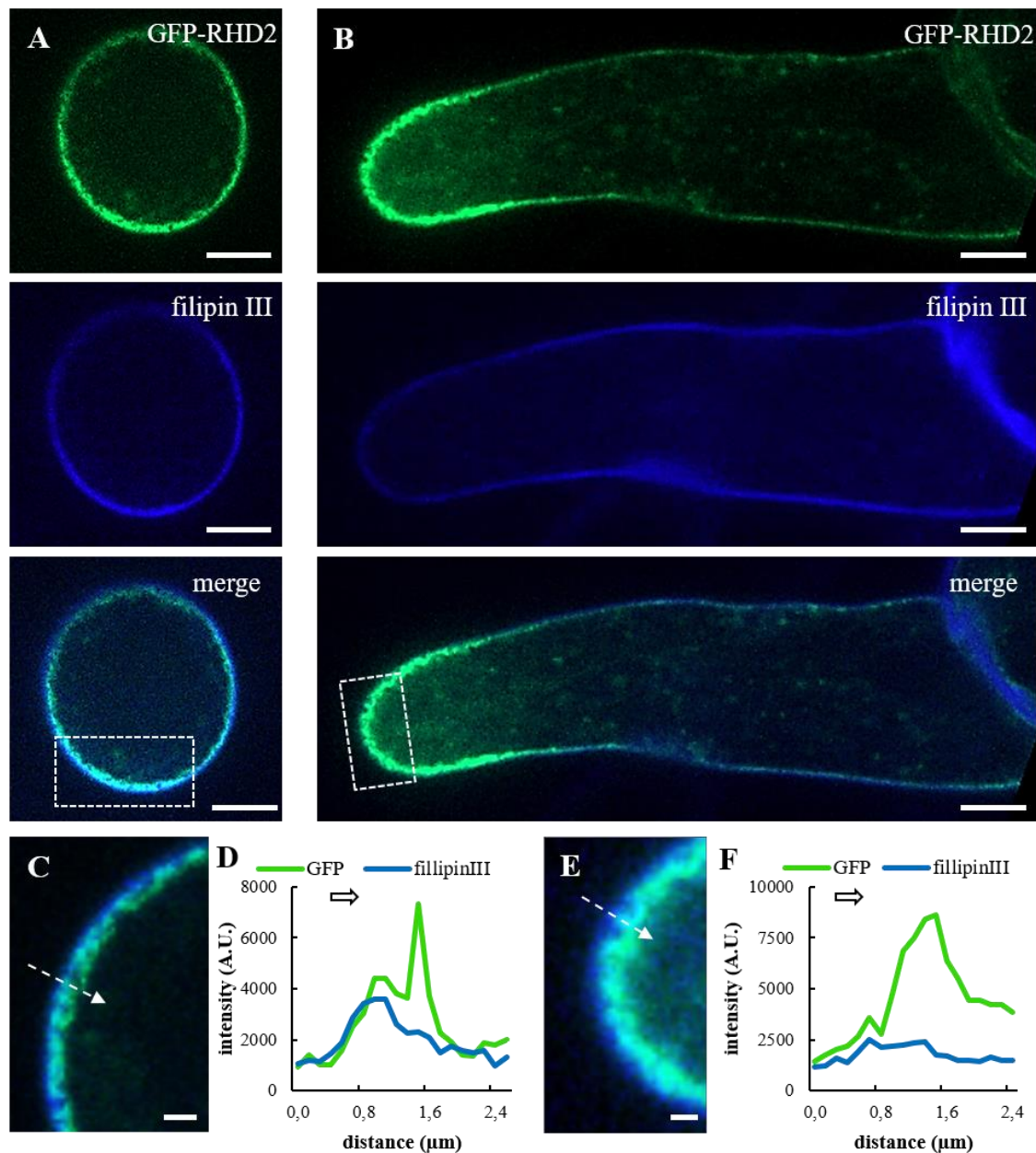


**Figure S10: Localization analysis of GFP-RHD2 in bulge and root hair after complexation of plasma membrane structural sterols with filipin III.** (A, B) Localization of GFP-RHD2 in the bulge (A) and RH (B), filipin III-positive signal at the PM, and merged images showing the distribution pattern of GFP-RHD2 compartments after filipin III treatment for 10 min. (C, E) Detailed image of the apical part of the bulge (C) and RH (E) within the white boxes in (A) and (B). Arrows indicate the position and the direction of the fluorescence intensity profile measurement. (D, F) Fluorescence intensity profiles of the GFP-RHD2 and filipin III-positive signal along arrows in (C) and (E). Arrows above the curves indicate the direction of the measurement. Scale bar = 5  $\mu\text{m}$  (A, B), 1  $\mu\text{m}$  (C, E). Adapted from Kuběnová *et al.*, 2022.

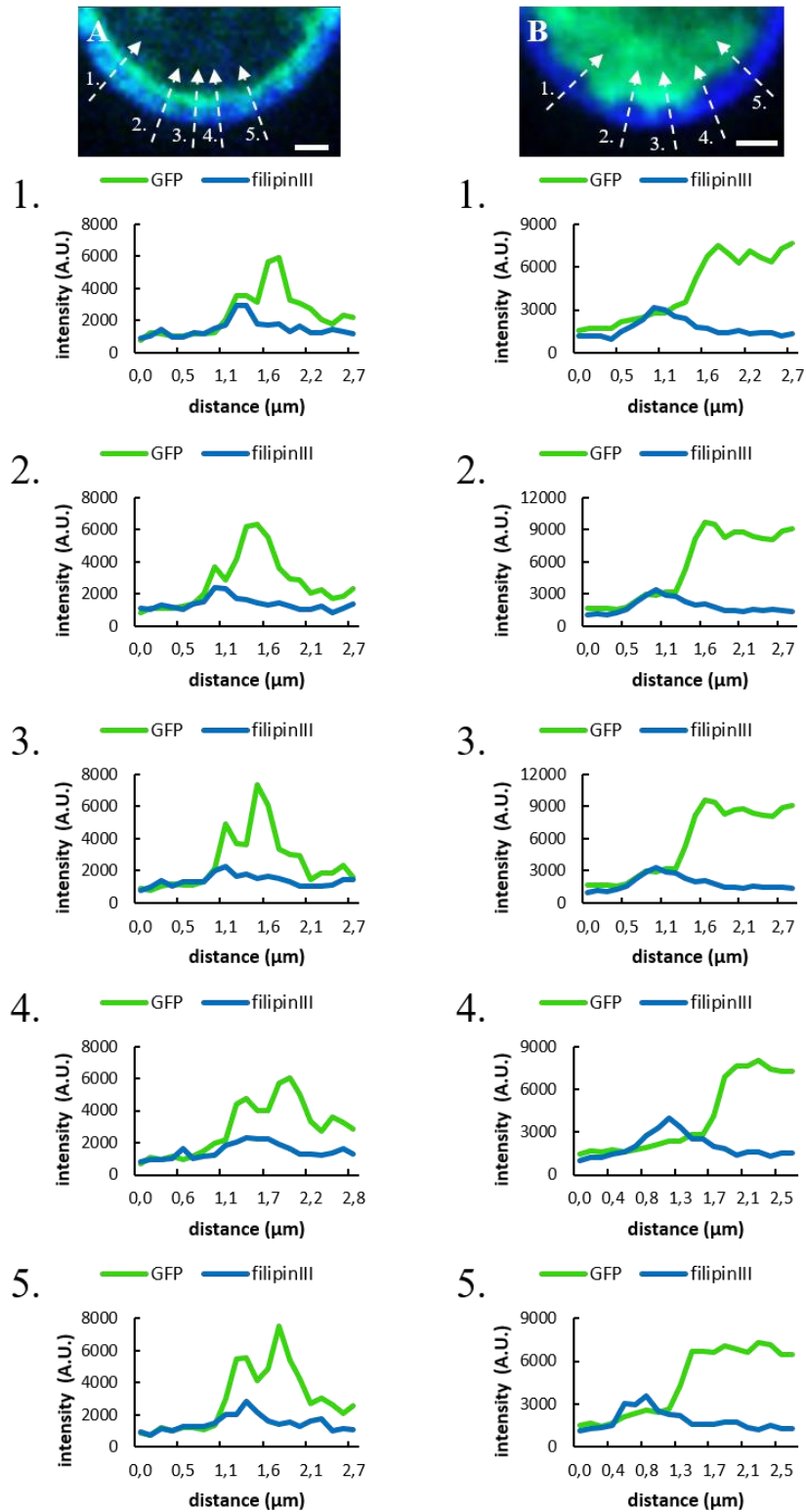


**Figure S11: Localization analysis of GFP-RHD2 and RabA1d-GFP in root hairs after complexation of plasma membrane structural sterols with filipin III.** Detailed image of the apical part of the RH showing localization of GFP-RHD2 (A) or of RabA1d-GFP (B) after filipin III treatment for 10 min. Five different arrows indicate positions and directions of independent fluorescence intensity profiles which were measured. Scale bar = 1  $\mu\text{m}$  (A, B). Adapted from Kuběnová *et al.*, 2022.

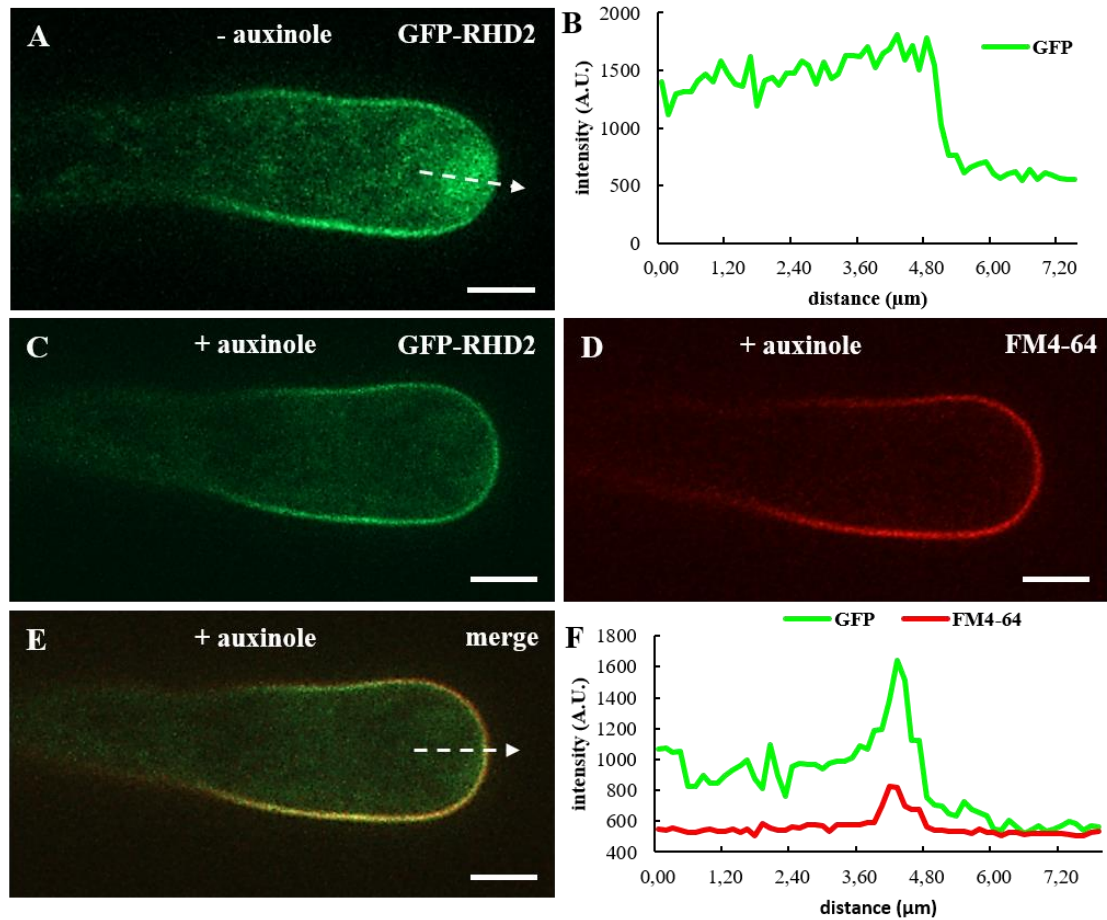


**Figure S12: Localization analysis of GFP-RHD2 in root hairs after treatment with auxinole.** (A, B) Localization pattern of GFP-RHD2 in control growing RH (A; - auxinole). White arrow indicates the position and the direction of the fluorescence intensity profile measurement. (B) Fluorescence intensity profile of the GFP-RHD2 signal along white arrow in (A). (C-F) Localization pattern of GFP-RHD2 in growing RH after treatment with auxinole (C; + auxinole). Auxinole was applied for 5 min by perfusion at the concentration 20  $\mu\text{M}$  and imaged 5 min after application (C). RH was then stained by FM4-64 (D). Both signals were colocalized in merged image (E) and semiquantitatively analysed (F). White arrow (E) indicates the position and the direction of the fluorescence intensity profile measurement. (F) Fluorescence intensity profiles of the GFP-RHD2 and FM4-64 signals along white arrow in (E). Scale bar = 5  $\mu\text{m}$  (A, C-E). Adapted from Kuběnová *et al.*, 2022.

## 5. General conclusions

Small dicotyledonous plant *Arabidopsis thaliana* serves as a model organism in almost all fields of plant biology (Boerjan *et al.*, 1992; Koornneef and Meinke 2010). Among other advantages, the small genome of *A. thaliana* has been sequenced (The Arabidopsis Genome Initiative, 2000), and relatively easy is preparation and selection of mutants and transgenic lines. Classical mutagenesis approaches were based on exposure of plants to chemical (discovered by Auerbach and Robson, 1944) or physical (firstly used by Muller, 1927) mutagens. This approach induced randomly generated single-point mutations that needed subsequent identification and description. Commonly used chemical mutagens were alkylating agents (such as EMS- ethyl methanesulphonate) and intercalating agents (for example ethidium bromide). As physical mutagens were mostly used electromagnetic radiation, such as gamma rays, X-rays or UV light (Mba *et al.*, 2010). Currently used mutagenesis techniques are based on T-DNA insertion or CRISPR/Cas9-based gene editing. These modern methods are used for targeted mutagenesis with known specific DNA localization in recipient organisms (Parinov *et al.*, 1999; Bortesi and Fischer, 2015).

*Arabidopsis thaliana* is very good model also for root biology. Arabidopsis root has simple anatomical structure, small size, and transparent appearance (Meyerowitz, 2001). The root system of Arabidopsis is formed from the main root and lateral roots. RHs are long tubular extensions of the root epidermal cells called trichoblasts (Foreman and Dolan, 2001). The support stronger anchoring of the root system in the soil, increase the root surface area for effective water and nutrients uptake, and often interact with soil microbes. Location of RHs on the root surface make them easily accessible for microscopic visualization and experimental manipulation. They are also easily treatable with different chemical and physical probes. On the other hand, RHs are dispensable for plant survival, allowing production of large numbers of viable RH mutants that provide a tool for study the mechanisms of RH development (Grierson and Schiefelbein, 2002).

Results presented in this Ph.D. thesis are arranged to three parts that describe different aspects of selected *A. thaliana* RHs mutants, including phenotypical and growth characteristics, defense reactions to specific abiotic stresses, and detailed microscopical analyses of transgenic lines carrying molecular markers. The first part is dedicated to phenotypical characterization of *der1-3* (*deformed root hairs1*) mutant, in which single



point mutation in *ACTIN2* gene influence not only structure and orientation of actin cytoskeleton, but also other cellular and developmental processes. The mutation has been induced in the *DER1* locus, which is located in the sequence of the *ACTIN2* gene, encoding the major vegetative actin (*ACTIN2*) in *A. thaliana*. Using EMS (ethyl methanesulphonate) mutagenesis in C24 ecotype a series of *der* mutants (*der1-der9*) has been isolated. Three *der1* allelic mutants were identified according to their RH phenotype. The strongest effect of the mutation on RHs development was observed in *der1-2* and *der1-3* mutants (Ringli *et al.*, 2002; 2005). The phenotype of *der1-3* mutant is characteristic by very short RHs, improper site selection for RH initiation at the outer tangential cell wall of the trichoblasts, and impairment of RH elongation after bulge establishment (Ringli *et al.*, 2002). We confirmed this RH phenotype of *der1-3* mutant plants in our study.

We demonstrated using cellular analysis of the cytoskeleton and plant phenotyping, that the single-point mutation in the *ACTIN2* gene had a more general influence on plant growth and development, as was thought before. The first novel developmental aspect revealed was delayed germination. Seeds of the *der1-3* mutant germinated more slowly than those of the C24 ecotype. Although mutant roots were shorter, the root growth rate was not affected. The main difference, however, was found in fresh weight of roots and shoots. The root system of *der1-3* mutant had a five-time less weight than root system of C24 ecotype. Similarly, leaves of *der1-3* mutant reached only half the weight of the C24 leaves. Though the leaf area of *der1-3* mutant was smaller in comparison to C24 control leaves, the *der1-3* mutant balanced it by higher number of leaves that was almost 20% higher than that of C24 plants. The similar effect was shown in another mutant *act7-1*, with disrupted encoding of the vegetative *ACTIN7*. This mutant showed also 24 h delay in seed germination, but without any other differences in further growth and development (Gilliland *et al.*, 2003).

Another modification in growth detected was a wavy root pattern of *der1-3* mutant. In order to find out the reason for this phenotype, we used three independent imaging methods, in particular FM4-64 PM staining in root cells, live cell imaging of root actin cytoskeleton through GFP-FABD2 fluorescence in transgenic lines by light-sheet microscopy, and whole-mount immunostaining of MTs in root cells. We found out that *der1-3* mutant had higher number of shifted cell division plates (CDPs) in roots than C24 plants. Quantitative measurements from FM4-64 vital labelling or fluorescence distribution of GFP-FABD2 in root meristematic cells of the *der1-3* mutant showed the

significantly higher number of oblique CDPs deviating from transverse orientation (with respect to the root longitudinal axis). Accumulation of oblique CDPs in root meristematic zone could generate random and asymmetrical forces leading to a wavy root growth pattern. It has already been described, that the MTs play a key role in determination of CDP during mitosis. They also associate with AFs during the formation of the pre-prophase band (PPB) of MTs already in the pre-prophase and prophase stages of the cell division (Takeuchi *et al.*, 2016). We confirmed this trend by immunostaining of MTs, together with live-cell imaging of GFP-MBD molecular marker, showing a higher number of tilted mitotic MTs arrays (PPBs, spindles, and phragmoplasts) in dividing root meristematic cells of the *der1-3* mutant. Such a high frequency of MTs arrays tilting was not observed in control C24 plants. On the other hand, the measurements of cortical MTs angular distribution in root epidermal cells did not show any differences between *der1-3* mutant and C24 control plants. It is obvious, that both MTs and AFs play an important role in determination of the future side and orientation of CDP, but in different ways. This was supported by other studies, when reduced expression of *ACT7*, a gene encoding an actin isoform highly expressed during mitosis, led to defects in CDP orientation (Gilliland *et al.*, 2003). Finally, actin cytoskeleton apparently plays relevant roles in cell division and in CDP determination in both asymmetrically and symmetrically dividing cells (Van Damme *et al.*, 2007; Rasmussen *et al.*, 2013; Kojo *et al.*, 2013, 2014).

After detailed microscopic analyses of actin cytoskeleton we found that AFs are shorter and thinner in cells of *der1-3* mutant as compared to AFs in cells of control C24 plants. This was confirmed by two different methods: live-cell imaging of hypocotyl and root cells of GFP-FABD transgenic lines, and imaging of AFs in fixed samples after the Alexa-488-phalloidin staining of cotyledon and hypocotyl cells. Quantitative analysis of the orientation showed that in cells of C24 plants actin bundles were longitudinally oriented, while actin bundles in cells of the *der1-3* mutant were mostly obliquely and sometimes transversely oriented. In general, plant cells contain individual AFs and actin bundles. The network of individual AFs is often randomly dispersed in the cortical cytoplasm and, although their high dynamicity, they have a shorter lifetime. The actin bundles are mostly oriented longitudinally along the cell's longer axis, they are less dynamic, but have a longer lifetime (Henty-Ridilla *et al.*, 2013). The changes in actin structure and orientation was described also in other mutants affected in the *ACT2* gene, such as *act2-2D* and *act2-5*. Single-point mutation in the *act2-2D* mutant led to formation of shorter actin bundles in root epidermal cells, showing also defects in actin

polymerization (Nishimura *et al.*, 2003). T-DNA insertion mutant *act2-5* have a modified pattern of actin cytoskeleton organization, where AFs are shorter and unbundled (Lanza *et al.*, 2012). Altogether, our data clearly indicate that single-point mutation of the *ACT2* gene in *der1-3* mutant does not influence only the RH development, but affects also other developmental parameters of mutant plants, such as growth pattern of the roots and properties of the actin cytoskeleton in cells of the whole plants. However, better understanding of the molecular mechanisms how the actin cytoskeleton contributes to the proper orientation of the cell division, and what is the role of ACTIN2 isoform in this process, will require more detailed future studies.

The second part of the results is devoted to the characterization of *der1-3* mutant under oxidative stress. We found as very interesting fact that *der1-3* mutant was clearly more resistant to oxidative stress as compared to control C24 plants. We proved the resistance on the level of plant phenotypes, root growth efficiency, integrity and dynamic parameters of the actin cytoskeleton in hypocotyl and root cells of GFP-FABD2 transgenic lines, and biochemical analyses of anti-oxidative defense mechanisms. In principle, a single-point mutation in the *der1-3* mutant leads to exchange of Arg97 to Cys97 (Ringli *et al.*, 2002). This change occurs in superdomain1 on the protein and topologically it is located on the surface, without effecting the tertiary protein structure, as shown by model comparison of control, and by mutation affected ACT2 proteins. ACT2 protein affected by the mutation is still functional, meanwhile the mutation might have an impact on its biochemical properties, such as post-translation modifications or protein-protein interactions. The phenotypical analyses and testing of the growth rate of C24 control and *der1-3* mutant plants, as well as GFP-FABD2 transgenic lines created in these two genetic backgrounds were performed with plants either directly germinated on, or transferred to oxidative stress condition after control germination. Oxidative stress was induced by different concentration of PQ (paraquat) and H<sub>2</sub>O<sub>2</sub> in the culture medium. We found out that PQ had stronger effect on root growth than H<sub>2</sub>O<sub>2</sub>. The higher resistance of *der1-3* mutant plants was determined based on lower root growth rate reduction (both after 0.1 μmol.l<sup>-1</sup> of PQ and 3 mmol.l<sup>-1</sup> of H<sub>2</sub>O<sub>2</sub> treatments) and more efficient production of root and shoot fresh weight after PQ treatment.

These facts led us to investigate actin cytoskeleton structure and organization in transgenic GFP-FABD2 lines under oxidative stress using live-cell imaging. Quantitative analyses showed that AFs in hypocotyl cells of C24 GFP-FABD2 transgenic line

underwent a massive bundling after treatment with  $0.1 \mu\text{mol.l}^{-1}$  PQ for 30 min. On the other hand, AFs in *der1-3* GFP-FABD2 hypocotyl cells were insensitive to the same treatment, preserved their structure and were still dynamic. This fact seems to be one of the main reasons supporting the higher tolerance of the *der1-3* mutant to the oxidative stress. It has been shown that a reduction in AF bundling can be directly associated with increased AF dynamics (Staiger and Blanchoin, 2006). The molecular mechanism how AFs are involved in plant response to oxidative stress is not fully understood yet, but some facts were already revealed. Protection of the actin cytoskeleton under the oxidative stress could be required for PIN2 auxin efflux carrier trafficking to the PM. This process is controlled by intracellular auxin level and it was shown that auxin amount reduction by ROS generation led to inhibition of PIN2 intracellular trafficking. The intracellular transport of PIN2 was reduced also after  $\text{H}_2\text{O}_2$  treatment, which affected directly actin cytoskeleton dynamics (Zwiewka *et al.*, 2019).

Moreover, our observations that *der1-3* mutant is more resistant to oxidative stress was corroborated by several biochemical experiments. The quantification of a relative malondialdehyde content showed that the *der1-3* mutant had a lower degree of lipid peroxidation after long-term PQ treatment, as compared to the C24 control plants. Also, increased abundance and activity of antioxidant enzymes, such as iron superoxide dismutase 1 (FeSOD1), two copper-zinc superoxide dismutase isoforms (CuZnSOD1 and CuZnSOD2), and redox buffering protein peroxiredoxin Q (PrxQ) supported better tolerance of the *der1-3* mutant against oxidative stress. This indicates that the *der1-3* mutant has a higher capacity to decompose  $\text{O}_2^-$  by increased level and activity of CuZnSOD1/2 and FeSOD1 enzymes as compared to the C24 control plants. These enzymes were proposed as important determinants of oxidative stress tolerance in plants (Sunkar *et al.*, 2006; Dvořák *et al.*, 2021). Due to a higher abundance of PrxQ, which is an atypical 2-cys peroxiredoxin using thioredoxin as an electron donor (Lamkemeyer *et al.*, 2006; Yoshida *et al.*, 2015), the *der1-3* mutant can also decompose  $\text{H}_2\text{O}_2$  more effectively. Altered ACTIN2 protein in *der1-3* mutant has one additional Cys compared to natural one, therefore we hypothesized that ACTIN2 in *der1-3* might undergo redox-mediated posttranslational modifications accelerating the antioxidant capacity via PrxQ and thioredoxins. It was published, that BEN1, a guanine exchange factor for ARF (ADP-ribosylation factor), regulating the AF-based intracellular trafficking of PIN2 during adaptation to oxidative stress, contains highly conserved cysteine residues (Mouratou *et al.*, 2005; Zhou *et al.*, 2010) that could be modified by  $\text{H}_2\text{O}_2$  treatment. Increased redox

status upon the accumulation of H<sub>2</sub>O<sub>2</sub> can initiate the oxidation of cysteine sulfhydryl groups in actins (Wang *et al.*, 2012). Our experiments with redox modification by DTT revealed that *der1-3* mutant had higher inclination to redox posttranslational modifications, which can directly influence its biochemical properties. This is another aspect leading to enhanced resistance of the *der1-3* mutant to oxidative stress. Direct oxidative posttranslational modifications of actins in mammalian cells, such as oxidation (Frémont *et al.*, 2017), glutathionylation (Sakai *et al.*, 2012) or S-sulphydration (Mustafa *et al.*, 2009), affected AFs depolymerization (Frémont *et al.*, 2017) and dynamics (Gellert *et al.*, 2015; Stojkov *et al.*, 2017). Thus, this section of the Ph.D. thesis brought some light to resistance against oxidative stress in *der1-3* mutant, in which the single-point mutation of the *ACT2* gene altered broadly also other cellular and molecular mechanisms. The complete mechanism, however, is still not clarified.

The third and last part of results deals with the role of AtRBOHC/RHD2 in the RH formation and their tip growth. Obviously, a mutation in the respective gene leads to a so-called “short root hair phenotype” of mutant plants. Process of RH tip growth requires vesicular transport and targeted delivery, localized cell wall deposition, and controlled PM extension. Critically important parameter is localized generation of ROS, creating typical tip-localized gradient together with Ca<sup>2+</sup> ions and pH at the apical cytoplasm (Šamaj *et al.*, 2006). ROS are produced by NADPH oxidase type C, which is encoded by *RHD2* (*ROOT HAIR DEFECTIVE 2*) gene. AtRBOHC/RHD2 is incorporated into apical PM and generates ROS into the apoplast (Foreman *et al.*, 2003). NADPH oxidase type C is also activated by Ca<sup>2+</sup> ions, but the main activators are Rop GTPases (Jones *et al.*, 2007). Rop GTPases were found to be accumulated at the site of future RHs initiation in trichoblasts (Molendijk *et al.*, 2001; Jones *et al.*, 2002). Single-point mutation in *RHD2* gene prevent transition from bulge to the tip growth. Importantly, rudimentary non-growing RHs in *rh2* mutant lack tip-focused gradients of ROS and Ca<sup>2+</sup> (Foreman *et al.*, 2003). The short RH phenotype is totally rescuable by *GFP:RHD2* construct expressed under control of the native promotor (Takeda *et al.*, 2008). In our experiments, we used *rh2* mutant and transgenic line carrying GFP-RHD2 in Col-0 background. We used different advanced microscopy methods for qualitative and quantitative characterization of GFP-RHD2 subcellular distribution and localization. We confirmed the published cellular localization pattern of GFP-RHD2, which was selective

accumulation in bulges and tips of developing RHs (Takeda *et al.*, 2008), and we extended this pattern at the subcellular and super-resolution levels.

We proved GFP-RHD2 signal localization in apical part of PM in growing RHs. Importantly, we found GFP-RHD2 signal localized in dynamic cytoplasmic vesicular compartments. These compartments were more abundant in trichoblasts than in atrichoblasts. The fluorescence was restricted to root epidermal cells. It was absent in root meristem and we started to detect it only in root elongation and differentiation zones, which correspond to the zone of RHs development. The pattern of fluorescence signal distribution found correlates with quantitative microarray analysis of roots, showing enhanced RHD2 transcript accumulation in root differentiation and elongation zones, epidermal cells, and RHs (Chapman *et al.*, 2019). In next experiments, we characterized in detail the pattern of temporal and spatial GFP-RHD2 redistribution during the process of RH initiation and growth. Quantitative single particle tracking analysis showed that GFP-RHD2 was targeted to, and removed back from the apical PM domains in developing bulges and growing RHs. Interestingly, the range of PM decorated by a fluorescent signal from GFP-RHD2 closely correlated with particular stages of RH development.

We defined the molecular signature of GFP-RHD2-positive compartments microscopically by subcellular colocalization studies. Vital staining with FM4-64 revealed colocalization of FM4-64 with GFP-RHD2 at the PM and in cytoplasmic vesicular compartments in growing RHs. FM4-64, as a membrane-specific styryl dye after labelling of the PM and after a short incubation time, serves as a fluorescent marker of early endocytic compartments in growing RHs (Ovečka *et al.*, 2005). This was corroborated positively by colocalization of FM4-64 with early/TGN endosomal marker GFP-RabA1d (Ovečka *et al.*, 2010; Berson *et al.*, 2014), and negatively by failed colocalization with late endosomal marker RabF2a-YFP (Voigt *et al.*, 2005; Berson *et al.*, 2014). In the next step, we prepared double transgenic fluorescence lines by crossing, carrying GFP-RHD2 together with mCherry-VTI12 (an early endosomal/TGN marker; Geldner *et al.*, 2009) and with mCherry-RabF2b (a late endosomal marker; Geldner *et al.*, 2009). Colocalization analyses corroborated previous results. Early endosomal/TGN marker mCherry-VTI12 showed colocalization with GFP-RHD2 in vesicular compartments in growing RHs, while late endosomal marker mCherry-RabF2b did not. We measured also a maximum speed of moving GFP-RHD2 vesicular compartments and we received a range of 4 - 8  $\mu\text{m}\cdot\text{s}^{-1}$ . This is well consistent with the measured dynamic

properties of early endosomal compartments carrying molecular markers GFP-RabA1d and YFP-VTI12 in RHs, which was in the range of 6 - 9  $\mu\text{m}\cdot\text{s}^{-1}$  (von Wangenheim *et al.*, 2016).

The quantitative particle tracking analysis revealed a complex pattern of GFP-RHD2 compartments distribution, both in movement and interactions with the PM. Based on data acquired, GFP-RHD2 compartments in growing RHs were divided into three different groups. The first group represented compartments moving to, and fusing with the apical PM. The proportion of this group was highest in early stages of RHs growth and corresponded with the largest area of apical PM containing accumulated fluorescence signal of the GFP-RHD2. The second group consisted GFP-RHD2 compartments moving only in the cytoplasm without any contact with the apical PM. They probably did not support GFP-RHD2 incorporation to the PM. The third group of compartments was particularly interesting, as they moved to and contacted the PM, while subsequently moved back to the cytoplasm. These events occurred mainly within the sub-apical zone of RHs and the number of these compartments proportionally increased in longer, rapidly growing RHs. GFP-RHD2-positive compartments behaving differently at the PM, and changes in their ratio typical for individual stages of RHs growth indicate that GFP-RHD2 incorporation into the PM and/or recycling back may represent an important part of the regulatory mechanism driving RH tip growth. GFP-RHD2-positive compartments from individual groups showed also different dynamic properties, such as mean and maximum speed of movement. According to these results, we also measured dynamic properties of early endosomes/TGN and late endosomes in trichoblasts of the *rhd2-1* mutant. Early endosomal/TGN compartments visualized by GFP-RabA1d marker had different dynamic properties in *rhd2-1* mutant as compared to control line. This indicate that loss of AtRBOHC/RHD2 functionality affects early endosomal/TGN compartments only, supporting their crucial role in RH formation and growth. Overall, our data from live-cell localization and quantitative microscopy clarified the pattern how dynamic vesicular compartments positive to GFP-RHD2 are delivered to the cortical cytoplasm and the clear zone of RHs. We provide an experimental proof that the AtRBOHC/RHD2 plays supportive role in the maintenance of apical PM domains in bulges and tip-growing RHs in Arabidopsis.

The delivery of GFP-RHD2 in motile compartments with to the growing apex of bulges and RHs requires physical interactions with the PM. In order to characterize the role of PM structural organization in GFP-RHD2 incorporation, we tested a possible role

of structural sterols, integral components of the PM. We treated plants with filipin III, a polyene antibiotic fluorochrome suitable as a vital probe for *in vivo* sterol localization in animal (Nichols *et al.*, 2001), yeast (Wachtler *et al.*, 2003), and plant cells (Grebe *et al.*, 2003; Boutté *et al.*, 2009; Liu *et al.*, 2009; Bonneau *et al.*, 2010). The sequestration of structural sterols in a physiologically high concentrations of filipin III or its prolonged exposure cause the formation of filipin-sterol complexes at the PM and a rapid arrest of RH tip growth (Milhaud *et al.*, 1988; Bonneau *et al.*, 2010; Ovečka *et al.*, 2010). Filipin III application ( $10 \mu\text{g}\cdot\mu\text{l}^{-1}$ ) caused labelling of the PM, and although GFP-RHD2 showed a residual signal at the PM, its majority was accumulated just beneath the PM. Filipin III at higher concentrations promote the formation of filipin III - sterol complexes, disrupting PM structural and physiological functions. Formation of a layer-like aggregates of GFP-RHD2 beneath the PM suggests that GFP-RHD2 was prevented from incorporating into the PM due to sterol sequestration. In addition, the depletion of GFP-RHD2 compartments from the clear zone of treated RHs might indicate that recycling from the PM was also inhibited after filipin III treatment. It has been proven that the appearance of filipin-sterol complexes at the PM was immediately connected with PM rigidification. It triggered ion leakage, extracellular pH alkalization, and changes in signalling, which depends on protein kinase-mediated phosphorylation (Bonneau *et al.*, 2010). The link between structural sterols at the PM and RH formation might be mediated by a regulatory role of Rho of plants (ROPs; Denninger *et al.*, 2019) that activate RHD2 during RH tip growth (Carol *et al.*, 2005). Transient S-acylation causes ROPs activation, which is required for their functionality and stabilizes their interaction with the PM and accumulation in lipid rafts (Sorek *et al.*, 2007, 2011). Another experiment with auxinole, a compound arresting independently RH tip growth, led to a different GFP-RHD2 distribution pattern, suggesting a specific role of structural sterols in GFP-RHD2 interactions with the PM. In conclusion, this observation indicates that structural sterols might be involved in localized anchoring and maintenance of GFP-RHD2 in the apical PM, particularly at the apex of developing RHs.

However, the detailed molecular mechanism of the whole process is still not clear. Future possibilities are in the use of super-resolution microscopy for detailed visualization and structural analysis of PM after filipin III treatment. Another task is related to a question, whether RHD2 is activated only after incorporating to the PM or is able to generate ROS already in the dynamic vesicular compartments. Remaining is also a clarification and identification of specific superoxide dismutase, which is involved in



conversion of superoxide to H<sub>2</sub>O<sub>2</sub> in the apoplast of growing RHs. Superoxide in the apoplast is generated by AtRBOHC/RHD2 (Mangano *et al.*, 2017).

Seminal parts of the thesis are based on cell biological approaches and utilization of advanced microscopy methods. Some of them, such as LSFM (Weber and Huisken, 2011; Stelzer, 2015) and Airyscan CLSM (Sheppard *et al.*, 2013) were applied in original and unique experiments with living plant samples. Therefore, an appropriate way for preparation of living plants for microscopy may represent a challenge. The development and adaptations of appropriate protocols for plant sample preparation, at least for long-term imaging by LSFM (Ovečka *et al.*, 2015) was an integral part of the thesis as well.

## 6. References

- Asaoka R, Uemura T, Ito J, Fujimoto M, Ito E, Ueda T, Nakano A (2013). Arabidopsis RABA1 GTPases are involved in transport between the trans-Golgi network and the plasma membrane, and are required for salinity stress tolerance. *The Plant Journal* 73: 240-249. doi: 10.1111/tpj.12023
- Ashtamker C, Kiss V, Sagi M, Davydov O, Fluhr R (2007). Diverse Subcellular Locations of Cryptogein-Induced Reactive Oxygen Species Production in Tobacco Bright Yellow-2 Cells. *Plant Physiology* 143: 1817-1826. doi: 10.1104/pp.106.090902
- Auerbach C, Robson JM (1944). Production of mutations by allyl isothiocyanate. *Nature* 154: 81. doi: 10.1038/154081a0
- Balcerowicz D, Schoenaers S, Vissenberg K (2015). Cell fate determination and the switch from diffuse growth to planar polarity in Arabidopsis root epidermal cells. *Frontiers in Plant Sciences* 6: 1163. doi:10.3389/fpls.2015.01163
- Baluška F, Hlavacka A, Šamaj J, Palme K, Robinson D., Matoh T, McCurdy DW, Menzel D, Volkmann D (2002). F-actin-dependent endocytosis of cell wall pectins in meristematic root cells. Insights from Brefeldin A-induced compartments. *Plant Physiology* 130: 422-431. doi: 10.1104/pp.007526
- Baluška F, Salaj J, Mathur J, Braun M, Jasper F, Šamaj J, Chua N-H, Barlow PW, Volkmann D (2000). Root hair formation: F-actin-independent tip growth is initiated by local assembly of profilin-supported F-actin meshworks accumulated within expansin-enriched bulges. *Developmental Biology* 227: 618-632. doi: 10.1006/dbio.2000.9908
- Bandmann V. *Mechanisms and Kinetics of Exocytosis and Endocytosis in Plant and in Yeast Cells*. Darmstadt, 2011. Technical University of Darmstadt, Department of Biology. Dissertation thesis. Advisor: PD Dr.Ulrike Homan.
- Barth M, Holstein SHE (2004). Identification and functional characterization of Arabidopsis AP180, a binding partner of plant  $\alpha$ C-adaptin. *Journal of Cell Science* 117: 2051–2062. doi: 10.1242/jcs.01062
- Beck M, Komis G, Müller J, Menzel D, Šamaj J (2010). Arabidopsis homologs of nucleus-and phragmoplast-localized kinase 2 and 3 and mitogen-activated protein kinase 4 are essential for microtubule organization. *Plant Cell* 22: 755–771. doi: 10.1105/tpc.109.071746
- Benfey PN, Scheres B (2000). Root development. *Current Biology* 10: R813-R815. doi: 10.1016/S0960-9822(00)00814-9
- Berson T, Wangenheim D, Takáč T, Šamajová O, Rosero A, Ovečka M, Komis G, Stelzer EH, Šamaj J (2014). Trans-Golgi network localized small GTPase RabA1d is involved in cell plate formation and oscillatory root hair growth. *BMC Plant Biology* 14: 252. doi: 10.1186/s12870-014-0252-0
- Berthet B, Maizel A (2016). Light sheet microscopy and live imaging of plants. *Journal of microscopy* 263: 158-164. doi: 10.1111/jmi.12393

- Bhat RA, Panstruga R (2005). Lipid rafts in plants. *Planta* 223: 5. doi: 10.1007/s00425-005-0096-9
- Bibikova TN, Blancaflor EB, Gilroy S (1999). Microtubules regulate tip growth and orientation in root hairs of *Arabidopsis thaliana*. *The Plant Journal* 17: 657-665. doi: 10.1046/j.1365-313X.1999.00415.x
- Bibikova TN, Zhigilei A, Gilroy S (1997). Root hair growth in *Arabidopsis thaliana* is directed by calcium and an endogenous polarity. *Planta* 203: 495-505. doi: doi.org/10.1007/s004250050219
- Boerjan W, den Boer B, van Montagu M (1992). Molecular genetic approaches to plant development. *The International Journal of Developmental Biology* 36: 59-66.
- Bonneau L, Gerbeau-Pissot P, Thomas D, Der C, Lherminier J, Bourque S, Roche Y, Simon-Plas F (2010). Plasma membrane sterol complexation, generated by filipin, triggers signalling responses in tobacco cells. *Biochimica et Biophysica Acta (BBA) - Biomembranes* 1798: 2150-2159. doi: 10.1016/j.bbamem.2010.07.026
- Bortesi L, Fischer R (2015). The CRISPR/Cas9 system for plant genome editing and beyond *Biotechnology Advances* 33: 41-52. doi: 10.1016/j.biotechadv.2014.12.006
- Bottanelli F, Foresti O, Hanton S, Denecke J (2011). Vacuolar transport in tobacco leaf epidermis cells involves a single route for soluble cargo and multiple routes for membrane cargo. *The Plant Cell* 23: 3007–3025. doi: 10.1105/tpc.111.085480
- Boutté Y, Frescatada-Rosa M, Men S, Chow C-M, Ebine K, Gustavsson A, Johansson L, Ueda T, Moore I, Jürgens G, Grebe M (2009). Endocytosis restricts *Arabidopsis* KNOLLE syntaxin to the cell division plane during late cytokinesis. *EMBO Journal* 29: 546-558. doi: 10.1038/emboj.2009.363
- Bowler C, Montagu MV, Inze D (1992). Superoxide dismutase and stress tolerance. *Annual Review of Plant Physiology and Plant Molecular Biology* 43: 83-116. doi: 10.1146/annurev.pp.43.060192.000503
- Braun M, Baluška F, von Witsch M, Menzel D (1999). Redistribution of actin, profilin and phosphatidylinositol-4,5-bisphosphate (PIP<sub>2</sub>) in growing and maturing root hairs. *Planta* 209: 435-443. doi: 10.1007/s004250050746
- Caliskan M, Cuming AC (1998). Spatial specificity of H<sub>2</sub>O<sub>2</sub>-generating oxalate oxidase gene expression during wheat embryo germination. *Plant Journal* 15: 165-171. doi: 10.1046/j.1365-313X.1998.00191.x
- Campanoni P, Blatt MR (2007). Membrane trafficking and polar growth in root hairs and pollen tubes. *Journal of Experimental Botany* 58: 65-74. doi: 10.1093/jxb/erl059
- Caplow M, Fee L (2003). Concerning the chemical nature of tubulin subunits that cap and stabilize microtubules. *Biochemistry* 42: 2122-2126. doi: 10.1021/bi027010s
- Capone R, Tiwari BS, Levine A (2004). Rapid transmission of oxidative and nitrosative stress signals from root to shoot in *Arabidopsis*. *Plant Physiology and Biochemistry* 4: 425-428. doi: 10.1016/j.plaphy.2004.03.005

- Carol RJ, Dolan L (2002). Building a hair: tip growth in *Arabidopsis thaliana* root hairs. *Philosophical Transactions of the Royal Society of London. Series B: Biological Sciences* 357: 815–821. doi: 10.1098/rstb.2002.1092
- Carol RJ, Takeda S, Linstead P, Durrant MC, Kakesova H, Derbyshire P, Drea S, Žárský V, Dolan L (2005). A RhoGDP dissociation inhibitor spatially regulates growth in root hair cells. *Nature* 438: 1013-1016. doi: 10.4161/psb.6.11.17477
- Carpenter JL, Ploense SE, Snustad DP, Silflow CD (1992). Preferential expression of an alphanubulin gene of *Arabidopsis* in pollen. *The Plant Cell* 4: 557-571. doi: 10.1105/tpc.4.5.557
- Carroll AD, Moyen C, Kesteren PV, Tooke F, Battey NH, Brownlee C (1998). Ca<sup>2+</sup>, Annexins, and GTP Modulate Exocytosis from Maize Root Cap Protoplasts. *The Plant Cell* 10: 1267-1276. doi: 10.1105/tpc.10.8.1267
- Chapman JM, Muhlemann JK, Gayomba SR, Muday GK (2019). RBOH-dependent ROS synthesis and ROS scavenging by plant specialized metabolites to modulate plant development and stress responses. *Chemical Research in Toxicology* 32: 370-396. doi: 10.1021/acs.chemrestox.9b00028
- Chen R, Rosen E, Masson PH (1999). Gravitropism in Higher Plants. *Plant Physiology* 120: 343–350. doi: 10.1104/pp.120.2.343
- Cheng Z, Snustad DP, Carter JV (2001). Temporal and spatial expression patterns of TUB9, a betatubulin gene of *Arabidopsis thaliana*. *Plant Molecular Biology* 47: 389-398. doi: 10.1023/A:1011628024798
- Chenouard N, Smal I, de Chaumont F *et al.* (2014). Objective comparison of particle tracking methods. *Nature Methods* 11: 281-289 (2014). doi: 10.1038/nmeth.2808
- Cheon J, Park SY, Schulz B, Choe S (2010). *Arabidopsis* brassinosteroid biosynthetic mutant dwarf7-1 exhibits slower rates of cell division and shoot induction. *BMC Plant Biology* 10: 270. doi: 10.1186/1471-2229-10-270
- Choe S, Noguchi T, Fujioka S, Takatsuto S, Tissier CP, Gregory BD, Ross AS, Tanaka A, Yoshida S, Tax FE, Feldmann KA (1999). The *Arabidopsis* *dwf7/ste1* mutant is defective in the delta7 sterol C-5 desaturation step leading to brassinosteroid biosynthesis. *The Plant Cell* 11: 207-221. doi: 10.1105/tpc.11.2.207
- Choe S, Tanaka A, Noguchi T, Fujioka S, Takatsuto S, Ross AS, Tax FE, Yoshida S, Feldmann KA (2000). Lesions in the sterol delta reductase gene of *Arabidopsis* cause dwarfism due to a block in brassinosteroid biosynthesis. *The Plant Journal: for cell and molecular biology* 21: 431-443. doi: 10.1046/j.1365-313x.2000.00693.x
- Clough SJ, Bent AF (1998). Floral dip: a simplified method for *Agrobacterium* mediated transformation of *Arabidopsis thaliana*. *Plant Journal* 16: 735–743. doi: 10.1046/j.1365-313x.1998.00343.x
- Clouse SD (2002). *Arabidopsis* mutants reveal multiple roles for sterols in plant development. *The Plant Cell* 14: 1995-2000. doi: 10.1105/tpc.140930

- Colcombet J, Hirt H (2008). *Arabidopsis* MAPKs: a complex signalling network involved in multiple biological processes. *Biochemical Journal* 413: 217-226. doi: 10.1042/BJ20080625
- Contento AL, Bassham DC (2012). Structure and function of endosomes in plant cells. *Journal of Cell Science* 125: 3511-3518. doi: 10.1242/jcs.093559
- Costa S, Shaw P (2006). Chromatin organization and cell fate switch respond to positional information in *Arabidopsis*. *Nature* 439: 493-496. doi: 10.1038/nature04269
- Dat J, Vandenabeele S, Vranová E, Van Montagu M, Inzé D, Breusegem F (2000). Dual action of the active oxygen species during plant stress responses. *Cellular and Molecular Life Sciences* 57: 779-795. doi: 10.1007/s000180050041
- Datta S, Kim CM, Pernas M, Pires ND, Proust H, Tam T, Vijayakumar P, Dolan L (2011). Root hairs: development, growth and evolution at the plant-soil interface. *Plant and Soil* 346: 1-14. doi: 10.1007/s11104-011-0845-4
- Daudi A, Cheng Z, O'Brien JA, Mammarella N, Khan S, Ausubel FM, Bolwell GP (2012). The apoplastic oxidative burst peroxidase in *Arabidopsis* is a major component of pattern-triggered immunity. *Plant Cell* 24: 275-287. doi: 10.1105/tpc.111.093039
- de Keijzer J, Mulder BM, Janson ME (2014). Microtubule networks for plant cell division. *Systems and Synthetic Biology* 8: 187-194. doi: 10.1007/s11693-014-9142-x
- Del Pozo JC (2016). Reactive Oxygen Species: from harmful molecules to finetuning regulators of stem cell niche maintenance. *PLoS Genetics* 12 (9), e1006251. doi: 10.1371/journal.pgen.1006251
- del Río LA, Sandalio LM, Corpas FJ, Palma JM, Barroso JB (2006). Reactive oxygen species and reactive nitrogen species in peroxisomes. Production, scavenging, and role in cell signaling. *Plant Physiology* 141: 330-335. doi: 10.1104/pp.106.078204
- Denninger P, Reichelt A, Schmidt VAF, Mehlhorn DG, Asseck LY, Stanley CE, Keinath NF, Evers JF, Grefen C, Grossmann G (2019). Distinct RopGEFs successively drive polarization and outgrowth of root hairs. *Current Biology* 29: 1854-1865. doi: 10.1016/j.cub.2019.04.059
- Desai A, Mitchison TJ (1997). Microtubule Polymerization Dynamics. *Annual Review Cell and Developmental Biology* 13: 83-117. doi: 10.1146/annurev.cellbio.13.1.83
- Dolan L, Duckett CM, Grierson C, Linstead P, Schneider K, Lawson E, Dean C, Roberts K (1994). Clonal relationships and cell patterning in the root epidermis of *Arabidopsis*. *Development* 120: 2465-2474. doi: 10.1242/dev.120.9.2465
- Dolan L, Janmaat K, Willemsen V, Linstead P, Poethig S, Roberts K, Scheres B (1993). Cellular organisation of the *Arabidopsis thaliana* root. *Development* 119: 71-84. doi: 10.1242/dev.119.1.71
- Dunsby C (2008). Optically sectioned imaging by oblique plane microscopy. *Optics Express* 16: 20306-20316. doi: 10.1364/OE.16.020306

- Dvořák P, Krasnylenko Y, Zeiner A, Samaj J, Takáč T (2021). Signaling toward reactive oxygen species-scavenging enzymes in plants. *Frontiers in Plant Science* 11: 1153. doi: 10.3389/fpls.2020.618835
- Ehrhardt DW, Shaw SL (2006). Microtubule dynamics and organization in the plant cortical array. *The Annual Review of Plant Biology* 57: 859-875. doi: 10.1146/annurev.arplant.57.032905.105329
- Engelmann R, Weisshart K (2014). Airyscanning: Evoking the full potential of confocal microscopy. *Imaging Microscopy* 3: 20-21.
- Era A, Tominaga M, Ebine K, Awai C, Saito C, Ishizaki K, Yamato KT, Kohchi T, Nakano A, Ueda T (2009). Application of Lifeact reveals F-actin dynamics in *Arabidopsis thaliana* and the liverwort, *Marchantia polymorpha*. *Plant & Cell Physiology* 50: 1041-1048. doi: 10.1093/pcp/pcp055
- Evert RF, Eichhorn SE, Esau K (2006). Esau's plant anatomy: meristems, cells, and tissues of the plant body: their structure, function, and development. Hoboken, N.J: Wiley-Interscience. ISBN 0-471-73843-3
- Falhof J, Pedersen JT, Fuglsang AT, Palmgren M (2016). Plasma Membrane H(+)-ATPase Regulation in the Center of Plant Physiology. *Molecular Plant* 9: 323-337. doi: 10.1016/j.molp.2015.11.002
- Fasshauer D, Sutton RB, Brunger AT, Jahn R (1998). Conserved structural features of the synaptic fusion complex: SNARE proteins reclassified as Q- and R-SNAREs. *Proceedings of the National Academy of Sciences USA* 95: 15781-15786. doi: 10.1073/pnas.95.26.15781
- Federico R, Angelini R (1986). Occurrence of diamine oxidase in the apoplast of pea epicotyls. *Planta* 167: 300-302. doi: 10.1007/BF00391430
- Flores-Rodriguez N, Rogers SS, Kenwright DA, Waigh TA, Woodman PG, Allan VJ (2011). Roles of dynein and dynactin in early endosome dynamics revealed using automated tracking and global analysis. *PLoS ONE* 6 :e24479. doi: 10.1371/journal.pone.0024479
- Foreman J, Demidchik V, Bothwell JH, Mylona P, Miedema H, Torres MA, Linstead P, Costa S, Brownlee C, Jones JD, et al. (2003). Reactive oxygen species produced by NADPH oxidase regulate plant cell growth. *Nature* 422: 442–446. doi: 10.1038/nature01485
- Foreman J, Dolan L (2001). Root hairs as a model system for studying plant cell growth. *Annals of Botany* 88: 1-7. doi: 10.1006/anbo.2001.1430
- Fowler JE, Quatrano RS (1997). PLANT CELL MORPHOGENESIS: Plasma membrane interactions with the cytoskeleton and cell wall. *Annual Review of Cell and Developmental Biology* 13: 697-743. doi: 10.1146/annurev.cellbio.13.1.697
- Foyer CH (2018). Reactive oxygen species, oxidative signaling and the regulation of photosynthesis. *Environmental and Experimental Botany* 154, 134–142. doi: 10.1016/j.envexpbot.2018.05.003

- Frémont S, Hammich H, Bai J, Wioland H, Klinkert K, Rocancourt M, Kikuti C, Stroebel D, Romet-Lemonne G, Pylypenko O, Houdusse A, Echard A (2017). Oxidation of F-Actin controls the terminal steps of cytokinesis. *Nature Communication* 8: 14528. doi: 10.1038/ncomms14528
- Fu Y, Gu Y, Zhen Z, Wasteneys G, Yang Z (2005). Arabidopsis interdigitating cell growth requires two antagonistic pathways with opposing action on cell morphogenesis. *Cell* 120: 687-700. doi: 10.1016/j.cell.2004.12.026
- Galway ME, Heckman Jr JW, Schiefelbein JW (1997). Growth and ultrastructure of *Arabidopsis* root hairs: the *rhd3* mutation alters vacuole enlargement and tip growth. *Planta* 201: 209–218. doi: 10.1007/BF01007706
- Gasman S, Kalaidzidis Y, Zerial M (2003). RhoD regulates endosome dynamics through Diaphanous-related Formin and Src tyrosine kinase. *Nature Cell Biology* 5: 195-204. doi: 10.1038/ncb935
- Gechev TS, Van Breusegem F, Stone JM, Denev I, Laloi C (2006). Reactive oxygen species as signals that modulate plant stress responses and programmed cell death. *Bioessays* 28: 1091-1101. doi: 10.1002/bies.20493
- Geldner N, Déneraud-Tendon V, Hyman DL, Mayer U, Stierhof YD, Chory J (2009). Rapid, combinatorial analysis of membrane compartments in intact plants with a multicolor marker set. *Plant Journal* 59: 169–178. doi: 10.1111/j.1365-313X.2009.03851.x
- Gellert M, Hanschmann E-M, Lepka K, Berndt C, Lillig CH (2015). Redox regulation of cytoskeletal dynamics during differentiation and de-differentiation. *Biochimica et Biophysica Acta (BBA) - General Subjects* 1850: 1575-1587. doi: 10.1016/j.bbagen.2014.10.030
- Gilliland LU, Kandasamy MK, Pawloski LC, Meagher RB (2002). Both vegetative and reproductive actin isovariants complement the stunted root hair phenotype of the Arabidopsis *act2-1* mutation. *Plant Physiology* 130: 2199-2209. doi: 10.1104/pp.014068
- Gilliland LU, McKinney EC, Asmussen MA, Meagher RB (1998). Detection of deleterious genotypes in multigenerational studies. I. Disruptions in individual *Arabidopsis* actin genes. *Genetics* 149: 717-725. doi: 10.1093/genetics/149.2.717
- Gilliland LU, Pawloski LC, Kandasamy MK, Meagher RB (2003). *Arabidopsis* actin gene *ACT7* plays an essential role in germination and root growth. *The Plant Journal* 33: 319-328. doi: 10.1046/j.1365-313X.2003.01626.x
- Gillooly DJ, Simonsen A, Stenmark H (2001). Cellular functions of phosphatidylinositol3-phosphate and FYVE domain proteins. *Biochemical Journal* 355: 249-258. doi: 10.1042/bj3550249
- Girkin JM, Carvalho MT (2018). The light-sheet microscopy revolution. *Journal of Optics* 20: 053002. doi: 10.1088/2040-8986/aab58a
- Girkin JM, McConnell G (2005). Advances in laser sources for confocal and multiphoton microscopy. *Microscopy Research & Technique* 67: 8-14. doi: 10.1002/jemt.20179
- Gleason C, Huang S, Thatcher LF, Foley RC, Anderson CR, Carroll AJ, Millar AH, Singh KB (2011). Mitochondrial complex II has a key role in mitochondrial-derived reactive oxygen species

- influence on plant stress gene regulation and defense. *Proceedings of the National Academy of Sciences of the USA* 108: 10768-10773. doi: 10.1073/pnas.101606010
- Goddard RH, Wick SM, Silflow CD, Snustad DP (1994). Microtubule components of the plant cell cytoskeleton. *Plant Physiology* 104: 1-6. doi: 10.1104/pp.104.1.1
- Goode BL, Drubin DG, Barnes G (2000). Functional cooperation between the microtubule and actin cytoskeletons. *Current Opinion in Cell Biology* 12: 63-71. doi: 10.1016/S0955-0674(99)00058-7
- Gräf R, Rietdorf J, Zimmermann T (2005). Live cell spinning disk microscopy. *Advances in Biochemical Engineering* 95: 57-75. doi: 10.1007/b102210
- Grebe M, Xu J, Möbius W, Ueda T, Nakano A, Geuze HJ, Rook MB, Scheres B (2003). Arabidopsis sterol endocytosis involves actin-mediated trafficking via ARA6-positive early endosomes. *Current Biology* 13: 1378-1387. doi: 10.1016/S0960-9822(03)00538-4
- Grierson C, Schiefelbein J (2002). Root hairs. *Arabidopsis Book* 1: e0060. doi: 10.1199/tab.0060
- Grosshans BL, Ortiz D, Novick P (2006). Rabs and their effectors: achieving specificity in membrane traffic. *Proceedings of the National Academy of Sciences USA* 103: 11821-11827. doi: 10.1073/pnas.0601617103
- Haas TJ, Sliwinski MK, Martínez DE, Preuss M, Ebine K, Ueda T, Nielsen E, Odorizzi G, Otegui MS (2007). The Arabidopsis AAA ATPase SKD1 is involved in multi vesicular endosome function and interacts with its positive regulator LYST-INTERACTING PROTEIN 5. *The Plant Cell* 19: 1295-1312. doi: 10.1105/tpc.106.049346
- Hao H, Fan L, Chen T, Li R, Li X, He Q, Botella MA, Lin J (2014). Clathrin and membrane microdomains cooperatively regulate RbohD dynamics and activity in Arabidopsis. *The Plant Cell* 26: 1729-1745. doi: 10.1105/tpc.113.122358
- Hawes C, Crooks K, Coleman J, Satiat-Jeunemaitrie B (1995). Endocytosis in plants: fact or artefact? *Plant, Cell and Environment* 18: 1245-1252. doi: 10.1111/j.1365-3040.1995.tb00184.x
- He H, Yan J, Yu X, Liang Y, Fang L, Scheller HV, Zhang A (2017). The NADPH-oxidase AtRbohI plays a positive role in drought-stress response in *Arabidopsis thaliana*. *Biochemical and Biophysical research communications* 491: 834-839. doi: 10.1016/j.bbrc.2017.05.131
- Henty-Ridilla JL, Li J, Blanchoin L, Staiger CJ (2013). Actin dynamics in the cortical array of plant cells. *Current Opinion in Plant Biology* 16: 678-687. doi: 10.1016/j.pbi.2013.10.012
- Hepler PK, Vidali L, Cheung AY (2001). Polarized cell growth in higher plants. *Annual Review of Cell and Developmental Biology* 17: 159-187. doi: 10.1146/annurev.cellbio.17.1.159
- Higaki T, Kutsuna N, Okubo E, Sano T, Hasezawa S (2006). Actin microfilaments regulate vacuolar structures and dynamics: dual observation of actin microfilaments and vacuolar membrane in living tobacco BY-2 Cells. *Plant & Cell Physiology* 47: 839-852. doi: 10.1093/pcp/pcj056



- Holekamp TF, Turaga D, Holy TE (2008). Fast three-dimensional fluorescence imaging of activity in neural populations by objective-coupled planar illumination microscopy. *Neuron* 57: 661-672. doi: 10.1016/j.neuron.2008.01.011
- Huff J (2015). The Airyscan detector from ZEISS: Confocal imaging with improved signal-to-noise ratio and super-resolution. *Nature Methods* 12. doi: 10.1038/nmeth.f.388
- Huisken J, Swoger J, Del Bene F, Wittbrodt J, Stelzer EH (2004). Optical sectioning deep inside live embryos by selective plane illumination microscopy. *Science* 305: 1007-1009. doi: 10.1126/science.110003
- Inoué S, Inoué T (2002). "Direct-view high-speed confocal scanner: the CSU-10," in: *Methods in Cell Biology*, eds. Wilson L, Matsudaira P (*Elsevier Science, USA*) 70: 87-127. doi: 10.1016/s0091-679x(02)70003-4
- Ishihama N, Yoshioka H (2012). Post-translational regulation of WRKY transcription factors in plant immunity. *Current Opinion in Plant Biology* 15: 431-437. doi: 10.1016/j.pbi.2012.02.003
- Ito E, Uemura T (2022). RAB GTPases and SNAREs at the trans-Golgi network in plants. *Journal of Plant Research* 135:389-403. doi: 10.1007/s10265-022-01392-x
- Jiang C, Belfield EJ, Mithani A, Visscher A, Ragoussis J, Mott R, Smith JAC, Harberd NP (2012). ROS-mediated vascular homeostatic control of root-to-shoot soil Na delivery in Arabidopsis. *The EMBO Journal* 31: 4359–4370. doi: 10.1038/emboj.2012.273
- Jiang K, Moe-Lange J, Hennen L, Feldman LJ (2016). Salt stress affects the redox status of Arabidopsis root meristems. *Frontiers in Plant Sciences* 7: 81. doi: 10.3389/fpls.2016.00081
- Jiang W-B, Li W-H (2013). Brassinosteroid functions in Arabidopsis seed development. *Plant Signaling & Behavior* 8: e25928. doi: 10.4161/psb.25928
- Jones MA, Raymond MJ, Yang Z, Smirnov N (2007). NADPH oxidase-dependent reactive oxygen species formation required for root hair growth depends on ROP GTPase. *Journal of Experimental Botany* 58: 1261-1270. doi: 10.1093/jxb/erl279
- Jones MA, Shen JJ, Fu Y, Li H, Yang Z, Grierson CS (2002). The Arabidopsis Rop2 GTPase is a positive regulator of both root hair initiation and tip growth. *The Plant Cell* 14: 763-776. doi: 10.1105/tpc.010359
- Jonkman J, Brown CM (2015). Any way you slice it—a comparison of confocal microscopy techniques. *Journal of Biomolecular Techniques* 26: 54-65. doi: 10.7171/jbt.15-2602-003
- Kandasamy MK, Burgos-Rivera B, McKinney EC, Ruzicka DR, Meagher RB (2007). Class-specific interaction of profilin and ADF isoforms with actin in the regulation of plant development. *Plant Cell* 19: 3111-3126. doi: 10.1105/tpc.107.052621
- Kandasamy MK, McKinney EC, Meagher RB (2002). Functional nonequivalency of actin isoforms in Arabidopsis. *Molecular Biology of the Cell* 13: 251-261. doi: 10.1091/mbc.01-07-0342

- Kang E, Zheng M, Zhang Y, Yuan M, Yalovsky S, Zhu L, Fu Y (2017). The microtubule-associated protein MAP18 affects ROP2 GTPase activity during root hair growth. *Plant Physiology* 174: 202–222. doi:10.1104/pp.16.01243
- Kartasalo K, Pölönen R-P, Ojala M, Rasku J, Leikkala J, Aalto-Setälä K, Kallio P (2015). CytoSpectre: a tool for spectral analysis of oriented structures on cellular and subcellular levels. *BMC Bioinformatics* 16: 344. doi: 10.1186/s12859-015-0782-y
- Ketelaar T, Anthony RG, Hussey PJ (2004). Green fluorescent protein-mTalin causes defects in actin organization and cell expansion in *Arabidopsis* and inhibits actin depolymerizing factor's actin depolymerizing activity in vitro. *Plant Physiology* 136: 3990-3998. doi: 10.1104/pp.104.050799
- Ketelaar T, Faivre-Moskalenko C, Esseling JJ, de Ruijter NCA, Grierson CS, Dogterom M, Emons AMC (2002). Positioning of nuclei in *Arabidopsis* root hairs: an actin-regulated process of tip growth. *The Plant Cell* 14: 2941-2955. doi: 10.1105/tpc.005892
- Kim SH, Woo DH, Kim JM, Lee SY, Chung WS, Moon YH (2011). *Arabidopsis* MKK4 mediates osmotic-stress response via its regulation of MPK3 activity. *Biochemical and Biophysical Research Communications* 412: 150-154. doi: 10.1016/j.bbrc.2011.07.064
- Klahre U, Noguchi T, Fujioka S, Takatsuto S, Yokota T, Nomura T, Yoshida S, Chua NH (1998). The *Arabidopsis* DIMINUTO/DWARF1 gene encodes a protein involved in steroid synthesis. *The Plant Cell* 10: 1677-1690. doi: 10.1105/tpc.10.10.1677
- Kojo KH, Higaki T, Kutsuna N, Yoshida Y, Yasuhara H, Hasezawa S (2013). Roles of cortical actin microfilament patterning in division plane orientation in plants. *Plant & Cell Physiology* 54: 1491-1503. doi: 10.1093/pcp/pct093
- Kojo KH, Yasuhara H, Hasezawa S (2014). Time-sequential observation of spindle and phragmoplast orientation in BY-2 cells with altered cortical actin microfilament patterning. *Plant Signaling & Behavior* 9: e29579. doi: 10.4161/psb.29579
- Komis G, Luptovčiak I, Doskočilová A, Šamaj J (2015a). Biotechnological aspects of cytoskeletal regulation in plants. *Biotechnology Advances* 33: 1043-1062. doi: 10.1016/j.biotechadv.2015.03.008
- Komis G, Novák D, Ovečka M, Šamajová O, Šamaj J (2018). Advances in Imaging Plant Cell Dynamics. *Plant Physiology* 176: 80-93. doi: 10.1104/pp.17.00962
- Komis G, Šamajová O, Ovečka M, Šamaj J (2015b). Super-resolution microscopy in plant cell imaging. *Trends in Plant Science* 20: 834-843. doi: 10.1016/j.tplants.2015.08.013.
- Koornneef M and Meinke D (2010). The development of *Arabidopsis* as a model plant. *The Plant Journal* 61: 909-921. doi: 10.1111/j.1365-3113X.2009.04086.x
- Kopczak SD, Haas NA, Hussey PJ, Silflow CD, Snustad DP (1992). The small genome of *Arabidopsis* contains at least six expressed  $\alpha$ -tubulin genes. *The Plant Cell* 4: 539-547. doi: 10.1105/tpc.4.5.539
- Korobchevskaya K, Lagerholm BC, Colin-York H, Fritzsche M (2017). Exploring the potential of airyscan microscopy for live cell imaging. *Photonics* 4: 41. doi: 10.3390/photonics4030041

- Kusano H, Testerink C, Vermeer JEM, Tsuge T, Shimada H, Oka A, Munnik T, Aoyama T (2008). The Arabidopsis Phosphatidylinositol Phosphate 5-Kinase PIP5K3 is a key regulator of root hair tip growth. *The Plant Cell* 20: 367-380. doi: 10.1105/tpc.107.056119
- Lamkemeyer P, Laxa M, Collin V, Li W, Finkemeier I, Schöttler MA, Holtkamp V, Tognetti VB, Issakidis-Bourguet E, Kandlbinder A, Weis E, Miginiac-Maslow M, Dietz K-J (2006). Peroxiredoxin Q of Arabidopsis thaliana is attached to the thylakoids and functions in context of photosynthesis. *The Plant Journal* 45: 968-981. doi: 10.1111/j.1365-313X.2006.02665.x
- Lanza M, Garcia-Ponce B, Castrillo G, Catarecha P, Sauer M, Rodriguez-Serrano m, Páez-García A, Sánchez-Bermejo E, TC M, del Puerto YL, Sandalio LM, Paz-Ares J, Leyva A (2012). Role of actin cytoskeleton in brassinosteroid signaling and in its integration with the auxin response in plants. *Developmental Cell* 22: 1275-1285. doi: 10.1016/j.devcel.2012.04.008
- Li H, Duan ZW, XieP, Liu YR, Wang WC, Dou SX, Wng P-Y (2012). Effects of paclitaxel on EGFR endocytic trafficking revealed using quantum dot tracking in single cells. *PLoS ONE* 7: e45465. doi: 10.1371/journal.pone.0045465
- Li P, Day B (2019). Battlefield Cytoskeleton: Turning the Tide on Plant Immunity. *Molecular Plant-Microbe Interactions* 32: 25-34. doi: 10.1094/MPMI-07-18-0195-FI
- Lima R, Wada S, Tsubota K, Yamaguchi T (2006). Measurement science and technology confocal micro-PIV measurements of three-dimensional profiles of cell suspension flow in a square microchannel. *Measurement Science and Technology* 17: 797. doi: 10.1088/0957-0233/17/4/026
- Lindsey K, Pullen ML, Topping JF (2003). Importance of plant sterols in pattern formation and hormone signalling. *Trends in Plant Science* 8: 521-525. doi: 10.1016/j.tplants.2003.09.012
- Liu B, Joshi HC, Wilson TJ, Silflow CD, Palevitz BA, Snustad DP (1994). Gamma-tubulin in Arabidopsis: gene sequence, immunoblot, and immunofluorescence studies. *The Plant Cell* 2: 303-314. doi: 10.1105/tpc.6.2.303
- Liu P, Zhang L, Li R, Wang Q, Niehaus K, Baluška F, Šamaj J, Lin J (2009). Lipid microdomain polarization is required for NADPH oxidase-dependent ROS signaling in Picea meyeri pollen tube tip growth. *The Plant Journal* 60: 303-313. doi: 10.1111/j.1365-313X.2009.03955.x
- Liu XM, Kim KE, Kim KC, Nguyen XC, Han HJ, Jung MS, Kim HS, Sun HoKim SH, Park HC, Yun D-J, Chung WS (2010). Cadmium activates Arabidopsis MPK3 and MPK6 via accumulation of reactive oxygen species. *Phytochemistry* 71: 614-618. doi: 10.1016/j.phytochem.2010.01.005
- Liu Y, He C (2016). Regulation of plant reactive oxygen species (ROS) in stress responses: learning from AtRBOHD. *Plant Cell Reports* 35: 995-1007. doi: 10.1007/s00299-016-1950-x
- Lloyd C, Chan J (2004). Microtubules and the shape of plants to come. *Nature Reviews Molecular Cell Biology* 5: 13-23. doi: 10.1038/nrm1277
- Lloyd CW, Traas JA (1988). The role of F-actin in determining the division plane of carrot suspension cells. *Development* 102: 211-221. doi: 10.1242/dev.102.1.211
- Lumbreras V, Vilela B, Irar S, Sole M, Capellades M, Valls M, Coca M, Pagès M (2010). MAPK phosphatase MKP2 mediates disease responses in Arabidopsis and functionally interacts with MPK3 and MPK6. *The Plant Journal* 63: 1017-1030. doi: 10.1111/j.1365-313X.2010.04297.x

- Maizel A, von Wangenheim D, Federici F, Haseloff J, Stelzer EHK (2011). High-resolution live imaging of plant growth in near physiological bright conditions using light sheet fluorescence microscopy. *Plant Journal* 68: 377-385. doi: 10.1111/j.1365-313X.2011.04692.x
- Mangano S, Juárez SPD, Estevez JM (2016). ROS Regulation of Polar Growth in Plant Cells. *Plant Physiology* 171: 1593-1605. doi: 10.1104/pp.16.00191
- Marc J, Granger CL, Brincat J, Fisher DD, Kao T, McCubbin AG, Cyr RJ (1998). A GFP-MAP4 reporter gene for visualizing cortical microtubule rearrangements in living epidermal cells. *Plant Cell* 10: 1927-1939. doi: 10.1105/tpc.10.11.1927
- Mauko A, Muck T, Mirtič B, Mladenovič A, Kreft M (2009). Use of confocal laser scanning microscopy (CLSM) for the characterization of porosity in marble. *Materials Characterization* 60: 603-609. doi: 10.1016/j.matchar.2009.01.008
- Mba C, Afza R, Bado S, Jain SM (2010). Induced mutagenesis in plants using physical and chemical agents. *Plant cell culture: essential methods*, ed. Davey MR, Anthony P (John Wiley & Sons) 20: 111-130.
- McCurdy DW, Kovar DR, Staiger CJ (2001). Actin and actin-binding proteins in higher plants. *Protoplasma* 215: 89-104. doi: 10.1007/BF01280306
- McDowell JM, An Y-Q, Huang S, McKinney EC, Meagher RB (1996). The Arabidopsis ACT7 actin gene is expressed in rapidly developing tissues and responds to several external stimuli. *Plant Physiology* 111: 699-711. doi: 10.1104/pp.111.3.699
- Meagher RB, McKinney EC, Vitale AV (1999). The evolution of new structures: clues from plant cytoskeletal genes. *Trends in Genetics* 15: 278-284. doi: 10.1016/S0168-9525(99)01759-X
- Meijering E., Dzyubachyk O, Smal I (2012). Methods for cell and particle tracking. *Methods in Enzymology* 504: 183-200. doi: 10.1016/B978-0-12-391857-4.00009-4
- Menon AK (2002). Lipid transport - an overview. *Seminars in Cell and Developmental Biology* 13: 159-162. doi: 10.1016/s1084-9521(02)00043-5
- Meyerowitz EM (2001). Prehistory of *Arabidopsis* research. *Plant Physiology* 125: 15-19. doi: 10.1104/pp.125.1.15
- Meyerowitz EM and Pruitt RE (1985). *Arabidopsis thaliana* and Plant Molecular Genetics. *Science* 229: 1214-1218. doi: 10.1126/science.229.4719.121
- Mhamdi A, Van Breusegem F (2018). Reactive oxygen species in plant development. *Development* 145: dev164376. doi: 10.1242/dev.164376
- Miedema H, Demidchik V, Véry AA, Bothwell JH, Brownlee C, Davies JM (2008). Two voltage-dependent calcium channels co-exist in the apical plasma membrane of *Arabidopsis thaliana* root hairs. *New Phytologist* 179: 378-385. doi: 10.1111/j.1469-8137.2008.02465.x
- Miles GP, Samuel MA, Ellis BE (2009). Suppression of MKK5 reduces ozone-induced signal trans- mission to both MPK3 and MPK6 and confers increased ozone sensitivity in *Arabidopsis thaliana*. *Plant Signal & Behavior* 4: 687-692. doi: 10.4161/psb.4.8.9298

- Miles GP, Samuel MA, Zhang Y, Ellis BE (2005). RNA interference-based (RNAi) suppression of AtMPK6, an *Arabidopsis* mitogen-activated protein kinase, results in hypersensitivity to ozone and misregulation of AtMPK3. *Environmental Pollution* 138: 230-237. doi: 10.1016/j.envpol.2005.04.017
- Milhaud J, Hartmann MA, Bolard J (1988). Interaction of the polyene antibiotic filipin with model and natural membranes containing plant sterols. *Biochimica et Biophysica Acta (BBA) – Biomembranes* 943: 315-325. doi: 10.1016/0005-2736(88)90563-9
- Miller DD, de Ruijter NCA, Bisseling T, Emons AM (1999). The role of actin in root hair morphogenesis: studies with lipochito-oligosaccharide as a growth stimulator and cytochalasin as an actin perturbing drug. *The Plant Journal* 17: 141-154. doi:10.1046/j.1365-313X.1999.00358.x
- Mittler R (2017). ROS Are Good. *Trends in Plant Sciences* 22: 11-19. doi: 10.1016/j.tplants.2016.08.002
- Molendijk AJ, Bischoff F, Rajendrakumar CS, Friml J, Braun M, Gilroy S, Palme K (2001). *Arabidopsis thaliana* Rop GTPases are localized to tips of root hairs and control polar growth. *The EMBO Journal* 20: 2779-2788. doi: 10.1093/emboj/20.11.2779
- Monshausen GB, Bibikova TN, Messerli MA, Shi C, Gilroy S (2007). Oscillations in extracellular pH and reactive oxygen species modulate tip growth of *Arabidopsis* root hairs. *Proceedings of the National Academy of Sciences of the USA* 104: 20996-21001. doi: 10.1073/pnas.0708586104
- Morel J, Clavero S, Mongrand S, Furt F, Fromentin J, Bessoule J-J, Blein J-P, Simon-Plas F (2006). Proteomics of plant detergent-resistant membranes. *Molecular & Cellular Proteomics* 5: 1396-1411. doi: 10.1074/mcp.M600044-MCP200
- Mouratou B, Biou V, Joubert A, Cohen J, Shields DJ, Geldner N, Jürgens G, Melançon P, Cherfils J (2005). The domain architecture of large guanine nucleotide exchange factors for the small GTP-binding protein Arf. *BMC Genomics* 6: 20. doi: 10.1186/1471-2164-6-20
- Muller HJ (1927). Artificial transmutation of gene. *Science* 66: 84-87. doi: 10.1126/science.66.1699.84
- Müller K, Carstens AC, Linkies A, Torres MA, Leubner-Metzger G (2009). The NADPH-oxidase AtrbohB plays a role in *Arabidopsis* seed after-ripening. *The New Phytologist* 184: 885-897. doi: 10.1111/j.1469-8137.2009.03005.x
- Müller S (2012). Universal rules for division plane selection in plants. *Protoplasma* 249: 239-253. doi: 10.1007/s00709-011-0289-y
- Mustafa AK, Gadalla MM, Sen N, Kim S, Mu W, Gazi SK, Barrow RK, Yang G, Wang R., Snyder SH (2009). H<sub>2</sub>S signals through protein S-sulfhydration. *Science Signaling* 2: ra72. doi: 10.1126/scisignal.2000464
- Neuhaus HE and Emes MJ (2000). Nonphotosynthetic metabolism in plastids. *Annual Review of Plant Physiology and Plant Molecular Biology* 51: 111-140.

- Nichols BJ, Kenworthy AK, Polishchuk RS, Lodge R, Roberts TH, Hirschberg K, Phair RD, Lippincott-Schwartz J (2001). Rapid cycling of lipid raft markers between the cell surface and Golgi complex. *Journal of Cell Biology* 153: 529542. doi: 10.1083/jcb.153.3.529
- Nishimura T, Yokota E, Wada T, Shimmen T, Okada K (2003). An *Arabidopsis* *ACT2* dominant-negative mutation, which disturbs F-actin polymerization, reveals its distinctive function in root development. *Plant & Cell Physiology* 44: 1131-1140. doi: 10.1093/pcp/pcg158
- Ohashi E, Tanabe K, Henmi Y, Mesaki K, Kobayashi Y, Takei K (2011). Receptor sorting within endosomal trafficking pathway is facilitated by dynamic actin filaments. *PLoS ONE* 6: e19942. doi: 10.1371/journal.pone.0019942
- Ovečka M, Berson T, Beck M, Derksen J, Šamaj J, Baluška F, Lichtscheidl IK (2010) Structural sterols are involved in both the initiation and tip growth of root hairs in *Arabidopsis thaliana*. *Plant Cell* 22: 2999–3019. doi: 10.1105/tpc.109.069880
- Ovečka M, Lang I, Baluška F, Ismail A, Illéš P, Lichtscheidl IK (2005). Endocytosis and vesicle trafficking during tip growth of root hairs. *Protoplasma* 226: 39–54. doi: 10.1007/s00709-005-0103-9
- Ovečka M, Lichtscheidl I, Šamaj J (2014). Live microscopy analysis of endosomes and vesicles in tip-growing root hairs. *Methods in Molecular Biology* 1209: 31–44. doi: 10.1007/978-1-4939-1420-3\_3
- Ovečka M, Vaškebová L, Komis G, Luptovčiak I, Smertenko A, Šamaj J (2015). Preparation of plants for developmental and cellular imaging by light-sheet microscopy. *Nature Protocols* 10: 1234-1247. doi: 10.1038/nprot.2015.081
- Ovečka M, von Wangenheim D, Tomančák P, Šamajová O, Komis G, Šamaj J (2018). Multiscale imaging of plant development by light-sheet fluorescence microscopy. *Nature Plants* 9: 639-650. doi: 10.1038/s41477-018-0238-2
- Overmyer K, Brosché M, Kangasjärvi J (2003). Reactive oxygen species and hormonal control of cell death. *Trends in Plant Science* 8: 335-342. doi: 10.1016/S1360-1385(03)00135-3
- Pallotta MA, Graham RD, Langridge P, Sparrow DHB, Barker SJ (2000). RFLP mapping of manganese efficiency in barley. *Theoretical and Applied Genetics* 101: 1100–1108. doi: 10.1007/s001220051585
- Pang L, Ma Z, Zhang X, Huang Y, Li R, Miao Y, Li R (2022). The small GTPase RABA2a recruits SNARE proteins to regulate the secretory pathway in parallel with the exocyst complex in *Arabidopsis*. *Molecular Plant* 15: 398-418. doi:10.1016/j.molp.2021.11.008
- Panteris E, Apostolakos P, Galatis B (2006). Cytoskeletal asymmetry in *Zea mays* subsidiary cell mother cells: a monopolar prophase microtubule half-spindle anchors the nucleus to its polar position. *Cell Motility and the Cytoskeleton* 63: 696–709. doi: 10.1002/cm.20155
- Parinov S, Sevugan M, Ye D, Yang W-C, Kumaran M, Sundaresan V (1999). Analysis of Flanking Sequences from *Dissociation Insertion Lines*: A database for reverse genetics in *Arabidopsis*. *Plant Cell* 11: 2263-2270. doi: 10.1105/tpc.11.12.2283

- Pei W, Du F, Zhang Y, He T, Ren H (2012). Control of the actin cytoskeleton in root hair development. *Plant Science* 187: 10-18. doi: 10.1016/j.plantsci.2012.01.008
- Pemberton LMS, Tsai S-L, Lovell PH, Harris PJ (2001). Epidermal patterning in seedling roots of eudicotyledons. *Annals of Botany* 87: 649–654. doi: 10.1006/anbo.2001.1385
- Pereira-Leal JB, Seabra MC (2001). Evolution of the Rab family of small GTP-binding proteins. *Journal of Molecular Biology* 313: 889-901. doi: 10.1006/jmbi.2001.5072
- Perilli S, Di Mambro R, Sabatini S (2012). Growth and development of the root apical meristem. *Current Opinion in Plant Biology* 15: 17-23. doi: 10.1016/j.pbi.2011.10.006
- Picton JM, Steer M (1983). Membrane recycling and the control of secretory activity in pollen tubes. *Journal of Cell Science* 63: 303-310. doi: 10.1242/jcs.63.1.303
- Pitzschke A, Djamei A, Bitton F, Hirt H (2009). A major role of the MEKK1–MKK1/2–MPK4 pathway in ROS signalling. *Molecular Plant* 2: 120-137. doi: 10.1093/mp/ssp079
- Pollard TD, Mooseker MS (1981). Direct measurement of actin polymerization rate constants by electron microscopy of actin filaments nucleated by isolated microvillus cores. *Journal of Cell Biology* 88: 654-659. doi: 10.1083/jcb.88.3.654
- Popescu SC, Popescu GV, Bachan S, Zhang Z, Gerstein M, Snyder M, Dinesh-Kumar SP (2009). MAPK target networks in *Arabidopsis thaliana* revealed using functional protein microarrays. *Genes Development* 23: 80-92. doi: 10.1101/gad.1740009
- Pospíšil P (2016). Production of reactive oxygen species by photosystem II as a response to light and temperature stress. *Frontiers in Plant Sciences* 7: 1950. doi: 10.3389/fpls.2016.01950
- Preuss ML, Serna J, Falbel TG, Bednarek SY, Nielsen E (2004). The Arabidopsis Rab GTPase RabA4b localizes to the tips of growing root hair cells. *The Plant Cell* 16: 1589-1603. doi:10.1105/tpc.021634
- Qi J, Wang J, Gong Z, Zhou JM (2017). Apoplastic ROS signaling in plant immunity. *Current Opinion in Plant Biology* 38: 92-100. doi: 10.1016/j.pbi.2017.04.022
- Qi X, Zheng H (2013). Rab-A1c GTPase defines a population of the trans-Golgi network that is sensitive to endosidin1 during cytokinesis in Arabidopsis. *Molecular Plant* 6: 847-859. doi: 10.1093/mp/sss116
- Ramachandran S, Christensen HEM, Ishimaru Y, Dong C-H, Chao-Ming W, Cleary AL, Chua N-H (2000). Profilin plays a role in cell elongation, cell shape maintenance, and flowering in Arabidopsis. *Plant Physiology* 124: 1637-1647. doi: 10.1104/pp.124.4.1637
- Ramel F, Sulmon C, Bogard M, Couée I, Gouesbet G (2009). Differential patterns of reactive oxygen species and antioxidative mechanisms during atrazine injury and sucrose induced tolerance in Arabidopsis thaliana plantlets. *BMC Plant Biology* 9: 28. doi: 10.1186/1471-2229-9-2
- Rasmussen CG, Wright AJ, Müller S (2013). The role of the cytoskeleton and associated proteins in determination of the plant cell division plane. *The Plant Journal* 75: 258-269. doi: 10.1111/tpj.12177

- Reddy GV, Gordon SP, Meyerowitz EM (2007). Unravelling developmental dynamics: transient intervention and live imaging in plants. *Nature Reviews Molecular Cell Biology* 8: 491-501. doi: 10.1038/nrm2188
- Rentel MC, Knight MR (2004). Oxidative stress-induced calcium signaling in Arabidopsis. *Plant Physiology* 135: 1471-1479. doi: 10.1104/pp.104.042663
- Reynaud EG, Peychl J, Huisken J, Tomančák P (2015). Guide to light-sheet microscopy for adventurous biologists. *Nature Methods* 12: 30-34. doi: 10.1038/nmeth.3222
- Ridge RW, Uozumi Y, Plazinski J, Hurley UA, Williamson RE (1999). Developmental transitions and dynamics of the cortical ER of *Arabidopsis* cells with green fluorescent protein. *Plant Cell Physiology* 40: 1253–1261. doi: 10.1093/oxfordjournals.pcp.a029513
- Ringli C, Baumberger N, Diet A, Frey B, Keller B (2002). ACTIN2 is essential for bulge site selection and tip growth during root hair development of Arabidopsis. *Plant Physiology* 129: 1464–1472. doi: 10.1104/pp.005777
- Ringli C, Baumberger N, Keller B (2005). The Arabidopsis root hair mutants *der2-der9* are affected at different stages of root hair development. *Plant & Cell Physiology* 46: 1046-1053. doi: 10.1093/pcp/pci115
- Rust MJ, Bates M, Zhuang XW (2006). Sub-diffraction-limit imaging by stochastic optical reconstruction microscopy (STORM). *Nature Methods* 3:793-795. doi: 10.1038/nmeth929
- Rutherford S, Moore I (2002). The Arabidopsis Rab GTPase family: another enigma variation. *Current Opinion in Plant Biology* 5: 518-528. doi: 10.1016/s1369-5266(02)00307-2
- Sagi M, Fluhr R (2006). Production of reactive oxygen species by plant NADPH oxidases. *Plant Physiology* 141: 336-34. doi: 10.1104/pp.106.078089
- Sakai J, Li J, Subramanian KK, Mondal S, Bajrami B, Hattori H, Jia Y, Dickinson BC, Zhong J, Ye K, Chang CJ, Ho Y-S, Zhou J, Luo HR (2012). Reactive oxygen species-induced actin glutathionylation controls actin dynamics in neutrophils. *Immunity* 37: 1037-1049. doi: 10.1016/j.immuni.2012.08.017
- Šamaj J, Baluška F, Voigt B, Schlicht M, Volkmann D, Menzel D (2004). Endocytosis, actin cytoskeleton, and signaling. *Plant Physiology* 135: 1150-1161. doi: 10.1104/pp.104.040683
- Šamaj J, Müller J, Beck M, Böhm N, Menzel D (2006). Vesicular trafficking, cytoskeleton and signalling in root hairs and pollen tubes. *Trends in Plant Science* 11: 594-600. doi: 10.1016/j.tplants.2006.10.002
- Šamaj J, Read ND, Volkmann D, Menzel D, Baluška F (2005). The endocytic network in plants. *TRENDS in Cell Biology* 15: 425-433. doi: 10.1016/j.tcb.2005.06.006
- Šamajová O, Komis G, Šamaj J (2013). Emerging topics in the cell biology of mitogen-activated protein kinases. *Trends in Plant Science* 18: 140-148. doi: 10.1016/j.tplants.2012.11.004
- Šamajová O, Komis G, Šamaj J (2014). Immunofluorescent localization of MAPKs and colocalization with microtubules in Arabidopsis seedling whole-mount probes. *Methods in Molecular Biology* 1171: 107–115. doi: 10.1007/978-1-4939-0922-3\_9



- Sampathkumar A, Lindeboom JJ, Debolt S, Gutierrez R, Ehrhardt DW, Ketelaar T, Persson S (2011). Live cell imaging reveals structural associations between the actin and microtubule cytoskeleton in Arabidopsis. *The Plant Cell* 23: 2302-2313. doi: 10.1105/tpc.111.087940
- Sanderfoot AA, Kovaleva V, Bassham DC, Raikhel NV (2001). Interactions between syntaxins identify at least five SNARE complexes within the Golgi/prevacuolar system of the Arabidopsis cell. *Molecular Biology of the Cell* 12: 3733-3743. doi: 10.1091/mbc.12.12.3733
- Saxton M (2008). Single-particle tracking: connecting the dots. *Nature Methods* 5: 671-672 doi: 10.1038/nmeth0808-671
- Schaeffer A, Bronner R, Benveniste P, Schaller H (2001). The ratio of campesterol to sitosterol that modulates growth in *Arabidopsis* is controlled by STEROL METHYLTRANSFERASE 2;1. *The Plant Journal: for cell and molecular biology* 25: 605-615. doi: 10.1046/j.1365-313x.2001.00994.x
- Scheres B, Benfey P, Dolan L (2002). Root development. *The Arabidopsis Book* 1, e0101. doi: 10.1199/tab.0101
- Scheres B, Wolkenfelt H, Willemsen V, Terlouw M, Lawson E, Dean C, Weisbeek P (1994). Embryonic origin of the Arabidopsis primary root and root meristem initials. *Development* 120: 2475-2487. doi: 10.1242/dev.120.9.2475
- Schiefelbein JW, Somerville C (1990). Genetic control of root hair development in Arabidopsis thaliana. *The Plant Cell* 2: 235-243. doi: 10.1105/tpc.2.3.235
- Schrack K, Mayer U, Horrichs A, Kuhnt C, Bellini C, Dangel J, Schmidt J, Jürgens G (2000). FACKEL is a sterol C-14 reductase required for organized cell division and expansion in Arabidopsis embryogenesis. *Genes & Development* 14: 1471-1484. doi: 10.1101/gad.14.12.1471
- Shaw PJ (2006). "Comparison of widefield/deconvolution and confocal microscopy for three-dimensional imaging," in: Handbook of Biological Confocal Microscopy, eds. Pawley J (Springer, Boston, MA), 453-467. doi: 10.1007/978-0-387-45524-2\_23.
- Sheppard CJR, Mehta SB, Heintzmann R (2013). Superresolution by image scanning microscopy using pixel reassignment. *Opt. Lett.* 38: 2889-2892. doi: 10.1364/OL.38.002889
- Sheterline P, Clayton J, Sparrow JC (1998). Actin. *Protein profile* 4: 1-272.
- Sieberer BJ, Ketelaar T, Esseling JJ, Emons AMC (2005). Microtubules guide root hair tip growth. *New Phytologist* 167: 711-719. doi: 10.1111/j.1469-8137.2005.01506.x
- Sieberer BJ, Timmers ACJ, Lhuissier FGP, Emons AMC (2002). Endoplasmic microtubules configure the subapical cytoplasm and are required for fast growth of *Medicago truncatula* root hairs. *Plant Physiology* 130: 977-988. doi: 10.1104/pp.004267
- Singh R, Singh S, Parihar P, Mishra R., Tripathi DhK, Singh VP, Chauhan DK, Prasad SM (2016). Reactive Oxygen Species (ROS): Beneficial Companions of Plants' Developmental Processes. *Frontiers in Plant Science* 7: 1299. doi: 10.3389/fpls.2016.01299
- Sinha AK, Jaggi M, Raghuram B, Tuteja N (2011). Mitogen-activated protein kinase signaling in plants under abiotic stress. *Plant Signal & Behavior* 6: 196-203. doi: 10.4161/psb.6.2.14701

- Sivaguru M, Urban MA, Fried G, Wesseln CJ, Mander L, Punyasena SW (2016). Comparative performance of airyscan and structured illumination superresolution microscopy in the study of the surface texture and 3D shape of pollen. *Microscopy Research & Technique* 81:101-114. doi: 10.1002/jemt.22732
- Smékalová V, Doskočilová A, Komis G, Šamaj J (2013). Crosstalk between secondary messengers, hormone and MAPK modules during abiotic stress signalling in plants. *Biotechnology Advances* 31: 2-11. doi: 10.1016/j.biotechadv.2013.07.009
- Smith LG (2001). Plant cell division: building walls in the right places. *Nature Reviews Molecular Cell Biology* 2: 33-39. doi: 10.1038/35048050
- Smolarkiewicz M, Dhonukshe P (2013). Formative cell divisions: principal determinants of plant morphogenesis. *Plant & Cell Physiology* 54: 333-342. doi: 10.1093/pcp/pcs175
- Snustad DP, Haas NA, Kopcak SD, Silflow CD (1992). The small genome of *Arabidopsis* contains at least nine expressed  $\beta$ -tubulin genes. *The Plant Cell* 4: 549-556. doi: 10.1105/tpc.4.5.549
- Snyman CJ, Raidoo DM, Bhoola KD (1999). "Localization of proteases and peptide receptors by confocal microscopy," in: *Methods in Enzymology*, ed. Conn EM (Academic Press, San Diego) 307: 368-394. doi: 10.1016/s0076-6879(99)07024-x
- Sorek N, Gutman O, Bar E, Abu-Abied M, Feng X, Running MP, Lewinsohn E, Ori N, Sadot E, Henis YI, et al. (2011). Differential effects of prenylation and S-acylation on type I and II ROPS membrane interaction and function. *Plant Physiology* 155: 706-720. doi: 10.1104/pp.110.166850
- Sorek N, Poraty L, Sternberg H, Bar E, Lewinsohn E, Yalovsky S (2007). Activation Status-Coupled Transient S Acylation Determines Membrane Partitioning of a Plant Rho-Related GTPase. *Molecular and Cellular Biology* 27: 2144-2154. doi: 10.1128/MCB.02347-06
- Souter M, Topping J, Pullen M, Friml J, Palme K, Hackett R, Grierson D, Lindsey K (2002). Hydra mutants of *Arabidopsis* are defective in sterol profiles and auxin and ethylene signaling. *The Plant Cell* 14: 1017-1031. doi:10.1105/tpc.001248
- Srivastava V, Malm E, Sundqvist G, Bulone V (2013). Quantitative proteomics reveals that plasma membrane microdomains from poplar cell suspension cultures are enriched in markers of signal transduction, molecular transport, and callose biosynthesis. *Molecular & Cellular Proteomics* 12: 3874-3885. doi: 10.1074/mcp.M113.029033
- Staiger CJ (2000). Signaling to the actin cytoskeleton in plants. *Annual Review of Plant Physiology and Plant Molecular Biology* 51: 257-288. doi: 10.1146/annurev.arplant.51.1.257
- Staiger CJ, Blanchoin L (2006). Actin dynamics: Old friends with new stories. *Current Opinion Plant in Biology* 9: 554-562. doi: 10.1016/j.pbi.2006.09.013
- Stanislas T, Hüser A, Barbosa IC, Kiefer CS, Brackmann K, Pietra S, Gustavsson A, Zourelidou M, Schwechheimer C, Grebe M (2015). *Arabidopsis* D6PK is a lipid domain-dependent mediator of root epidermal planar polarity. *Nature Plants* 1: 15162. doi: 10.1038/NPLANTS.2015.162

- Stehbens S, Pemble H, Murrow L, Wittmann T (2012). Imaging intracellular protein dynamics by spinning disk confocal microscopy. *Methods in Enzymology* 504: 293-313. doi: 10.1016/B978-0-12-391857-4.00015-X
- Stelzer EHK (2015). Light-sheet fluorescence microscopy for quantitative biology. *Nature Methods* 12: 23-26. doi: 10.1038/nmeth.3219
- Stenzel I, Ischebeck T, König S, Hołubowska A, Sporysz M, Hause B, Heilmann I (2008). The type B Phosphatidylinositol-4-Phosphate 5-Kinase 3 is essential for root hair formation in *Arabidopsis thaliana*. *The Plant Cell* 20: 124-141. doi: 10.1105/tpc.107.052852
- Stojkov D, Amini P, Oberson K, Sokollik C, Duppenhaler A, Simon H-U, Yousefi S (2017). ROS and glutathionylation balance cytoskeletal dynamics in neutrophil extracellular trap formation. *Journal of Cell Biology* 216: 4073-4090. doi: 10.1083/jcb.201611168
- Sunkar R, Kapoor A, Zhu J-K (2006). Posttranscriptional induction of two Cu/Zn superoxide dismutase gene in *Arabidopsis* is mediated by downregulation of miR398 and important for oxidative stress tolerance. *Plant Cell* 18: 2051-2065. doi: 10.1105/tpc.106.041673
- Takatsuka H, Umeda M (2015). Epigenetic Control of Cell Division and Cell Differentiation in the Root Apex. *Frontiers in Plant Science* 6: 1178. doi: 10.3389/fpls.2015.01178
- Takeda S, Gapper C, Kaya H, Bell E, Kuchitsu K, Dolan L (2008). Local positive feedback regulation determines cell shape in root hair cells. *Science* 319: 1241-1244. doi: 10.1126/science.1152505
- Takeuchi M, Karahara I, Kajimura N, Takaoka A, Murata K, Misaki K, Yonemura S, Staehelin LA, Mineyuki Y (2016). Single microfilaments mediate the early steps of microtubule bundling during preprophase band formation in onion cotyledon epidermal cells. *Molecular Biology of the Cell* 27: 1809-1820. doi: 10.1091/mbc.e15-12-0820
- Tanaami T, Otsuki S, Tomosada N, Kosugi Y, Shimizu M, Ishida H (2002). High-speed 1-frame/ms scanning confocal microscope with a microlens and Nipkow disks. *Applied Optics* 41: 4704-4708. doi: 10.1364/ao.41.004704
- The Arabidopsis Genome Initiative (2000). Analysis of the genome sequence of the flowering plant *Arabidopsis thaliana*. *Nature* 408: 796-815. doi: 10.1038/35048692
- Tichá M, Illéšová P, Hrbáčková M, Basheer J, Novák D, Hlaváčková K, Šamajová O, Niehaus K, Ovečka M, Šamaj J (2020). Tissue culture, genetic transformation, interaction with beneficial microbes, and modern bio-imaging techniques in alfalfa research. *Critical Reviews in Biotechnology* 40: 1265-1280. doi: 10.1080/07388551.2020.1814689
- Torres MA, Dangl JL, Jones JD (2002). *Arabidopsis* gp91phox homologues AtrbohD and AtrbohF are required for accumulation of reactive oxygen intermediates in the plant defense response. *Proceedings of the National Academy of Sciences of the USA* 99: 517-522. doi: 10.1073/pnas.012452499
- Toshima JY, Toshima J, Kaksonen M, Martin AC, King DS, Drubin DG (2006). Spatial dynamics of receptor-mediated endocytic trafficking in budding yeast revealed by using fluorescent alpha-factor derivatives. *Proceedings of the National Academy of Sciences USA* 103: 5793-5798. doi: 10.1073/pnas.0601042103

- Trejo HE, Lecuona E, Grillo D, Szeleifer I, Nekrasova OE, Gelfand VI, Sznajder JI (2010). Role of kinesin light chain-2 of kinesin-1 in the traffic of Na, K-ATPase-containing vesicles in alveolar epithelial cells. *The FASEB Journal* 24: 374-382. doi:10.1096/fj.09-137802
- Trevisan S, Trentin AR, Ghisi R, Masi A, Quaggiotti S (2019). Nitrate affects transcriptional regulation of UPBEAT1 and ROS localisation in roots of *Zea mays* L. *Physiologia Plantarum* 166: 794-811. doi: 10.1111/pp.12839
- Tsukagoshi H (2016). Control of root growth and development by reactive oxygen species. *Current Opinion in Plant Biology* 29: 57-63. doi: 10.1016/j.pbi.2015.10.012
- Tsukagoshi H, Busch W, Benfey PN (2010). Transcriptional regulation of ROS controls transition from proliferation to differentiation in the root. *Cell* 143: 606-616. doi: 10.1016/j.cell.2010.10.020
- Ueda T, Nakano A (2002). Vesicular traffic: an integral part of plant life. *Current Opinion in Plant Biology* 5: 513-517. doi: 10.1016/s1369-5266(02)00299-6
- Ueda T, Uemura T, Sato MH, Nakano A (2004). Functional differentiation of endosomes in Arabidopsis cells. *The Plant Journal* 40:783-789. doi: 10.1111/j.1365-313X.2004.02249.x
- Uemura T, Ueda T, Ohniwa RL, Nakano A, Takeyasu K, Sato MH (2004). Systematic analysis of SNARE molecules in Arabidopsis: dissection of the post-Golgi network in plant cells. *Cell Structure and Function* 29: 49–65. doi: 10.1247/csf.29.49
- Valitova JN, Sulkarnayeva AG, Minibayeva F (2016). Plant sterols: Diversity, biosynthesis, and physiological functions. *Biochemistry (Moscow)* 81: 819-834. doi: 10.1134/S0006297916080046
- Van Bruaene N, Joss G, van Oostveldt P (2004). Reorganization and in vivo dynamics of microtubules during Arabidopsis root hair development. *Plant Physiology* 136: 3905-3919. doi: 10.1104/pp.103.031591
- Van Damme D, van Poucke K, Boutant E, Ritzenthaler C, Inzé D, Geelen D (2004). In vivo dynamics and differential microtubule-binding activities of MAP65 proteins. *Plant Physiology* 136: 3956-3967. doi: 10.1104/pp.104.051623
- Van Damme D, Vanstraelen M, Geelen D (2007). Cortical division zone establishment in plant cells. *Trends in Plant Science* 12: 458-464. doi: 10.1016/j.tplants.2007.08.011
- Vanderauwera S, Suzuki N, Miller G, van de Cotte B, Morsa S, Ravanat J-L, Hegie A, Triantaphylidès C, Shulaev V, Van Montagu MCE, Van Breusegem F, Mittler R (2011). Extranuclear protection of chromosomal DNA from oxidative stress. *Proceedings of the National Academy of Sciences of the US* 108: 1711-1716. doi: 10.1073/pnas.1018359108
- Vazquez LAB, Sanchez R, Hernandez-Barrera A, Zepeda-Jazo I, Sánchez F, Quinto C, Torres LC (2014). Actin polymerization drives polar growth in Arabidopsis root hair cells. *Plant Signaling & Behavior*, 9, e29401. doi: 10.4161/psb.29401
- Verveer PJ, Swoger J, Pampaloni F, Greger K, Marcello M, Stelzer EHK (2007). High-resolution threedimensional imaging of large specimens with light sheet-based microscopy. *Nature methods* 4:311-313. doi: 10.1038/nmeth1017

Viotti C, Bubeck J, Stierhof YD, Krebs M, Langhans M, van den Berg W, van Dongen W, Richter S, Geldner N, Takano J, *et al.* (2010). Endocytic and secretory traffic in Arabidopsis merge in the trans-Golgi network/early endosome, an independent and highly dynamic organelle. *The Plant Cell*, 22: 1344-1357, <https://doi.org/10.1105/tpc.109.072637>

Voigt B, Timmers A, Šamaj J, Hlavacka A, Ueda T, Preuss M, Nielsen E, Mathur J, Emans N, Stenmark H, *et al.* (2005a). Actin-based motility of endosomes is linked to the polar tip growth of root hairs. *European Journal of Cell Biology* 84: 609-621. doi: 10.1016/j.ejcb.2004.12.029

Voigt B, Timmers ACJ, Šamaj J, Müller J, Baluška F, Menzel D (2005b). GFP-FABD2 fusion construct allows in vivo visualization of the dynamic actin cytoskeleton in all cells of Arabidopsis seedlings. *European Journal of Cell Biology* 84: 595-608. doi: 10.1016/j.ejcb.2004.11.011

Volkman D, Baluška F (1999). The actin cytoskeleton in plants: from transport networks to signaling networks. *Microscopy Research and Technique* 47: 135-154. doi: 10.1002/(SICI)1097-0029(19991015)47:2<135::AID-JEMT6>3.0.CO;2-1

von Wangenheim D, Fangerau J, Schmitz A, Smith RS, Leitte H, Stelzer EHK, Maizel A (2016a). Rules and self-organizing properties of post-embryonic plant organ cell division patterns. *Current Biology* 26: 439-449. doi: 10.1016/j.cub.2015.12.047

von Wangenheim D, Rosero A, Komis G, Šamajová O, Ovečka M, Voigt B, Šamaj J (2016b). Endosomal interactions during root hair growth. *Frontiers in Plant Science* 6: 1262. doi: 10.3389/fpls.2015.01262

Wachtler V, Rajagopalan S, Balasubramanian MK (2003). Sterol-rich plasma membrane domains in the fission yeast *Schizosaccharomyces pombe*. *Journal of Cell Science* 116: 867-874. doi: 10.1242/jcs.00299

Wang E, Babbey CM, Dunn KW (2005). Performance comparison between the high-speed Yokogawa spinning disc confocal system and single-point scanning confocal systems. *Journal of Microscopy* 218: 148-159. doi: 10.1111/j.1365-2818.2005.01473.x

Wang H (2016). Visualizing plant cells in a brand new way. *Molecular Plant* 9:633-635. doi: 10.1016/j.molp.2016.02.006

Wang H, Wang S, Lu Y, Alvarez S, Hicks LM, Ge X, Xia Y (2012). Proteomic analysis of early-responsive redox-sensitive proteins in Arabidopsis. *Journal of Proteome Research* 11: 412-424. doi: 10.1021/pr200918f

Wasteneys GO, Galway, ME (2003). Remodeling the cytoskeleton for growth and form: An overview with some new views. *Annual Review of Plant Biology* 54: 691-722. doi: 10.1146/annurev.arplant.54.031902.134818

Weber M, Huisken (2011). Light sheet microscopy for real-time developmental biology. *Current Opinion in Genetics & Development* 21: 566-572. doi: 10.1016/j.gde.2011.09.009

Willemsen V, Friml J, Grebe M, van den Toorn A, Palme K, Scheres B (2003). Cell polarity and PIN protein positioning in Arabidopsis require STEROL METHYLTRANSFERASE1 function. *The Plant Cell* 15: 612-625. doi: 10.1105/tpc.008433

- Woollard AA, Moore I (2008). The functions of Rab GTPases in plant membrane traffic. *Current Opinion in Plant Biology* 11: 610-619. doi: 10.1016/j.pbi.2008.09.010
- Wright SJ, Centonze VE, Stricker SA, DeVries PJ, Paddock SW, Schatten G (1993). "Introduction to confocal microscopy and three-dimensional reconstruction," in: *Methods in Cell Biology*, ed. Matsumoto B (*Academic Press, San Diego*) 38: 1-45. doi: 10.1016/S0091-679X(08)60998-X
- Wright SJ, Wright DJ (2002). "Introduction to confocal microscopy," in: *Methods in Cell Biology*, eds. Wilson L, Matsudaira P (*Elsevier Science, USA*), 70: 1-85. doi:10.1016/s0091-679x(02)70002-2
- Xie HT, Wan ZY, Li S, Zhang Y (2014). Spatiotemporal Production of Reactive Oxygen Species by NADPH Oxidase Is Critical for Tapetal Programmed Cell Death and Pollen Development in *Arabidopsis*. *The Plant Cell* 26: 2007-2023. doi: 10.1105/tpc.114.125427
- Xing Y, Cao Q, Zhang Q, Qin L, Jia W, Zhang J (2013). MKK5 regulates high light-induced gene expression of Cu/Zn superoxide dismutase 1 and 2 in *Arabidopsis*. *Plant & Cell Physiology* 54: 1217-1227. doi: 10.1093/pcp/pct072
- Xu C-R, Liu C, Wang Y-L, Li L-C, Chen W-Q, Xu Z-H, Bai S-N (2005). Histone acetylation affects expression of cellular patterning genes in the *Arabidopsis* root epidermis. *Proceedings of the National Academy of Sciences USA* 102: 14469–14474. doi: 10.1073/pnas.05031431
- Xue B, Robinson RC (2013). Guardians of the actin monomer. *European Journal of Cell Biology* 92: 316-332. doi: 10.1016/j.ejcb.2013.10.012
- Yang S, Yu Q, Zhang Y, Jia Y, Wan S, Kong X, Ding Z (2018). ROS The fine tuner of plant stem cell fate. *Trends in Plant Science* 23: 850–853. doi: 10.1016/j.tplants.2018.07.010
- Yang Z (2002). Small GTPases: versatile signaling switches in plants. *The Plant Cell* 14: S375-S388. doi: 10.1105/tpc.001065
- Yang Z (2008). Cell polarity signaling in *Arabidopsis*. *Annual Review of Cell and Developmental Biology* 24: 551-575. doi: 10.1146/annurev.cellbio.23.090506.123233
- Yoshida K, Hara S, Hisabori T (2015). Thioredoxin selectivity for thiol-based redox regulation of target proteins in chloroplasts. *Journal of Biological Chemistry* 290: 14278-14288. doi: 10.1074/jbc.M115.647545
- Zeng J, Dong Z, Wu H, Tian, Zhao Z (2017). Redox regulation of plant stem cell fate. *The EMBO Journal* 36: 2844-285. doi: 10.15252/embj.201695955
- Zerial M, McBride H (2001). Rab proteins as membrane organizers. *Nature Reviews Molecular Cell Biology* 2:107-117. doi: 10.1038/35052055
- Zhang Y, Iakovidis M, Costa S (2016). Control of patterns of symmetric cell division in the epidermal and cortical tissues of the *Arabidopsis* root. *Development* 143: 978-982. doi: 10.1242/dev.129502
- Zheng H, Chen J (2011). Emerging aspects of ER organization in root hair tip growth: lessons from RHD3 and Atlastin. *Plant Signaling & Behavior* 6: 1710-1713.

Zhou X, Xiang Y, Li C, Yu G (2020). Modulatory Role of Reactive Oxygen Species in Root Development in Model Plant of *Arabidopsis thaliana*. *Frontiers in Plant Sciences* 11: 485932. doi: 10.3389/fpls.2020.485932

Zhou Y, Yang Z, Guo G, Guo Y (2010). Microfilament dynamics is required for root growth under alkaline stress in *Arabidopsis*. *Journal of Integrative Plant Biology* 52: 952-958. doi: 10.1111/j.1744-7909.2010.00981.x

Zwiewka M, Bielach A, Tamizhselvan P, Madhavan S, Ryad EE, Tan S, Hrtyan M, Dobrev P, Vanková R, Friml J, Tognetti VB (2016). Root adaptation to H<sub>2</sub>O<sub>2</sub>-induced oxidative stress by ARF-GEF BEN1- and cytoskeleton-mediated PIN2 trafficking. *Plant Cell & Physiology* 60: 255-273. doi: 10.1093/pcp/pcz001

## 7. Abbreviations

$^1\text{O}_2$	Singlet oxygen
<i>A. thaliana</i>	<i>Arabidopsis thaliana</i>
ABA	Abscisic acid
ABP	Actin binding protein
ACLSM	Airyscan confocal laser scanning microscopy
ACT	Actin
ADP	Adenosine diphosphate
AF	Actin filament
AHA	H <sup>+</sup> -ATPases
ARA medium	Arabidopsis modified medium
ARF	Actin related factor
Arg	Arginine
AtRbohC	<i>Arabidopsis thaliana</i> respiratory burst oxidase homolog protein C
AU	Airy Unit
BEN1	Nad(p)-binding rossmann-fold superfamily protein
BP	Band-pass filter
BSA	Bovine serum albumin
Ca (NO <sub>3</sub> ) <sub>2</sub> .4 H <sub>2</sub> O	Calcium nitrate tetrahydrate
Ca <sup>2+</sup>	Calcium ions
CaC	Calcium channel
CaCl <sub>2</sub>	Calcium chloride
Cas9	CRISPR associated protein 9
CDP	Cell division plane
CLSM	Confocal laser scanning microscopy
CMOS	Complementary metal-oxide-semiconductor
CMT	Cortical microtubules
CoCl <sub>2</sub> .6 H <sub>2</sub> O	Cobalt (II) chloride hexahydrate
Col-0	Columbia ecotype
CRISPR	Clustered regularly interspaced short palindromic repeats
CuSO <sub>4</sub> .5 H <sub>2</sub> O	Copper sulfate pentahydrate



CuZnSOD	Copper-zinc superoxide dismutase
Cys	Cysteine
Da	Dalton
DAB	Diaminobenzidine
DAPI	4',6-diamidino-2-phenylindole
<i>der</i>	<i>deformed root hairs</i>
DIC	Differential interference contrast
<i>dim</i>	<i>diminuto</i>
DTT	Dithiotreitol
<i>dwf</i>	<i>dwarf</i>
EE	Early endosome
EMCCD	Electron multiplication charge-coupled device
EMS	Ethyl methanesulphonate
EMT	Endoplasmic microtubules
ER	Endoplasmic reticulum
FABD2	F-actin binding domain 2 of <i>Arabidopsis</i>
	FIMBRIN1
FEP	Fluorinated ethylene propylene
FeSO <sub>4</sub> .7 H <sub>2</sub> O	Iron (II) sulfate heptahydrate
FeSOD1	Iron superoxide dismutase 1
<i>Fk</i>	<i>fackel</i>
FM4-64	N-(3-triethylammoniumpropyl)-4-(6-(4(diethylamino)phenyl)hexatrienyl)pyridinium dibromide, styryl dye for plasma membrane visualization
FYVE	A zinc finger domain named according to the four cysteine-rich proteins: Fab 1, yeast ortholog of PIKfyve, YOTB, Vac 1, vesicle transport protein, and EEA1
GA	Golgi apparatus
GaAsP	Gallium arsenide phosphide
GDP	Guanosine diphosphate
GEF	Guanine nucleotide exchange factor
GFP	Green fluorescence protein

GPI	Glycosylphosphatidylinositol
GTP	Guanosine triphosphate
GTPase	Hydrolase enzymes binding to the nucleotide guanosine triphosphate
H <sub>2</sub> O <sub>2</sub>	Hydrogen peroxide
H <sub>3</sub> BO <sub>3</sub>	Boric acid
IgG	Immunoglobulin G
KH <sub>2</sub> PO <sub>4</sub>	Potassium dihydrogen phosphate
KNO <sub>3</sub>	Potassium nitrate
KOH	Potassium hydroxide
Ler	Landsberg erecta
LSFM	Light-sheet fluorescence microscopy
MAP4	MICROTUBULE-ASSOCIATED PROTEIN 4
MBD	Microtubule binding protein
MgSO <sub>4</sub> .7H <sub>2</sub> O	Magnesium sulfate heptahydrate
MnCl <sub>2</sub> .4 H <sub>2</sub> O	Manganese (II) chloride tetrahydrate
mRNA	Messenger ribonucleic acid
MS medium	Murashige & Skoog medium
MT	microtubule
MTOC	Microtubule organization centre
MVB	Multivesicular bodies
NA	Numerical aperture
Na <sub>2</sub> EDTA	Ethylenedinitrilotetraacetic acid disodium salt dihydrate
Na <sub>2</sub> MoO <sub>4</sub> .2 H <sub>2</sub> O	Sodium molybdate dihydrate
NaCl	Sodium chloride
NADPH	Nicotinamide adenine dinucleotide phosphate
NBT	Nitrotetrazolium blue
NOX	NADPH oxidase proteins
NtRBOH	<i>Nicotiana tabacum</i> respiratory burst oxidase homologue
O <sub>2</sub> <sup>·-</sup>	Superoxide
OH <sup>·</sup>	Hydroxyl radical
PBS	Phosphate-buffered saline

pH	Potential of hydrogen
PIN2	Auxin efflux carrier component 2
PIP	Prolactin-induced protein
PIP5K3	Phosphatidylinositol Phosphate 5-Kinase 3
PM	Plasma membrane
PMT	Photomultiplier tube
PPB	Pre-prophase band
PQ	Paraquat
Pro	Promotor
PrxQ	Peroxiredoxin Q
PSF	Point spread function
PtdIns(4,5)P2	PhosphatidylInositol-4,5-bisphosphate
PVC	Prevacuolar compartment
RabA1d	Rab actin related factor GTPase Homolog A1d
RFP	Red fluorescence protein
RH	Root hair
RHD2	Root hair defective2
Rho	Ras homologous protein family
ROI	Region of interest
ROP	Rho of plants
ROS	Reactive oxygen species
SD	Spinning disk microscopy
SIM	Structured illumination microscopy
<i>smt</i>	<i>sterol methyltransferase</i>
SNARE	Soluble N-ethylmaleimide-sensitive fusion protein Attachment protein Receptor
SNR	Signal-to-noise ration
SOD	Superoxide dismutase
SPT	Single-particle tracking
<i>ste1</i>	<i>sterol1</i>
STED	Stimulated emission depletion microscopy
StRBOH	<i>Solanum tuberosum</i> respiratory burst oxidase homologue
T-DNA	Transfer deoxyribonucleic acid

TGN	Trans-Golgi network
TUA	Tubulin $\alpha$
TUB	Tubulin $\beta$
UBQ	Ubiquitin
UPB1	UPBEAT1
VTI12	Vesicle transport v-SNARE 12
YFP	Yellow fluorescence protein
ZnSO <sub>4</sub> .7 H <sub>2</sub> O	Zinc sulfate heptahydrate

## **8. Curriculum vitae**

### **Personal Data**

Name and Surname: Lenka Kuběňová  
Meiden name: Vaškebová  
Date and Place of Birth: 27th of May 1992, Frýdek-Místek

### **Employment:**

Ph.D. student/researcher at the Department of Biotechnology, Faculty of Science, Palacký University in Olomouc (1/2020 until present)

### **Education:**

Ph.D. – Biochemistry, Palacký University in Olomouc (2016-until present)

Title of Ph.D. thesis: Dynamic properties of membranes, cytoskeleton and reactive oxygen species during polar growth of plant cells

Master – Molecular and Cellular Biology, Palacký University in Olomouc (2016)

Title of master's thesis: Influence of actin mutation in plants of *Arabidopsis thaliana* on integrity and dynamic properties of the cytoskeleton in control and stress conditions

Bachelor – Molecular and Cellular Biology, Palacký University in Olomouc (2014)

Title of bachelor's thesis: Sensitivity of selected root hair mutants of *Arabidopsis* to abiotic stress

### **Foreign Research Fellowships:**

Three-month scientific-research internship – Max Planck Institute of Molecular Cell Biology and Genetics in Dresden, Germany (1.6.2022 - 31.8.2022)

14th day traineeship – Department of Ecological and Biological Sciences, Pavol Jozef Šafárik University in Košice, Faculty of Science, Slovakia (7. 9. – 19. 9. 2014)

### **Research Activities**

**Research Focus:** cell and developmental plant biology, cytoskeleton and vesicular trafficking in plants, under diverse environmental conditions (abiotic stress), study of root

hair growth of *A. thaliana* plants, microscopic techniques (standard epifluorescence, confocal and spinning-disk microscopy, but also advanced methods such as light-sheet microscopy, confocal laser scanning microscopy with Airyscan module, and also experience with lattice light-sheet microscopy)

**List of attended conferences:**

- **Kuběnová L**, Tichá M, Šamaj J, Ovečka M (2021). Spatiotemporal pattern of AtrbohC/ROOT HAIR DEFECTIVE 2 redistribution during root hair formation in *Arabidopsis thaliana* (2021) Online SEB Annual Conference, Antverpy, Belgium, 29. June - 8. July 2021. Oral presentation.
- Ovečka M, **Vaškebová L**, Takáč T, Šamaj J (2017). Cytoskeletal fluorescent markers enhance plant vigour, biomass production and stress response in C24 ecotype of *Arabidopsis thaliana*. Plant Biotechnology: Green for Good IV, Olomouc, Czech Republic, 19.-22. June 2017. Poster presentation.
- **Vaškebová L**, Ovečka M, Šamaj J (2015). Is sensitivity to selected abiotic stresses compromised in root hair mutants of *Arabidopsis thaliana*? Plant Biotechnology: Green for Good III, Olomouc, Czech Republic, 15.-18. June 2015. Poster presentation.
- **Vaškebová L**, Šatná B, Ovečka M, Šamaj J (2014). Sensitivity of selected root hair mutants of *Arabidopsis thaliana* to abiotic stress. 16th European Congress on Biotechnology, Edinburgh, Scotland, 13.-16. July 2014. Poster presentation.

**Grant Projects (Team Member):** IGA grants (number of projects IGA\_PrF\_2014\_033, IGA\_PrF\_2015\_015 and IGA\_PrF\_2016\_012); grant LO1204 NPU – Czech Republic; GAČR (2019-2021)\_19-18675S.

**Grant Projects (Main solver):** student IGA project (IGA\_PrF\_2022\_014)

**Teaching Experience:** Practical course CRH/PKR Plant tissue culture (2016, 2017)

Supervisor of bachelor's student Jan Haberland (defence 28 June 2021)

Supervisor of magister's student Jan Haberland (defence planned for 2023)

**Publication and Review Activities:** 5 published papers or reviews (4 first-author), 80 citations (ResearchGate; as of 29 September 2022); h-index 3; total impact factor 36.972

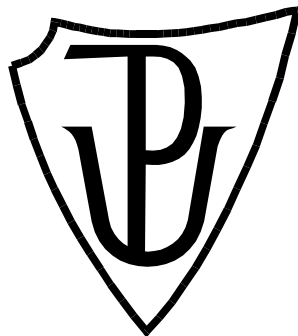
### **List of Publications:**

- **Kuběnová L**, Tichá M, Šamaj J, Ovečka M (2022). ROOT HAIR DEFECTIVE 2 vesicular delivery to the apical plasma membrane domain during Arabidopsis root hair development. *Plant Physiology* **188**: 1563-1585; kiab595. doi: 10.1093/plphys/kiab595 (IF=8.972)
- Ovečka M, Sojka J, Tichá M, Komis G, Basheer J, Marchetti C, Šamajová O, **Kuběnová L**, Šamaj J (2022). Imaging plant cells and organs with light-sheet and super-resolution microscopy. *Plant Physiology* **188**: 683-702; kiab349. doi: 10.1093/plphys/kiab349 (IF=8.972)
- **Kuběnová L**, Takáč T, Šamaj J, Ovečka M (2021). Single Amino Acid Exchange in ACTIN2 confers Increased Tolerance to Oxidative Stress in Arabidopsis *der1-3* Mutant. *International Journal of Molecular Sciences* **22**: 1879. doi: 10.3390/ijms22041879 (IF=5.542)
- **Vaškebová L**, Šamaj J, Ovečka M (2018). Single-point ACT2 gene mutation in the Arabidopsis root hair mutant *der1-3* affects overall actin organization, root growth and plant development. *Annals of Botany* **122**: 889-901. doi: 10.1093/aob/mcx180 (IF= 3.454)
- Ovečka M, **Vaškebová L**, Komis G, Luptovčíak I, Smertenko A, Šamaj J (2015). Preparation of plants for developmental and cellular imaging by light-sheet microscopy. *Nature Protocols* **10**: 1234-1247. doi: 10.1038/nprot.2015.081 (IF=10.032)

**PALACKÝ UNIVERSITY OLOMOUC**

Faculty of Science

Department of Biochemistry



**Dynamic properties of membranes, cytoskeleton and reactive  
oxygen species during polar growth of  
plant cells**

**Ph.D. thesis summary**

**Mgr. Lenka Kuběnová**

P1416 Biochemistry

Olomouc

2022



This Ph.D. thesis was prepared as a part of a full-time doctoral study program in Biochemistry P1416 at the Department of Biotechnology, Faculty of Science, Palacký University Olomouc in the period 2016 - 2022 under the supervision of prof. Mgr. Miroslav Ovečka, Ph.D.

**Ph.D. candidate**                    **Mgr. Lenka Kuběnová (Vaškebová)**  
Department of Biotechnology  
Faculty of Science, Palacký University Olomouc  
Šlechtitelů 241/27, 783 71, Olomouc, Czech Republic

**Supervisor:**                        **prof. Mgr. Miroslav Ovečka, Ph.D.**  
Department of Biotechnology  
Faculty of Science, Palacký University Olomouc  
Šlechtitelů 241/27, 783 71, Olomouc, Czech Republic

**Opponents:**                        **prof. RNDr. Jana Albrechtová, Ph.D**  
Department of Experimental Plant Biology  
Faculty of Science, Charles University  
Viničná 5, 128 44 Praha 2, Czech Republic

**doc. Mgr. Martin Černý, Ph.D.**  
Institute of Molecular Biology and Radiobiology  
Faculty of Agronomy, Mendel University  
Zemědělská 1/1665, 613 00 Brno, Czech Republic

The summary of the thesis was sent for distribution on .....

The oral defense will take place at the Faculty of Science, Palacký University in Olomouc, Šlechtitelů 27 on .....

The PhD thesis is available at the Biology Branch Library in Holicе of the Faculty of Science, Šlechtitelů 27, Olomouc.

prof. Mgr. Marek Petřivalský, Dr.  
Chairman of Doctoral Study Board in Biochemistry

## Content

<b>1. Abstract</b> .....	<b>5</b>
<b>2. Aims of the thesis</b> .....	<b>6</b>
<b>3. PART I - General introduction</b> .....	<b>7</b>
3.1 Introduction to the structure and function of <i>Arabidopsis thaliana</i> root hairs .....	7
3.2 Sub-cellular organization and polarity of root hairs .....	7
3.3 Essential factors influencing the polar tip growth of root hairs .....	8
3.3.1 Organization and dynamics of the endomembrane system .....	8
3.3.2 Structural sterols and lipid rafts .....	9
3.3.3 Reactive oxygen species .....	9
3.3.4 Cytoskeleton .....	10
3.4. Selected root hairs mutants .....	11
3.4.1 <i>rhd2</i> mutant .....	11
3.4.2 <i>der1-3</i> mutant .....	11
3.4 Conventional and advanced microscopy techniques and quantitative analyses .....	12
<b>4. PART II - Single-point <i>ACT2</i> gene mutation in the <i>Arabidopsis</i> root hair mutant <i>der1-3</i> affects overall actin organization, root growth and plant development</b> .....	<b>13</b>
4.1. Material and Methods .....	13
4.2 Results .....	14
4.2.1 <i>Developmental, growth parameters and phenotype of der1-3 mutant</i> .....	14
4.2.2 <i>Structure and organization of actin filaments and microtubules of der1-3 mutant</i> .....	17
4.3 Discussion .....	18
<b>5. PART III - Single amino acid exchange in <i>ACTIN2</i> confers increased tolerance to oxidative stress in <i>Arabidopsis der1-3</i> mutant</b> .....	<b>21</b>
5.1 Material and Methods .....	21
5.2 Results .....	22
5.2.1 <i>Impact of the der1-3 mutation and its topology on protein tertiary structure</i> .....	22
5.2.2 <i>Effect of oxidative stress on post-germination root growth, plant development and biomass production of the der1-3 mutant</i> .....	22
5.2.3 <i>Phenotype of der1-3 mutant plants after long-term exposure to oxidative stress</i> .....	23
5.2.4 <i>Response of the actin cytoskeleton to oxidative stress</i> .....	25
5.2.5 <i>Lipid peroxidation and antioxidant activity</i> .....	26
5.3 Discussion .....	27
<b>6. PART IV - ROOT HAIR DEFECTIVE 2 vesicular delivery to the apical plasma membrane domain during <i>Arabidopsis</i> root hair development</b> .....	<b>29</b>

6.1 Material and Methods.....	29
6.2 Results .....	30
6.2.1 <i>Cell type-specific and subcellular distribution patterns of GFP-RHD2 signal in root.....</i>	30
6.2.2 <i>Quantitative microscopic analysis of motile compartments containing GFP-RHD2 at different stages of root hair development .....</i>	32
6.2.3 <i>Identification of GFP-RHD2-positive compartments.....</i>	32
6.2.4 <i>Distribution of GFP-RHD2 in root hairs after filipin III treatment .....</i>	34
6.3 Discussion .....	36
<b>7. General conclusion .....</b>	<b>38</b>
<b>8. References .....</b>	<b>39</b>
<b>9. List of publication.....</b>	<b>47</b>
<b>10. List of attended conferences .....</b>	<b>47</b>
<b>11. Abstrakt.....</b>	<b>48</b>

## 1. Abstract

Root hair (RH) tip growth represents an excellent model of polar apical cell expansion in plants. RHs play important functions in anchoring plants in soil, increasing root absorption surface for water and nutrient uptake, and interactions with microbes. The process of RH initiation and root hair tip growth maintenance is a complex process. It requires polarization of the cytoskeleton, membrane trafficking, and localized cell wall deposition at the RH initiation side of the trichoblasts. The current knowledge linked to the process of RH formation and tip growth is summarized in the theoretical part of the thesis. The main topic of the thesis was thorough characterization of two different *Arabidopsis thaliana* mutants (*der1-3* and *rhd2-1*), that are defective in RH tip growth.

The mutant *der1-3* (*deformed root hairs 1*) possess a single-point mutation in the *ACTIN2* gene. Product of this gene, ACTIN2, is the most abundant vegetative actin isoform, and is required for RH tip growth. Based on this fact, *der1-3* mutant was identified according to its RH phenotype. Our thorough plant phenotyping, tissue patterning, and subcellular localization analyses revealed that this mutation in the *ACT2* gene has deeper effects on plant growth and development, which has not been known before. Moreover, we found that *der1-3* mutant is more resistant to mild and severe oxidative stress. This was demonstrated by better growth parameters, enhanced preservation of actin dynamics, and more effective biochemical protection of the mutant in stress conditions. These data supported a better understanding of the actin cytoskeleton roles not only in plant growth and development, but also in plant reactions to oxidative stress, which is promising for potential future agricultural and biotechnological applications.

NADPH oxidase type C in *A.thaliana*, annotated as respiratory burst oxidase homolog protein C/ROOT HAIR-DEFECTIVE 2 (AtRBOHC/RHD2), is localized at the apical plasma membrane (PM) of growing RHs where it generates reactive oxygen species (ROS), indispensable for the maintenance of the RH tip growth. Single point mutation in *RBOHC/RHD2* gene generates mutant *rhd2* (*root hair defective 2*) with RH phenotype. We characterized in detail the spatiotemporal pattern and mechanism of the AtRBOHC/RHD2 subcellular delivery to the PM during RH formation. Quantitative microscopy, single particle tracking, and subcellular colocalization analyses using different advanced microscopic methods demonstrated the complex nature of AtRBOHC/RHD2 delivery, maintenance, and recycling at the apical PM during RH formation in *Arabidopsis*.

Novel data presented in the thesis were received by utilization of advanced microscopy methods for fast image acquisition (spinning disk confocal microscopy), near environmental developmental imaging (light-sheet fluorescence microscopy), and super-resolution (Airyscan confocal laser scanning microscopy). Combining lower value of phototoxicity, enhanced resolution, and faster imaging speed with longer observation allowed study of living plants in almost natural conditions, bringing physiologically relevant results.

## 2. Aims of the thesis

- Summary of the recent knowledge on polar growth of plant cells (especially on root hair growth) and its regulation at molecular and cellular levels, in particular the proportion of vesicular transport, cytoskeleton and signalling of reactive oxygen species (ROS).
- Optimization of cultivation conditions; test of different types, quality, composition and mechanic properties of cultivation media and conditions for long-term experiments of continuous primary root growth and root hairs development under the physiological conditions.
- Preparation of transgenic plants with control or mutant genotype (carrying genetically encoded markers for actin cytoskeleton, vesicular transport, and NADPH oxidase) by crossing or transformation and their subsequent selection and genotyping.
- Microscopic study of structural and dynamic parameters of the cytoskeleton and endosomal compartments during root hair development in living transgenic plants.
- Qualitative and quantitative evaluations of mutant root hair growth with fluorescence markers expression and observation of interactions between plasma membrane, endosomal compartments, and cytoskeleton during individual stages of root hair tip growth.

### 3. PART I - General introduction

#### 3.1 Introduction to the structure and function of *Arabidopsis thaliana* root hairs

Plants of *A. thaliana* as model organism is widely used in all fields of plant biology, mainly because their individual organs generally have a small number of cell layers, and therefore one can observe them microscopically as a whole without the need to prepare anatomical sections (Boerjan *et al.*, 1992; Koornneef and Meinke 2010). The Arabidopsis root system consists of primary root, lateral roots and root hairs (RHs). RHs are lateral tubular extension of the basal side of the root epidermal cells called trichoblasts. They are involved in anchoring the plant, considerably increase root surface area and help with water and mineral ions uptake from the soil, and in interaction with microbes. Their position at the root surface, simple structure, and fast growth enable easy visualization and manipulation during experiments. On the other hand, RHs are not essential for plant survival, allowing the isolation and analysis different types of mutant plants, that have RH-specific alternations in structure, function, and development (Carol and Dolan, 2002; Grierson and Schiefelbein, 2002).

#### 3.2 Sub-cellular organization and polarity of root hairs

RHs are a typical model of polar growth in higher plants such as pollen tubes. RH tip elongation is supported by proper organization of polarized cytoplasm, rapid exocytosis, endocytosis, and vesicle recycling, cell wall biosynthesis, and an incorporation of membrane material at the tip (**Fig. 1**; Dolan *et al.*, 1994; Foreman and Dolan, 2001). Endocytic and exocytic vesicles are transported along actin filaments (AFs) in a so called “reverse fountain” type of streaming (Ovečka *et al.*, 2005; Balcerowicz *et al.*, 2015). AFs are localized between secretory vesicles in the apical part of RH, where they form bundles. Bundles of AFs are oriented parallel to the longitudinal axis of the RH. Microtubules (MT) have also the same orientation as the AFs, but MT are located at the cell cortex directly under the PM and they are important for controlling of RH growth direction (Galway *et al.*, 1997; Era *et al.*, 2009; Balcerowicz *et al.*, 2015). Most other RH organelles do not reach the apex, but they are in the shank region (Ridge *et al.*, 1999).

The major signal mechanism indispensable for the polar RH growth is a tip-focused gradient of  $\text{Ca}^{2+}$  in the cytosol (yellow gradient in **Fig. 1**), which regulates the activity of vesicular trafficking, generation of reactive oxygen species (ROS), and organization of the cytoskeleton in growing tip.  $\text{Ca}^{2+}$ - permeable ion channels (green rectangle in **Fig. 1**) are localized at the apical PM (Miedema *et al.*, 2008). ROS (yellow gradient in **Fig. 1**) are required for RH growth and they are generated by NADPH oxidase encoded by *AtrbohC/RHD2* gene. RHD2 is localized in apical part of root hair PM (yellow rhombus in **Fig. 1**). This ROS production is regulated by ROP GTPases (blue triangle in **Fig. 1**; Foreman *et al.*, 2003). RHD2, ROS, and  $\text{Ca}^{2+}$  are interconnected by a positive feedback mechanism, which determines RH polarity and its tip growth (Carol *et al.*, 2005, Takeda *et al.*, 2008).

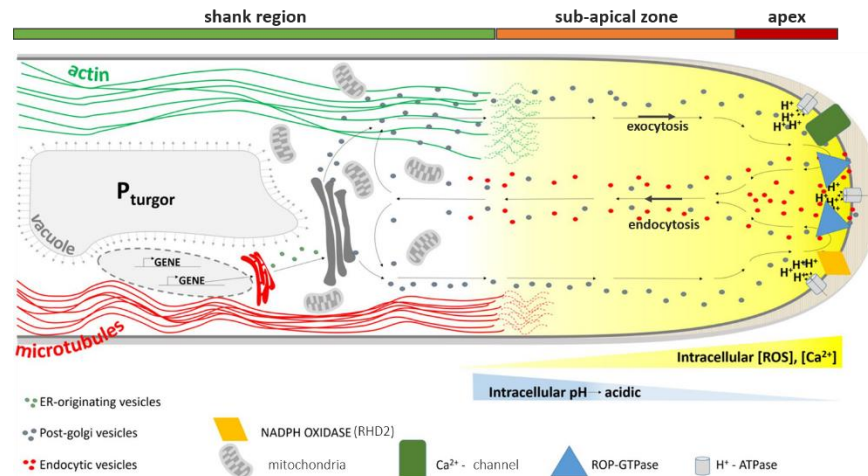


**Figure 1:** Schematic cytoarchitecture of growing root hair tip. Tip-focused vesicles are formed from exocytotic and endocytotic vesicles (in apex and sub-apical zone), which are transported by actin cables (green). Microtubules cables (red) control the growth direction of RH. Also, NADPH oxidase (RHD2), ROP proteins and  $\text{Ca}^{2+}$ - permeable ion channels are localized at the RH tip. All of this together creates a tip-focused calcium and ROS gradient (yellow gradient). The remaining organelles are located in shank region of RH. Adapted from Balcerowicz *et al.*, 2015.

### 3.3 Essential factors influencing the polar tip growth of root hairs

#### 3.3.1 Organization and dynamics of the endomembrane system

Endomembrane transport is ensured by vesicles that move between membrane-bound organelles (i.e. the endoplasmic reticulum-ER, Golgi apparatus-GA, the trans-Golgi network-TGN, multivesicular endosomes/bodies-MVB, lysosomes/vacuoles/pre-vacuolar compartments-PVC and the plasma membrane-PM) in eukaryotic cells (Baluška *et al.*, 2002; Ito and Uemura, 2022). Although plant cells have a rigid cell wall and high turgor pressure, their endocytotic activity is very dynamic (Hawes *et al.*, 1995; Baluška *et al.*, 2002; Šamaj *et al.*, 2004). Generation, targeted transport, and fusion of vesicles are essential processes also for development and polar tip growth of RHs. The apical zone of growing RH is enriched with secretory (exocytotic), endocytic, and recycling vesicles, balancing fine equilibrium of macromolecule supply, retrieval, and recycling mainly materials for growing PM and cell wall (Šamaj *et al.*, 2006; Campanoni and Blatt, 2007). The exocytosis (secretion) by the vesicles fusing with the PM deliver the cargo outside of the cell. The endocytosis supports movement of cargo molecules from PM into the cell. Moreover, it supports also the recycling of the PM and the cell wall material, and the uptake of signalling molecules for further degradation (Šamaj *et al.*, 2005). These two pathways are very closely linked during polar tip growth of RHs. The process of exocytosis is controlled by many important proteins including Rop-GTPases that regulate actin cytoskeleton. For example, ROP2 is localized in the apical part of the growing RH and serves as their positive regulator. ARFs (ADP-ribosyl factors) mediate the formation of vesicles on the donor membrane and group of Rab GTPases are responsible for the vesicle fusion with the target membrane (Campanoni and Blatt, 2007; Kang *et al.*, 2017). Rab GTPases are also the main regulators of endocytotic pathway and belong to Ras GTPase superfamily. They exist in two stages: GTP-bound „active” and GDP-bound „inactive” form. Activation of Rab GTPase is caused by exchange of GDP for GTP, which is catalyzed by GEFs (GUANINE NUCLEOTIDE EXCHANGE FACTORS; Zerial

*et al.* 2001; Grosshans *et al.* 2006). In Arabidopsis genome has been identified 57 *RAB* genes. Their products are divided into 8 groups (Rab1/RabD, Rab5/RabF, Rab6/RabH, Rab7/RabG, Rab8/RabE, Rab11/RabA, Rab2/RabB and Rab18/RabC). Each of them has different subcellular localization and marks different membranes of the endomembrane system (Pereira-Leal *et al.*, 2001; Rutherford *et al.*, 2002; Ueda *et al.*, 2002; Woollard *et al.*, 2008). The second most important regulators are SNARE (Soluble *N*-ETHYLMALEIMIDE-SENSITIVE FACTOR ATTACHMENT PROTEIN RECEPTORS) proteins. They play a key role in regulation of fusion between the transport intermediate vesicles and its target membrane. Intermediate vesicles contain R-SNARE (or vesicles v-SNAREs) proteins and Q-SNARE (target t-SNAREs) proteins are in the membrane of target compartment (Fasshauer *et al.* 1998; Ito and Uemura, 2022). Other most important regulators are other small GTPases, called Rho GTPases, which control structure, rearrangements and dynamic properties of F-actin cytoskeleton (Yang, 2002).

### **3.3.2 Structural sterols and lipid rafts**

Plants structural sterols are an indispensable part of biological membranes and they are derived from isoprenoids. The most common plant sterols are  $\beta$ -sitosterol, stigmasterol and campesterol. Structural sterols interact with membrane phospholipids and sphingolipids, which is essential for modulation of membrane fluidity and permeability (Clouse, 2002; Ovečka *et al.*, 2010; Valitova *et al.*, 2016). Structural sterols are locally accumulated in the PM of future site of the RH formation in the trichoblast. The PM-specific sterol accumulation is an early indicator of the initiation site of RH. This accumulation was documented also in the „bulge” and in apical part of growing RHs. The relation of this specific structural sterols accumulation to the tip growth was approved by the observation that this gradient disappears, when the RHs terminate the tip growth. (Ovečka *et al.*, 2010). The other earliest markers of RH initiation on trichoblasts are small GTPases ROP2 and ROP4 (Molendijk *et al.*, 2001; Jones *et al.*, 2002). It has been shown that the activation-dependent acylation of ROPs and their consequent partitioning in „lipid rafts” could play a central role during the establishment of polarity in plants (Sorek *et al.*, 2007). Structural sterols regulate vesicular trafficking, signalling, protein localization in membranes and selecting exo- and endocytic cargo molecules (Menon, 2002; Lindsey *et al.*, 2003), particularly in tip-growing RHs (Ovečka *et al.*, 2010) and pollen tubes (Liu *et al.*, 2009).

### **3.3.3 Reactive oxygen species**

Reactive oxygen species (ROS) are modified forms of atmospheric oxygen. ROS have dual role in plants biology. They are present mainly as toxic by-products originating from aerobic metabolism or they can be accumulated after exposure to environmental stresses. These ROS has strong ability to react with proteins, lipids or nucleic acids and cause serious damage to these biomacromolecules (Singh *et al.*, 2016). However, ROS also serve as signalling molecules. Since ROS are very small molecules, they can pass through the membranes (Overmyer *et al.*, 2003; Mittler, 2017). As signalling molecules, they regulate numerous plant developmental processes, including cell proliferation and differentiation, programmed cell death, seed germination, gravitropism, RH and pollen tube growth (Singh *et al.*, 2016). ROS can be generated inside the cell (intracellularly) or in apoplast (extracellularly). Intracellular ROS in growing RHs originates mainly from mitochondria, peroxisomes and from cytosolic reaction mediated by ER. The main producer of apoplastic ROS are



NADPH oxidases (NOX), which are located at the PM. The other producers of apoplastic ROS are cell wall peroxidases and amino-oxidases (Qi *et al.*, 2017). Plants NADPH oxidases are encoded by *RESPIRATORY BURST OXIDASE HOMOLOG (RBOH)*; Sagi and Fluhr, 2006) genes. In *A. thaliana*, there is 10 type of AtRBOHs (AtRBOHA-J) produced, and the functions of most of them are well described. Preferentially in the root RBOHB, RBOHC, RBOHG members are present, nevertheless RBOHD, RBOHE a RBOHF also play a role in growth of the main root and lateral roots. RBOHH and RBOHJ are important for growth of pollen tubes (Mhamdi and Van Breusegem, 2018). It has been shown, that NADPH oxidases activity is connected to structural sterols in the membranes. Proteomic studies identified NADPH oxidases NtRBOHD, StRBOHB, and AtRBOHB with other PM proteins enriched in the detergent-resistant membrane fraction of suspension cells (Morel *et al.*, 2006; Srivastava *et al.*, 2013). In parallel, subcellular visualization revealed AtRBOHD localization to the PM and dynamic spots in the cells and its endocytosis via membrane microdomains can be induced by salt stress (Hao *et al.*, 2014).

### 3.3.4 Cytoskeleton

The plant cytoskeleton consists of MTs, AFs, and associated proteins that are involved in intracellular processes and facilitates their reorganization. MTs and AFs together form a flexible network, which mainly participate on cell growth, morphogenesis and polarity (Foreman and Dolan, 2001; Sampathkumar, 2011). Furthermore, it is also important for cell division, vesicular trafficking, migration of organelles and signalling (Fu *et al.*, 2005; Goode *et al.*, 2000). MTs are hollow tubules from tubulin heterodimers of one  $\alpha$ - and one  $\beta$ -tubulin polypeptides. Both tubulin subunits have a molecular weight of 55 kDa. (Goddard *et al.*, 1994; Lloyd and Chan, 2004). The genome of *A. thaliana* encodes 6 isoforms of  $\alpha$ -tubulin, designated AtTUA1-AtTUA6 (Kopczak *et al.*, 1992), 9 isoforms of  $\beta$ -tubulin, designed as AtTUB1-AtTUB9 (Snustad *et al.*, 1992), and 2 isoforms  $\gamma$ - tubulins, which are functionally redundant (Liu *et al.*, 1994). RHs have two independent networks of MTs (CMTs - cortical microtubules; EMTs - endoplasmic microtubules). CMTs are present along the entire length of the RHs and EMTs are inside the RHs and interconnect nuclei with RH tips (Foreman and Dolan, 2001; Sieberer *et al.*, 2002, 2005). Depolymerization of MTs by oryzalin or MTs stabilization by taxol showed that RHs continue their growth without a significant drop in growth rate, but with a wavy pattern. This proves that MTs control RHs growth direction, but they are dispensable for tip growth of RHs (Bibikova *et al.*, 1997, 1999; Ketelaar *et al.*, 2002).

AF has the shape of a double helix, which is formed by globular actin subunits (G-actins; Staiger, 2000). AFs are important in many cellular processes (which was mentioned before), but also have important functions in signalling events triggered by diverse external stimuli and their remodelling is part of abiotic and biotic stress response mechanisms in plants (Zhou *et al.*, 2010). Actin dynamic is regulated by actin binding proteins (ABP), which have a different distribution in the cells (Ramachandran *et al.*, 2000). The *A. thaliana* genome encodes vegetative class of actins, which is typically expressed in all vegetative tissues, possess 3 actin genes (*ACT2*, *ACT7* and *ACT8*). The second group of genes (reproductive class) are expressed mainly in pollen tubes and ovules and contains *ACT1*, *ACT3*, *ACT4*, *ACT11* and *ACT12* (Meagher *et al.*, 1999; Kandasamy *et al.*, 2007). Members of the vegetative and reproductive actin have different expression pattern and function, although they only have 4-7 % differences at the amino acid sequence level (Kandasamy *et al.*, 2007). In RHs, actin cytoskeleton has more diverse structure in comparison to MTs (Higaki *et al.*, 2006). RH

tips are enriched in vesicles, where AFs, among others, regulate vesicular trafficking, which is essential for tip growth. Interestingly, actin (+) plus ends are highly enriched in the apical dome of RHs (Vazquez *et al.*, 2014). Different kinds of studies with actin disrupting drugs (such as cytochalasin D or latrunculin B) proved, that actin cytoskeleton is essential in both the process of RH initiation and proper RH tip growth (Braun *et al.*, 1999; Pei *et al.*, 2012).

### 3.4. Selected root hairs mutants

#### 3.4.1 *rhb2* mutant

Only NADPH oxidase type C (AtRBOHC) is present in growing RHs. RBOHC, which is encoded by the *RHD2* (*ROOT HAIR DEFECTIVE2*) gene locus, is localized at the apical PM in RH. Loss-of-function mutations in the *AtRBOHC/RHD2* locus in *rhb2* mutants resulted in short RHs (**Fig. 2**). Therefore, absent *RHD2* means, that gradients of ROS and  $Ca^{2+}$  ions in the apical zone of RHs is not generated (Schiefelbein and Somerville, 1990; Foreman *et al.*, 2003). The application of external ROS or pH alkalization has ability partially rescue the polar tip growth of RHs in *rhb2* mutant, due to renewed activity of  $Ca^{2+}$  channels in the PM (Monshausen *et al.*, 2007). The same short RH phenotype was achieved by the NADPH oxidases inhibitor application (diphenyleneiodonium; DPI) in wild-type plants, which disrupted ROS production at the apex of growing RHs (Foreman *et al.*, 2003). These studies confirm, that the interplay between RBOHC/*RHD2* activity, accumulation of ROS and  $Ca^{2+}$  ions are essential for the polar RH tip growth (Foreman *et al.*, 2003; Carol *et al.*, 2005). RBOHC activation involves ROP ("Rho of plants") GTPases, namely ROP2, ROP4 and ROP6, and they are transported already to the future RH initiation site in trichoblasts with the involvement of RopGEF3 factors (Carol *et al.*, 2005; Denninger *et al.*, 2019). The transformation of *rhb2* mutant with *GFP:RHD2* construct driven under the native promotor fully rescued its short RH phenotype. Tissue- and cell type-specific localization studies of GFP-*RHD2* lines showed, that signal is particularly prominent in trichoblasts and accumulate at the bulges and apices of growing RHs (Takeda *et al.*, 2008).

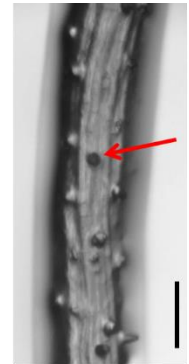


**Figure 2:** Root hair phenotype (arrow) of *rhb2* mutant. Scale bar is 100  $\mu$ m.

#### 3.4.2 *der1-3* mutant

The essential role of *ACT2* for proper RH tip growth has been proven by genetic approaches using either chemically-induced single-point mutations (Ringli *et al.*, 2002) or insertional knockout mutations (Gilliland *et al.*, 2002). Varying degrees of the short RH phenotype were shown by three *der1* (*deformed root hairs*) allelic mutants, isolated after EMS (ethyl methanesulphonate) mutagenesis in the C24 ecotype background. The strongest effect on RHs growth was described in *der1-2* and *der1-3* mutants (**Fig. 3**; Ringli *et al.*, 2002). Surprisingly, the *ACT2* expression level is not affected by single point mutation in *DER1* locus (Ringli *et al.*, 2002). Other mutations in the *ACT2* gene also showed a defect in the growth of RHs, but they have accumulated also other types of phenotypic changes. For example, *act2-2D* mutant (EMS mutagenesis in *Ler* background) has trichoblasts without any bulges and has shorter AF bundles as comparing to wild type (Nishimura *et al.*, 2003).

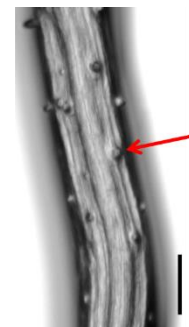


**Figure 3:** Root hair phenotype (arrow) of *der1-3* mutant. Scale bar is 100  $\mu$ m.

T-DNA insertional loss-of-function mutants in *ACT2* gene, *act2-1* (Gilliland *et al.*, 2002) and *act2-3* (Nishimura *et al.*, 2003) do not show defects in RH initiation, but their RHs are shorter than those of wild-type plants (Gilliland *et al.*, 2002; Nishimura *et al.*, 2003). Studies based on mutagenesis of genes for vegetative actins revealed that *ACT7* is involved in root growth, epidermal cell specification, cell division and root architecture, while *ACT2* and *ACT8* are essential for RH tip growth (Gilliland *et al.*, 1998).

### **3.4 Conventional and advanced microscopy techniques and quantitative analyses**

Microscopy is analytical instrumental technique for imaging of different organisms, including plants, at the supra-cellular, cellular, and sub-cellular levels. Advances of microscopy techniques combining wide-field light microscopy, multispectral fluorescent microscopy, up to sub-diffraction super-resolution microscopy have made it possible to observe the organization and dynamics of cells; and most of the organelles and subcellular compartments in cells of living plants down to the nanoscale (Komis *et al.*, 2018). After development of fluorescent recombinant proteins technology (such as GFP, YFP, RFP and other), fluorescence microscopy exploded in further development. Traditionally, the most frequently used are techniques of confocal laser scanning microscopy (CLSM) and spinning-disk microscopy (SD) that were among the first techniques capturing cells localized mostly on the surface of living or fixed plant samples (Berthet and Maizel, 2016).

Plants are very sensitive to changes in external environmental conditions. Therefore, the live-cell imaging by conventional microscopy methods with traditional sample preparation approaches may often generate some artefacts. This is mainly caused by enclosing plants to small observation chambers that are exposed to high laser light intensity, which often leads to temperature and photo-oxidation far from ideal (Reddy *et al.*, 2007). Hence, a compromise between achieving conditions allowing the observation of biological processes at the appropriate spatial and temporal resolution and maintaining conditions as close to natural as possible for the sample is a goal of advanced microscopic methods in live cell imaging (Stelzer, 2015). The presented thesis was elaborated by utilization of several microscopy methods. From conventional microscopy, was used confocal laser scanning microscope (CLSM), which is the best for fixed specimens (Wright *et al.*, 1993; Mauko *et al.*, 2009); and spinning-disk microscope (SD) is the most useable for very dynamic processes in living cells (Wang *et al.*, 2005; Stehbens *et al.*, 2012). From advanced microscopy methods were used Airyscan confocal laser scanning microscope (ACLSM), which is high-resolution method for improved dynamic live-cell imaging (Sivaguru *et al.*, 2016); and light-sheet fluorescence microscope (LSFM) is well suited for long-term live-cell imaging (Reynaud *et al.*, 2015; Stelzer, 2015).

Obtained images from microscopic methods is not the last step in the evaluation procedure. Firstly, follows deconvolution process and then various quantitative analyses (such as orientation and structure of cytoskeleton, single-particle tracking, fluorescence intensities, dynamic properties, and many others). In conclusion, the combination of these analyses will give us a comprehensive view of the qualitative and quantitative properties of processes in living cells.

## **4. PART II - Single-point *ACT2* gene mutation in the *Arabidopsis* root hair mutant *der1-3* affects overall actin organization, root growth and plant development**

### **4.1. Material and Methods**

Used material and methods are briefly introduced here. All detailed information is described in the Ph.D. thesis.

For this study were used C24 control and *der1-3* mutant (Ringli *et al.*, 2002) plants and their transgenic lines expressing *35S::GFP:FABD2* or *35S::GFP:MBD* construct. Transgenic lines were prepared by transformation *A. thaliana* plants using *A. tumefaciens*. All lines were phenotypically analysed and their developmental and growth parameters were measured. Pictures from a scanner (Image Scanner III, EpsonScan) were used for measurements of primary root length. Phenotypes of 18-days old plants *in vitro*, rosettes of 19-days old plants growing *in vivo* and the sizes of individual leaves were documented using a Nikon 7000 camera equipped with macro-objective (50 mm, 2.8; Sigma). The phenotypes of entire roots and root tips of 5-days old plants *in vitro* were recorded with an M165FC stereo microscope equipped with LAS V 4.0 software (Leica).

The wavy root pattern of *der1-3* mutant were analysed by FM4-64 staining of root tips and live-cell imaging of transgenic C24 GFP-FABD2 and *der1-3* GFP-FABD2 lines using two different microscopic methods. Roots, from 3-days old plants, stained by FM4-64 dye, were observed by the spinning-disk fluorescence microscope (Cell Observer Z.1; Carl Zeiss, Germany) equipped with an EC Plan-Neofluar 40x/1.3 NA and Plan-Apochromat 63x/1.4 NA oil immersion objectives. Actin cytoskeleton structure of C24 GFP-FABD2 and *der1-3* GFP-FABD2 lines were observed using light-sheet Z.1 fluorescence microscope (LSFM; Carl Zeiss, Germany) equipped with a W Plan-Apochromat 20x/1.0 NA water immersion detection objective and two LSFM 10x/0.2 NA illumination objectives. Samples were prepared according to Ovečka *et al.*, 2015 protocol. The angular positioning of cross-walls with respect to the root axis (quantification of CDP orientation) was measured on microscopic images of root cells labelled with FM4-64. The data obtained were divided into three categories according to the recorded angles: cross-walls at right angles ( $90^\circ \pm 5\%$ ), cross-walls at acute angles ( $<85^\circ$ ) and cross-walls with obtuse angles ( $>95^\circ$ ).

Differences in actin structure and orientation were done by phalloidin staining in fixed plants and live-cell imaging of transgenic C24 GFP-FABD2 and *der1-3* GFP-FABD2 lines. Phalloidin staining samples were observed by confocal laser scanning microscope (LSM 710; Carl Zeiss, Germany) equipped with a Plan-Apochromat 40x/1.4 numerical aperture (NA) oil immersion objective. Analyses of MTs structure and orientation were performed using the immuno-labelling of MTs in root tips and live-cell imaging of transgenic C24 GFP-MBD and *der1-3* GFP-MBD lines by confocal laser scanning or spinning-disk microscope (type of microscopes was mentioned before). Quantitative analysis of AFs and MTs angular distribution was done with CytoSpectre Version 1.2 software using the cell axis as a reference (Kartasalo *et al.*, 2015).

All graphical plots were prepared in Microsoft Excel software and statistical analyses were done using STATISTICA 12 (StatSoft) software using analysis of variance (ANOVA) and subsequent Fisher's LSD tests ( $p < 0.05$ ). Microscopic data were processed and evaluated in Zen 2014 software, black and blue editions (Carl Zeiss, Germany).

## 4.2 Results

### 4.2.1 Developmental, growth parameters and phenotype of *der1-3* mutant

The *der1-3* mutant was isolated for its short RH phenotype and no other phenotypic changes have been reported (Ringli *et al.*, 2002, 2005). We confirmed, that RH of the *der1-3* mutant were much shorter than in the C24 wild-type (**Fig. 4A, B**). Our phenotypic studies comprised seed germination test, evaluation of the root growth rate of young seedlings and biomass quantification in more advanced plants of C24 and *der1-3* mutant under *in vitro* and *in vivo* conditions. Survival and progress of early plant growth and development are highly dependent on the efficiency and speed of seed germination. Importantly, within the first 24 h after placing of seeds in the growing chamber,  $95 \pm 0.05$  % of the C24 wild-type seeds germinated, while only  $55 \pm 0.05$  % of *der1-3* mutant seeds started germination in same time period (**Fig. 4E**). Size comparison of 18-days old entire plants revealed visually smaller green aerial parts (**Fig. 4C, D**) and a less developed root system (**Fig. 4D**) of *der1* mutants. However, measurement of average root growth per 24 h measured within the first 5 days after germination, with no significant difference between control and mutant plants (**Fig. 4F**). Then, we measured the biomass of leaves and roots. Shoot and root fresh weights of 19-days old plants cultured *in vitro* were significantly higher in the control C24 wild-type plants than in the *der1-3* mutant (**Fig. 4K**). Nevertheless, average fresh weight of all true leaves (**Fig. 4L**), average leaf area (**Fig. 4M**), size of leaf rosettes (**Fig. 4G, H**) and size of individual leaves (**Fig. 4I, J**) in plants cultured *in vivo* suggested that the reduced development of the *der1-3* mutant might not be related to delay in germination. This suggestion was supported by the higher average number of leaves in 19-days old *der1-3* mutant plants (**Fig. 4N**), which may functionally compensate for the suppressed development of green aerial part.

Further, C24 wild-type had primary roots developed in a straight direction along a longitudinal vector (**Fig. 5A**), but primary roots of *der1-3* mutant showed a more irregular and wavy growth pattern (**Fig. 5B**). C24 and *der1-3* seedlings stably expressing a *35S::GFP-FABD2* marker were used for AF organization analyses in the apex of the primary roots. In order to maintain intact living plants in near-environmental conditions and avoid any artefacts in the speed and directionality of root growth induced by prolonged irradiation during imaging, we utilized light-sheet microscopy. The actin cytoskeleton was visualized in cells of the whole root apex of transgenic C24 (**Fig. 5C**) and *der1-3* mutant (**Fig. 5F**) plants. Detailed images of the root apex revealed boundaries between individual cells at their cross-walls in cell files. The planes of these cross-walls in non-dividing cells corresponded to CDP orientation during cell division. Cross-walls between individual cells were predominantly transverse in cell files of C24 control (**Fig. 5C, E**). In contrast, many cross-walls were obliquely oriented in cell files of *der1-3* mutant root (**Fig. 5D, F**). Roots of C24 and *der1-3* mutant plants stained with FM4-64 and examined by spinning-disk fluorescence microscopy used as the different method to quantify differences in cross-wall orientation. This method confirmed, that C24 wild-type root contained mostly perpendicular oriented cross-walls (**Fig. 5G**), compared to more frequent oblique orientation of the cross-walls in cell files of *der1-3* mutant roots (**Fig. 5H**). Quantitative evaluation of cross wall orientations was measured in angle (see material and methods).

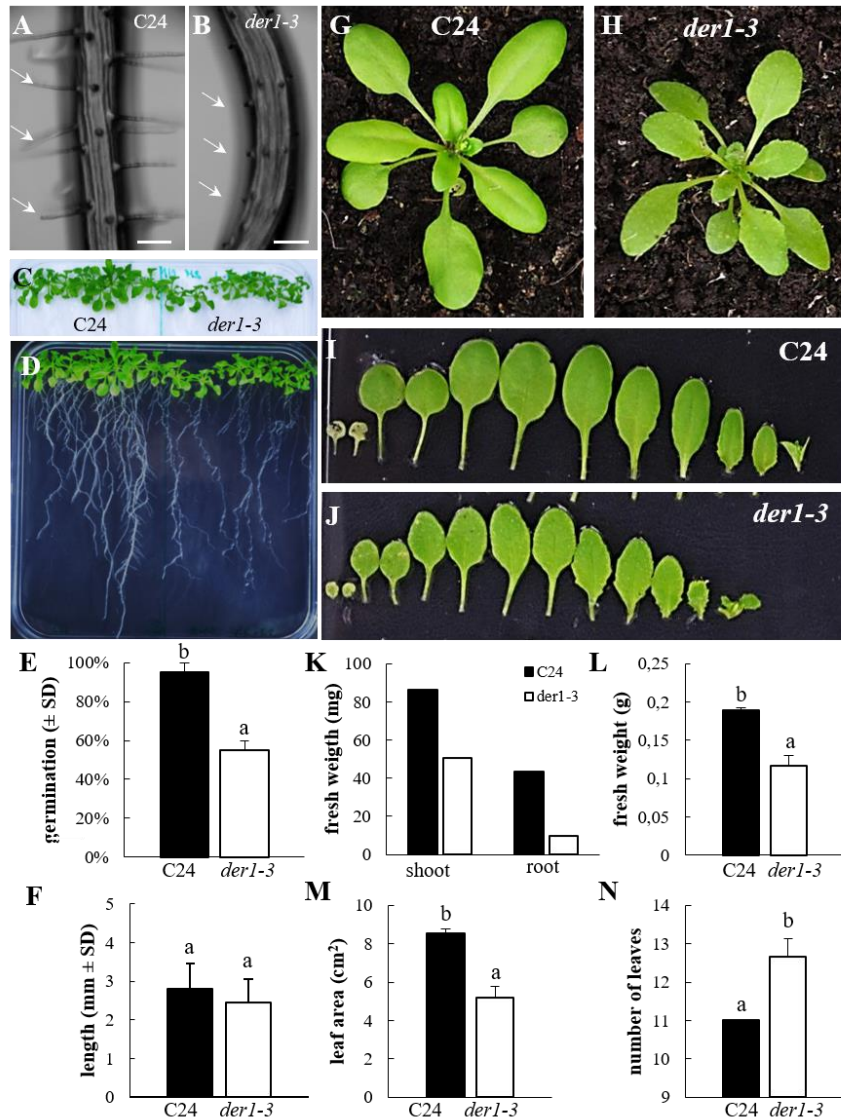


**Figure 4. Growth parameters and phenotype of C24 wild-type and *der1-3* mutant plants.** (A, B) Mature part of the root of 5-days old seedlings showing normal long RHs in C24 wild-type (A, arrows) and much shorter RHs in *der1-3* mutant (B, arrows). Size and phenotype of above grown parts (C) and entire plants (D) 18-days old cultivated on Phytigel-solidified culture medium *in vitro*. (E) Average germination rate within first 24 h (n=40). (F) Average root growth per 24 h of plants cultivated *in vitro* within the first 5 days after germination (n=16). (G-J) Comparison of leaf rosettes and individual true leaves in 19-days old plants cultivated in pots *in vivo*. Size of the leaf rosette in C24 wild-type (G) and *der1-3* mutant (H) plants. Number and size of individual true leaves in C24 wild-type (I) and *der1-3* mutant (J) plants. (K) Average fresh weight of shoots and roots of 19-days old C24 wild-type and *der1-3* mutant plants cultivated *in vitro*. Shoots and roots were collected separately from 10 plants and weighted together. Experiment was repeated three times. (L-N) Quantitative parameters of shoots of 19-days old C24 wild-type and *der1-3* mutant plants cultivated in pots *in vivo* (n=3). Analysed were fresh weight of above grown plant parts (L), total area of true leaves per plant (M) and number of true leaves per plant (N). Different letters above the bars represent statistical significance according to one-way ANOVA test and subsequent LSD test at p value < 0.05. Scale bars = 100  $\mu$ m (A, B). Adapted from Vaškebová *et al.*, 2018.

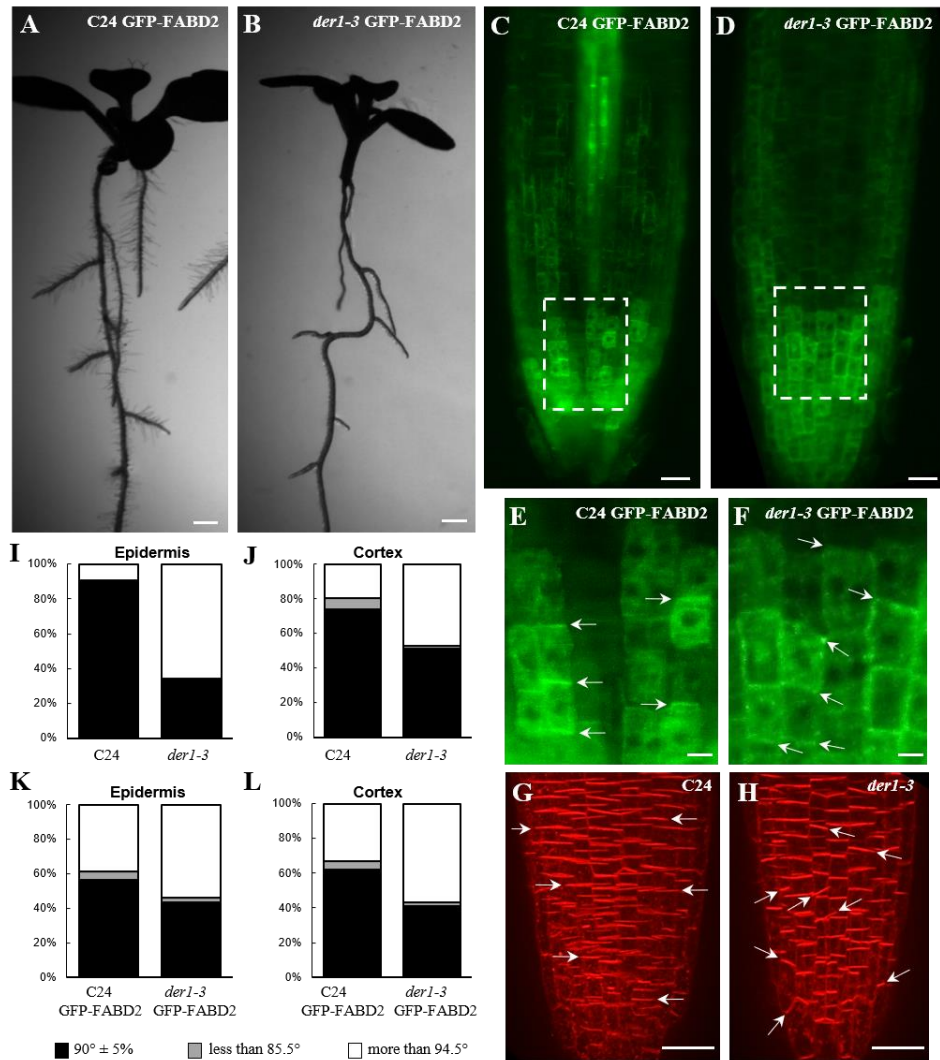


**Figure 5. Phenotype of the root system, pattern of the root growth and quantitative evaluation of cross wall orientations in C24 wild-type and *der1-3* mutant plants.** Morphology of the root system of 8-days old seedlings of C24 wild-type (A) and *der1-3* mutant (B) cultivated *in vitro*. (C-F) Light-sheet fluorescence microscopy imaging of transgenic GFP-FABD2 lines. Overview of the C24 GFP-FABD2 (C) and *der1-3* GFP-FABD2 mutant (D) root apex. Detailed images of cell files in the root apex of C24 (E, magnified inset from C) and *der1-3* mutant (F, magnified inset from D) harbouring GFP-FABD2 marker. Cell boundaries within the cells files at cross walls defining orientation of cell division planes during cell division are marked by arrows. (G, H) Vital labelling of root apices using fluorescent membrane marker FM4-64. Prominent labelling of the PM at the cross walls of C24 wild-type (G) and *der1-3* mutant (H) root cells indicating orientation of cell division planes during cell division are marked by arrows and quantitatively evaluated in (I-L). Relative frequencies of angle distributions in cell files of epidermis and cortex of C24 wild-type and *der1-3* mutant plants (I, J) and transgenic C24 GFP-FABD2 and *der1-3* GFP-FABD2 plants (K, L). Experiments repeated three times with 10-17 cells from 3 plants per line. Scale bars = 400  $\mu$ m (A, B), 20  $\mu$ m (C, D, G, H), 5  $\mu$ m (E, F). Adapted from Vaškebová *et al.*, 2018.

Data were collected from cells in cell files of root epidermis and cortex. To exclude the possible influence of GFP-FABD2 overexpression on CDP orientation, the same measurements were done in both transgenic (Fig. 5K, L) and non-transformed C24 and *der1-3* seedlings (Fig. 5I, J). CDP

orientation measurements of transgenic plants were similar to FM4-64 data. These results clearly indicate that the wavy pattern of root growth in the *der1-3* mutant is somehow related to alterations in CDP orientations during cell division in the root meristem.

#### 4.2.2 Structure and organization of actin filaments and microtubules of *der1-3* mutant

We performed detailed qualitative and quantitative analyses of the actin cytoskeleton in the *der1-3* mutant in order to see how the ACT2 mutation could be involved in the phenotypical and developmental changes of roots. The AFs were visualized in hypocotyls of fixed and fluorescent phalloidin-labelled 3-days old seedlings. This was followed by live-cell imaging in hypocotyl cell of transgenic lines expressing the GFP-FABD2 marker for AFs. These microscopic observations were supported by quantitative analysis of AF angular distribution in transverse (defined as perpendicular to the cell axis at an angle of 0° or 180°), longitudinal (parallel to the cell axis at an angle of 90° or 270°) or random (angles between 0° and 180°) orientations (Kartasalo *et al.*, 2015). Actin visualization using Alexa Fluor 488-phalloidin labelling in hypocotyl epidermal cells revealed the presence of long AFs and actin bundles, arranged mostly in longitudinal or slightly oblique orientations in C24 plants (**Fig. 6A**), which was confirmed by quantification of angular distribution of AFs in these cells (**Fig. 6B**). In contrast, hypocotyl epidermal cells of the *der1-3* mutant contained thinner and shorter AFs and actin bundles (**Fig. 6C**) and the angular distribution of AFs revealed more random AF orientation compared with the C24 control plants (**Fig. 6D**). Live-cell imaging of the actin cytoskeleton in epidermal hypocotyl cells of transgenic C24 GFP-FABD2 lines revealed actin bundles spanning these cells longitudinally as well as longitudinally, and obliquely oriented fine AFs forming a dense meshwork (**Fig. 6E**). Thus, quantification of angular distribution revealed a high degree of longitudinal orientation of AFs (**Fig. 6F**). The actin cytoskeleton in hypocotyl epidermal cells of the *der1-3* GFP-FABD2 mutant consisted of very short AFs arranged in a random and loose network. In addition, thick and rather short actin cables were oriented preferentially in oblique orientation with respect to the longitudinal axis of the hypocotyl epidermal cells (**Fig. 6G**). Quantification of AF angularity confirmed random and oblique orientation of AFs (**Fig. 6H**). These data conclusively confirmed alterations in the organization of the actin cytoskeleton in hypocotyls cells of *der1-3* mutant plants caused by mutation of *ACT2*.

To provide a more complex overview of the cytoskeleton regulating phenotype of the *der1-3* mutant, we also characterized the organization of MTs. Cortical and mitotic MTs in root cells of C24 wild-type and the *der1-3* mutant were visualized *in situ* by immune-fluorescence localization using an anti-tubulin antibody. In addition, transgenic C24 and *der1-3* mutant plants carrying the MT fluorescent marker GFP-MBD were used for live-cell imaging of MTs in root cells. The CDP is clearly defined by the positioning of the PPB during preprophase and prophase and by the orientation of the phragmoplast during telophase and subsequent cytokinesis. Thus, we observed regular transverse orientation of the CDP in dividing root cells of the C24 wild-type (**Fig. 7A**). On the other hand, we observed frequent deviation of the CDP from its expected transverse orientation in root meristematic cells of the *der1-3* mutant (**Fig. 7B**). Importantly, the organization of cortical (**Fig. 7C**) and mitotic (**Fig. 7D**) MTs in root epidermal cells of control C24 did not differ significantly from that in root epidermal cells of the *der1-3* mutant, as revealed by live-cell imaging (**Fig. 7E-G**). Determination of the CDP was apparent in dividing cells of control C24, showing coordinated orientation of the PPB,



the equatorial plane of the mitotic spindle and the phragmoplast. All of these were transversely oriented to the axis of root cell files (**Fig. 7D**). On the other hand, the CDP orientation of the dividing cells was not so strictly determined in the *der1-3* mutant as it was frequently observed in oblique orientation with respect to the axis of root cell files (**Fig. 7F, G**). Because quantitative analysis of cortical MT angular distribution in root epidermal cells of control C24 (**Fig. 7H**) and *der1-3* mutant (**Fig. 7I**) did not reveal significant differences, we can conclude that the point mutation of *ACT2* in the *der1-3* mutant does not have a considerable influence on the organization of the MT cytoskeleton in root cells.

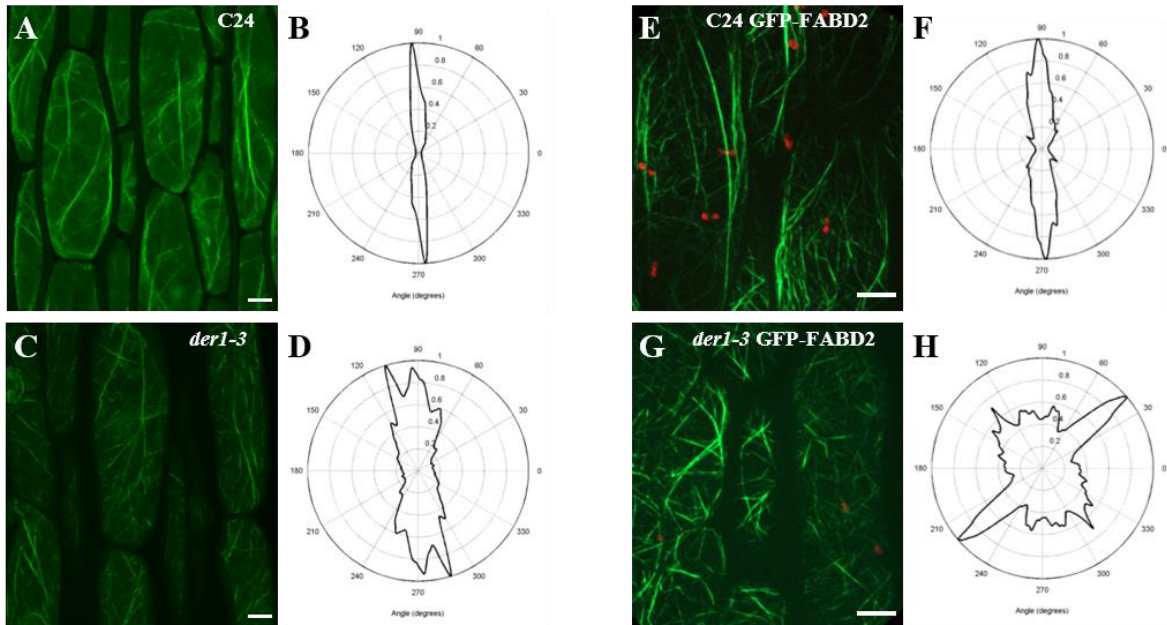


**Figure 6. Structure of the actin cytoskeleton in C24 wild-type and *der1-3* mutant plants.** Microscopic observations (**A, C**) and quantitative analysis of AF angular distribution (**B, D**) in hypocotyl epidermal cells of 3-days old C24 wild-type and *der1-3* mutant plants after phalloidin visualization of AFs. Microscopic observations (**E, F**) and quantitative analysis of AF angular distribution (**G, H**) in hypocotyl epidermal cells of 3-days old transgenic C24 GFP-FABD2 and *der1-3* GFP-FABD2 plants. Quantitative analysis of AF angular distribution was performed from three independent microscopy images of examined cell types from 3-5 plants of each line under study. Scale bars = 10  $\mu$ m. Adapted from Vaškebová *et al.*, 2018.

### 4.3 Discussion

We demonstrated using cellular analysis of the cytoskeleton and plant phenotyping, that the single-point mutation in the *ACTIN2* gene had a more general influence on plant growth and development, as was thought before. The first novel developmental aspect revealed was delayed germination. Seeds of the *der1-3* mutant germinated more slowly than those of the C24 ecotype. Although mutant roots were shorter, the root growth rate was not affected. The main difference, however, was found in fresh weight of roots and shoots. The root system of *der1-3* mutant had a five-time less weight than root system of C24 ecotype. Similarly, leaves of *der1-3* mutant reached only half the weight of the C24 leaves. Though the leaf area of *der1-3* mutant was smaller in comparison to C24 control leaves, the *der1-3* mutant balanced it by higher number of leaves that was almost 20%

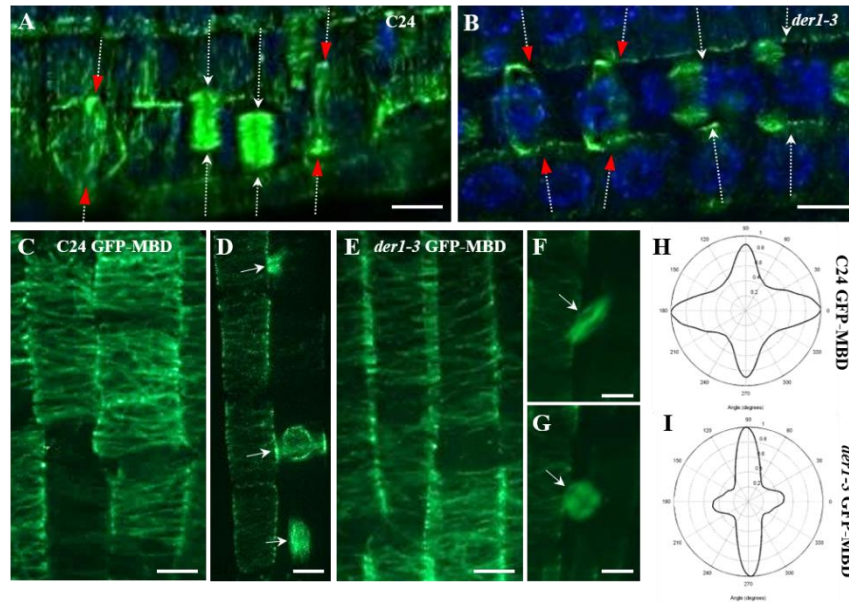


**Figure 7. Structure of the microtubules in C24 wild-type and *der1-3* mutant plants.** Cortical and mitotic MTs in root cells of C24 wild-type (A) and *der1-3* mutant (B) after immuno-fluorescence localization with anti-tubulin antibody. In dividing cells, position of PPBs in prophase cells is indicated by red arrowheads and by arrows in telophase cells by position of phragmoplast in telophase and during the cytokinesis is indicated by white arrowheads. Extended lines above arrowheads indicate orientation of CDP. DNA in nuclei is counterstained by DAPI. Microscopic documentation of cortical and mitotic MTs in root cells of living transgenic C24 GFP-MBD (C, D) and *der1-3* GFP-MBD plants (E-G). Cortical MTs in root epidermal cells of C24 wild-type (C) and of *der1-3* mutant (E). Mitotic MTs in dividing root epidermal cells of C24 wild-type (D) and *der1-3* mutant (F, G). The white arrows show different mitotic stages (D, F, G). Quantitative analysis of cortical MT angular distribution in root epidermal cells of C24 wild-type (H, analysed MTs from C) and in root epidermal cells of *der1-3* mutant (I, analysed MTs from E). Data from 4-5 cells of 5-6 plants. Scale bars = 5  $\mu$ m. Adapted from Vaškebová *et al.*, 2018.

higher than that of C24 plants. The similar effect was shown in another mutant *act7-1*, with disrupted encoding of the vegetative ACTIN7. This mutant showed also 24 h delay in seed germination, but without any other differences in further growth and development (Gilliland *et al.*, 2003).

Another modification in growth detected was a wavy root pattern of *der1-3* mutant. In order to find out the reason for this phenotype, we used two independent imaging methods, in particular FM4-64 PM staining in root cells and live-cell imaging of root actin cytoskeleton through GFP-FABD2 fluorescence in transgenic lines by light-sheet microscopy. We found out that *der1-3* mutant had higher number of shifted cell division plates (CDPs) in roots than C24 plants. It has already been described, that the MTs play a key role in determination of CDP during mitosis. They also associate with actin AFs during the formation of the PPB of MTs already in the pre-prophase and prophase stages of the cell division (Takeuchi *et al.*, 2016). We confirmed this trend by immunostaining of MTs, together with live-cell imaging of GFP-MBD molecular marker, showing a higher number of tilted mitotic MTs arrays (PPBs, spindles, and phragmoplasts) in dividing root meristematic cells of the *der1-3* mutant. Such a high frequency of MTs arrays tilting was not observed in control C24 plants. On the other hand, the measurements of cortical MTs angular distribution in root epidermal cells did not show any differences between *der1-3* mutant and C24 control plants. It is obvious, that both MTs

and AFs play an important role in determination of the future side and orientation of CDP, but in different ways. This was supported by other studies, when reduced expression of *ACT7*, a gene encoding an actin isoform highly expressed during mitosis, led to defects in CDP orientation (Gilliland *et al.*, 2003). Finally, actin cytoskeleton apparently plays relevant roles in cell division and in CDP determination in both asymmetrically and symmetrically dividing cells (Van Damme *et al.*, 2007; Rasmussen *et al.*, 2013; Kojo *et al.*, 2013, 2014).

After detailed microscopic analyses of actin cytoskeleton we found that AFs are shorter and thinner in cells of *der1-3* mutant as compared to AFs in cells of control C24 plants. This was confirmed by two different methods: live-cell imaging of hypocotyl of GFP-FABD transgenic lines, and imaging of AFs in fixed samples after the Alexa-488-phalloidin staining of hypocotyl cells. Quantitative analysis of the orientation showed that in cells of C24 plants actin bundles were longitudinally oriented, while actin bundles in cells of the *der1-3* mutant were mostly obliquely and sometimes transversely oriented. In general, plant cells contain individual AFs and actin bundles. The network of individual AFs is often randomly dispersed in the cortical cytoplasm and, although their high dynamicity, they have a shorter lifetime. The actin bundles are mostly oriented longitudinally along the cell's longer axis, they are less dynamic, but have a longer lifetime (Henty- Ridilla *et al.*, 2013). The changes in actin structure and orientation was described also in other mutants affected in the *ACT2* gene, such as *act2-2D* and *act2-5*. Single-point mutation in the *act2-2D* mutant led to formation of shorter actin bundles in root epidermal cells, showing also defects in actin polymerization (Nishimura *et al.*, 2003). T-DNA insertion mutant *act2-5* have a modified pattern of actin cytoskeleton organization, where AFs are shorter and unbundled (Lanza *et al.*, 2012). Altogether, our data clearly indicate that single-point mutation of the *ACT2* gene in *der1-3* mutant does not influence only the RH development, but affects also other developmental parameters of mutant plants, such as growth pattern of the roots and properties of the actin cytoskeleton in cells of the whole plants.

## **5. PART III - Single amino acid exchange in ACTIN2 confers increased tolerance to oxidative stress in Arabidopsis *der1-3* mutant**

### **5.1 Material and Methods**

Herein, the plant material and methods used are summarized. All details are described in the Ph.D. thesis.

For this analyses were used C24 control and *der1-3* mutant (Ringli *et al.*, 2002) plants and their transgenic lines expressing *35S::GFP:FABD2* construct. Transgenic lines were prepared by transformation *A. thaliana* plants using *A. tumefaciens*. All lines grew on control ½ MS media without vitamins solidified with Gellan gum or media containing different oxidative stress factors. Oxidative stress was induced by adding three different concentrations of paraquat (0.1; 0.2 and 0.5  $\mu\text{mol.l}^{-1}$  PQ), and four different concentrations of  $\text{H}_2\text{O}_2$  (0.5; 1; 1.5 and 3  $\text{mmol.l}^{-1}$ ) to the culture medium. Either seeds were planted directly on ½ MS media containing different concentrations of PQ, or 3-days old plants germinated on the control media were transferred to media containing different concentrations of PQ or  $\text{H}_2\text{O}_2$ . For root growth measurements, plants are scanned every 24 h by Image Scanner III, EpsonScan. Images documenting the phenotype of plants growing in plates were prepared with a Nikon 7000 camera equipped with a macro objective Sigma 50 mm (2.8 focal distance) in time points indicated in the corresponding figure captions.

Organization and dynamics of AFs, in control conditions and after oxidative stress treatment, were observed by live-cell imaging of transgenic C24 GFP-FABD2 and *der1-3* GFP-FABD2 lines using spinning-disk fluorescence microscope (Cell Observer Z.1; Carl Zeiss, Germany) equipped with an EC Plan-Neofluar 40x/1.3 NA and Plan-Apochromat 63x/1.4 NA oil immersion objectives.

Biochemical analyses were done with the help of Tomáš Takáč. Lipid peroxidation was assayed using the TBARS (thiobarbituric acid reactive substances) assay as described in Larkindale and Knight, 2002. Superoxide dismutase (SOD) activity examination was prepared by Takáč *et al.*, 2014 protocol. For the immunoblotting of CSD and PrxQ, the enzyme extracts were enriched with a 4x Laemmli SDS buffer (to reach a final concentration of 10% (v/v) glycerol, 60  $\text{mmol.l}^{-1}$  of Tris/HCl pH 6.8, 2% (w/v) SDS, 0.002% (w/v) bromophenol blue and 5% (v/v)  $\beta$ -mercaptoethanol). Afterwards, the samples were boiled at 95 °C for 5 min. Equal amounts of proteins (15  $\mu\text{g}$ ) were loaded on 10% SDS PAGE gels. Immunoblotting analysis and chemiluminescence signal development were carried out according to Takáč *et al.*, 2017. Analyses were performed in three biological replicates.

Evaluated parameters such as root growth, skewness (representing an extent of AF bundling), AF fluorescence integrated density (representing a percentage of occupancy) and the band optical densities of immunoblots were measured in ImageJ (<http://rsb.info.nih.gov/ij/>). All graphical plots were prepared in Microsoft Excel software and statistical significance between treatments at  $p < 0.05$  was performed using a t-Test in Microsoft Excel or in program the STATISTICA 12 (StatSoft, TIBCO Software Inc.) by ANOVA and subsequent Fisher's LSD test. Microscopic data were processed and evaluated in Zen 2014 software, black and blue editions (Carl Zeiss, Germany).

## 5.2 Results

### 5.2.1 Impact of the *der1-3* mutation and its topology on protein tertiary structure

*A. thaliana* mutant *der1-3* has been produced in the C24 ecotype background by an ethylmethanesulfonate (EMS)-mutagenesis of the *DER1* locus, leading to a single-point mutation in the *ACTIN2* gene (Ringli *et al.*, 2002). Single-point mutation in the genomic DNA sequence was determined at the position 1114 (changing cytosine to thymine), leading to an altered protein sequence exchanging Arg97 to Cys97 in the *der1-3* mutant (Ringli *et al.*, 2002). We translated a nucleotide sequence, both in a natural and mutated variant, to a primary protein sequence and we prepared a model of a tertiary protein structure. We found that this position, both in the natural (**Fig. 8A**) and mutated (**Fig. 8B**). Importantly, based on the 3D model, the mutation does not alter the overall tertiary structure of the protein (**Fig. 8A, B**), while this single amino acid exchange is topologically exposed to the protein surface (**Fig. 8C, D**). This analysis indicates that single-point mutation exchanging Arg to Cys at the position 97 in the *ACTIN2* protein of the *der1-3* mutant might rather influence its biochemical properties.

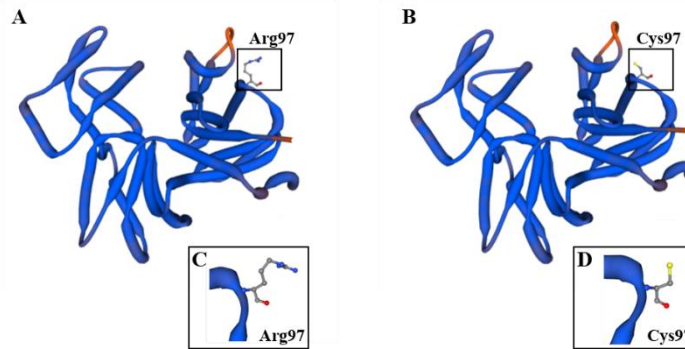


**Figure 8. Model of the nature *ACTIN2* protein structure and its mutated version in the *der1-3* mutant.** SWISS model of the tertiary protein structure of *ACTIN2* based on wild-type gene sequence (**A**) and based on gene sequence altered by single-point mutation in *der1-3* mutant (**B**). Topological location of arginine in the position 97 of natural *ACTIN2* (**A**, detailed structure in **C**) and substituted cysteine in the position 97 of mutated *ACTIN2* (**B**, detailed structure in **D**) of *der1-3* mutant are showed in boxes. Models of protein structures were produced in: <https://swissmodel.expasy.org/interactive>. Adapted from Kuběnová *et al.*, 2021.

### 5.2.2 Effect of oxidative stress on post-germination root growth, plant development and biomass production of the *der1-3* mutant

The plants of C24 wild-type, *der1-3* mutant and their transgenic GFP-FABD2 lines germinated and grew directly on control media or media with oxidative stress factor (PQ or H<sub>2</sub>O<sub>2</sub>); or 3-days old plants were transferred from control to oxidative stress conditions. Post-germination root growth analysis confirmed that, unlike the wild-type lines, root growth and development of the *der1-3* mutant and *der1-3* GFP-FABD2 line is better adapted to the mild oxidative stress. In order to characterize solely oxidative stress-related inhibition of root growth, we performed seed germination on the control media and after that, we transferred 3-days old seedlings to a culture media containing different concentrations of PQ. Comparison of the root growth rate within 4 days after transfer showed that it is very similar for the three lines. Nevertheless, only root growth rate on the control media of the C24

GFP-FABD2 line was significantly higher in comparison to others (**Fig. 9A, C, E**). Transfer of the C24 wild-type, *der1-3* mutant and their transgenic lines seedlings germinated on the control media to media containing  $0.1 \mu\text{mol.l}^{-1}$  of PQ led to a similarly decreased root growth rate (**Fig. 9B, D**). However, the reaction of seedlings to  $0.1 \mu\text{mol.l}^{-1}$  of PQ revealed a much better tolerance of the both *der1-3* mutant lines, as their average root growth rate was significantly higher than in both C24 wild-type lines, respectively (**Fig. 9F**). These observations were corroborated by the quantitative characterization of differences in average root growth rate by a reduction ratio between the control and PQ-containing media in the fold changes. The root growth reduction ratio caused by  $0.1 \mu\text{mol.l}^{-1}$  of PQ was lower in seedlings of the both *der1-3* mutant lines (**Fig. 9G**). Additional analysis of the biomass production showed, that the *der1-3* mutant and *der1-3* GFP-FABD2 had bigger aerial and underground part of plants under the stress conditions. This analysis clearly revealed the physiological resistance of the *der1-3* mutant against mild and severe oxidative stress.

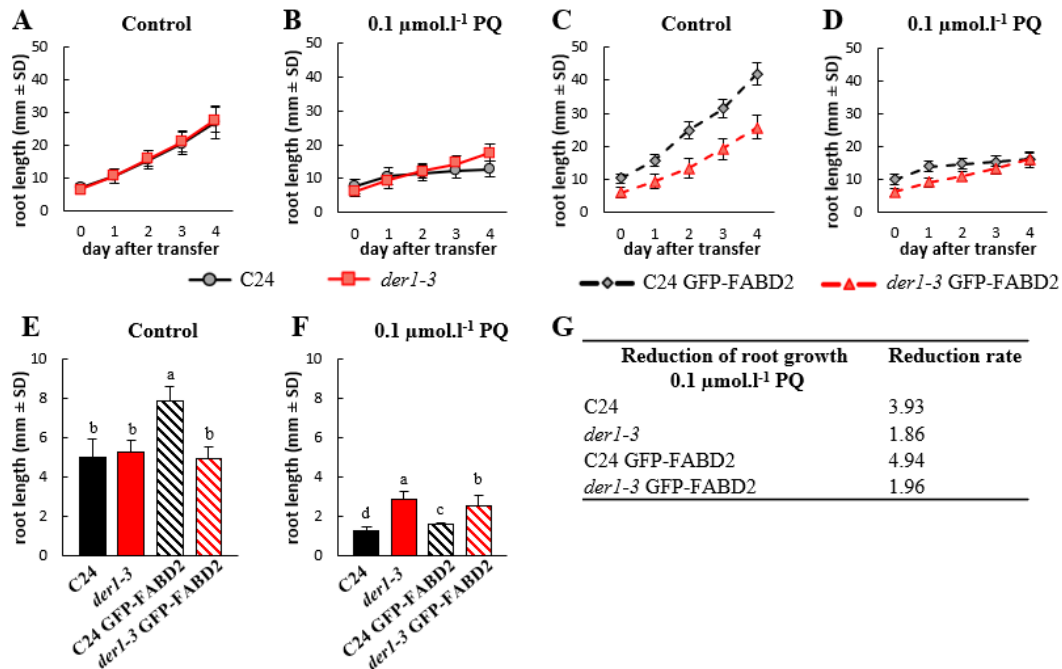


**Figure 9.** Root growth rate in plants of control C24, *der1-3* mutant and transgenic C24 and *der1-3* lines expressing *pro35S::GFP:FABD2* after their transfer to PQ-containing media. Root growth rate of the control C24 and *der1-3* mutant plants on the control media (**A**) and on media containing  $0.1 \mu\text{mol.l}^{-1}$  of PQ (**B**). Root growth rate of the transgenic C24 GFP-FABD2 and *der1-3* GFP-FABD2 lines on the control media (**C**) and on media containing  $0.1 \mu\text{mol.l}^{-1}$  of PQ (**D**). Average root growth per 24 h on the control media (**E**) and on media containing  $0.1 \mu\text{mol.l}^{-1}$  of PQ (**F**). Reduction ratio (fold change in respect to control) of the average root growth in the respective lines on media containing  $0.1 \mu\text{mol.l}^{-1}$  of PQ (**G**). Experiments were repeated two times with 16 plants per line (control) and 12 plants per line (PQ). Different lowercase letters above the bars (**E, F**) represent statistical significance according to one-way ANOVA and subsequent LSD test at  $p$  value  $< 0.05$ . Adapted from Kuběnová *et al.*, 2021.

### 5.2.3 Phenotype of *der1-3* mutant plants after long-term exposure to oxidative stress

The phenotype of plants germinated and grown on the control media for 20 days confirmed smaller aboveground parts and more irregular, and wavy root growth pattern of the *der1-3* mutant

(**Fig. 10A**), in comparison to the C24 control plants (**Fig. 10B**). Transgenic plants of C24 GFP-FABD2 and *der1-3* GFP-FABD2 grown on the control media were bigger, but similar phenotypes as in non-transgenic plants (**Fig. 10C, D**). However, plants transferred from the control to PQ-containing culture media revealed a better development of the *der1-3* mutant in comparison to the C24 control (**Fig. 10E, F**) and *der1-3* GFP-FABD2 line in comparison to the C24 GFP-FABD2 line (**Fig. 10G, H**). After 0.1  $\mu\text{mol.l}^{-1}$  of PQ treatment, the aboveground parts and root system of the *der1-3* mutant and *der1-3* GFP-FABD2 plants did not show such a strong stress reaction and developmental arrest (**Fig. 10F, H**). Putting together analyses of plant development after transfer to PQ-containing media from control conditions confirmed, that plants of the *der1-3* mutant and *der1-3* GFP-FABD2 line are more tolerant, particularly to the mild oxidative stress.

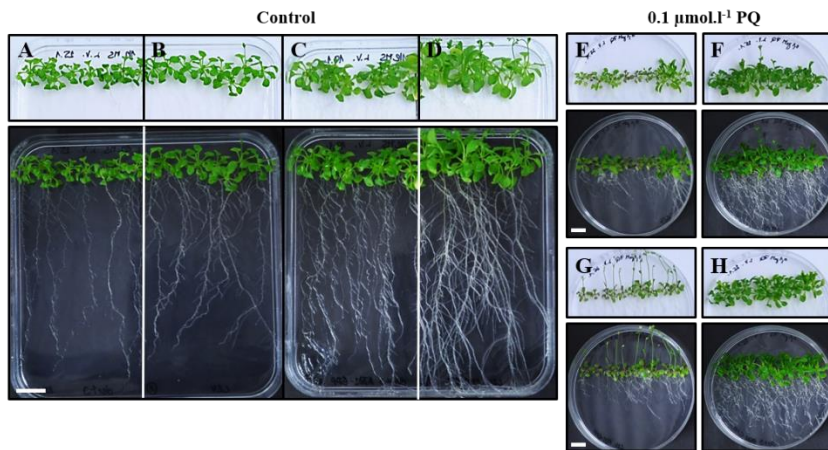


**Figure 10. Plant phenotype of control C24, *der1-3* mutant and transgenic C24 and *der1-3* lines expressing *pro35S::GFP:FABD2* on control media or after their transfer to PQ-containing media.** Plants of *der1-3* mutant (**A**), control C24 (**B**), *der1-3* GFP-FABD2 (**C**) and C24 GFP-FABD2 (**D**) line germinating and growing for 20 days on control media. (**E-H**) Plants 3-days old germinated on control media were transferred to PQ-containing media and photographed 17 days after transfer. Plants of control C24 (**E**), *der1-3* mutant (**F**), C24 GFP-FABD2 (**G**) and *der1-3* GFP-FABD2 (**H**) line growing on media containing 0.1  $\mu\text{mol.l}^{-1}$  PQ. Aboveground parts of plants were photographed on white background (upper row of images), and whole plants including roots were documented on black background (lower row of images). Scale bars = 1 cm. Adapted from Kuběnová *et al.*, 2021.

Considering the inhibitory effects of PQ in photosynthetically active plant tissues, we also employed a  $\text{H}_2\text{O}_2$  treatment, as an alternative oxidative stress-inducing agent that directly affects the root system and its development. Four different concentrations of  $\text{H}_2\text{O}_2$  (0.5; 1; 1.5 and 3  $\text{mmol.l}^{-1}$ ) were tested in post-germination root growth rate analysis within 4 days after the transfer of 3-days old seedlings germinated on the control media. We observed a  $\text{H}_2\text{O}_2$  dose-dependent response in the inhibition of root elongation and average root length (**Fig. 11A-E**). Interestingly, the stronger concentration of  $\text{H}_2\text{O}_2$  (3  $\text{mmol.l}^{-1}$ ) inhibited root elongation in the C24 wild-type significantly more than in the *der1-3* mutant plants (**Fig. 11E**). The quantitative characterization of differences in the average root growth rate presented as a reduction ratio between the control and  $\text{H}_2\text{O}_2$ -containing media showed no differences between the C24 wild-type and *der1-3* mutant on media containing 0.5 and 1  $\text{mmol.l}^{-1}$  of  $\text{H}_2\text{O}_2$  (**Fig. 11F**). However, a moderate difference caused by 1.5  $\text{mmol.l}^{-1}$  of  $\text{H}_2\text{O}_2$  and a considerably increased difference induced by 3  $\text{mmol.l}^{-1}$  of  $\text{H}_2\text{O}_2$  (**Fig. 11F**) suggested that root

growth and development of the *der1-3* mutant plants are substantially more resistant to moderate and severe oxidative stress than of the C24 wild-type plants.

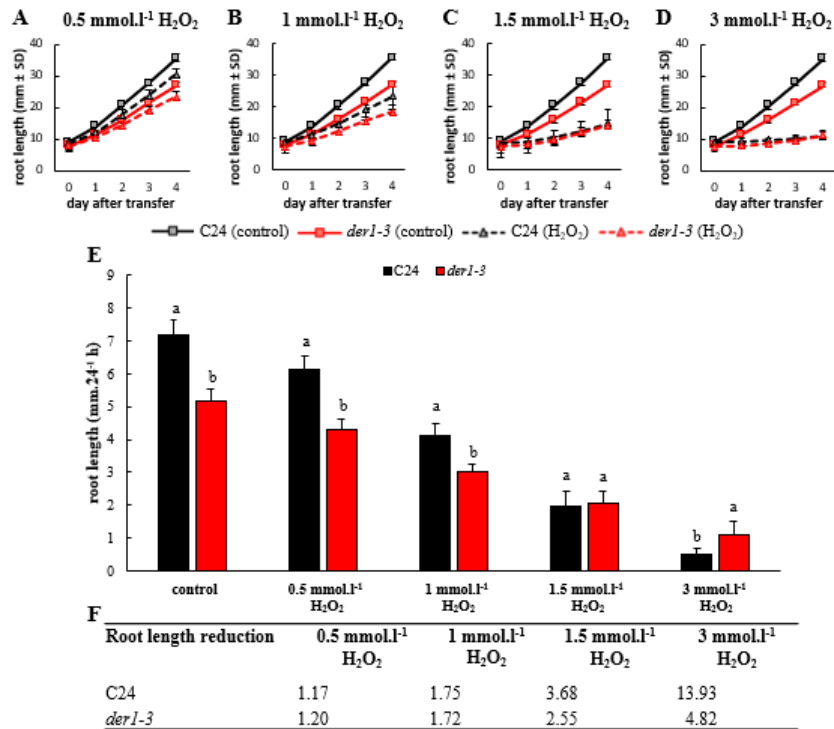


**Figure 11. Root growth rate of control C24 and *der1-3* mutant plants after their transfer to H<sub>2</sub>O<sub>2</sub>-containing media.** Root growth rate of control C24 and *der1-3* mutant plants on media containing 0.5 (A), 1 (B), 1.5 (C) and 3 (D) mmol.l<sup>-1</sup> H<sub>2</sub>O<sub>2</sub>. (E) Average root growth per 24 h on the control media and on media containing indicated concentrations of H<sub>2</sub>O<sub>2</sub>. (F) Reduction ratio (fold change in respect to control) of averaged root growth in control C24 and *der1-3* mutant plants on media containing 0.5 (A), 1 (B), 1.5 (C) and 3 (D) mmol.l<sup>-1</sup> H<sub>2</sub>O<sub>2</sub>. Experiments were repeated two times with 10 plants per line. Different lowercase letters above the bars (E) represent statistical significance according to one-way ANOVA and subsequent LSD test at p value < 0.05. Adapted from Kuběnová *et al.*, 2021.

#### 5.2.4 Response of the actin cytoskeleton to oxidative stress

In order to characterize the organization and dynamic properties of the actin cytoskeleton under PQ-induced oxidative stress, we utilized transgenic C24 and *der1-3* lines expressing *pro35S::GFP:FABD2* construct. In hypocotyl epidermal cells of 3-days old plants of the C24 GFP-FABD2 line in control conditions, AF were arranged in an extensive, well-organized and dynamic network. However, we observed massive bundling, particularly in cortical layers of the cell after treatment with 0.1 μmol.l<sup>-1</sup> of PQ for 30 min (Fig. 12A). The semi-quantitative evaluation of AF skewness, determining a degree of AF bundling, showed increased values after application of oxidative stress (Fig. 12B). The semi-quantitative evaluation of integrated density, determining fluorescence signal intensity per 1 μm<sup>2</sup>, was also significantly increased after PQ treatment (Fig. 12C). AF organization was slightly different in hypocotyl epidermal cells of 3-days old *der1-3* GFP-FABD2 plants in control conditions, showing mainly thinner, less organized, but dynamic AF in cell cortex. Treatment with 0.1 μmol.l<sup>-1</sup> of PQ for 30 min induced partial bundling of AFs, but overall changes in



their organization and dynamics were not so dramatic (**Fig. 12D**). As a result, both AF skewness (**Fig. 12E**) and integrated density, determining mean fluorescence signal intensity (**Fig. 12F**), were not significantly affected by oxidative stress. This analysis showing alterations in structure and dynamic properties of the actin cytoskeleton in the *der1-3* GFP-FABD2 line, that were not considerably affected by PQ treatment, may significantly support observed physiological resistance of the *der1-3* mutant and the related transgenic *der1-3* GFP-FABD2 line against oxidative stress.

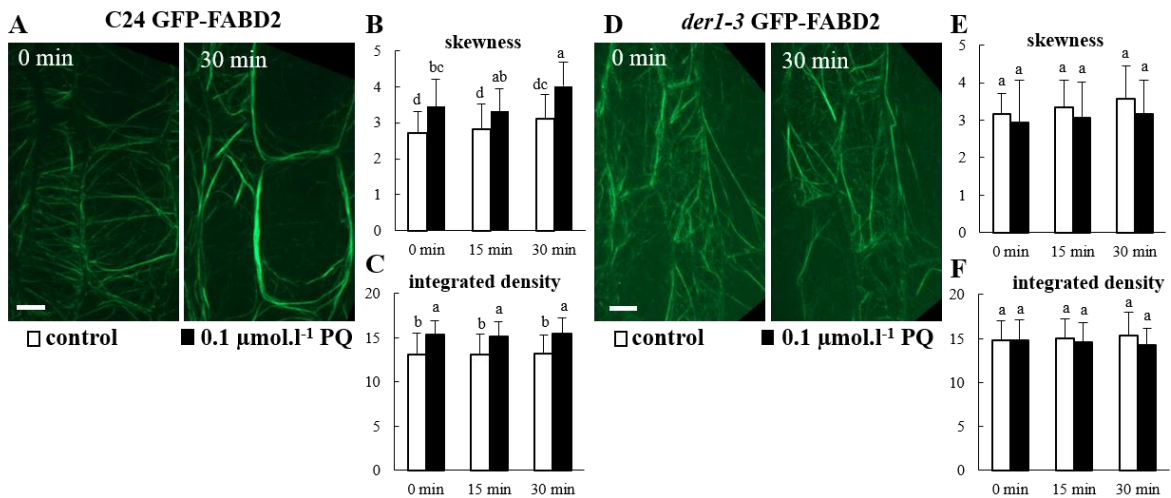


**Figure 12. Organization and dynamics of actin filaments in hypocotyl epidermal cells of transgenic C24 and *der1-3* lines expressing *pro35S::GFP:FABD2* under PQ-induced oxidative stress.** AFs in hypocotyl epidermal cells of 3-days old plant of C24 GFP-FABD2 (**A**) and *der1-3* GFP-FABD2 (**D**) line in control conditions and after treatment with  $0.1 \mu\text{mol.l}^{-1}$  PQ for 30 min. Quantitative analysis of AFs bundling extent (skewness, **B**, **E**) and AFs density (percentage of occupancy, **C**, **F**) in control conditions and after application of  $0.1 \mu\text{mol.l}^{-1}$  PQ. Experiments were repeated 5-6 times with 4-5 cells per plant in each line. Different lowercase letters above the bars (**B**, **C**, **E**, **F**) represent statistical significance according to one-way ANOVA and subsequent LSD test at  $p$  value  $< 0.05$ . Scale bar =  $10 \mu\text{m}$ . Adapted from Kuběnová *et al.*, 2021.

### 5.2.5 Lipid peroxidation and antioxidant activity

Based on observed phenotypical differences, we aimed to provide evidence about the biochemical mechanisms underlying an increased tolerance of the *der1-3* mutant to oxidative stress. Our analyses showed that the *der1-3* mutant exhibited a lower degree of lipid peroxidation after long-term PQ treatment compared to the C24 wild-type, while cultivation on  $\text{H}_2\text{O}_2$ -containing media did not cause lipid peroxidation in any examined line (**Fig. 13A**). This indicated that PQ treatment was less damaging to the *der1-3* mutant compared to C24 in terms of membrane integrity. Next, we also examined activities of important antioxidant enzymes in the C24 wild-type and the *der1-3* mutant. We found the elevated capacity to decompose  $\text{O}_2^{\cdot-}$  in the *der1-3* mutant, as manifested by a more intensive activation of iron superoxide dismutase 1 (FeSOD1) in these plants when exposed to both PQ and  $\text{H}_2\text{O}_2$ , compared to the C24 wild-type (**Fig. 13C**). Both treatments substantially decreased the activity of copper-zinc superoxide dismutase (CuZnSOD) isoforms in both the *der1-3* mutant and the C24 wild-type, while this reduction was less pronounced in the *der1-3* mutant (**Figure 13C**). This was also observed on protein abundance levels, as shown by immunoblotting (**Fig. 13D**). In addition, we

also encountered a substantially increased abundance of chloroplastic Peroxidase Q (PrxQ), a H<sub>2</sub>O<sub>2</sub> decomposing enzyme, in the *der1-3* mutant in response to both PQ and H<sub>2</sub>O<sub>2</sub> treatments, while a slight increase (in the case of PQ), or unchanged abundance (in the case of H<sub>2</sub>O<sub>2</sub>), were observed in the C24 wild-type (**Fig. 13B**). Altogether, these results showed that an increased tolerance of the *der1-3* mutant plants to oxidative stress is determined by an elevated enzymatic capacity to decompose ROS.

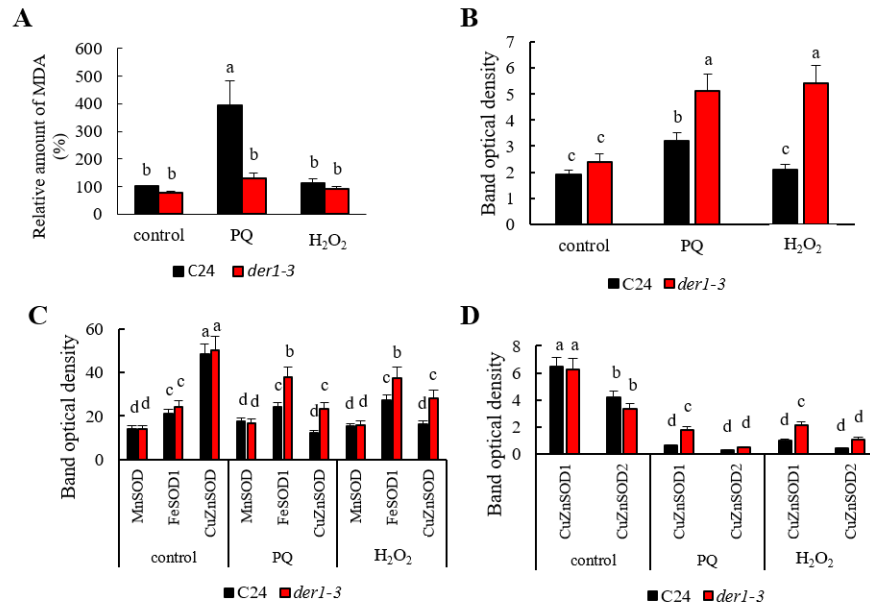


**Figure 13. Estimation of lipid peroxidation and antioxidant capacity in plants of C24 wild-type and *der1-3* mutant.** Plants 3-days old germinated on control media were transferred to 0.1  $\mu\text{mol.l}^{-1}$  PQ- and 3  $\text{mmol.l}^{-1}$  H<sub>2</sub>O<sub>2</sub>-containing media. (A) Relative quantification of malondialdehyde content. (B) Quantification of band densities of peroxidase Q abundance (B); of superoxide dismutase (SOD) isoforms activity on native polyacrylamide gels (C); and of CuZnSOD1 and CuZnSOD2 isoforms (D). Different lowercase letters above the bars represent statistical significance between treatments according to t-Test at p value < 0.05. These analyses were done with the help of Tomáš Takáč. Adapted from Kuběnová *et al.*, 2021.

### 5.3 Discussion

In the second part of the results, we found as very interesting fact that *der1-3* mutant was clearly more resistant to oxidative stress as compared to control C24 plants. We proved the resistance on the level of plant phenotypes, root growth efficiency, integrity and dynamic parameters of the actin cytoskeleton in hypocotyl cells of GFP-FABD2 transgenic lines, and biochemical analyses of anti-oxidative defense mechanisms. In principle, a single-point mutation in the *der1-3* mutant leads to exchange of Arg97 to Cys97 (Ringli *et al.*, 2002). This change occurs in superdomain1 on the protein and topologically it is located on the surface, without effecting the tertiary protein structure, as shown by model comparison of control, and by mutation affected ACT2 proteins. ACT2 protein affected by the mutation is still functional, meanwhile the mutation might have an impact on its biochemical properties, such as post-translation modifications or protein-protein interactions. The phenotypical analyses and testing of the growth rate of C24 control and *der1-3* mutant plants, as well as GFP-FABD2 transgenic lines created in these two genetic backgrounds were performed with plants either

directly germinated on, or transferred to oxidative stress condition after control germination. Oxidative stress was induced by different concentration of PQ and H<sub>2</sub>O<sub>2</sub> in the culture medium. We found out that PQ had stronger effect on root growth than H<sub>2</sub>O<sub>2</sub>. The higher resistance of *der1-3* mutant plants was determined based on lower root growth rate reduction (both after 0.1 μmol.l<sup>-1</sup> of PQ and 3 mmol.l<sup>-1</sup> of H<sub>2</sub>O<sub>2</sub> treatments) and more efficient production of root and shoot fresh weight after PQ treatment.

These facts led us to investigate actin cytoskeleton structure and organization in transgenic GFP-FABD2 lines under oxidative stress using live-cell imaging. Quantitative analyses showed that AFs in hypocotyl cells of C24 GFP-FABD2 transgenic line underwent a massive bundling after treatment with 0.1 μmol.l<sup>-1</sup> PQ for 30 min. On the other hand, AFs in *der1-3* GFP-FABD2 hypocotyl cells, preserved their structure and were still dynamic. This fact seems to be one of the main reasons supporting the higher tolerance of the *der1-3* mutant to the oxidative stress. It has been shown that a reduction in AF bundling can be directly associated with increased AF dynamics (Staiger and Blanchoin, 2006). The molecular mechanism how AFs are involved in plant response to oxidative stress is not fully understood yet, but some facts were already revealed. Protection of the actin cytoskeleton under the oxidative stress could be required for PIN2 auxin efflux carrier trafficking to the PM. The intracellular transport of PIN2 was reduced after H<sub>2</sub>O<sub>2</sub> treatment, which affected directly actin cytoskeleton dynamics (Zwiewka *et al.*, 2019).

Moreover, our observations that *der1-3* mutant is more resistant to oxidative stress was corroborated by several biochemical experiments. These analyses showed that the *der1-3* mutant had a lower degree of lipid peroxidation, and also increased abundance and activity of antioxidant enzymes, such as iron superoxide dismutase 1 (FeSOD1), two copper-zinc superoxide dismutase isoforms (CuZnSOD1 and CuZnSOD2), and redox buffering protein peroxiredoxin Q (PrxQ). This indicates that the *der1-3* mutant has a higher capacity to decompose O<sub>2</sub><sup>-</sup> by increased level and activity of CuZnSOD1/2 and FeSOD1 enzymes as compared to the C24 control plants. These enzymes were proposed as important determinants of oxidative stress tolerance in plants (Sunkar *et al.*, 2006; Dvořák *et al.*, 2021). Due to a higher abundance of PrxQ, which is an atypical 2-cys peroxiredoxin using thioredoxin as an electron donor (Lamkemeyer *et al.*, 2006; Yoshida *et al.*, 2015), the *der1-3* mutant can also decompose H<sub>2</sub>O<sub>2</sub> more effectively. Altered ACTIN2 protein in *der1-3* mutant has one additional Cys compared to natural one, therefore we hypothesized that ACTIN2 in *der1-3* might undergo redox-mediated posttranslational modifications accelerating the antioxidant capacity via PrxQ and thioredoxins. It was published, that BEN1, a guanine exchange factor for ARF (ADP-ribosylation factor), regulating the AF-based intracellular trafficking of PIN2 during adaptation to oxidative stress, contains highly conserved cysteine residues (Mouratou *et al.*, 2005; Zhou *et al.*, 2010) that could be modified by H<sub>2</sub>O<sub>2</sub> treatment. Increased redox status upon the accumulation of H<sub>2</sub>O<sub>2</sub> can initiate the oxidation of cysteine sulfhydryl groups in actins (Wang *et al.*, 2012). Direct oxidative posttranslational modifications of actins in mammalian cells, such as oxidation (Frémont *et al.*, 2017), glutathionylation (Sakai *et al.*, 2012) or S-sulfhydration (Mustafa *et al.*, 2009), affected AFs depolymerization (Frémont *et al.*, 2017) and dynamics (Gellert *et al.*, 2015; Stojkov *et al.*, 2017). Thus, this section of the thesis brought some light to resistance against oxidative stress in *der1-3* mutant, in which the single-point mutation of the *ACT2* gene altered broadly also other cellular and molecular mechanisms.

## **6. PART IV - ROOT HAIR DEFECTIVE 2 vesicular delivery to the apical plasma membrane domain during Arabidopsis root hair development**

### **6.1 Material and Methods**

The plant material and methods are described in more detail in the dissertation thesis and summarization is mentioned here.

Experiments were performed with plants of *A. thaliana*, wild-type of the Col-0 ecotype, *rhd2-1* (Foreman *et al.*, 2003) mutant, stably transformed *A. thaliana* plants (of Col-0 wild-type background) carrying constructs with GFP-RHD2 under the native promotor (Takeda *et al.*, 2008). Plants of the *rhd2-1* mutant, were crossed with transgenic plants bearing fluorescent markers for early endosomes/TGN, GFP-RabA1d (Ovečka *et al.*, 2010), or late endosomes, RabF2a-YFP (Voigt *et al.*, 2005). Transgenic plants GFP-RHD2 were crossed with transgenic plants carrying fluorescent markers of endosomal compartments (Wave line W13R producing mCherry-VTI12 for early endosomes/TGN, and Wave line W2R producing mCherry-RabF2b for late endosomes; Geldner *et al.*, 2009).

Cell type-specific and subcellular distribution patterns of GFP-RHD2 in root was done by Airyscan CLSM and light-sheet fluorescence microscope. LSM880 equipped with Airyscan (Carl Zeiss, Germany) was used for subcellular distribution pattern of GFP-RHD2 signal and images were used for quantitative analyses of compartment positive to GFP-RHD2 signal during RH development and growth. Image acquisition was performed with a 20x/0.8 NA dry Plan-Apochromat objective (Carl Zeiss, Germany). Developmental and cell type-specific localization pattern of GFP-RHD2 was observed by light-sheet Z.1 fluorescence microscope (Carl Zeiss, Germany) equipped with two LSM 10x/0.2 NA illumination objectives (Carl Zeiss, Germany), Plan-Apochromat 20x/1.0 NA water immersion detection objective (Carl Zeiss, Germany), and the PCO Edge sCMOS camera (PCO AG, Germany). All colocalization studies were prepared by a Cell Observer SD Axio Observer Z1 spinning disk microscope (Carl Zeiss, Germany) equipped with alpha Plan-Apochromat 100x/1.57 NA DIC Korr oil immersion objective (Carl Zeiss, Germany). Images were acquired simultaneously with two Evolve 512 EMCCD cameras (Photometrics) using a camera-streaming mode.

Fluorescence probes were individually applied directly to the microscopy chamber by perfusion. The PM and vesicular marker in the RHs (FM4-64) is used in 4  $\mu\text{mol.l}^{-1}$  concentration. Filipin III was used as a vital fluorescence probe of structural strolls in 10  $\mu\text{g.ml}^{-1}$  concentration. RHs labelled by filipin III or FM4-64 was observed by spinning disk microscope.

Arivis Vision4D program, version 3.1.4. (Arivis AG, Germany) was used for quantitative tracking of the GFP-RHD2 compartments. All graphical plots were prepared in Microsoft Excel software and statistical analyses were done using STATISTICA 12 (StatSoft) software using analysis of variance (ANOVA) and subsequent Fisher's LSD tests ( $p < 0.05$ ). Microscopic data were processed and evaluated (such as fluorescence intensities, quantification of colocalization studies - Pearson's coefficient and kymographs) in Zen 2014 software, blue or black edition (Carl Zeiss, Germany).

## 6.2 Results

### 6.2.1 Cell type-specific and subcellular distribution patterns of GFP-RHD2 signal in root

Light-sheet fluorescence microscopy (LSFM) provided visualization for developmentally regulated and cell type-specific distribution patterns of GFP-RHD2 in growing roots. The GFP-RHD2 signal was observed in epidermal cells in RH formation zone, and was explicitly accumulated in the bulges and apices of developing RHs (**Fig. 14A**). Orthogonal projections from different root developmental zones confirmed GFP-RHD2 localization in the root epidermis, preferably in trichoblasts within the root differentiation and elongation zone (**Fig. 14B**). Specifically, GFP-RHD2 accumulated at the tips of emerging (**Fig. 14A, C**) and growing (**Fig. 14A, D**) RHs. Most importantly, Airyscan CLSM imaging revealed GFP-RHD2 presence in small motile compartments in the cytoplasm (**Fig. 14E, F**). Their number was considerably higher in trichoblasts (**Fig. 14E**), and there was an apparent progressive accumulation in developing bulges (arrowhead in **Fig. 14E, F**). In addition to the visualization of GFP-RHD2 in small compartments in the cytoplasm, Airyscan CLSM revealed localization in the PM, particularly at bulging sites and apical domains of developing bulges (**Fig. 14E, F**).

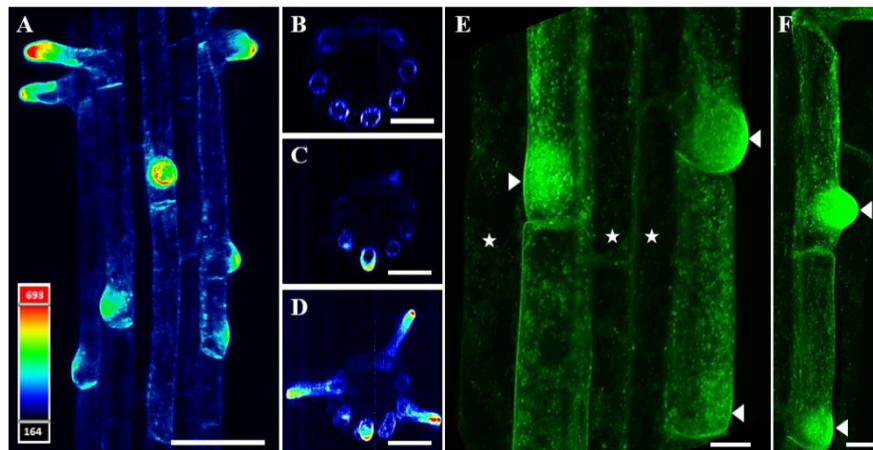


**Figure 14. Expression pattern and cell type-specific distribution of GFP-RHD2 in growing root.** Distribution pattern in RH formation zone (**A**), where GFP-RHD2 was expressed mainly in trichoblasts (**B**) and accumulated at tips of emerging (**C**) and growing (**D**) RHs. Maximum intensity projection of from light-sheet fluorescence microscopy imaging as visualized using semi-quantitative fluorescence intensity distribution and pseudo-color-coded scale, where dark blue represents minimal intensity (164 arbitrary units) and pale red represents maximum intensity (693 arbitrary units). (**E, F**) Detailed visualization of subcellular compartments containing GFP-RHD2 in trichoblasts and their progressive accumulation in developing bulges (arrowheads) using Airyscan CLSM. A substantially lower number of compartments with GFP-RHD2 was detected in atrichoblasts (asterisks). Scale bar = 50  $\mu\text{m}$  (**A**), 40  $\mu\text{m}$  (**B-D**), 10  $\mu\text{m}$  (**E, F**). Adapted from Kuběnová *et al.*, 2022.

Localization analysis showed a different range of GFP-RHD2 specific targeting to the apical PM domain at distinct stages of RH development. Therefore, we analysed the range of PM decorated with GFP-RHD2 (**Fig. 15A**). A quantitative evaluation revealed that the extent of the PM zone containing GFP-RHD2 increased progressively from early to late bulges. This zone was enlarged in short RHs and reached a maximum in longer growing RHs but declined considerably in nongrowing

RHs (**Fig. 15B**). Thus, the distribution pattern of GFP-RHD2 at the apical PM was tightly associated with the individual developmental stages of RHs (**Fig. 15A, B**). Live-cell imaging revealed targeted delivery of GFP-RHD2 in dynamic vesicular compartments to the cortical cytoplasm and apical PM of developing RHs. Based on the nature of their movements, we determined three groups of vesicular compartments carrying GFP-RHD2. The first group was represented by compartments with targeted movement to the apical PM (marked in red). The second group consisted of compartments moving in the cytoplasm without any contact with the apical PM (marked in blue). The third group of compartments moved toward the PM and subsequently moved back to the cytoplasm after making contact (marked in cyan). The quantitative evaluation showed a high proportion of GFP-RHD2 vesicular compartments moving toward the apical PM. A low number of compartments moved without contact or moved back after contact with the PM in the early bulge stage (**Fig. 15C**). However, this turned to a different pattern during RH development. The proportions of compartments from the red group, was relatively high in short- and longer growing RHs, while the compartments from the cyan group, considerably increased (**Fig. 15C**). With the cessation of tip growth, there was a considerable reduction in compartments moving to the apical PM (**Fig. 15C**). This analysis showed that the extent of GFP-RHD2 specifically targeted to the apical PM corresponded with the stages of RH formation. Importantly, this association was directly affected by the ratio between GFP-RHD2 vesicular compartments targeted to the apical PM and those moving back to the cytoplasm after contacting the PM.

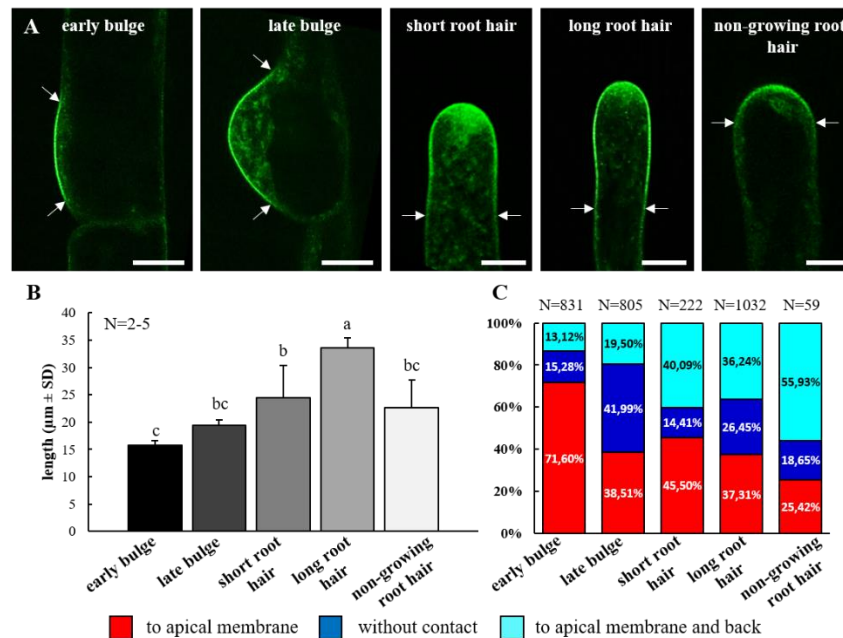


**Figure 15. Determination of GFP-RHD2 localization at the apical plasma membrane domain at different stages of root hair formation and growth.** (A) Delineation of the area (by two arrows) where GFP-RHD2 was specifically targeted to the apical PM domain at early and late bulging stage, in short and longer growing RHs, and in non-growing RHs. (B) Quantitative evaluation of the apical PM domain length decorated by GFP-RHD2 at different stages of RH development (N = 2-5). Different lowercase letters indicate statistical significance between treatments ( $p < 0.05$ ). (C) Quantitative determination of the ratio between three group of the compartments containing GFP-RHD2. The GFP-RHD2 positive compartments were tracked and analysed at denoted stages of RH development as depicted in (A). More than 59 compartments from 3 to 7 growing RHs from individual plants were analysed. Scale bar = 5 µm (A). Adapted from Kuběnová *et al.*, 2022.

### 6.2.2 Quantitative microscopic analysis of motile compartments containing GFP-RHD2 at different stages of root hair development

Live-cell imaging of developing RHs by advanced microscopy enabled the qualitative determination of compartments containing GFP-RHD2. We analysed the quantitative parameters of their movements in different stages of RH formation using the single-particle tracking method and characterized three independent groups of the GFP-RHD2 compartments, which was mentioned before. Movement distances of GFP-RHD2 compartments during a 60 s period imaged by Airyscan CLSM were tracked using the “tracked cells function” of the ARIVIS Vision4D software. These trajectories were directly displayed in a color-coded mode in the image sequences of early and late bulges, as well as short and longer growing RHS. **Figure 16** shows only selection of RH growth stages (late bulge **Fig. 16A**, longer RH **Fig. 16C**). In addition, the values of the maximum and the average speed of movement were analysed. Line tracking trajectories in different stages of RH development clearly distinguished spatial separation of GFP-RHD2 compartments from different groups (**Fig. 16A, C**). Compartments from the red group were located almost exclusively in the whole bulges (**Fig. 16A**) as well as in the clear and subapical zones of growing RHs (**Fig. 16C**). In contrast, GFP-RHD2 compartments from the cyan group were located mainly at the periphery of the developing bulging domains (**Fig. 16A**) and in growing RHs moved preferably in the subapical and shank regions, contacting the lateral PM (**Fig. 16C**) exclusively. Differences in the spatial distribution of individual compartments might be associated with the distance and speed of movement in different RH developmental stages. Compartments from the blue group showed the shortest displacement distances in almost all cases, with the lowest values in maximum movement speed (**Fig. 16B, D**). However, the average speed of these compartments was the highest (with the highest variability) at all stages of RH development (**Fig. 16B, D**). Compartments from the red group moved along short distances in late bulging stages (**Fig. 16B**). These distances increased significantly during RH tip growth compared to the cyan group (**Fig. 16D**). Compartments from the cyan group moved over the longest distance in late bulging stages (**Fig. 16B**), but these values decreased in the growing RH stage (**Fig. 16D**). The maximum movement speed was comparable between compartments from the red and cyan groups. Still, the average speed was significantly higher in compartments from the cyan group compared to the red group (**Fig. 16B, D**).

### 6.2.3 Identification of GFP-RHD2-positive compartments

Next, we analysed the nature of compartments containing GFP-RHD2 by colocalization with the selective membrane styryl dye FM4-64 and with early endosomal marker mCherry-VTI12 (Geldner *et al.*, 2009). In RHs, the FM4-64 dye is able to stain the PM and early endocytotic/recycling vesicular compartments after a minute-long exposure period (Ovečka *et al* 2005). After 10 min of application FM4-64 colocalized with GFP-RHD2 at the PM and in motile vesicular compartments in the apical and subapical zones of growing RHs (**Fig. 17A**). A high degree of colocalization in moving vesicular compartments within the subapical zone of growing RHs (**Fig. 17C**) was revealed by fluorescence intensity profile measurements (**Fig. 17D**). The quantitative colocalization analysis showing a high degree of Pearson’s correlation coefficients between FM4-64 and GFP-RHD2, and

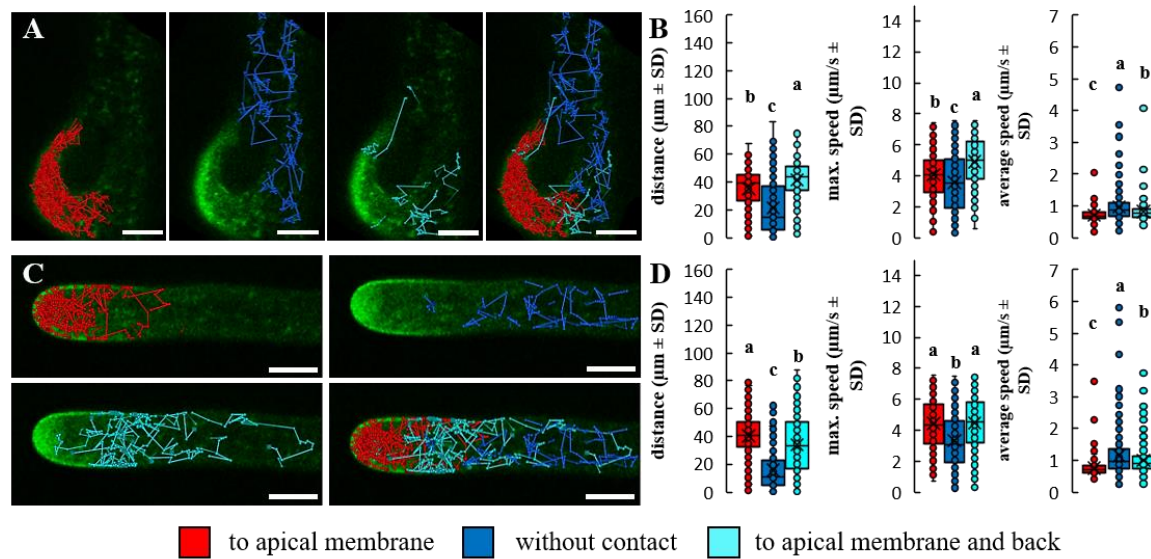


**Figure 16. Qualitative determination and quantitative tracking of moving compartments containing GFP-RHD2 at different stages of root hair development.** Line tracking of three different groups of compartments positive to GFP-RHD2 signal and merged images of all three types of tracks in the late bulge (A), and longer (C) growing RHs. (B, D) Quantitative determination of tracked distances of these compartments, maximum and average speeds of their movements during tracking analysis, as compared separately for the compartments in the late bulge (B) and longer (D) growing RHs. More than 222 compartments from 3 to 7 growing RHs from individual plants were analysed. Box plots show the first and third quartiles, split by the median (line) and mean (cross). Whiskers extend to include the max/min values. Different lowercase letters indicate statistical significance between treatments ( $p < 0.05$ ). Scale bar = 5  $\mu\text{m}$ . Adapted from Kuběnová *et al.*, 2022.

also with GFP-RabA1d, as an early endosomal/TGN marker, but not with RabF2a-YFP, as a late endosomal marker in intracellular compartments (Fig. 17G). Colocalization analysis GFP-RHD2 with mCherry-VTI12 was used for confirmation of hypothesis, that vesicular compartments containing GFP-RHD2 might belong to the early endosomal group. Markers mCherry-VTI12 and mCherry-RabF2b were not detected in the PM of growing RHs. However, the early endosomal/TGN marker mCherry-VTI12 showed colocalization with GFP-RHD2 in motile compartments (Fig. 17B, E). This was confirmed by fluorescence intensity profile quantification (Fig. 17F) and a high degree of Pearson's correlation coefficients (Fig. 17H). Concluding from colocalization results with FM4-64 and endosomal markers, vesicular trafficking and targeted delivery of GFP-RHD2 during RH development seem to depend on early endosomal/TGN compartments.



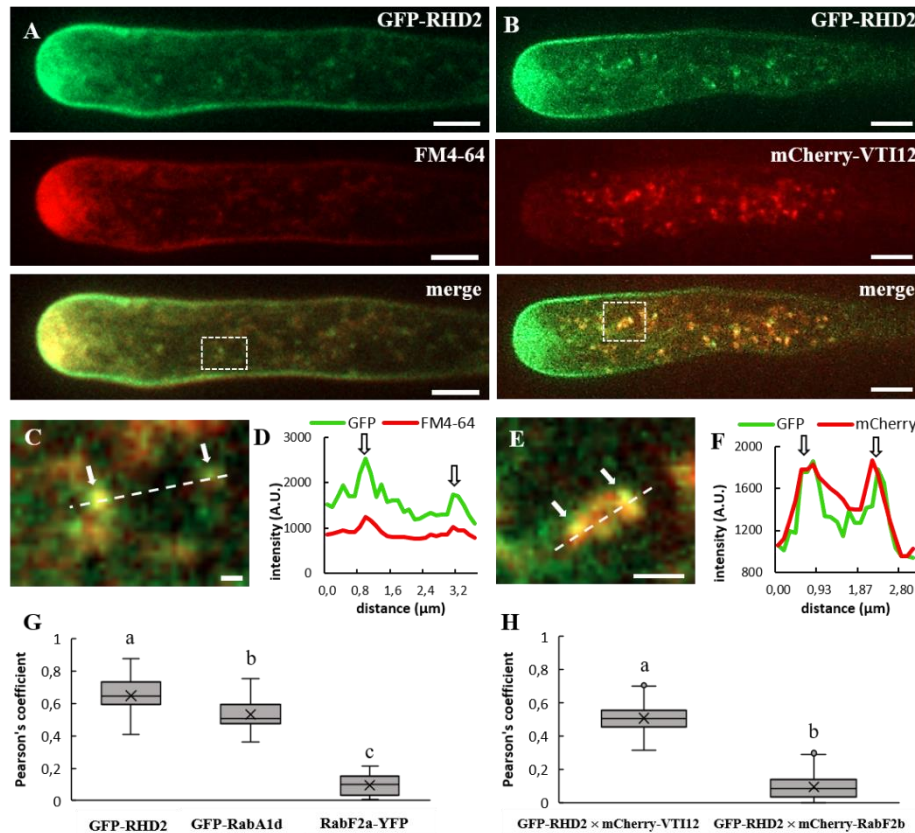


**Figure 17. Colocalization analyses of GFP-RHD2 with selective membrane styryl dye FM4-64 and with early endosomal marker (mCherry-VTI12) in growing root hairs.** Localization pattern of GFP-RHD2 in the apical PM domain, the cytoplasm of the apical and subapical zone, and in motile compartments of growing RH co-labelled with membrane styryl dye FM4-64 (A) or in double line with the early endosomal/trans-Golgi network marker mCherry-VTI12 (B). Detailed images of compartments containing GFP-RHD2 and FM4-64 (C) within the white box depicted in (A) and GFP-RHD2 and mCherry-VTI12 (E) within the white box in (B). Arrows indicate the position of the compartments and the interrupted white line depicts the profile for fluorescence intensity quantification. Fluorescence intensity profiles of the GFP and FM4-64 signal (D) along the interrupted white line in (C) and the GFP and mCherry-VTI12 signal (F) along the interrupted white line in (E). Arrows indicate the position of the compartments. Quantitative colocalization analyses using Pearson's correlation coefficients between FM4-64 with GFP-RHD2, early endosomal marker GFP-RabA1d and late endosomal marker RabF2a-YFP in intracellular compartments (G) or between GFP-RHD2 with the early endosomal/trans-Golgi network marker mCherry-VTI12, and between GFP-RHD2 with the late endosomal marker mCherry-RabF2b, in intracellular compartments (H). Scale bar = 5  $\mu\text{m}$  (A, B), 1  $\mu\text{m}$  (C, E). Adapted from Kuběnová *et al.*, 2022.

#### 6.2.4 Distribution of GFP-RHD2 in root hairs after filipin III treatment

The delivery of motile compartments positive to GFP-RHD2 signal with to the growing apex of bulges and RHs requires physical interactions with the PM. Therefore, the RHs of the GFP-RHD2 line were treated with 10  $\mu\text{g}\cdot\text{ml}^{-1}$  filipin III (sterol vital dye) for 10 min, and subcellular changes in GFP-RHD2 distribution were directly examined using a spinning disk microscope. The appearance of filipin III fluorescence in the PM of RHs after application coincided with the tip growth arrest. Treatment with filipin III led to a layer-like accumulation of GFP-RHD2 closely associated with PM

at the apex of RHs (**Fig. 18A, C**). Because filipin III positive blue staining served as a PM marker under these circumstances. Therefore, the layer-like accumulation of GFP-RHD2 beneath the PM suggests that GFP-RHD2 was prevented from incorporating into the PM after filipin III treatment. This localization pattern was unique because equivalent experiments on GFP-RabA1d RHs treated with filipin III revealed accumulation of early endosomal/TGN compartments in the apical part of the RHs, but not in close contact with filipin III-positive apical PM (**Fig. 18B, E**). Semi-quantitative analysis of the fluorescence intensity distribution using a profile function across the RH apex (**Fig. 18C**) revealed a “basal” level of GFP-RHD2 in filipin III-positive PM but mostly accumulated in a thin layer beneath the PM (**Fig. 18D**). Simultaneously, the clear zone was depleted of GFP-RHD2 fluorescence after filipin III treatment (**Fig. 18C, D**). Interestingly, GFP-RabA1d accumulation in the clear zone after filipin III treatment showed a different pattern (**Fig. 18E**) because it was detached and did not show direct contact with the filipin III-positive PM (**Fig. 18E, F**). These experiments with filipin III and independent auxinol treatment suggest that structural sterols, abundant in the apical PM of growing RHs, might be involved in the dynamic relocation of GFP-RHD2.

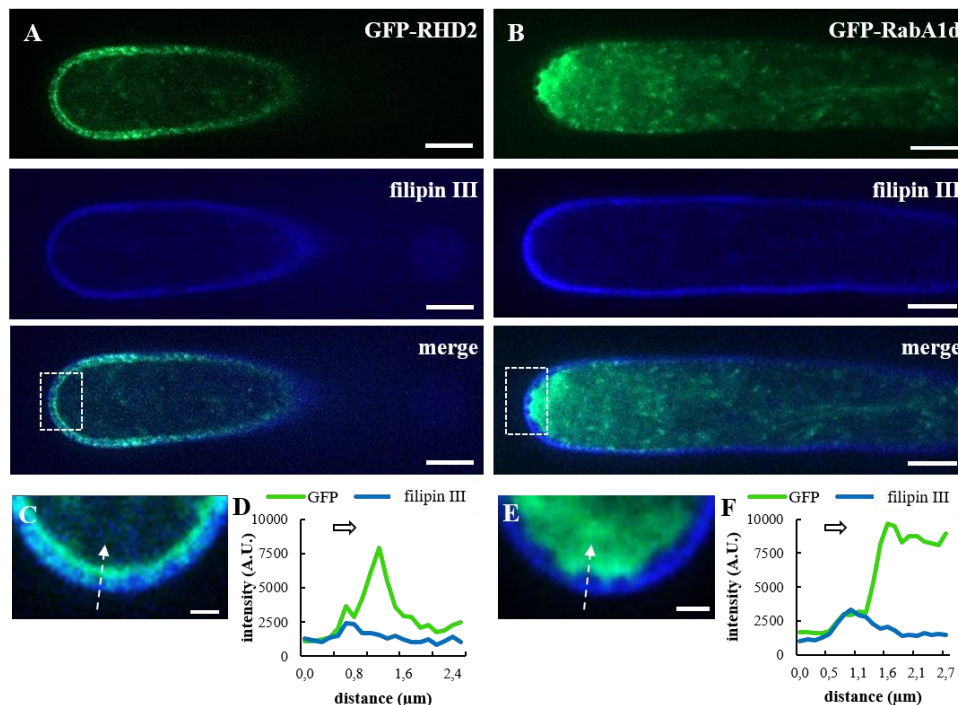


**Figure 18. Localization analysis of GFP-RHD2 and GFP-RabA1d in root hairs after filipin III treatment.** Merged images of localization patterns of GFP-RHD2 (**A**) and GFP-RabA1d (**B**) in the RH and filipin III-positive signal (blue) at the PM after 10 min treatment. (**C, E**) Detailed images of the apical part of the RH within the white box in (**A, B**). Arrows indicate the position and the direction of the fluorescence intensity profile measurement. Fluorescence intensity profile of the GFP-RHD2 and filipin III-positive signal (**D**) along the arrow in (**C**) and of the RabA1d-GFP and filipin III-positive signal (**F**) along the arrow in (**E**). The arrows above the curves indicates the direction of the measurements. Scale bar = 5  $\mu\text{m}$  (**A, B**), 1  $\mu\text{m}$  (**C, E**). Adapted from Kuběnová *et al.*, 2022.

### 6.3 Discussion

In this part of results deals with the role of AtRBOHC/RHD2 in the RH formation and their tip growth. Process of RH tip growth requires vesicular transport and targeted delivery, localized cell wall deposition, and controlled PM extension. Critically important parameter is localized generation of ROS, creating typical tip-localized gradient together with  $\text{Ca}^{2+}$  ions and pH at the apical cytoplasm (Šamaj *et al.*, 2006). ROS are produced by NADPH oxidase type C, which is encoded by *RHD2* (*ROOT HAIR DEFECTIVE 2*) gene. AtRBOHC/RHD2 is incorporated into apical PM and generates ROS into the apoplast (Foreman *et al.*, 2003). NADPH oxidase type C is also activated by  $\text{Ca}^{2+}$  ions, but the main activators are Rop GTPases (Jones *et al.*, 2007). Rop GTPases were found to be accumulated at the site of future RHs initiation in trichoblasts (Molendijk *et al.*, 2001; Jones *et al.*, 2002). The short RH phenotype is totally rescuable by *GFP:RHD2* construct expressed under control of the native promotor (Takeda *et al.*, 2008). In our experiments, we used *rhd2* mutant and transgenic line carrying GFP-RHD2 in Col-0 background. We used different advanced microscopy methods for qualitative and quantitative characterization of GFP-RHD2 subcellular distribution and localization. We confirmed the published cellular localization pattern of GFP-RHD2, which was selective accumulation in bulges and tips of developing RHs (Takeda *et al.*, 2008), and we extended this pattern at the subcellular and super-resolution levels.

We proved GFP-RHD2 signal localization in apical part of PM in growing RHs. Importantly, we found GFP-RHD2 signal localized in dynamic cytoplasmic vesicular compartments. These compartments were more abundant in trichoblasts than in atrichoblasts. In next experiments, we characterized in detail the pattern of temporal and spatial GFP-RHD2 redistribution during the process of RH initiation and growth. Quantitative single particle tracking analysis showed that GFP-RHD2 was targeted to, and removed back from the apical PM domains in developing bulges and growing RHs. Interestingly, the range of PM decorated by a fluorescent signal from GFP-RHD2 closely correlated with particular stages of RH development.

The quantitative particle tracking analysis revealed a complex pattern of GFP-RHD2 compartments distribution, both in movement and interactions with the PM. Based on data acquired, GFP-RHD2 compartments in growing RHs were divided into three different groups. The first group represented compartments moving to, and fusing with the apical PM. The proportion of this group was highest in early stages of RHs growth and corresponded with the largest area of apical PM containing accumulated fluorescence signal of the GFP-RHD2. The second group consisted GFP-RHD2 compartments moving only in the cytoplasm without any contact with the apical PM. They probably did not support GFP-RHD2 incorporation to the PM. The third group of compartments was particularly interesting, as they moved to and contacted the PM, while subsequently moved back to the cytoplasm. These events occurred mainly within the sub-apical zone of RHs and the number of these compartments proportionally increased in longer, rapidly growing RHs. GFP-RHD2-positive compartments behaving differently at the PM, and changes in their ratio typical for individual stages of RHs growth indicate that GFP-RHD2 incorporation into the PM and/or recycling back may represent an important part of the regulatory mechanism driving RH tip growth.

Then, we defined the molecular signature of GFP-RHD2-positive compartments microscopically by subcellular colocalization studies. Vital staining with FM4-64 revealed

colocalization of FM4-64 with GFP-RHD2 at the PM and in cytoplasmic vesicular compartments in growing RHs. FM4-64, as a membrane-specific styryl dye after labelling of the PM and after a short incubation time, serves as a fluorescent marker of early endocytic compartments in growing RHs (Ovečka *et al.*, 2005). This was corroborated positively by colocalization of FM4-64 with early/TGN endosomal marker GFP-RabA1d (Ovečka *et al.*, 2010; Berson *et al.*, 2014), and negatively by failed colocalization with late endosomal marker RabF2a-YFP (Voigt *et al.*, 2005; Berson *et al.*, 2014). In the next step, we prepared double transgenic fluorescence lines by crossing, carrying GFP-RHD2 together with mCherry-VTI12 (an early endosomal/TGN marker; Geldner *et al.*, 2009) and with mCherry-RabF2b (a late endosomal marker; Geldner *et al.*, 2009). Colocalization analyses corroborated previous results. Early endosomal/TGN marker mCherry-VTI12 showed colocalization with GFP-RHD2 in vesicular compartments in growing RHs. We measured also a maximum speed of moving GFP-RHD2 vesicular compartments and we received a range of 4 - 8  $\mu\text{m}\cdot\text{s}^{-1}$ . This is well consistent with the measured dynamic properties of early endosomal compartments carrying molecular markers GFP-RabA1d and YFP-VTI12 in RHs, which was in the range of 6 - 9  $\mu\text{m}\cdot\text{s}^{-1}$  (von Wangenheim *et al.*, 2016).

The delivery of GFP-RHD2 in motile compartments with to the growing apex of bulges and RHs requires physical interactions with the PM. Therefore, we tested a possible role of structural sterols, integral components of the PM. We treated plants with filipin III, a polyene antibiotic fluorochrome suitable as a vital probe for *in vivo* sterol localization in animal (Nichols *et al.*, 2001), yeast (Wachtler *et al.*, 2003), and plant cells (Grebe *et al.*, 2003; Boutté *et al.*, 2009; Liu *et al.*, 2009; Bonneau *et al.*, 2010). Filipin III application (10  $\mu\text{g}\cdot\mu\text{l}^{-1}$ ) caused labelling of the PM, and although GFP-RHD2 showed a residual signal at the PM, its majority was accumulated just beneath the PM. Filipin III at higher concentrations promote the formation of filipin III – sterol complexes, disrupting PM structural and physiological functions. Formation of a layer-like aggregates of GFP-RHD2 beneath the PM suggests that GFP-RHD2 was prevented from incorporating into the PM due to sterol sequestration. In addition, the depletion of GFP-RHD2 compartments from the clear zone of treated RHs might indicate that recycling from the PM was also inhibited after filipin III treatment. It has been proven that the appearance of filipin-sterol complexes at the PM was immediately connected with PM rigidification. It triggered ion leakage, extracellular pH alkalization, and changes in signalling, which depends on protein kinase-mediated phosphorylation (Bonneau *et al.*, 2010). The link between structural sterols at the PM and RH formation might be mediated by a regulatory role of Rho of plants (ROPs; Denninger *et al.*, 2019) that activate RHD2 during RH tip growth (Carol *et al.*, 2005). Transient S-acylation causes ROPs activation, which is required for their functionality and stabilizes their interaction with the PM and accumulation in lipid rafts (Sorek *et al.*, 2007, 2011). In conclusion, this observation indicates that structural sterols might be involved in localized anchoring and maintenance of GFP-RHD2 in the apical PM, particularly at the apex of developing RHs.

## 7. General conclusion

Results presented in this Ph.D. thesis are arranged to three parts that describe different aspects of selected *A. thaliana* RHs mutants, including phenotypical and growth characteristics, defense reactions to selected abiotic stresses, and detailed microscopical analyses of transgenic lines carrying molecular markers. The first part is dedicated to phenotypical characterisation of *der1-3* (*deformed root hairs1*) mutant, in which single point mutation in *ACTIN2* gene influence not only growth of RHs, but affects also other developmental parameters of mutant plants, such as growth pattern of the roots and properties of the actin cytoskeleton in cells of the whole plants. However, better understanding of the molecular mechanisms how the actin cytoskeleton contributes to the proper orientation of the cell division, and what is the role of *ACTIN2* isoform in this process, will require more detailed future studies.

The second part described that *der1-3* mutant was clearly more resistant to oxidative stress as compared to control C24 plants. Enhanced resistance of *der1-3* mutant to mild and severe oxidative stress induced by PQ or H<sub>2</sub>O<sub>2</sub> in the culture medium, was confirmed by better growth parameters, alterations in the actin cytoskeleton, enhanced protection of membrane integrity, higher activity of antioxidant enzymes, and increased capacity for redox modifications. Thus, this section brought some light to resistance against oxidative stress in *der1-3* mutant, in which the single-point mutation of the *ACT2* gene altered broadly also other cellular and molecular mechanisms. The complete mechanism, however, is still not clarified.

The third and last part of results clarified the pattern of polarized AtRBOHC/RHD2 movement, targeting, maintenance, and recycling at the apical PM domain, and helped to better understanding how this pattern could be coordinated with different developmental stages of RH initiation and growth in Arabidopsis. It was confirmed by several qualitative and quantitative microscopic analysis in control condition or after filipin III labelling using advanced microscopic methods. However, the detailed molecular mechanism of the whole process is still not clear.

Seminal parts of the thesis are based on cell biological approaches and utilization of advanced microscopy methods. Some of them, such as light-sheet fluorescence microscopy (LSFM; Weber and Huisken, 2011; Stelzer, 2015) and Airyscan confocal laser scanning microscopy (ACLSM; Sheppard *et al.*, 2016) were applied in original and unique experiments with living plant samples. Therefore, an appropriate way for preparation of living plants for microscopy may represent a challenge. The development and adaptations of appropriate protocols for plant sample preparation, at least for long-term imaging by light-sheet fluorescence microscopy (Ovečka *et al.*, 2015) was an integral part of the Ph.D. thesis as well.

## 8. References

- Balcerowicz D, Schoenaers S, Vissenberg K (2015). Cell fate determination and the switch from diffuse growth to planar polarity in Arabidopsis root epidermal cells. *Frontiers in Plant Sciences* 6: 1163. doi:10.3389/fpls.2015.01163
- Baluška F, Hlavacka A, Šamaj J, Palme K, Robinson D., Matoh T, McCurdy DW, Menzel D, Volkmann D (2002). F-actin-dependent endocytosis of cell wall pectins in meristematic root cells. Insights from Brefeldin A-induced compartments. *Plant Physiology* 130: 422-431. doi: 10.1104/pp.007526
- Berson T, Wangenheim D, Takáč T, Šamajová O, Rosero A, Ovečka M, Komis G, Stelzer EH, Šamaj J (2014). Trans-Golgi network localized small GTPase RabA1d is involved in cell plate formation and oscillatory root hair growth. *BMC Plant Biology* 14: 252. doi: 10.1186/s12870-014-0252-0
- Berthet B, Maizel A (2016). Light sheet microscopy and live imaging of plants. *Journal of microscopy* 263: 158-164. doi: 10.1111/jmi.12393
- Bibikova TN, Blancaflor EB, Gilroy S (1999). Microtubules regulate tip growth and orientation in root hairs of Arabidopsis thaliana. *The Plant Journal* 17: 657-665. doi: 10.1046/j.1365-313X.1999.00415.x
- Bibikova TN, Zhigilei A, Gilroy S (1997). Root hair growth in Arabidopsis thaliana is directed by calcium and an endogenous polarity. *Planta* 203: 495-505. doi: doi.org/10.1007/s004250050219
- Boerjan W, den Boer B, van Montagu M (1992). Molecular genetic approaches to plant development. *The International Journal of Developmental Biology* 36: 59-66.
- Bonneau L, Gerbeau-Pissot P, Thomas D, Der C, Lherminier J, Bourque S, Roche Y, Simon-Plas F (2010). Plasma membrane sterol complexation, generated by filipin, triggers signalling responses in tobacco cells. *Biochimica et Biophysica Acta (BBA) - Biomembranes* 1798: 2150-2159. doi: 10.1016/j.bbamem.2010.07.026
- Boutté Y, Frescatada-Rosa M, Men S, Chow C-M, Ebine K, Gustavsson A, Johansson L, Ueda T, Moore I, Jürgens G, Grebe M (2009). Endocytosis restricts Arabidopsis KNOLLE syntaxin to the cell division plane during late cytokinesis. *EMBO Journal* 29: 546-558. doi: 10.1038/emboj.2009.363
- Braun M, Baluška F, von Witsch M, Menzel D (1999). Redistribution of actin, profilin and phosphatidylinositol-4,5-bisphosphate (PIP2) in growing and maturing root hairs. *Planta* 209: 435-443. doi: 10.1007/s004250050746
- Campanoni P, Blatt MR (2007). Membrane trafficking and polar growth in root hairs and pollen tubes. *Journal of Experimental Botany* 58: 65-74. doi: 10.1093/jxb/erl059
- Carol RJ, Dolan L (2002). Building a hair: tip growth in Arabidopsis thaliana root hairs. *Philosophical Transactions of the Royal Society of London. Series B: Biological Sciences* 357: 815-821. doi: 10.1098/rstb.2002.1092
- Carol RJ, Takeda S, Linstead P, Durrant MC, Kakesova H, Derbyshire P, Drea S, Žárský V, Dolan L (2005). A RhoGDP dissociation inhibitor spatially regulates growth in root hair cells. *Nature* 438: 1013-1016. doi: 10.4161/psb.6.11.17477
- Clouse SD (2002). Arabidopsis mutants reveal multiple roles for sterols in plant development. *The Plant Cell* 14: 1995-2000. doi: 10.1105/tpc.140930
- Denninger P, Reichelt A, Schmidt VAF, Mehlhorn DG, Asseck LY, Stanley CE, Keinath NF, Evers JF, Grefen C, Grossmann G (2019). Distinct RopGEFs successively drive polarization and outgrowth of root hairs. *Current Biology* 29: 1854-1865. doi: 10.1016/j.cub.2019.04.059
- Dolan L, Duckett CM, Grierson C, Linstead P, Schneider K, Lawson E, Dean C, Roberts K (1994). Clonal relationships and cell patterning in the root epidermis of Arabidopsis. *Development* 120: 2465-2474. doi: 10.1242/dev.120.9.2465
- Dvořák P, Krasnylenko Y, Zeiner A, Šamaj J, Takáč T (2021). Signaling toward reactive oxygen species-scavenging enzymes in plants. *Frontiers in Plant Science* 11: 1153. doi: 10.3389/fpls.2020.618835

- Era A, Tominaga M, Ebine K, Awai C, Saito C, Ishizaki K, Yamato KT, Kohchi T, Nakano A, Ueda T (2009). Application of Lifeact reveals F-actin dynamics in *Arabidopsis thaliana* and the liverwort, *Marchantia polymorpha*. *Plant & Cell Physiology* 50: 1041-1048. doi: 10.1093/pcp/pcp055
- Fasshauer D, Sutton RB, Brunger AT, Jahn R (1998). Conserved structural features of the synaptic fusion complex: SNARE proteins reclassified as Q- and R-SNAREs. *Proceedings of the National Academy of Sciences USA* 95: 15781-15786. doi: 10.1073/pnas.95.26.15781
- Foreman J, Demidchik V, Bothwell JH, Mylona P, Miedema H, Torres MA, Linstead P, Costa S, Brownlee C, Jones JD, et al. (2003). Reactive oxygen species produced by NADPH oxidase regulate plant cell growth. *Nature* 422: 442-446. doi: 10.1038/nature01485
- Foreman J, Dolan L (2001). Root hairs as a model system for studying plant cell growth. *Annals of Botany* 88: 1-7. doi: 10.1006/anbo.2001.1430
- Frémont S, Hammich H, Bai J, Wioland H, Klinkert K, Rocancourt M, Kikuti C, Stroebel D, Romet-Lemonne G, Pylypenko O, Houdusse A, Echard A (2017). Oxidation of F-Actin controls the terminal steps of cytokinesis. *Nature Communication* 8: 14528. doi: 10.1038/ncomms14528
- Fu Y, Gu Y, Zhen Z, Wasteneys G, Yang Z (2005). Arabidopsis interdigitating cell growth requires two antagonistic pathways with opposing action on cell morphogenesis. *Cell* 120: 687-700. doi: 10.1016/j.cell.2004.12.026
- Galway ME, Heckman Jr JW, Schiefelbein JW (1997). Growth and ultrastructure of *Arabidopsis* root hairs: the *rhd3* mutation alters vacuole enlargement and tip growth. *Planta* 201: 209-218. doi: 10.1007/BF01007706
- Geldner N, Dénerveau-Tendon V, Hyman DL, Mayer U, Stierhof YD, Chory J (2009). Rapid, combinatorial analysis of membrane compartments in intact plants with a multicolor marker set. *Plant Journal* 59: 169-178. doi: 10.1111/j.1365-313X.2009.03851.x
- Gellert M, Hanschmann E-M, Lepka K, Berndt C, Lillig CH (2015). Redox regulation of cytoskeletal dynamics during differentiation and de-differentiation. *Biochimica et Biophysica Acta (BBA) - General Subjects* 1850: 1575-1587. doi: 10.1016/j.bbagen.2014.10.030
- Gilliland LU, Kandasamy MK, Pawloski LC, Meagher RB (2002). Both vegetative and reproductive actin isoforms complement the stunted root hair phenotype of the Arabidopsis *act2-1* mutation. *Plant Physiology* 130: 2199-2209. doi: 10.1104/pp.014068
- Gilliland LU, McKinney EC, Asmussen MA, Meagher RB (1998). Detection of deleterious genotypes in multigenerational studies. I. Disruptions in individual *Arabidopsis* actin genes. *Genetics* 149: 717-725. doi: 10.1093/genetics/149.2.717
- Gilliland LU, Pawloski LC, Kandasamy MK, Meagher RB (2003). Arabidopsis actin gene *ACT7* plays an essential role in germination and root growth. *The Plant Journal* 33: 319-328. doi: 10.1046/j.1365-313X.2003.01626.x
- Goddard RH, Wick SM, Silflow CD, Snustad DP (1994). Microtubule components of the plant cell cytoskeleton. *Plant Physiology* 104: 1-6. doi: 10.1104/pp.104.1.1
- Goode BL, Drubin DG, Barnes G (2000). Functional cooperation between the microtubule and actin cytoskeletons. *Current Opinion in Cell Biology* 12: 63-71. doi: 10.1016/S0955-0674(99)00058-7
- Grebe M, Xu J, Möbius W, Ueda T, Nakano A, Geuze HJ, Rook MB, Scheres B (2003). Arabidopsis sterol endocytosis involves actin-mediated trafficking via ARA6-positive early endosomes. *Current Biology* 13: 1378-1387. doi: 10.1016/S0960-9822(03)00538-4
- Grierson C, Schiefelbein J (2002) Root hairs. *Arabidopsis Book* 1: e0060. doi: 10.1199/tab.0060
- Grosshans BL, Ortiz D, Novick P (2006). Rabs and their effectors: achieving specificity in membrane traffic. *Proceedings of the National Academy of Sciences USA* 103: 11821-11827. doi: 10.1073/pnas.0601617103
- Hao H, Fan L, Chen T, Li R, Li X, He Q, Botella MA, Lin J (2014). Clathrin and membrane microdomains cooperatively regulate RbohD dynamics and activity in Arabidopsis. *The Plant Cell* 26: 1729-1745. doi: 10.1105/tpc.113.122358

- Hawes C, Crooks K, Coleman J, Satiat-Jeuematrie B (1995). Endocytosis in plants: fact or artefact? *Plant. Cell and Environment* 18: 1245-1252. doi: 10.1111/j.1365-3040.1995.tb00184.x
- Henty-Ridilla JL, Li J, Blanchoin L, Staiger CJ (2013). Actin dynamics in the cortical array of plant cells. *Current Opinion in Plant Biology* 16: 678-687. doi: 10.1016/j.pbi.2013.10.012
- Higaki T, Kutsuna N, Okubo E, Sano T, Hasezawa S (2006). Actin microfilaments regulate vacuolar structures and dynamics: dual observation of actin microfilaments and vacuolar membrane in living tobacco BY-2 Cells. *Plant & Cell Physiology* 47: 839-852. doi: 10.1093/pcp/pcj056
- Ito E, Uemura T (2022). RAB GTPases and SNAREs at the trans-Golgi network in plants. *Journal of Plant Research* 135:389-403. doi: 10.1007/s10265-022-01392-x
- Jones MA, Raymond MJ, Yang Z, Smirnov N (2007). NADPH oxidase-dependent reactive oxygen species formation required for root hair growth depends on ROP GTPase. *Journal of Experimental Botany* 58: 1261-1270. doi: 10.1093/jxb/erl279
- Jones MA, Shen JJ, Fu Y, Li H, Yang Z, Grierson CS (2002). The Arabidopsis Rop2 GTPase is a positive regulator of both root hair initiation and tip growth. *The Plant Cell* 14: 763-776. doi: 10.1105/tpc.010359
- Kandasamy MK, Burgos-Rivera B, McKinney EC, Ruzicka DR, Meagher RB (2007). Class-specific interaction of profilin and ADF isoforms with actin in the regulation of plant development. *Plant Cell* 19: 3111-3126. doi: 10.1105/tpc.107.052621
- Kang E, Zheng M, Zhang Y, Yuan M, Yalovsky S, Zhu L, Fu Y (2017). The microtubule-associated protein MAP18 affects ROP2 GTPase activity during root hair growth. *Plant Physiology* 174: 202–222. doi:10.1104/pp.16.01243
- Kartasalo K, Pölonen R-P, Ojala M, Rasku J, Leikkala J, Aalto-Setälä K, Kallio P (2015). CytoSpectre: a tool for spectral analysis of oriented structures on cellular and subcellular levels. *BMC Bioinformatics* 16: 344. doi: 10.1186/s12859-015-0782-y
- Ketelaar T, Faivre-Moskalenko C, Esseling JJ, de Ruijter NCA, Grierson CS, Dogterom M, Emons AMC (2002). Positioning of nuclei in Arabidopsis root hairs: an actin-regulated process of tip growth. *The Plant Cell* 14: 2941-2955. doi: 10.1105/tpc.005892
- Kojo KH, Higaki T, Kutsuna N, Yoshida Y, Yasuhara H, Hasezawa S (2013). Roles of cortical actin microfilament patterning in division plane orientation in plants. *Plant & Cell Physiology* 54: 1491-1503. doi: 10.1093/pcp/pct093
- Kojo KH, Yasuhara H, Hasezawa S (2014). Time-sequential observation of spindle and phragmoplast orientation in BY-2 cells with altered cortical actin microfilament patterning. *Plant Signaling & Behavior* 9: e29579. doi: 10.4161/psb.29579
- Komis G, Novák D, Ovečka M, Šamajová O, Šamaj J (2018). Advances in Imaging Plant Cell Dynamics. *Plant Physiology* 176: 80-93. doi: 10.1104/pp.17.00962
- Koornneef M and Meinke D (2010). The development of Arabidopsis as a model plant. *The Plant Journal* 61: 909-921. doi: 10.1111/j.1365-313X.2009.04086.x
- Kopczak SD, Haas NA, Hussey PJ, Silflow CD, Snustad DP (1992). The small genome of *Arabidopsis* contains at least six expressed  $\alpha$ -tubulin genes. *The Plant Cell* 4: 539-547. doi: 10.1105/tpc.4.5.539
- Lamkemeyer P, Laxa V, Collin V, Li W, Finkemeier I, Schöttler MA, Holtkamp V, Tognetti VB, Issakidis-Bourguet E, Kandlbinder A, Weis E, Miginiac-Maslow M, Dietz K-J (2006). Peroxiredoxin Q of Arabidopsis thaliana is attached to the thylakoids and functions in context of photosynthesis. *The Plant Journal* 45: 968-981. doi: 10.1111/j.1365-313X.2006.02665.x
- Lanza M, Garcia-Ponce B, Castrillo G, Catarecha P, Sauer M, Rodriguez-Serrano m, Pérez-García A, Sánchez-Bermejo E, TC M, del Puerto YL, Sandalio LM, Paz-Ares J, Leyva A (2012). Role of actin cytoskeleton in brassinosteroid signaling and in its integration with the auxin response in plants. *Developmental Cell* 22: 1275-1285. doi: 10.1016/j.devcel.2012.04.008



- Larkindale J, Knight MR (2002). Protection against heat stress-induced oxidative damage in Arabidopsis involves calcium, abscisic acid, ethylene, and salicylic acid. *Plant Physiology* 128: 682-695. doi: 10.1104/pp.010320
- Lindsey K, Pullen ML, Topping JF (2003). Importance of plant sterols in pattern formation and hormone signalling. *Trends in Plant Science* 8: 521-525. doi: 10.1016/j.tplants.2003.09.012
- Liu B, Joshi HC, Wilson TJ, Silflow CD, Palevitz BA, Snustad DP (1994). Gamma-tubulin in Arabidopsis: gene sequence, immunoblot, and immunofluorescence studies. *The Plant Cell* 2: 303-314. doi: 10.1105/tpc.6.2.303
- Liu P, Zhang L, Li R, Wang Q, Niehaus K, Baluška F, Šamaj J, Lin J (2009). Lipid microdomain polarization is required for NADPH oxidase-dependent ROS signaling in *Picea meyeri* pollen tube tip growth. *The Plant Journal* 60: 303-313. doi: 10.1111/j.1365-313X.2009.03955.x
- Lloyd C, Chan J (2004). Microtubules and the shape of plants to come. *Nature Reviews Molecular Cell Biology* 5: 13-23. doi: 10.1038/nrm1277
- Mauko A, Muck T, Mirtič B, Mladenovič A, Kreft M (2009). Use of confocal laser scanning microscopy (CLSM) for the characterization of porosity in marble. *Materials Characterization* 60: 603-609. doi: 10.1016/j.matchar.2009.01.008
- Meagher RB, McKinney EC, Vitale AV (1999). The evolution of new structures: clues from plant cytoskeletal genes. *Trends in Genetics* 15: 278-284. doi: 10.1016/S0168-9525(99)01759-X
- Menon AK (2002). Lipid transport - an overview. *Seminars in Cell and Developmental Biology* 13: 159-162. doi: 10.1016/s1084-9521(02)00043-5
- Mhamdi A, Van Breusegem F (2018). Reactive oxygen species in plant development. *Development* 145: dev164376. doi: 10.1242/dev.164376
- Miedema H, Demidchik V, Véry AA, Bothwell JH, Brownlee C, Davies JM (2008). Two voltage-dependent calcium channels co-exist in the apical plasma membrane of *Arabidopsis thaliana* root hairs. *New Phytologist* 179: 378-385. doi: 10.1111/j.1469-8137.2008.02465.x
- Mittler R (2017). ROS Are Good. *Trends in Plant Sciences* 22: 11-19. doi: 10.1016/j.tplants.2016.08.002
- Molendijk AJ, Bischoff F, Rajendrakumar CS, Friml J, Braun M, Gilroy S, Palme K (2001). Arabidopsis thaliana Rop GTPases are localized to tips of root hairs and control polar growth. *The EMBO Journal* 20: 2779-2788. doi: 10.1093/emboj/20.11.2779
- Monshausen GB, Bibikova TN, Messerli MA, Shi C, Gilroy S (2007). Oscillations in extracellular pH and reactive oxygen species modulate tip growth of Arabidopsis root hairs. *Proceedings of the National Academy of Sciences of the USA* 104: 20996-21001. doi: 10.1073/pnas.0708586104
- Morel J, Clavero S, Mongrand S, Furt F, Fromentin J, Bessoule J-J, Blein J-P, Simon-Plas F (2006). Proteomics of plant detergent-resistant membranes. *Molecular & Cellular Proteomics* 5: 1396-1411. doi: 10.1074/mcp.M600044-MCP200
- Mouratou B, Biou V, Joubert A, Cohen J, Shields DJ, Geldner N, Jürgens G, Melançon P, Cherfils J (2005). The domain architecture of large guanine nucleotide exchange factors for the small GTP-binding protein Arf. *BMC Genomics* 6: 20. doi: 10.1186/1471-2164-6-20
- Mustafa AK, Gadalla MM, Sen N, Kim S, Mu W, Gazi SK, Barrow RK, Yang G, Wang R., Snyder SH (2009). H<sub>2</sub>S signals through protein S-sulfhydration. *Science Signaling* 2: ra72. doi: 10.1126/scisignal.2000464
- Nichols BJ, Kenworthy AK, Polishchuk RS, Lodge R, Roberts TH, Hirschberg K, Phair RD, Lippincott-Schwartz J (2001). Rapid cycling of lipid raft markers between the cell surface and Golgi complex. *Journal of Cell Biology* 153: 529542. doi: 10.1083/jcb.153.3.529
- Nishimura T, Yokota E, Wada T, Shimmen T, Okada K (2003). An Arabidopsis ACT2 dominant-negative mutation, which disturbs F-actin polymerization, reveals its distinctive function in root development. *Plant & Cell Physiology* 44: 1131-1140. doi: 10.1093/pcp/pcg158

- Ovečka M, Berson T, Beck M, Derksen J, Šamaj J, Baluška F, Lichtscheidl IK (2010). Structural sterols are involved in both the initiation and tip growth of root hairs in *Arabidopsis thaliana*. *Plant Cell* 22: 2999–3019. doi: 10.1105/tpc.109.069880
- Ovečka M, Lang I, Baluška F, Ismail A, Illěš P, Lichtscheidl IK (2005). Endocytosis and vesicle trafficking during tip growth of root hairs. *Protoplasma* 226: 39–54. doi: 10.1007/s00709-005-0103-9
- Ovečka M, Vaškebová L, Komis G, Luptovčíak I, Smertenko A, Šamaj J (2015). Preparation of plants for developmental and cellular imaging by light-sheet microscopy. *Nature Protocols* 10: 1234–1247. doi: 10.1038/nprot.2015.081
- Overmyer K, Brosché M, Kangasjärvi J (2003). Reactive oxygen species and hormonal control of cell death. *Trends in Plant Science* 8: 335–342. doi: 10.1016/S1360-1385(03)00135-3
- Pei W, Du F, Zhang Y, He T, Ren H (2012). Control of the actin cytoskeleton in root hair development. *Plant Science* 187: 10–18. doi: 10.1016/j.plantsci.2012.01.008
- Pereira-Leal JB, Seabra MC (2001). Evolution of the Rab family of small GTP-binding proteins. *Journal of Molecular Biology* 313: 889–901. doi: 10.1006/jmbi.2001.5072
- Qi J, Wang J, Gong Z, Zhou JM (2017). Apoplastic ROS signaling in plant immunity. *Current Opinion in Plant Biology* 38: 92–100. doi: 10.1016/j.cpb.2017.04.022
- Ramachandran S, Christensen HEM, Ishimaru Y, Dong C-H, Chao-Ming W, Cleary AL, Chua N-H (2000). Profilin plays a role in cell elongation, cell shape maintenance, and flowering in *Arabidopsis*. *Plant Physiology* 124: 1637–1647. doi: 10.1104/pp.124.4.1637
- Rasmussen CG, Wright AJ, Müller S (2013). The role of the cytoskeleton and associated proteins in determination of the plant cell division plane. *The Plant Journal* 75: 258–269. doi: 10.1111/tj.12177
- Reddy GV, Gordon SP, Meyerowitz EM (2007). Unravelling developmental dynamics: transient intervention and live imaging in plants. *Nature Reviews Molecular Cell Biology* 8: 491–501. doi: 10.1038/nrm2188
- Reynaud EG, Peychl J, Huisken J, Tomančák P (2015). Guide to light-sheet microscopy for adventurous biologists. *Nature Methods* 12: 30–34. doi: 10.1038/nmeth.3222
- Ridge RW, Uozumi Y, Plazinski J, Hurley UA, Williamson RE (1999). Developmental transitions and dynamics of the cortical ER of *Arabidopsis* cells with green fluorescent protein. *Plant Cell Physiology* 40: 1253–1261. doi: 10.1093/oxfordjournals.pcp.a029513
- Ringli C, Baumberger N, Diet A, Frey B, Keller B (2002). ACTIN2 is essential for bulge site selection and tip growth during root hair development of *Arabidopsis*. *Plant Physiology* 129: 1464–1472. doi: 10.1104/pp.005777
- Rutherford S, Moore I (2002). The *Arabidopsis* Rab GTPase family: another enigma variation. *Current Opinion in Plant Biology* 5: 518–528. doi: 10.1016/s1369-5266(02)00307-2
- Sagi M, Fluhr R (2006). Production of reactive oxygen species by plant NADPH oxidases. *Plant Physiology* 141: 336–34. doi: 10.1104/pp.106.078089
- Sakai J, Li J, Subramanian KK, Mondal S, Bajrami B, Hattori H, Jia Y, Dickinson BC, Zhong J, Ye K, Chang CJ, Ho Y-S, Zhou J, Luo HR (2012). Reactive oxygen species-induced actin glutathionylation controls actin dynamics in neutrophils. *Immunity* 37: 1037–1049. doi: 10.1016/j.immuni.2012.08.017
- Šamaj J, Baluška F, Voigt B, Schlicht M, Volkmann D, Menzel D (2004). Endocytosis, actin cytoskeleton, and signaling. *Plant Physiology* 135: 1150–1161. doi: 10.1104/pp.104.040683
- Šamaj J, Müller J, Beck M, Böhm N, Menzel D (2006). Vesicular trafficking, cytoskeleton and signalling in root hairs and pollen tubes. *Trends in Plant Science* 11: 594–600. doi: 10.1016/j.tplants.2006.10.002
- Šamaj J, Read ND, Volkmann D, Menzel D, Baluška F (2005). The endocytic network in plants. *TRENDS in Cell Biology* 15: 425–433. doi: 10.1016/j.tcb.2005.06.006

- Sampathkumar A, Lindeboom JJ, Debolt S, Gutierrez R, Ehrhardt DW, Ketelaar T, Persson S (2011). Live cell imaging reveals structural associations between the actin and microtubule cytoskeleton in *Arabidopsis*. *The Plant Cell* 23: 2302-2313. doi: 10.1105/tpc.111.087940
- Schieffelbein JW, Somerville C (1990). Genetic control of root hair development in *Arabidopsis thaliana*. *The Plant Cell* 2: 235-243. doi: 10.1105/tpc.2.3.235
- Sheppard CJR, Mehta SB, Heintzmann R (2013). Superresolution by image scanning microscopy using pixel reassignment. *Opt. Lett.* 38: 2889-2892. doi: 10.1364/OL.38.002889
- Sieberer BJ, Ketelaar T, Esseling JJ, Emons AMC (2005). Microtubules guide root hair tip growth. *New Phytologist* 167: 711-719. doi: 10.1111/j.1469-8137.2005.01506.x
- Sieberer BJ, Timmers ACJ, Lhuissier FGP, Emons AMC (2002). Endoplasmic microtubules configure the subapical cytoplasm and are required for fast growth of *Medicago truncatula* root hairs. *Plant Physiology* 130: 977-988. doi: 10.1104/pp.004267
- Singh R, Singh S, Parihar P, Mishra R., Tripathi DhK, Singh VP, Chauhan DK, Prasad SM (2016). Reactive Oxygen Species (ROS): Beneficial Companions of Plants' Developmental Processes. *Frontiers in Plant Science* 7: 1299. doi: 10.3389/fpls.2016.01299
- Sivaguru M, Urban MA, Fried G, Wesseln CJ, Mander L, Punyasena SW (2016). Comparative performance of airyscan and structured illumination superresolution microscopy in the study of the surface texture and 3D shape of pollen. *Microscopy Research & Technique* 81:101-114. doi: 10.1002/jemt.22732
- Snustad DP, Haas NA, Kopczak SD, Silflow CD (1992). The small genome of *Arabidopsis* contains at least nine expressed  $\beta$ -tubulin genes. *The Plant Cell* 4: 549-556. doi: 10.1105/tpc.4.5.549
- Sorek N, Gutman O, Bar E, Abu-Abied M, Feng X, Running MP, Lewinsohn E, Ori N, Sadot E, Henis YI, et al. (2011). Differential effects of prenylation and S-acylation on type I and II ROPS membrane interaction and function. *Plant Physiology* 155: 706-720. doi: 10.1104/pp.110.166850
- Sorek N, Poraty L, Sternberg H, Bar E, Lewinsohn E, Yalovsky S (2017). Activation Status-Coupled Transient S Acylation Determines Membrane Partitioning of a Plant Rho-Related GTPase. *Molecular and Cellular Biology* 27: 2144-2154. doi: 10.1128/MCB.02347-06
- Srivastava V, Malm E, Sundqvist G, Bulone V (2013). Quantitative proteomics reveals that plasma membrane microdomains from poplar cell suspension cultures are enriched in markers of signal transduction, molecular transport, and callose biosynthesis. *Molecular & Cellular Proteomics* 12: 3874-3885. doi: 10.1074/mcp.M113.029033
- Staiger CJ (2000). Signaling to the actin cytoskeleton in plants. *Annual Review of Plant Physiology and Plant Molecular Biology* 51: 257-288. doi: 10.1146/annurev.arplant.51.1.257
- Staiger CJ, Blanchoin L (2006). Actin dynamics: Old friends with new stories. *Current Opinion Plant in Biology* 9: 554-562. doi: 10.1016/j.pbi.2006.09.013
- Stehbens S, Pemble H, Murrow L, Wittmann T (2012). Imaging intracellular protein dynamics by spinning disk confocal microscopy. *Methods in Enzymology* 504: 293-313. doi: 10.1016/B978-0-12-391857-4.00015-X
- Stelzer EHK (2015). Light-sheet fluorescence microscopy for quantitative biology. *Nature Methods* 12: 23-26. doi: 10.1038/nmeth.3219
- Stojkov D, Amini P, Oberson K, Sokollik C, Duppenhaler A, Simon H-U, Yousefi S (2017). ROS and glutathionylation balance cytoskeletal dynamics in neutrophil extracellular trap formation. *Journal of Cell Biology* 216: 4073-4090. doi: 10.1083/jcb.201611168
- Sunkar R, Kapoor A, Zhu J-K (2006). Posttranscriptional induction of two Cu/Zn superoxide dismutase gene in *Arabidopsis* is mediated by downregulation of miR398 and important for oxidative stress tolerance. *Plant Cell* 18: 2051-2065. doi: 10.1105/tpc.106.041673

- Takáč T, Šamajová O, Luptovčiak I, Pechan T, Šamaj J (2017). Feedback microtubule control and microtubule-actin cross-talk in *Arabidopsis* revealed by integrative proteomic and cell biology analysis of *KATANIN 1* mutants. *Molecular & Cellular Proteomics* 16: 1591-1609. doi: 10.1074/mcp.M117.068015
- Takáč T, Šamajová O, Vadovič P, Pechan T, Košútová P, Ovečka M, Husičková A, Komis G, Šamaj J (2014). Proteomic and biochemical analyses show a functional network of proteins involved in antioxidant defense of the *Arabidopsis anp2anp3* double mutant. *Journal of Proteome Research* 13: 5347-5361. doi: 10.1021/pr500588c
- Takeda S, Gapper C, Kaya H, Bell E, Kuchitsu K, Dolan L (2008). Local positive feedback regulation determines cell shape in root hair cells. *Science* 319: 1241-1244. doi: 10.1126/science.1152505
- Takeuchi M, Karahara I, Kajimura N, Takaoka A, Murata K, Misaki K, Yonemura S, Staehelin LA, Mineyuki Y (2016). Single microfilaments mediate the early steps of microtubule bundling during preprophase band formation in onion cotyledon epidermal cells. *Molecular Biology of the Cell* 27: 1809-1820. doi: 10.1091/mbc.e15-12-0820
- Ueda T, Nakano A (2002). Vesicular traffic: an integral part of plant life. *Current Opinion in Plant Biology* 5: 513-517. doi: 10.1016/s1369-5266(02)00299-6
- Valitova JN, Sulkarnayeva AG, Minibayeva F (2016). Plant sterols: Diversity, biosynthesis, and physiological functions. *Biochemistry (Moscow)* 81: 819-834. doi: 10.1134/S0006297916080046
- Van Damme D, Vanstraelen M, Geelen D (2007). Cortical division zone establishment in plant cells. *Trends in Plant Science* 12: 458-464. doi: 10.1016/j.tplants.2007.08.011
- Vazquez LAB, Sanchez R, Hernandez-Barrera A, Zepeda-Jazo I, Sánchez F, Quinto C, Torres LC (2014). Actin polymerization drives polar growth in *Arabidopsis* root hair cells. *Plant Signaling & Behavior*, 9, e29401. doi: 10.4161/psb.29401
- Voigt B, Timmers A, Šamaj J, Hlavacka A, Ueda T, Preuss M, Nielsen E, Mathur J, Emans N, Stenmark H, *et al.* (2005). Actin-based motility of endosomes is linked to the polar tip growth of root hairs. *European Journal of Cell Biology* 84: 609-621. doi: 10.1016/j.ejcb.2004.12.029
- von Wangenheim D, Rosero A, Komis G, Šamajová O, Ovečka M, Voigt B, Šamaj J (2016). Endosomal interactions during root hair growth. *Frontiers in Plant Science* 6: 1262. doi: 10.3389/fpls.2015.01262
- Wachtler V, Rajagopalan S, Balasubramanian MK (2003). Sterol-rich plasma membrane domains in the fission yeast *Schizosaccharomyces pombe*. *Journal of Cell Science* 116: 867-874. doi: 10.1242/jcs.00299
- Wang E, Babbey CM, Dunn KW (2005). Performance comparison between the high-speed Yokogawa spinning disc confocal system and single-point scanning confocal systems. *Journal of Microscopy* 218: 148-159. doi: 10.1111/j.1365-2818.2005.01473.x
- Wang H, Wang S, Lu Y, Alvarez S, Hicks LM, Ge X, Xia Y (2012). Proteomic analysis of early-responsive redox-sensitive proteins in *Arabidopsis*. *Journal of Proteome Research* 11: 412-424. doi: 10.1021/pr200918f
- Weber M, Huisken (2011). Light sheet microscopy for real-time developmental biology. *Current Opinion in Genetics & Development* 21: 566-572. doi: 10.1016/j.gde.2011.09.009
- Woollard AA, Moore I (2008). The functions of Rab GTPases in plant membrane traffic. *Current Opinion in Plant Biology* 11: 610-619. doi: 10.1016/j.pbi.2008.09.010
- Wright SJ, Centonze VE, Stricker SA, DeVries PJ, Paddock SW, Schatten G (1993). "Introduction to confocal microscopy and three-dimensional reconstruction," in: *Methods in Cell Biology*, ed. Matsumoto B (*Academic Press, San Diego*) 38: 1-45. doi: 10.1016/S0091-679X(08)60998-X
- Yang Z (2002). Small GTPases: versatile signaling switches in plants. *The Plant Cell* 14: S375-S388. doi: 10.1105/tpc.001065
- Yoshida K, Hara S, Hisabori T (2015). Thioredoxin selectivity for thiol-based redox regulation of target proteins in chloroplasts. *Journal of Biological Chemistry* 290: 14278-14288. doi: 10.1074/jbc.M115.647545

Zerial M, McBride H (2001). Rab proteins as membrane organizers. *Nature Reviews Molecular Cell Biology* 2:107-117. doi: 10.1038/35052055

Zhou Y, Yang Z, Guo G, Guo Y (2010). Microfilament dynamics is required for root growth under alkaline stress in *Arabidopsis*. *Journal of Integrative Plant Biology* 52: 952-958. doi: 10.1111/j.1744-7909.2010.00981.x

Zwiewka M, Bielach A, Tamizhselvan P, Madhavan S, Ryad EE, Tan S, Hrtyan M, Dobrev P, Vanková R, Friml J, Tognetti VB (2019). Root adaptation to H<sub>2</sub>O<sub>2</sub>-induced oxidative stress by ARF-GEF BEN1- and cytoskeleton-mediated PIN2 trafficking. *Plant Cell & Physiology* 60: 255-273. doi: 10.1093/pcp/pcz001

## 9. List of publication

1. **Kuběnová L**, Tichá M, Šamaj J, Ovečka M (2022) ROOT HAIR DEFECTIVE 2 vesicular delivery to the apical plasma membrane domain during Arabidopsis root hair development. *Plant Physiology* **188**: 1563-1585. doi: 10.1093/plphys/kiab595. (IF=8.972)
2. Ovečka M, Sojka J, Tichá M, Komis G, Basheer J, Marchetti C, Šamajová O, **Kuběnová L**, Šamaj J (2022) Imaging plant cells and organs with light-sheet and super-resolution microscopy. *Plant Physiology* **188**: 683-702. doi: 10.1093/plphys/kiab349. (IF=8.972)
3. **Kuběnová L**, Takáč T, Šamaj J, Ovečka M (2021). Single Amino Acid Exchange in ACTIN2 confers Increased Tolerance to Oxidative Stress in Arabidopsis *der1-3* Mutant. *International Journal of Molecular Sciences* **22**: 1879. doi: 10.3390/ijms22041879. (IF=5.542)
4. **Vaškebová L**, Šamaj J, Ovečka M (2018). Single-point ACT2 gene mutation in the Arabidopsis root hair mutant *der1-3* affects overall actin organization, root growth and plant development. *Annals of Botany* **122**: 889-901. doi: 10.1093/aob/mcx180. (IF= 3.454)
5. Ovečka M, **Vaškebová L**, Komis G, Luptovčíak I, Smertenko A, Šamaj J (2015). Preparation of plants for developmental and cellular imaging by light-sheet microscopy. *Nature Protocols* **10**: 1234-1247. doi: 10.1038/nprot.2015.081. (IF=10.032)

## 10. List of attended conferences

1. **Kuběnová L**, Tichá M, Šamaj J, Ovečka M (2021). Spatiotemporal pattern of AtrbohC/ROOT HAIR DEFECTIVE 2 redistribution during root hair formation in *Arabidopsis thaliana*. Online SEB Annual Conference, Antwerp, Belgium, 29. June - 8. July 2021. Oral presentation.
2. Ovečka M, **Vaškebová L**, Takáč T, Šamaj J (2017). Cytoskeletal fluorescent markers enhance plant vigour, biomass production and stress response in C24 ecotype of *Arabidopsis thaliana*. Plant Biotechnology: Green for Good IV, Olomouc, Czech Republic, 19.-22. June 2017. Poster presentation.
3. **Vaškebová L**, Ovečka M, Šamaj J (2015). Is sensitivity to selected abiotic stresses compromised in root hair mutants of *Arabidopsis thaliana*? Plant Biotechnology: Green for Good III, Olomouc, Czech Republic, 15.-18. June 2015. Poster presentation.
4. **Vaškebová L**, Šatná B, Ovečka M, Šamaj J (2014). Sensitivity of selected root hair mutants of *Arabidopsis thaliana* to abiotic stress. 16th European Congress on Biotechnology, Edinburgh, Scotland, 13.-16. July 2014. Poster presentation.

## 11. Abstrakt

Kořenové vlásky a jejich apikální růst slouží jako excelentní model pro studium polárního prodlužování buněk. Díky nim je rostlina stabilněji ukotvena v půdě, zvětšují povrch kořenového systému, což vede k efektivnějšímu příjmu vody a živin, a v neposlední řadě se podílejí na interakci s mikroby. Iniciační a následný polární růst kořenových vlásků je velice složitý proces, který zahrnuje mnoho navzájem propojených mechanismů. Mezi nezbytné děje nutné k založení a udržení polárního růstu kořenových vlásků patří polarizace cytoskeletu, vezikulární transport a lokalizované ukládání buněčné stěny v místě trichoblastu, ze kterého budoucí kořenových vlásek vyrůstá. Současný stav poznání, zabývající se právě procesy vývoje kořenových vlásků a jejich polárního růstu, je shrnutý v teoretické části této disertační práce. Hlavním cílem praktické části byla důkladná charakteristika dvou rozdílných mutantů (*der1-3* a *rhd2-1*) rostlin *Arabidopsis thaliana*, kteří mají poruchu růstu kořenových vlásků.

Mutant *der1-3* („*defective root hairs 1*“) má bodovou mutaci v *ACTIN2* genu. *ACTIN2* je nejvíce se vyskytující isovarianta aktinu ze skupiny isovariant vegetativního aktinu. *ACTIN2* je zároveň nezbytnou součástí mechanismu růstu kořenových vlásků. Identifikace *der1-3* mutantu byla proto založená na vyhledávání fenotypu krátkých kořenových vlásků. Pomocí důkladného fenotypování rostlin, studia pletiv kořenového systému a analýz na subcelulární úrovni jsme zjistili, že mutace v *ACT2* genu má výraznější efekt na celkový vývoj a růst rostlin, což v předchozích studiích tohoto mutantu popsáno nebylo. Dále pak, díky lepším růstovým parametrům, zvýšené dynamiky aktinového cytoskeletu a účinnější biochemické ochrany *der1-3* mutantu po působení oxidativního stresu bylo zjištěno, že je více odolný na tento typ stresu oproti kontrolním rostlinám. Získané výsledky podpořili fakt, že aktinový cytoskelet nehraje roli jen při růstu a vývoji rostlin a kořenových vlásků, ale že ovlivňuje i reakci rostlin na oxidativní stres. To vše dohromady by mohlo mít slibný potenciál v budoucím zemědělském a biotechnologickém využití.

V apikální části plazmatické membrány (PM) rostoucích kořenových vlásků *A. thaliana* se nachází NADPH oxidasa typu C, pojmenována jako „respiratory burst oxidase homolog protein C/ROOT HAIR-DEFECTIVE 2“ (*AtRBOHC/RHD2*). Tato oxidasa tvoří reaktivní formy kyslíku (ROS), které mimo jiné udržují polární růst kořenových vlásků. Bodová mutace v *RHD2* genu způsobuje fenotyp krátkých kořenových vlásků, čímž je *rhd2-1* („*root hair defective 2*“) mutant charakteristický. V této části jsme detailně popsali časoprostorovou distribuci a dynamické vlastnosti transportu *AtRBOHC/RHD2* proteinu do plazmatické membrány rostoucích kořenových vlásků. S využitím různých pokročilých mikroskopických metod a pomocí následných kvantitativních mikroskopických analýz, trasování jednotlivých kompartmentů a pomocí subcelulárních kolokalizací jsme popsali komplexní mechanismus transportu a recyklace *AtRBOHC/RHD2* v rámci apikální PM během tvorby a následného apikálního růstu kořenového vlásku u *Arabidopsis*.

Nová data, prezentovaná v této disertační práci, byla získána s využitím pokročilých mikroskopických metod pro rychlé snímání dynamických procesů (konfokální mikroskopie s rotujícím diskem), dlouhodobé vývojové snímání za podmínek, blížících se těm environmentálním („*light-sheet*“ fluorescenční mikroskopie) a pro snímání s vysokým rozlišením (konfokální laserová skenovací mikroskopie s Airyscan detektorem). Kombinace nižší míry fototoxicity, většího rozlišení a vyšší rychlosti snímání v průběhu delšího časového úseku umožnila studium živých rostlin v téměř přirozených podmínkách, přinášející fyziologicky relevantní výsledky.